UNIVERSITY OF CALIFORNIA, SAN DIEGO

Vibration-based Structural Health Monitoring of Highway Bridges

A dissertation submitted in partial satisfaction of

the requirements for the degree Doctor of Philosophy

in

Structural Engineering

by

Hong Guan

Committee in charge:

Vistasp M. Karbhari, Chair
Gilbert A. Hegemier
Hidenori Murakami
P. Benson Shing
Mohan Trivedi
Frank Vernon

2006

The dissertation of Hong Guan is approved, and it is acceptable in quality and form for publication on microfilm:

_____

_____

_____

_____

_____

_____

Chair

University of California, San Diego

2006

To my wife and my parents

TABLE OF CONTENTS

LIST OF FIGURES

LIST OF TABLES

LIST OF SYMBOLS

a_k — crack size

Δa_e — element damage index

A — area of the plate surface

A — cross sectional area of the beam

A_m^e — Element Modal Strain Damage Index

$[A]$ — state space system matrix A

$\{b\}$ — parameter vector containing the storey mass and stiffness of the shear building

$\{b'\}$ — $(2n-2)\times(1)$ vector in which the last two members of $\{b\}$ are eliminated

$[B]$ — matrix containing eigenvalues and eigenvectors of shear building

$[B']$ — $(2n-2)\times(2n-2)$ matrix in which the last rows and last two columns of $[B]$ are eliminated

B^+ — Penrose generalized inverse of the matrix B

$c_{i(j)}$ — damping parameter of the j^{th} storey

c_j — cutoff of singular values

$[C]$ — damping matrix

$[C_j]$ — element stiffness matrix

$\left[C_{j0}\right]$ — portion of the element stiffness matrix containing only geometric quantities

$\left[\Delta C\right]$ — damping correction matrix

$\mathbf{d}_{i(j)}(t)$ — relative displacement between the j^{th} storey and $(j\text{-}1)^{\text{th}}$ storey for the i^{th} mode of vibration

$\dot{\mathbf{d}}_{i(j)}(t)$ — relative velocity between the j^{th} storey and $(j\text{-}1)^{\text{th}}$ storey for the i^{th} mode of vibration

d_{ik} — linear combination coefficient of mode shape change in terms of original mode shapes

$\mathbf{d}_k$ — search direction at iteration k

D — flexural rigidity of a plate

DF — change in dynamically measured flexibility

e_{ij} — damage index of j^{th} element calculated using i^{th} mode modal parameters

EI — dynamic bending stiffness / flexural rigidity

E_j — parameter representing material stiffness properties related to the undamaged structure / updated Young's modulus of element group j

E_j^* — parameter representing material stiffness properties related to the damaged structure

E_j^{ref} — baseline Young's modulus of element group j

$[E_n]$ — autocorrelation of the n^{th} mode-isolated acceleration time history

$\mathbf{f}_{i(j)}(t)$ — inertia force acting on storey masses of j^{th} storey

$\{f(t)\}$ — vector of input forcing functions

F_{ij} — sensitivity of fractional change of i^{th} eigen-frequency to fractional reduction in j^{th} element's stiffness parameter, undamaged structure

F_{ij}^{*} — sensitivity of fractional change of i^{th} eigen-frequency to fractional reduction in j^{th} element's stiffness parameter, damaged structure

F_D — flexibility of damaged states

F_U — flexibility of undamaged states

$[F]$ — stiffness sensitivity matrix

$\{F(t)\}$ — vectors of external force at each degrees-of-freedom

g_i — fractional change of modal stiffness for mode i

$g_i(\mathbf{p})$ — nonlinear constraints

$g[x_i, x_{i+1}]$ — second divided difference of a function g

$G_{ij}(j\omega)$ — cross-spectral density function

GJ — torsional stiffness of the beam

$[G]$ — mass sensitivity matrix

$\left[G_{ij}(\omega)\right]$ — $N_o \times N_{Ref}$ cross-spectrum matrix

h — spacing between measurement sites

$h_{ij}(t)$ — impulse response function between DOF i and j

H — beam depth

$H_{ij}(j\omega)$ — accelerance frequency response function

H_k — Hessian of objective function

J — least squares error function

$\mathbf{J}(\mathbf{p})$ — objective function of model updating

k_i — stiffness parameter of i^{th} storey

k_e — element stiffness matrix

$\tilde{k}_r$ — the estimate of parameters k_i

$\tilde{k}^{(0)}$ — the initial estimate of parameters k_i

$k_{i(j)}$ — stiffness parameter of the j^{th} storey

K — updated mass and stiffness matrix

K_0 — portion of the stiffness matrix that remain unchanged before and after the updating

K_j^E — element mass matrix for element j

K^d — stiffness matrix of damaged structure

[K] — stiffness matrix

$[\Delta K]$ — stiffness correction matrix

l_e — beam element length

L — length of the beam element

$L(\mathbf{p}, \lambda)$ — Lagrangian function

m — number of total constraints

m_e — number of equality constraints

m_i — mass parameter of i^{th} storey

M — bending moment

M_4 — constant term determined by the maximum value of the 4th derivative of ϕ

M_i — modal bending moment

M_j^E — element mass matrix for element j

M_0 — portion of the mass matrix that remain unchanged before and after the updating

$MAC(\mathbf{\Phi}_i, \mathbf{\Phi}_j)$ — modal assurance criterion for mode i and j

$MSEC_{ij}$ — change of modal strain energy of element j and mode i

$MSCER_j^i$ — Modal Strain Energy Change Ratio of element j and mode i

MSE_{ij} — modal strain energy of j^{th} element of the intact structure for mode i

$MSE_{ij}^{\ d}$ — modal strain energy of j^{th} element of the damaged structure for mode i

[M] — mass matrix

$[\Delta M]$ — mass correction matrix

nsi_j — normalized stress index vector

N — number of elements

N_d — degrees-of-freedom in a system

N_E — number of elements with updated parameters

N_p — number of parameters to be updated

N_R — total number of residues

N_{Ref} — number of reference locations used to calculate the cross-spectrum function

N_s — number of discrete time points at which acceleration response is sampled

N_ϕ — number of modes used in the correlation process

N_ω — total number of natural frequencies compared in the model updating process

NE — number of elements

$N_i(\tilde{x})$ — cubic shape function

$[N_e]$ — geometric configuration matrix

p — number of suspected damaged sites

p_k — updated value of k^{th} parameter

p_k^{ref} — reference value of k^{th} parameter

$\delta\mathbf{p}$ — change of parameters at k^{th} iteration

$\{\mathbf{p}\}$ — vector of structural parameters

$\mathbf{p}_k$, $\mathbf{p}_{k+1}$ — vector of structural parameters at k^{th} and $k+1^{\text{th}}$ iteration

$\mathbf{P}_L$, $\mathbf{P}_U$ — vectors of lower and upper bounds for the structural parameters

$q_r(t)$ — generalized coordinate for mode r at time instant t

$\ddot{\mathbf{q}}_r$ — $N_s \times 1$ vector containing values of the r^{th} generalized coordinate

Q_{jr} — modal contribution factor of NExT technique for mode r

Q_n — modal contribution of n^{th} mode

$\mathbf{R}$ — residual vector

$\mathbf{R}_k$ — residual function vector at iteration k

ΔR_{ij} — residue caused by damage

$R_{ij}(T)$ — cross-correlation function between the two stationary responses from the i^{th} DOF and the j^{th} DOF

$R''_{ijk}(T)$ — cross-correlation of acceleration response between the i^{th} DOF and the j^{th} DOF due to input at k^{th} DOF

$\mathrm{R}(\mathrm{x})$ — constraint function

s_2 — singular values

s_i — free parameter of cubic polynomial

svn_j — svn index

S_1 — singular values

S_{ik} — sensitivity of the k^{th} location in the i^{th} modal strain energy

$\mathbf{S}_k$ — sensitivity matrix at iteration k

$\tilde{\mathrm{u}}(\mathrm{x})$ — analytically calculated vibration response

$\overline{\mathrm{u}}$ — experimentally measured vibration response

$\mathbf{u}_n(x,t)$ — n^{th} modal contribution to the response

U — left singular vectors

U_i — modal strain energy of mode i

U_s — bending strain energy of an Euler-Bernoulli beam

U_i^S — instantaneous strain energy of the structure

$[U]$ — $N_d \times N_s$ response matrix

$v''(x)$ — 2nd derivative of the beam transverse displacement

V — right singular vectors

V_i — modal shear force

w_i — transverse degree of freedom at node i

w_r^e — rotational DOFs of a four-node plate element

w_t^e — transverse DOFs of a four-node plate element

$\mathbf{W}$ — weighting matrix

W_{ir} — modal participation factor

$\mathbf{W}_p$ — weighting matrix of the parameters

$\mathbf{W}_R$ — weighting matrix of residues

WSI — vector of weighted stress indices

x — system parameters

X — vector spaces of the system parameters

x_i, x_{i-1}, x_{i+1} — current, previous, and next measurement sites where displacement mode shapes are available

$x_i(t)$ — response at the i^{th} degree of freedom (DOF)

$\{x(t)\}$ — structure response vector

$X_{i(j)}(t)$ — absolute displacement of the j^{th} storey for the i^{th} mode of vibration

Z_i — fractional change of i^{th} eigenfrequency

Z_j — normalized damage indicator

$\{Z\}$ — vector of measured frequency changes

$\alpha_{i,j}$ — receptance FRF measured at location i for a force input at location j

α_j — fractional reduction in j^{th} element's stiffness parameter

α_k — correction factor for k^{th} parameter / coefficients of rational fractional polynomial model

$\{\alpha\}$ — vector of changes in system stiffness parameters

β_j — damage index for the j^{th} member

β_k — coefficients of rational fractional polynomial model

$\overline{\beta}$ — mean value of β

β_{st} — sensitivity coefficient of MSEC to damage

$\{\beta\}$ — vector of changes in system mass parameters

Δ_{ij} — deformation of j^{th} element in i^{th} mode

Δ^i_{EMSDI} — EMSDI difference of the i^{th} element

$\overline{\Delta}_{EMSDI}$ — mean value of EMSDI difference

$\tilde{\Delta}_{EMSDI}^{i}$ — normalized EMSDI difference value for the i^{th} element

ε — maximum relative random multiplicative error of mode shape ϕ

ε_i — normally distributed random error

η — shape factor related to the beam geometry

θ_i — rotational degree of freedom at node i

θ_i and θ_j — mode shape amplitude at the rotation degree-of-freedom at node i and j

$\Theta_j^A(\mathbf{p})$ — analytical modal parameter

Θ_j^E — experimental modal parameter

κ — modal curvature

λ_i — i^{th} eigenvalue

λ_l — l^{th} eigenvalue

λ_i — i^{th} Lagrange multiplier

$[\Lambda]$ — $2N_d \times 2N_d$ complex eigenvalue matrix

ρ — material density

$\Pi_{<4}$ — linear space of the polynomials of order 4

Π_E — error function

σ_Δ — standard deviation of EMSDI difference

σ_β — standard deviation of β

σ_m — standard deviation of measured noisy modal displacements

υ — vector spaces of measured vibration responses

υ^c — subspace of υ consisting of vibration responses corresponding to the whole domain of system parameters X

ϕ_i — i^{th} eigenvector

ϕ_l — l^{th} eigenvector

ϕ_{ie} — ith element mode shape of element e

ϕ_{ir} — i^{th} component of r^{th} mode shape

ϕ_{kr} — k^{th} component of r^{th} mode shape

ϕ_i and ϕ_j — mode shape amplitude at transverse degree-of-freedom of node i and j

$\phi_{lj}^A(\mathbf{p})$ — analytical mode shapes of l^{th} mode at DOF j

ϕ_{lj}^E — experimental mode shapes of l^{th} mode at DOF j

$\phi(x_i)$ — mode shape value at a measurement site x_i

$\{\phi_r\}$ — the r^{th} mode shape vector

Φ_i — undamaged mode shape of mode i

$\tilde{\Phi}_j$ — damaged mode shape of jth mode

$\Delta\Phi_i$ — mode shape change of i^{th} mode

φ_i — i^{th} transformed eigenvector of the system

$\boldsymbol{\varphi}_r(x)$ — r^{th} mode shape function

$\boldsymbol{\varphi}_r$ — $N_d \times 1$ r^{th} mode shape vector

φ^b — modal curvature

φ^t — torsion rate

$[\Phi]$ — $N_d \times 2N_d$ system eigenvector or mode shape matrix

ψ_j — eigenvector calculated from the initial estimate of system stiffness matrix

$[\Psi]$ — $2N_d \times 2N_d$ complex modal matrix

ω_i^2 — eigenvalue for mode i

$\tilde{\omega}_j^2$ — damaged frequency of jth mode

$\delta\omega_i^2$ — change of eigenvalue for mode i

$\omega_k^A(\mathbf{p})$ — k^{th} analytical natural frequency

ω_k^E — k^{th} experimental natural frequency

ACKNOWLEDGEMENTS

I would like to express my deepest appreciation to my committee chair and my advisor, Professor Vistasp M. Karbhari.

I would also like to thank my committee members, Professor Gilbert A. Hegemier, Professor Hidenori Murakami, Professor P. Benson Shing, Professor Mohan Trivedi, and Dr. Frank Vernon, for their helpful comments.

The funding support from the California Department of Transportation for this research is hereby gratefully acknowledged. I would also like to thank Dr. Charles Sikorsky and Professor Norris Stubbs for their valuable inputs during the various phases of this research.

I also owe my gratitude for the many lively discussions with all of my colleagues. Thank you all for the great help.

Assistance from Mr. James Batti, Mr. Kenny Kenzel, Mr. Frank Ho, Dr. Christopher Latham and Mr. Larry Berman, among others, during the experimental part of this research is highly appreciated.

Chapter 4 of this dissertation, in part, has been submitted for publication in the Journal of Sound and Vibration under the title "Improved Damage Detection Method Based on Element Modal Strain Damage Index Using Sparse Measurement" in 2006. The dissertation author was the principle researcher/author on this paper.

VITA

1998	B.E., Tongji University, Shanghai, China
2000	M.Phil., Hong Kong University of Science and Technology, Hong Kong, China
2002-2006	Research Assistant, University of California, San Diego
2006	Ph.D., University of California, San Diego

PUBLICATIONS

Journal Papers

Hong Guan, Charles Sikorsky and Vistasp M. Karbhari, *Web-based Structural Health Monitoring of a FRP Composite Bridge,* Computer-Aided Civil and Infrastructure Engineering, Vol. 21, No. 1, pp39-56, January 2006.

Hong Guan and Vistasp M. Karbhari*, Improved Damage Detection Method Based on Element Modal Strain Damage Index Using Sparse Measurement*, Journal of Sound and Vibration (Submitted for publication, 2006).

Hong Guan, Vistasp M. Karbhari and Charles Sikorsky*, Long-Term Structural Health Monitoring System for A FRP Composite Highway Bridge Structure*, Smart Materials and Structures (Submitted for publication, 2005).

Conference Papers

Hong Guan, Vistasp M. Karbhari and Charles Sikorsky, *Operational Modal Analysis for Long-term Bridge Performance Monitoring,* Submitted to the Third International Conference on Bridge Maintenance, Safety and Management, July 16-19, 2006, Porto-Portugal.

Hong Guan, Vistasp M. Karbhari and Charles Sikorsky, *Vibration-based Health Monitoring of Highway Bridge Structure using Output Only Modal Parameter*

Estimation Technique, Proceedings of the 2005 Caltrans Bridge Research Conference, Sacramento, CA, October 31 - November 1, 2005.

Hong Guan, Vistasp M. Karbhari and Charles Sikorsky, *Time-Domain Output Only Modal Parameter Extraction and Its Application,* Proceedings of the 1st International Operational Modal Analysis Conference, Copenhagen, Denmark, April 26-27, 2005.

Hong Guan, Vistasp M. Karbhari and Charles Sikorsky, *Health Monitoring Of A FRP Composite Bridge Augmented By Use Of Web Based And Wireless Technologies,* Proceedings of the 1st International Conference on Bridge Maintenance, Safety and Management, IABMAS '04, 8pp, Kyoto, Japan, October 18-22, 2004.

Hong Guan, Vistasp M. Karbhari and Charles Sikorsky, *Remote Structural Health Monitoring Of A FRP Composite Bridge*, Proceedings of the 60th SAMPE Technical Conference, 14pp, Long Beach, CA, May 16-20, 2004.

Vistasp M. Karbhari, Hong Guan, Luke S. Lee and Charles S. Sikorsky, *Characterization and Health Monitoring of FRP Bridge Systems*, Proceedings of the Second International Conference on Advanced Polymer Composites for Structural Applications in Construction: ACIC 2004, pp 18-29, Surrey, United Kingdom, April 20-22, 2004.

Vistasp M. Karbhari, Hong Guan and Charles S. Sikorsky, *Web-Based Structural Health Monitoring of a FRP Composite Bridge*, Proceedings of the 1st International Conference on Structural Health Monitoring and Intelligent Infrastructure, pp 217-226, Tokyo, Japan, November 2003.

C. Sikorsky, N. Stubbs and H. Guan, *The Impact of Natural Frequency Variation on Damage Detection*, Proceedings of the 4th International Workshop on Structural Health Monitoring, Stanford University, Stanford, CA, September 15-17, 2003.

Vistasp M. Karbhari, Hong Guan and Lei Zhao, *Composite Structural Systems – From Characterization to Field Implementation*, Proceedings of the Sixth International Symposium on Fibre-Reinforced Polymer Reinforcement for Concrete Structures, pp 1381-1390, Singapore, July 2003.

<u>*Technical Reports*</u>

Vistasp M. Karbhari, Charles S. Sikorsky, Hong Guan and Luke S. Lee, *Kings Stormwater Channel Crossing FRP Structure (Bridge #56-0778R): March 26, 2003 Trip Report*, TR2003-06, Department of Structural Engineering, University of California, San Diego, May, 2003.

Hong Guan, James Batti, Charles S. Sikorsky and Vistasp M. Karbhari, *Kings Stormwater Channel Bridge Load Test*, TR2002-09, Department of Structural Engineering, University of California, San Diego, September, 2002.

Thesis

Hong Guan, *Construction Control of Cable-Stayed Bridges*, Master of Philosophy Thesis, Hong Kong University of Science and Technology, July, 2000.

Hong Guan, *Formula to Predict the Ultimate Moment Capacity of Large Diameter Confined RC Bridge Columns*, Bachelor of Engineering Thesis, Tongji University, July 1998 (In Chinese).

ABSTRACT OF THE DISSERTATION

Vibration-based Structural Health Monitoring of Highway Bridges

by

Hong Guan

Doctor of Philosophy in Structural Engineering

University of California, San Diego, 2006

Professor Vistasp M. Karbhari, Chair

In recent years, the conditions of aging transportation infrastructure have drawn great attention to the maintenance and inspection of highway bridges. With the increasing importance of life-lines, such as highways, to the national economy and the well-being of the nation, there is a need to maximize the degree of mobility of the system. This requires not just routine, or critical event (such as an earthquake) based, inspections, but rather a means of continuous monitoring of a structure to provide an assessment of changes as a function of time and an early warning of an unsafe condition using real-time data.

A promising technique, namely Vibration-based Structural Health Monitoring, has been proposed to address this problem. The basic premise of Vibration-Based Structural Health Monitoring is that changes in structural characteristics, such as mass,

stiffness and damping, will affect the global vibrational response of the structure. Thus, by studying the changes in measured structural vibration behavior and in essence solving an inverse problem, the unknown changes of structural properties can be identified.

A new vibration-based structural health monitoring methodology for highway bridges is proposed in this dissertation. Progress is made in several key areas, including operation modal analysis, damage localization and finite element model updating. The real-world implementation of a health monitoring system on a highway bridge demonstrated the effectiveness of the proposed technique and pointed out directions for future research.

Chapter 1 Introduction

1.1 Problem Statement and Motivation of Research

All structures, including critical civil infrastructure facilities like bridges and highways, deteriorate with time. This deterioration is due to various reasons including fatigue failure caused by repetitive traffic loads, effects of environmental elements, and extreme events such as an earthquake. In recent years, the situation of aging infrastructure has become a global concern. This is especially true in the case of highway bridges in the Unite States, because a large number of structures in the current bridge inventory were built decades ago and are now considered structurally deficient (Chase and Laman 2000). In order to maintain the safety of the these "life-line" structures, the States are mandated by the National Bridge Inspection program to periodically inventory and inspect all highway bridges on public roads. The National Bridge Inspection Standards (NBIS 1998), implemented in 1971, prescribe minimum requirements for the inspection of highway bridges in the United States. A substantial amount of research has been conducted in this area in order to improve the speed and reliability of such inspections. According to a recent survey performed by the Federal Highway Administration (Moore et al. 2001), visual inspection is still the primary tool used to perform these inspections. The implementation of these inspections consists of scheduled field trips to bridge sites at routine intervals, usually once every several years.

If a significant increase in distress between inspections is noted the period between inspections is decreased and the level of inspection is increased till such time that the distress has been corrected by replacement or repair. Research has shown that such inspections have limited accuracy and efficiency (FHWA 2001). Not only is this method of time-based inspection inefficient in terms of resources, because all bridges are inspected with the same frequency, regardless of the condition of the bridge, but there is also a potential danger that serious damage could happen to the bridge in between two inspections, thus posing a hazard to public safety. Furthermore, rapid assessment of structural conditions after major events such as earthquakes is not possible using such an approach.

With the increasing importance of life-lines, such as highways, to the national economy and the well-being of the nation, there is a need to maximize the degree of mobility of the system. During inspections, issues such as serviceability, reliability and durability need to be answered in precise terms. More specifically the owners (the Federal Highway Administration, State Departments of Transportation etc.) need to be able to answer the following questions: " (a) Has the load capacity or resistance of the structure (serviceability) changed?; (b) What is the probability of failure of the structure (reliability)?; and (c) How long will the structure continue to function as designed (durability)?" (Sikorsky et al. 1999). This requires not just routine, or critical event (such as an earthquake) based, inspections, but rather a means of continuous monitoring of a structure to provide an assessment of changes as a function of time and an early warning of an unsafe condition using real-time data.

Over the past decade, the implementation of Structural Health Monitoring (SHM) systems has emerged as a potential solution to the above challenges. Housner et al. (1997) provide an extensive summary of the state of the art in the control and monitoring of civil engineering structures, and the link between structural control and other forms of control theory. They also define structural health monitoring as "the use of in-situ, nondestructive sensing and analysis of structural characteristics, including the structural response, for detecting changes that may indicate damage or degradation."

Work to date on structural health monitoring systems for civil structures has been useful, but resembles existing bridge management systems. These management systems focus on processing collected data, but are unable to measure or evaluate the rate of structural deterioration for a specific bridge. While most ongoing work related to structural health monitoring conforms to the definition given by Housner et al. (1997), this definition also identifies the weakness associated with these methods. "A health monitoring system, which detects only changes that may indicate damage or degradation in the civil structure without providing a measure of quantification, is of little use to the owner of that structure." (Sikorsky et al. 1999) While researchers have attempted to integrate quantitative Non-Destructive Testing (NDT) with health monitoring, the focus to date has primarily been on data collection, not evaluation. It could be concluded that these efforts have produced better research tools than approaches to bridge management. What is needed is an efficient method to collect data from an in-service structure and process the data to evaluate key performance measures, needed by the owner, such as serviceability, reliability and durability. For the current work, the definition by Housner et al. (1997) is modified and structural

health monitoring is defined as the use of in-situ, nondestructive sensing and analysis of structural characteristics, including the structural response, for the purpose of estimating the severity of damage and evaluating the consequences of damage on the structure in terms of response, capacity, and service-life (Guan et al. 2006). More simply, structural health monitoring represents the implementation of a Level IV (Rytter 1993) non-destructive damage evaluation method.

Based on this, a more effective "condition-based" approach could conceivably be implemented, in which, the condition of the bridge is constantly monitored using an appropriate non-destructive evaluation (NDE) technique without requiring the inspector to actually be on site, with the "in-person" visual inspection being only performed when necessary. The word "constantly" is used to indicate that the assessment of bridge condition would be performed at much shorter intervals than would be possible using current visual inspection procedures. More importantly, the condition assessment could include more quantitative content than could be provided by a visual inspection. The following assessment, for example, would be typically desired by the bridge management authority: (a) damage to the structure and changes in structural resistance, (b) probability of failure or of the structure's performance falling below a certain threshold, and (c) estimation of the severity of damage and the remaining service life. Condition-based monitoring can thus not only reduce resources needed for inspection, but when combined with advances in sensors, computational and telecommunications technology, could also provide for continuous and autonomous assessment of structural response.

On the other hand, structural health monitoring systems can also contribute to rapid post-extreme-event condition screening. With automated monitoring systems in place on critical life-line structures, the condition of these structures can be evaluated shortly after an extreme event has occurred. This rapid evaluation would not be possible using traditional inspection techniques. Necessary decisions to best utilize the remaining intact life-lines can be made based on these evaluations. This could potentially give the authority faster access to the affected areas and thus improving public safety.

1.2 Vibration-Based Structural Health Monitoring Paradigm

Of the various structural health monitoring techniques proposed to date, Vibration-Based Structural Health Monitoring (VBSHM) has drawn significant attention. The basic premise of Vibration-Based Structural Health Monitoring is that changes in structural characteristics, such as mass, stiffness and damping, will affect the global vibrational response of the structure. Thus, by studying the changes in measured structural vibration behavior and in essence solving an inverse problem, the unknown changes of structural properties can be identified. In cases where the changes in structural properties that adversely affect the performance of the structure are defined as ‘damage’, the process of identifying such changes is also referred to as Vibration-Based Damage Identification (VBDI) or Vibration-Based Damage Detection (VBDD).

The global nature of the vibrational characteristics of interest to VBSHM provides advantages compared to other health monitoring techniques. Utilization of

global vibration signatures such as natural frequencies and mode shapes leads to the monitoring of the entire structural system, not just each structural component, which means a large civil engineering structure can be effectively monitored with a relatively small set of sensors and equipment.

In this dissertation, a Vibration-based Structural Health Monitoring paradigm for highway bridge structures is proposed. The paradigm is based on the same premise mentioned above that the global dynamics of structures can be used to quantify changes in structural properties. Efforts are made to tailor various components of the paradigm to highway bridge applications.

Conceptually, the general procedure of the proposed VBSHM system consists of five steps, as shown in Figure 1-1, namely: (1) Measurement of structural dynamic response, e.g., in terms of accelerations or displacements, (2) Characterization of an initial bridge model through dynamic and static tests, (3) Continuous monitoring and damage localization of the structure, (4) Performing finite element model updating in order to obtain up-to-date structure model, and (5) Evaluation of structural performance using the updated finite element model.

The measurement of structural dynamic responses is achieved with an instrumentation system handling the sensing, transmission and storage of dynamic response data. Various characteristics of the instrumentation system, such as sensor types, sampling rate, and storage capacity, etc, need to be customized based on each unique application. Acceleration, velocity and displacement are the most common types of measurement for dynamic response. It should be noted that in order to achieve

continuous monitoring of the bridge structure, large amount of dynamic data need to be collected and processed. The instrumentation system must be designed to handle such types of data throughput.

In order to identify structural properties, the raw dynamic response of the structure such as acceleration time history can be utilized. However, it is more common that vibrational features such as modal parameters are extracted from the raw dynamic response. Modal parameters contain important characteristics of the structural dynamic response but are highly compressed compared to raw data, easing further analysis and storage. Operational modal analysis is typically used to identify the modal model in terms of modal parameters of the structure from the dynamic responses under operational conditions.

The initial characterization of the structure provides a baseline model that adequately predicts the structural behavior in its pristine state. Through continuous monitoring, an up-to-date modal model reflecting the current dynamic characteristics of the structure can be maintained. Finite element model updating can then be performed to obtain an up-to-date representative model of structure based on the changes in modal parameters observed. The purpose of the finite element model updating is to make certain that the model accurately represents the structure and is able to predict structural behavior. Damage localization based on modal data can be utilized to facilitate the process of finite element model updating by reducing the number of unknown structural parameters in the updating process.

Finally, by comparing the baseline model with the current model of the structure, information regarding the location and magnitude of the damage that the structure has experienced can be deduced. Current structural performance can be evaluated and a prediction regarding the remaining life of the structure can be made.

The content and structure of this dissertation is arranged as follows:

Chapter 2 presents a literature review of the state-of-the-art of vibration-based structural health monitoring and vibration-based damage identification techniques.

Chapter 3 discusses two methods for the operational modal analysis of civil engineering structures. These two methods are proposed to improve the efficiency of modal parameter extraction using operational data and make it more applicable to a continuous monitoring application.

Chapter 4 presents a novel damage localization technique based on an energy criterion. It is shown the proposed method exhibits superior performance under noisy conditions and sparse measurements compared with some traditional techniques based on modal curvature.

Chapter 5 outlines the procedure of finite element model updating using modal data. Special attention is paid to the ill-conditioning of the model updating problem and several measures are suggested to alleviate this problem.

Chapter 6 discusses the implementation of Vibration-based Structural Health Monitoring System on a highway bridge.

Chapter 7 summarizes and concludes the dissertation.

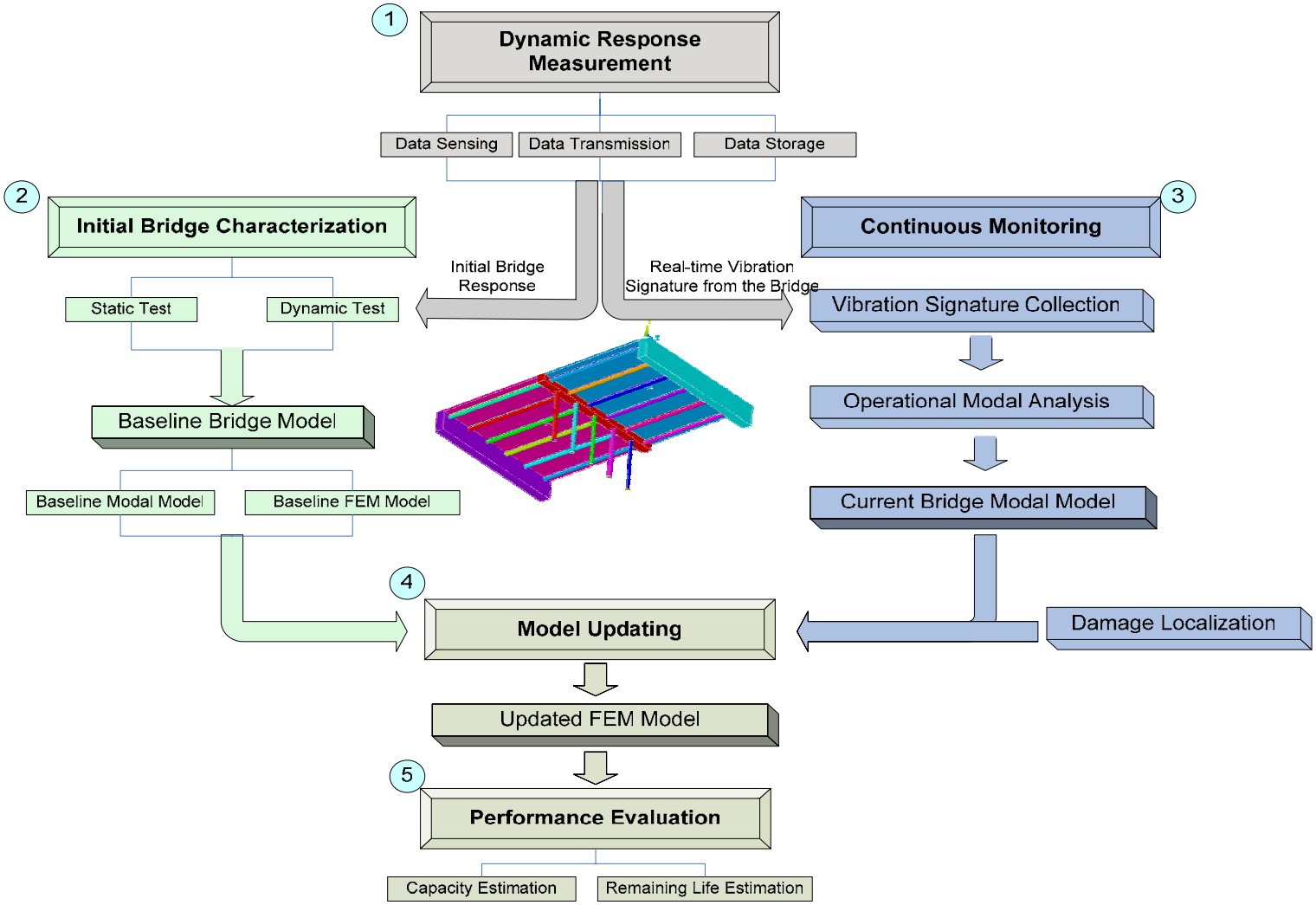

Figure 1-1 Flowchart of the Vibration-based Structural Health Monitoring System

Chapter 2 Literature Review

2.1 Overview of Research Area and Statement of Scope

The last three decades have seen a great increase of interest in the field of structures of *Vibration-Based Structural Health Monitoring*. Research papers on the theory and application of damage identification using structural dynamic properties, pioneered by the research in the field of offshore oil platforms, began emerging in the late 70's. On the other hand, development in some of the related fields, such as modern modal testing techniques and system identification theory, can be dated back to the early 60's. As a result, there has been a tremendous amount of literature published in these fields. It is impossible to provide a comprehensive review of all the literature within the context of this dissertation, nor is this the author's intent. However, in order to facilitate the discussion in the later parts of this dissertation, it is necessary to provide a brief review of some of the literature of importance and relevance to the current research.

2.1.1 Overview of Research Area

The basic premise of *Vibration-Based Structural Health Monitoring* is that changes of structural properties, such as mass, stiffness and damping, will affect the vibrational response of the structure. Thus, by studying the changes in measured structural vibration behavior and in essence solving an inverse problem, the unknown

changes of structural properties can be identified. In cases where the changes in structural properties that adversely affect the performance of the structure are defined as 'damage', the process of identifying such changes is also referred to as *Vibration-Based Damage Identification* (VBDI) or *Vibration-Based Damage Detection* (VBDD). The integration of VBDI with an appropriate damage prognosis technique can lead to the estimation of the effect of damage on structural response.

There are two integral components of *Vibration-Based Damage Identification*: feature extraction and damage identification. The first step of VBDI is the identification and extraction of vibration-related features. Many features can be used to characterize a structure's vibrational response. For example, acceleration time history measured by accelerometers mounted on the structure during its vibration can be directly used as a feature. Modal parameters of the structure, such as natural frequency, damping, mode shape and its derivatives, can also be used as features. Other candidate features include model parameters of the Autoregressive Moving Average (ARMA) models fitted to the response time-history, system frequency response functions and transfer functions, residual modal forces in the formulation of equations of motion, the stability and dimension of attractors in the state space, analytic signal generated by Hilbert transform, etc. A large amount of research effort has been devoted to identifying vibration-related features that are sensitive to changes of structural properties and the experimental techniques to extract those (see, for example, Doebling et al. 1996).

The second step of VBDI is the correlation of features to the structural properties, i.e., using vibration-related features to infer the condition of the structure.

The most straight forward method is to compare the features at two different states. It is customary to define one of the structural states as the ‘baseline’ or ‘undamaged’ state, and use it as the level that all subsequent states will be compared with. The change in the features can reveal information about the occurrence, location (if the feature contains spatial information, for example, mode shape), type and relative severity of the damage (if data about more than one damage states are available). More sophisticated techniques have been developed to statistically discriminate the features for the purpose of damage detection. Statistical pattern recognition and neural networks are two common used techniques. Through supervised or unsupervised learning, these techniques can successfully distinguish changes in specific features between undamaged and damage states and thus obtain information about change of structural properties. Sohn et al. (Sohn et al. 2003) provides an extensive review on these areas which is hence not repeated herein.

Another approach that has been adopted by some researchers directly relates features to the changes in structural properties. The finite element model updating technique is commonly used for this purpose. The initial, or as-built, finite element model is first updated to reproduce as closely as possible the measured dynamic response of the baseline structure. Then the updating process is repeated for each set of measured response from different damage stages using the same technique and the changes of finite element model properties in-between stages, in theory, should reflect the changes in actual structural properties.

The task of relating certain features to structural properties can also be achieved without a finite element model. Such methods usually require the features involved to have a direct physical interpretation. One prominent example is that of modal curvature, which is analogous to the deflection curvature of structural static response. Modal curvature can be related to the stiffness of the structure through a simple moment-curvature relationship. The dynamic flexibility matrix is another example. Computed from structural dynamic response, the dynamic flexibility matrix is the dynamic equivalent of the static flexibility matrix. The elements of the matrix carry information regarding the local flexibility of the structure.

To date, most of the research found in the existing literature is targeted at solving Level I to Level III VBDI problems with very few attempts to address the Level IV (i.e., the integration of VBDI with damage prognosis) problem. Furthermore, most of existing literature is related to the application of theories of damage detection to either numerical or laboratory test examples. Real world applications of vibration-based structural health monitoring system, especially applications on civil engineering structures such as bridges, are relatively rare. The reviews of Doebling et al. (1996) and Sohn et al. (Sohn et al. 2003) discussed some applications of vibration-based damage detection on civil engineering structures. These applications are mostly for the purpose of proving the feasibility of vibration-based damage detection techniques and were usually carried out during a short duration of time. To date, little information can be found about long-term application of vibration-based structural health monitoring system on civil engineering structures.

In the broadest sense, *Vibration-Based Structural Health Monitoring* also includes applications that utilize wave propagation phenomenon to monitor changes in structures, such as lamb wave and ultra-sonic techniques. However, the frequencies of vibrational phenomenon used in these applications are usually much higher compared with the applications discussed in the earlier part of this chapter. The area of investigation of these techniques is typically limited to a comparatively small area. As a result, these techniques are usually categorized as local non-destructive evaluation (NDE) techniques and will not be discussed in detail here.

2.1.2 Statement of Scope

The global *Vibration-Based Damage Identification* (VBDI) technique is the core of the *Vibration-Based Structural Health Monitoring* system considered in this thesis. Based on the different types of models used in the second step of the damage identification process, the various techniques found in existing literature can be classified into two main categories: *Physical Model Based* (PMB) methods and *Data-driven Model Based* (DMB) methods.

Physical Model Based methods refer to the techniques that are based on directly relating features to structural properties, such as mass, stiffness and damping, with or without a finite element model. In this approach, an inherent assumption is that the form of the physical model of the structure is known a priori. An example of a physical model that can be utilized to model the structure is the moment-curvature relationship of a beam. *Physical Model Based* methods generally are capable of estimating both the location and absolute severity of the damage and are thus at least Level III techniques.

For the case where a finite element model is not available, the physical models are usually expressed in the form of analytical equations containing uncertain parameters that need to be identified. The process of damage detection is a means of identifying these parameters using experimentally measured features. A significant difficulty in such an approach lies in the fact that, for complex structures, an analytical model is not always available and solutions of the analytical equations may be difficult to obtain.

When a finite element model of the structure is utilized in the damage identification process, such *Physical Model Based* methods are sometimes also referred to as *Finite Element Model Updating* (FEMU) based methods. Typical approaches for the *Finite Element Model Updating* based methods include sensitivity-based approaches (Abdel Wahab et al. 1999), Optimal Matrix Update based approaches (Kaouk and Zimmerman 1994) and optimization-based approaches (Teughels et al. 2003). Extensive reviews of *Finite Element Model Updating* techniques can be found in Friswell and Mottershead (Friswell and Mottershead 1995) and Maia and Montalväao e Silva (Maia and Montalväao e Silva 1997). Previous researchers have shown that FEMU can be an extremely useful technique for damage identification under certain conditions. But it should also be noted that some difficulties still exists when implementing FEMU technique in a VBSHM system. Firstly, due to the fact that only a small number of degree-of-freedoms can be measured experimentally and there exist a large number of uncertain parameters to be updated, the updating problem is usually ill-conditioned. This directly leads to the second problem of numerical convergence difficulties. A small amount of noise in the measured structural response can sometime corrupt the result to a great extent.

Data-driven Model Based methods refer to techniques that rely on comparing features between different states to assess structural conditions without a physically meaningful model of the structure. The comparison can be made either directly or through more sophisticated techniques such as those associated with statistical pattern recognition. For example, methods that utilize neural networks to relate changes in frequencies and mode shapes to changes in system parameters fall into this category. These techniques do not require a known physical model of the structure or a finite element model. However, methods in this category often have the drawback that they cannot provide information about the type and absolute severity of the damage unless incorporated in a supervised learning mode. Here, supervised learning refers to the situation when information of the feature from both undamaged and damage states is known a priori (Farrar 2005). In contrast, unsupervised learning refers to the situation when data is available only from the undamaged state. While it is possible to obtain features for each damage states in a manufactured environment, it is typically not possible for civil structures, due to their complexity and uniqueness. Although some researchers have suggested the use of finite element models to simulate the structural response under damaged states when experimental data are not available, the applicability and accuracy of such simulations to replicate the complex damaged behavior of real world structures is questionable. Hence *Data-driven Model Based* methods are typically limited to Level II techniques when applied to civil engineering structure since an unsupervised learning mode has to be used.

As mentioned in the previous chapter, the ultimate goal of structural health monitoring for civil engineering structures is the prediction of the capacity and

remaining life of the structure. This is essentially a Level IV task based on the classification discussed in Chapter 1. *Data-driven Model Based* methods have considerable difficulties in accomplishing such a task, because they cannot provide estimation of absolute damage severity under an unsupervised learning mode. At the same time, *Physical Model Based* methods, despite the difficulties mentioned, appears to be a very promising technique for such applications due to their direct physical interpretation and the ability to determine both location and severity of damage. Based on this, the scope of the first part of the current literature review is limited to *Physical Model Based* methods that are at least Level III techniques. The examples of Level IV techniques are relatively rare but will also be included in the discussion.

Again, it should be noted that the current review is not intended to be comprehensive. Hence, only methods that are considered to be relevant to the overall scope of this research will be covered. At the same time, emphasis will be placed on recent advances in this field since 2001 because most previous research has been covered in previous literature reviews (Doebling et al. 1998; Mackerle 1999; Salawu 1997) and hence will not be repeated herein. However, when papers published before 2001 and already been included in other literature reviews formed the basis of more recent research, those papers will usually be included in the current review for the sake of completeness. There also exist several excellent books regarding the experimental extraction of vibration-related features (see, for example, Ewins 2000; Ljung 1999; Maia and Montalväao e Silva 1997), and the topic of vibration feature extraction will not be covered in detail.

Due to the fact that this thesis is specially focused on aspects related to long-term VBSHM application on highway bridge structures, the second part of the literature review is dedicated to the application of long-term VBSHM system on civil engineering structures, specifically, bridge structures. A schematic of the scope of the literature review was given in Figure 2-1. It is hoped that this organization can give the readers a clear overview of the state of the art in terms of both theory and application of *Vibration-based Structural Health Monitoring* of civil engineering structures.

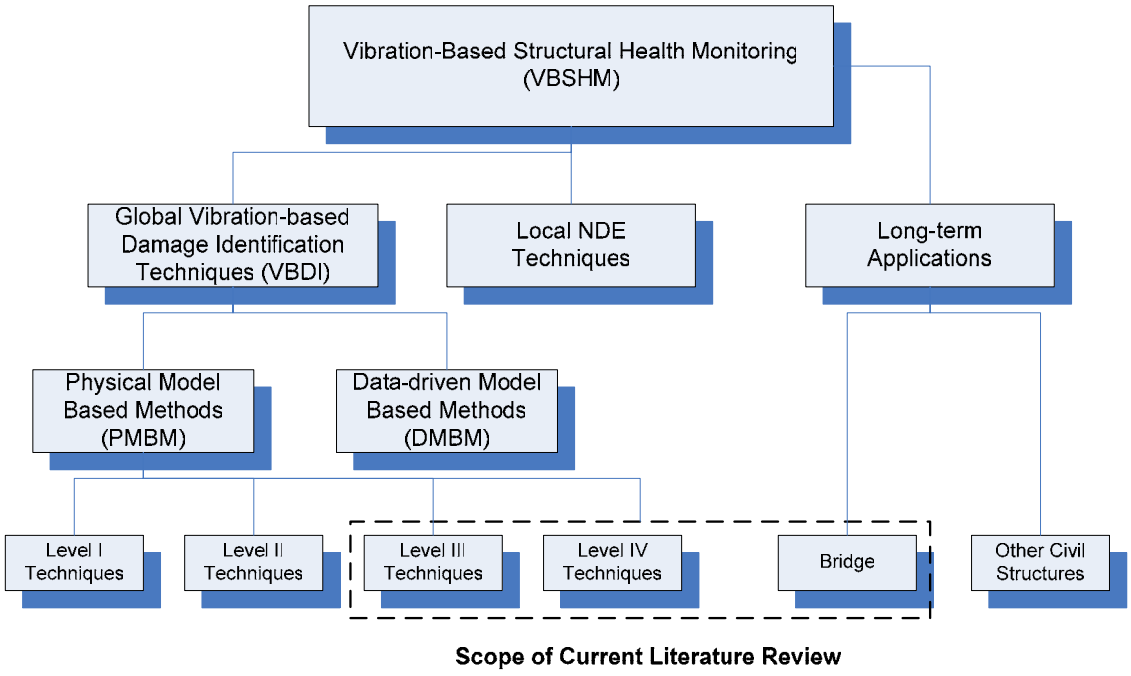

Figure 2-1 Scope of Literature Review

2.2 Physical Model Based methods

2.2.1 Methods using Frequency and Mode Shape

Stubbs and Osegueda (Stubbs 1990) proposed a method to identify the change in system properties using measured changes in natural frequencies. The method relates the change in the stiffness matrix and mass matrix to changes in system eigenvalues using the sensitivity formulation:

$$\{Z\} = [F]\{\alpha\} + [G]\{\beta\} \tag{2.1}$$

where, $\{Z\}$ is the vector of measured frequency changes, $\{\alpha\}$ and $\{\beta\}$ are the vectors of changes in system stiffness and mass parameters, respectively, and $[F]$ and $[G]$ are the sensitivity matrices. In order to calculate $\{\alpha\}$ and $\{\beta\}$ from measured $\{Z\}$, the values of elements in $[F]$ and $[G]$ must be known. There are two ways to generate values in $[F]$ and $[G]$; they can either be determined theoretically with a closed-form solution for the system eigenvalues, or they can be computed numerically using a perturbation method in conjunction with a finite element model. The accuracy of the proposed method is determined to a large extent by the accuracy of the sensitivity matrix. Thus, the need to obtain a closed-form solution or an accurate finite element model constitutes the primary drawback of this method and is typically very difficult to apply to complex civil engineering structures. At the same time, the method also suffers from numerical difficulties because the number of measured frequencies changes, i.e., the number of elements in $\{Z\}$, is usually far less than the number of unknown

parameters in $\{\alpha\}$ and $\{\beta\}$. Hence the inverse problem of Eq. (2.1) will become ill-conditioned.

Kim et al. (Kim et al. 2003; Kim and Stubbs 2003) further developed the aforementioned method in an effort to alleviate the ill-conditioning of the inverse problem. Assuming that the change in mass matrix before and after damage was negligible, they formulated the sensitivity equation as:

$$Z_i = \sum_{j=1}^{NE} F_{ij}\alpha_j \tag{2.2}$$

where Z_i is the fractional change of i^{th} eigenfrequency and α_j is the fractional reduction in j^{th} element's stiffness parameter. The term F_{ij} is the sensitivity of Z_i to α_j and it was asserted that F_{ij} can be expressed as the fraction of modal energy for the *i*th mode that is concentrated in *j*th element:

$$F_{ij} = \frac{\{\phi_i\}^T \left[C_j\right] \{\phi_i\}}{\{\phi_i\}^T [C] \{\phi_i\}} \tag{2.3}$$

where $[C]$ and $\left[C_j\right]$ are the global and element stiffness matrices, respectively. Once the system stiffness matrix and mode shape is known, F_{ij} can be generated numerically. Dividing Eq. (2.2) for mode *i* by its value for mode *j*:

$$\frac{Z_m}{Z_n} = \frac{\sum_{j=1}^{NE} F_{mj}\alpha_j}{\sum_{j=1}^{NE} F_{nj}\alpha_j} \tag{2.4}$$

If there is only one element that is damaged, then Eq. (2.4) reduces to

$$Z_m / Z_n = F_{mq} / F_{nq} \tag{2.5}$$

Assuming that ratio F_{mq}/F_{nq} is unique for the q^{th} location, then Eq. (2.5) only holds true for the correct damage element q. Summing over all measured NM modes and defining the error index as:

$$e_{ij} = Z_m \Big/ \sum_{k=1}^{NM} Z_k - F_{mq} \Big/ \sum_{k=1}^{NM} F_{kq} \tag{2.6}$$

then $e_{ij} = 0$ indicates that the damage is located at the j^{th} location.

The above formulation is unable to provide an estimate for damage severity, so a damage-sizing algorithm was added based on the results of Gudmundson (1982),

$$\frac{\delta\omega_i^2}{\omega_i^2} = \eta S_{ik} \left(\frac{a_k}{H} \right)_i^2 \tag{2.7}$$

in which $\frac{\delta\omega_i^2}{\omega_i^2}$ is the fractional change of eigenvalue for mode i, $\left(\frac{a_k}{H} \right)$ is the dimensionless crack size normalized to beam depth, η is a shape factor related to the beam geometry and S_{ik} represents the sensitivity of the k^{th} location in the i^{th} modal strain energy. If the fractional change of eigenvalues is measured experimentally, the crack size can be determined through Eq. (2.7). Numerical simulation was used to verify this method and acceptable localization and severity estimation results were obtained. However, the method can only correctly locate and size damage when there is only one damage location present. Moreover, the formulation of the damage sizing

algorithm in Eq. (2.7) depends on the assumption that the damage is in the form of a single crack, and hence the solution is not applicable to other damage types.

Yuan et al. (1998) proposed a method to estimate mass and stiffness matrices of a shear building from modal test data. The shear building model was formulated using the undamped equation of motion:

$$M\ddot{X} + KX = F \tag{2.8}$$

The corresponding characteristic equation can then be expressed as:

$$(K - \lambda_l M)\phi_l = 0 \tag{2.9}$$

where λ_l is the l^{th} eigenvalue, and ϕ_l the l^{th} corresponding eigenvector. The stiffness matrix [K] is a tridiagonal matrix and the mass matrix [M] is a diagonal matrix:

$$K = \begin{bmatrix} k_1 + k_2 & -k_2 & \cdots & \cdots & 0 \\ -k_2 & k_2 + k_3 & -k_3 & & \vdots \\ \vdots & & \ddots & & \\ & & -k_{n-1} & k_{n-1} + k_n & -k_n \\ 0 & \cdots & \cdots & -k_n & k_n \end{bmatrix}$$

$$M = \begin{bmatrix} m_1 & \cdots & \cdots & 0 \\ \vdots & m_2 & & \vdots \\ \vdots & & \ddots & \\ 0 & & \cdots & m_n \end{bmatrix} \tag{2.10}$$

where k_i and m_i are the stiffness and mass parameter of i^{th} storey, respectively. Expanding Eq. (2.9) for modes *l* and *r* and reorganizing in terms of stiffness and mass parameters,

$$\begin{bmatrix} \phi_{l1} & -\lambda_l\phi_{l1} & \phi_{l1}-\phi_{l2} & \cdots & & \\ \phi_{r1} & -\lambda_r\phi_{r1} & \phi_{r1}-\phi_{r1} & & & \\ \vdots & \cdots & & \ddots & & \\ & & & \phi_{\mathrm{ln}}-\phi_{\mathrm{ln}-1} & \lambda_l\phi_{\mathrm{ln}} \\ & & & \phi_{r\mathrm{n}}-\phi_{r\mathrm{n}-1} & \lambda_r\phi_{rn} \end{bmatrix} \times \begin{Bmatrix} k_1 \\ m_1 \\ k_2 \\ m_2 \\ \vdots \\ k_n \\ m_n \end{Bmatrix} = \begin{Bmatrix} \\ \\ \\ 0 \\ \\ \\ \end{Bmatrix} \tag{2.11}$$

or simply,

$$[B]\{b\} = \{0\} \tag{2.12}$$

If $m_n = 1$, Eq. (2.12) can be expressed as

$$[B']\{b'\} = \begin{Bmatrix} 0 \\ \vdots \\ \lambda_l\phi_{\mathrm{ln}} \\ \lambda_r\phi_{rn} \end{Bmatrix} \tag{2.13}$$

where $[B']$ is the $(2n-2)\times(2n-2)$ matrix in which the last rows and last two columns of $[B]$ are eliminated, and $\{b'\}$ is the $(2n-2)\times(1)$ vector in which the last two members of $\{b\}$ are eliminated. Solving for the unknown mass and stiffness parameters k_i and m_i,

$$\{b'\} = \left([B']^T \cdot [B']\right)^{-1}[B']^T \begin{Bmatrix} 0 \\ \vdots \\ \lambda_l\phi_{\mathrm{ln}} \\ \lambda_r\phi_{rn} \end{Bmatrix} \tag{2.14}$$

$$k_n = \frac{\lambda_l\phi_{\mathrm{ln}}}{\phi_{\mathrm{ln}} - \phi_{\mathrm{ln}-1}} \tag{2.15}$$

The mass and stiffness parameters obtained by Eq. (2.14) and Eq. (2.15) are relative values. That is, the values obtained are all relative to m_n, since the assumption was made that $m_n = 1$.

This method is conceptually straight forward. Only mode shapes and natural frequencies from two modes are required. However, it utilizes the special mass and stiffness matrix formulation of the shear buildings which directly leads to Eq. (2.11). It is questionable if the same principle can be applied to other types of structures. Moreover, the formulation does not include damping effects and it was not discussed in the paper whether the matrix inverse in Eq. (2.14) would be ill-conditioned.

Chakraverty (2005) presented a refined version of the same method mentioned above. By using Holzer criteria along with other numerical methods to estimate the global mass and stiffness matrices, the efficiency and accuracy of the methodology discussed in (Yuan et al. 1998) was improved. The author also applied the method to numerical models of different shear buildings to verify its accuracy. However, the limitations mentioned previously for this method such as numerical stability and applicability to other structures were not addressed.

Udwadia (2005) generalized the above method by formulating the equation of motion of an undamped system in the form:

$$K\varphi_i = \lambda_i \varphi_i \tag{2.16}$$

where λ_i is the i^{th} system eigenvalue, φ_i is the i^{th} transformed eigenvector of the system and is related to the original system eigenvector through the equation

$$\hat{\varphi}_i = M^{-1/2}\varphi_i \tag{2.17}$$

$$K = \hat{K}M^{-1/2} \tag{2.18}$$

where $\hat{K}$ and M are the system stiffness and mass matrix, respectively. By assuming that the structure of the matrix is known from the analytic model and each element of the matrix K is a linear combination of some parameters k_i, it is concluded that each of the n equations in Eq. (2.16) is linear in these parameters. Eq. (2.16) can then be rewritten as

$$\Phi_i k = \lambda_i \varphi_i \tag{2.19}$$

in which, k is the vector of parameters k_i, and Φ_i is a matrix of coefficients of k_i. Eq. (2.19) is the general form of Eq. (2.11) when the system mass matrix is assumed to be known. Usually, because of the limited connectivity between the elements of $\hat{K}$, the number of parameters in k that need to identified is much less than the number of unknown parameters in a general symmetric matrix, i.e. $n(n+1)/2$.

If measured modal parameters from r number of different modes are available, Eq. (2.19) can be further written as:

$$B\tilde{k}_r = \begin{bmatrix} \Phi_1^m \\ \Phi_2^m \\ \vdots \\ \Phi_r^m \end{bmatrix} \tilde{k}_r = \begin{bmatrix} \lambda_1^m \varphi_1^m \\ \lambda_2^m \varphi_2^m \\ \vdots \\ \lambda_r^m \varphi_r^m \end{bmatrix} = b_r \tag{2.20}$$

in which, superscript *m* indicates measured values and subscripts in the matrix indicate the number of individual modes. The minimum-norm-least-square solution to this system of equation is given by

$$\tilde{k}_r = B^+ b_r \tag{2.21}$$

where B^+ stands for the Penrose generalized inverse of the matrix B and $\tilde{k}_r$ stands for the estimate of parameters k_i. It was argued that the use of Eq. (2.21) to obtain the parameter estimates is less susceptible to noise in the measurement. A numerical example of shear building was then used to verify the effectiveness of Eq. (2.20) and Eq. (2.21). It was shown that when measurement noise is present, Eq. (2.20) yield considerable improved results compared with using Eq. (2.19) alone. Once the initial estimate $\tilde{k}^{(0)}$ is obtained, the results can be further improved through an iterative procedure where the measured mode shapes were expanded using the eigenvectors ψ_j calculated from the initial estimate of system stiffness matrix $\tilde{K}^{(1)}$

$$\varphi_i^m = \sum_{j=1}^{n} \delta_j^i \psi_j \tag{2.22}$$

then

$$\tilde{K}^{(1)} \varphi_i^m = \tilde{K}^{(1)} \sum_{j=1}^{n} \delta_j^i \psi_j = \sum_{j=1}^{n} \delta_j^i \tilde{K}^{(1)} \psi_j = \sum_{j=1}^{n} \delta_j^i \mu_j \psi_j \tag{2.23}$$

where μ_j is the calculated j^{th} eigenvalue using the initial estimate of system stiffness matrix. Again, expressing $\tilde{K}^{(1)} \varphi_i^m$ as $\Phi_i^m \tilde{k}^{(0)}$, i.e.,

$$\tilde{K}^{(1)}\varphi_i^m = \Phi_i^m \tilde{k}^{(0)} = \sum_{j=1}^{n} \delta_j^i \mu_j \psi_j \tag{2.24}$$

an updated estimate can then be obtained by replacing μ_j with measured natural frequencies which is assumed to be less affected by noise compared with measured mode shapes

$$\Phi_i^m \tilde{k}^{(1)} = \tilde{K}^{(1)}\varphi_i^m = \sum_{j=1}^{n} \delta_j^i \lambda_j^m \psi_j \tag{2.25}$$

where the superscripts in brackets are the number of iterations. λ_j^m is the set of measured natural frequencies and ψ_j is the calculated eigenvectors using the initial estimate $\tilde{k}^{(0)}$. One potential weakness of this technique is the need to know the full structure of the system stiffness matrix K (although the values are not required). Obtaining the full mode shape amplitudes at all degrees-of-freedom and the mass matrix can also be difficult.

Yoshimoto et al. (2005) proposed a damage identification technique that is based on a lumped mass structure model and applied this technique to identify storey stiffness and damping parameters of base-isolated shear buildings. Considering the dynamic equilibrium of the forces acting the j^{th} storey and all the stories above:

$$k_{i(j)} \cdot \mathbf{d}_{i(j)}(t) + c_{i(j)} \cdot \dot{\mathbf{d}}_{i(j)}(t) = \mathbf{f}_{i(j)}(t) \tag{2.26}$$

where $k_{i(j)}$ and $c_{i(j)}$ are the stiffness and damping parameter of the j^{th} storey. $\mathbf{f}_{i(j)}(t)$ is the inertia force acting on storey masses of j^{th} storey and all the stories above it and can be calculated as:

$$\mathbf{f}_{i(j)}(t) = -\sum_{k=j}^{N} m_k \cdot \ddot{X}_{i(k)}(t) = -\lambda_i^2 e^{\lambda_i t} \cdot \sum_{k=j}^{N} m_k \phi_{i(k)} \tag{2.27}$$

in which m_k is the storey mass of *k*th storey. $\mathbf{d}_{i(j)}(t)$ and $\dot{\mathbf{d}}_{i(j)}(t)$ are the relative displacement and velocity between the j^{th} storey and $(j\text{-}1)^{\text{th}}$ storey for the i^{th} mode of vibration and can be expressed as

$$\mathbf{d}_{i(j)}(t) = X_{i(j)}(t) - X_{i(j-1)}(t) = \left\{\phi_{i(j)} - \phi_{i(j-1)}\right\} \cdot e^{\lambda_i t} \tag{2.28}$$

$$\dot{\mathbf{d}}_{i(j)}(t) = \dot{X}_{i(j)}(t) - \dot{X}_{i(j-1)}(t) = \left\{\phi_{i(j)} - \phi_{i(j-1)}\right\} \cdot \lambda_i e^{\lambda_i t} \tag{2.29}$$

where $\phi_{i(j)}$ and λ_i are the eigenvector and eigenvalue of *i*th mode respectively. Using the measured eigenvalue λ_i and eigenvector ϕ_i, Eq. (2.26) can be formulated for the j^{th} storey at each every time interval. Utilizing a short data length that is approximately equal to the first natural period of the object building, Eq. (2.26) can be solved in a least square manner. Repeating the procedure for other stories of the building, the stiffness and damping parameters of each storey can be identified. This technique assumes a known storey mass and is only applicable to shear buildings that can be modeled accurately with a lumped mass model.

Ren and De Roeck (2002a; 2002b) proposed another method that utilizes measured natural frequencies and mode shapes for structural damage identification based on the concept of element damage index. Premultiplying the damaged system equation by the undamaged mode shape Φ_i^T (i = 1, …, n) to

$$\Phi_i^T \tilde{K} \tilde{\Phi}_j = \tilde{\omega}_j^2 \Phi_i^T \tilde{M} \tilde{\Phi}_j \tag{2.30}$$

where $\tilde{\omega}_j^2$ and $\tilde{\Phi}_j$ are the damaged frequency and mode shape of *j*th mode, respectively. It is assumed that the mass matrix of the structure remains unchanged before and after damage. Expressing the global system stiffness matrix with element stiffness matrix and utilizing the modal orthogonality condition, Eq. (2.30) can be written as

$$\sum_{e=1}^{N} \tilde{\phi}_{je}^T k_e \phi_{ie} \Delta a_e = \left(1 - \frac{\tilde{\omega}_j^2}{\omega_i^2}\right) \tilde{\Phi}_j^T K \Phi_i \tag{2.31}$$

where ϕ_{ie} is the *i*th element mode shape of element e and $\Phi_i = \sum_{e=1}^{N} \phi_{ie}$. k_e is the element stiffness matrix and it is assumed that the stiffness reduction in element e can be expressed as linear combination of k_e and element damage index Δa_e , i.e., $\tilde{k}_e = (1 - \Delta a_e) k_e$. Eq. (2.31) can be written in matrix notation as

$$[S]\{\Delta a\} = \{\Delta R\} \tag{2.32}$$

or

$$\begin{bmatrix} S_{111} & \cdots & S_{11N} \\ \vdots & \vdots & \vdots \\ S_{1m1} & \cdots & S_{1mN} \\ S_{211} & \cdots & S_{21N} \\ \vdots & \vdots & \vdots \\ S_{2m1} & \cdots & S_{2mN} \\ \vdots & \vdots & \vdots \\ S_{n11} & \cdots & S_{n1N} \\ \vdots & \vdots & \vdots \\ S_{nm1} & \cdots & S_{nmN} \end{bmatrix}_{(n\times m)\times N} \begin{Bmatrix} \Delta a_1 \\ \Delta a_2 \\ \vdots \\ \vdots \\ \vdots \\ \vdots \\ \vdots \\ \vdots \\ \Delta a_N \end{Bmatrix}_{N\times 1} = \begin{Bmatrix} \Delta R_{11} \\ \vdots \\ \Delta R_{1m} \\ \Delta R_{21} \\ \vdots \\ \Delta R_{2m} \\ \vdots \\ \Delta R_{n1} \\ \vdots \\ \Delta R_{nm} \end{Bmatrix}_{(n\times m)\times 1} \tag{2.33}$$

in which,

$$S_{ije} = \tilde{\phi}_{je}^{T} k_e \phi_{ie} \tag{2.34}$$

$$\Delta R_{ij} = \left(1 - \frac{\tilde{\omega}_i^2}{\omega_i^2}\right) \tilde{\Phi}_j^T K \Phi_i \tag{2.35}$$

Each row of Eq. (2.33) is a modal orthogonality equation between mode *i* of undamaged structure and mode *j* of damaged structure and ΔR_{ij} is the residue caused by damage. Ren and De Roeck proposed solving Eq. (2.33) with Moore-Penrose pseudo-inverse or non-negative least squares (NNLS) technique. An error-based truncation technique, SVD-R, was utilized to deal with the numerical problem when linear dependent columns in matrix $[S]$ are encountered and the problem became ill-posed. When applied to a numerical modal, it can be shown that the proposed method can accurately determine the location and severity of the damage. However, numerical difficulties begin to emerge when the complexity of the target structure increases (Ren and De Roeck 2002b). A further drawback of the proposed method is that it did not take into account the effect of damping.

In summary, there exist many different damage detection techniques utilizing measured natural frequencies or mode shapes as features. However, such techniques often suffer from three drawbacks: First, the sensitivity of natural frequency and mode shape to damage is usually low (Yam et al. 2002). Thus the ability of such techniques in detecting low level of damage in the presence of noise is questionable. Second, many of these techniques require detailed knowledge about the system stiffness matrix of the undamaged structure. Accurate estimation of system stiffness matrix is hard to obtain for complex real world structures hence more difficulty will be encountered if one tries

to apply these techniques to structures beyond numerical simulation or laboratory experiment. Third, some techniques in this category only works for specific structural type – for example, a shear building – and can not be extended to other types of structure.

2.2.2 Methods using Mode Shape Curvature

In view of the shortcomings of the damage detection methods using natural frequency or mode shape, researchers start to seek other features that are more sensitive to damage. Among the features studied, modal curvature has been shown to have high sensitivity to localized damage (Pandey et al. 1991) and draws a great deal of attention. There exist a great number of studies utilizing mode shape curvature in the existing literature. Their pros and cons will be discussed in detail in Chapter 4 and hence will be omitted here. Only one recent study was described below as a example.

Maeck and De Roeck (2003) and Maeck et al. (2000) presented a method to estimate the dynamic stiffness of the structure using direct stiffness calculation. Maeck and De Roeck claimed that the advantage of such a method is that no numerical model is needed to obtain the dynamic stiffness distribution for statically determinate structures. For statically inderminate structure, the reaction forces and internal forces are dependent on the stiffness of the structure. It was therefore pointed out that for such a situation an iterative procedure needs to be used. The method makes use of the basic relation that the dynamic bending stiffness EI in each section is equal to the bending moment M in that section divided by the corresponding curvature, i.e.,

$$EI = \frac{M}{d^2\varphi^b / dx^2} \tag{2.36}$$

Similarly, torsional stiffness can be calculated from

$$GJ = \frac{T}{d\varphi^t / dx} \tag{2.37}$$

Modal curvature φ^b and torsion rate φ^t can be measured experimentally, but to use the above two equations modal internal force M and T needs to be calculated.

The eigenvalue problem of the undamped system can be written as

$$K_m\varphi_m = \omega_m^2 M_a\varphi_m \tag{2.38}$$

which can be seen as a pseudo-static system: for each mode, the internal force are due to the inertial load $\omega_m^2 M_a\varphi_m$. From internal force equilibrium, the modal internal force can be calculated as

$$\begin{aligned} M_{i+1} &= M_i + V_i\left(x_{i+1} - x_i\right) - \int_{x_i}^{x_{i+1}} \omega_m^2 \rho A \varphi_m^b(x)\left(x_{i+1} - x_i\right)dx \\ V_{i+1} &= V_i - \int_{x_i}^{x_{i+1}} \omega_m^2 \rho A \varphi_m^b(x)dx \end{aligned} \tag{2.39}$$

where M_i and V_i are modal bending moment and modal shear force, respectively. In the recursive formula shown in Eq. (2.39), the values for M_0 and V_0 are zero for a free-free beam and the inertia forces should be in static equilibrium. Subsequently, the dynamic stiffness of each section can be calculated using Eq. (2.36). Maeck and De Roeck applied their method to an experimental reinforced concrete beam tested ove a

range of load levels. The results showed generally good agreement with observations in the experiment. However, the method appeared to suffer from numerical difficulties when the modal curvature is close to zero. Furthermore, the authors did not explain how such a method could be applied to statically indeterminate structures.

2.2.3 Methods using Modal Strain Energy and Modal Stiffness

A class of techniques that is related to the modal curvature techniques described in the previous section is the Modal Strain Energy and Modal Stiffness technique. The definition of modal strain energy and modal stiffness will be give below and it will be shown that the two quantities are essentially identical except for a scalar factor of 2.

Stubbs and Kim (1996) developed a damage identification method using element modal stiffness. In a linear, undamaged structure, the i^{th} modal stiffness of a linear undamaged structure can be represented as

$$K_i = \vec{\phi}_i^T \left[C\right] \vec{\phi}_i \tag{2.40}$$

where $\vec{\phi}_i$ is the i^{th} mode shape vector and $\left[C\right]$ is the system stiffness matrix. The contribution of j^{th} member to the i^{th} modal stiffness is then given by

$$K_{ij} = \vec{\phi}_i^T \left[C_j\right] \vec{\phi}_i \tag{2.41}$$

where $\left[C_j\right]$ is the j^{th} member contribution to the stiffness matrix. The fraction of modal energy of the i^{th} mode contributed by the j^{th} member, also called modal sensitivity, can be defined as

$$F_{ij} = K_{ij} / K_i \tag{2.42}$$

Correspondingly, using "*" to represent quantities pertaining to the damaged structure, the fraction of modal energy of a damaged structure as can be defined as

$$F^*_{ij} = K^*_{ij} / K^*_i \tag{2.43}$$

wherein

$$K^*_{ij} = \vec{\phi}_i^{*T} \left[C^*_j \right] \vec{\phi}_i^* \quad K^*_i = \vec{\phi}_i^{*T} \left[C^* \right] \vec{\phi}_i^* \tag{2.44}$$

and,

$$C_j = E_j \left[C_{j0} \right] \quad C^*_j = E^*_j \left[C_{j0} \right] \tag{2.45}$$

where the scalars E_j and E^*_j are parameters representing material stiffness properties related to the undamaged and damaged structure, respectively, and the matrix $\left[C_{j0} \right]$ contains only geometric quantities, which are assumed to remain unchanged after damage occurs.

A basic underlying assumption of this method is that the modal sensitivity for the i^{th} mode and j^{th} member remain approximately unchanged in both the undamaged and damaged structural states, i.e.

$$F_{ij} / F^*_{ij} = (K^*_{ij} K_i) / (K^*_i K_{ij}) = 1 \tag{2.46}$$

Stubbs and Kim (1996) asserted that this assumption is valid for various damage scenarios up to a damage severity of 30%, and defined damage index β_j for the j^{th} member as

$$\beta_j = \frac{E_j}{E_j^*} \tag{2.47}$$

Substituting equations (2.42), (2.43) and (2.44) into (2.46), an expression for β_j can be obtained as

$$\beta_j = \frac{\gamma_{ij}^* K_i}{\gamma_{ij} K_i^*} = \frac{\vec{\phi}_i^{*T}\left[C_{j0}\right]\vec{\phi}_i^* K_i}{\vec{\phi}_i^{T}\left[C_{j0}\right]\vec{\phi}_i K_i^*} \tag{2.48}$$

where $\gamma_{ij} = \vec{\phi}_i^{T}\left[C_{j0}\right]\vec{\phi}_i \quad \gamma_{ij}^* = \vec{\phi}_i^{*T}\left[C_{j0}\right]\vec{\phi}_i^*$. To avoid numerical problems when the denominator of Eq. (2.48) becomes close to zero, the equation (2.46) can be reformulated as

$$1 = \left(F_{ij}^* + 1\right)/\left(F_{ij} + 1\right) \tag{2.49}$$

in which case β_j can be approximated as

$$\beta_j \approx \frac{\left(\vec{\Phi}_i^{*T}\left[C_{j0}\right]\vec{\Phi}_i^* + \sum_{k=1}^{NE}\vec{\Phi}_i^{*T}\left[C_{j0}\right]\vec{\Phi}_i^*\right)}{\left(\vec{\Phi}_i^{T}\left[C_{j0}\right]\vec{\Phi}_i + \sum_{k=1}^{NE}\vec{\Phi}_i^{T}\left[C_{j0}\right]\vec{\Phi}_i\right)} \cdot \frac{K_i}{K_i^*} \tag{2.50}$$

in which, the stiffness of undamaged and damaged structure are both assumed to be approximately uniform. A normalized damage indicator is further given as

$$Z_j = \left(\beta_j - \bar{\beta}\right)/\sigma_\beta \tag{2.51}$$

where $\overline{\beta}$ is the mean value of β and σ_β is its standard deviation. The authors used hypothesis testing to determine the damage location by setting a damage threshold value. The severity of damage can be estimated as

$$E_j^* = E_j\left(1+\frac{dE_j}{E_j}\right) = E_j(1+\alpha_j) \tag{2.52}$$

where

$$\alpha_j = \frac{\gamma_{ij}K_i^*}{\gamma_{ij}^*K_i} - 1 \tag{2.53}$$

This method was referred by Stubbs and Kim (1996) as the Damage Index method. They applied this method to a finite element model of two-span continuous beam, where the modal strain energy for an Euler-Bernoulli beam can be expressed as $K_i = \int_0^L EI_z\left\{\phi_i''(x)\right\}^2 dx$. The method was shown to be able to pinpoint the position of the damage with reasonable accuracy. There have been several papers published with the purpose of comparing the effectiveness of this method with other damage identification techniques (Farrar and Jauregui 1998; Wang et al. 2000) and the Damage Index method was shown be more effective in locating damage regions compared with other methods but was unable to give an accurate prediction of damage severity.

Choi and Stubbs (1997) extended the Damage Index method to 2D plate structures, where the modal strain energy can be formulated as

$$U_i = \frac{1}{2}\iint_A D\left\{\left(\frac{\partial^2\phi_i}{\partial x^2}+\frac{\partial^2\phi_i}{\partial y^2}\right)^2 - 2(1-\nu)\left[\frac{\partial^2\phi_i}{\partial x^2}\frac{\partial^2\phi_i}{\partial y^2}-\left(\frac{\partial^2\phi_i}{\partial x\partial y}\right)^2\right]\right\}dxdy \qquad (2.54)$$

where A is the area of the plate surface and D is the flexural rigidity of a plate. Using a similar process of reasoning as in the paper by Stubbs and Kim (1996) leads to:

$$F_{ij}^* = U_{ij}^*/U_i^* = F_{ij} = U_{ij}/U_i \qquad (2.55)$$

and the damage index β_{ij} can be obtained as

$$\beta_{ij} = \frac{D_j}{D_j^*} = \frac{f_{ij}^*}{f_{ij}}\frac{U_i}{U_i^*} \qquad (2.56)$$

where f_{ij} represents the integrand in Eq. (2.54) except parameter D.

Kim and Stubbs (Kim et al. 2003) presented an updated version of their previous work (Stubbs and Kim 1996). Following the definition of Eqs. (2.40) and (2.41), express the change in element modal stiffness as

$$dK_{ij} = K_{ij}^* - K_{ij} = \gamma_{ij}^* E_j^* - \gamma_{ij}E_j = \gamma_{ij}^*\left(E_j + dE_j\right) - \gamma_{ij}E_j \qquad (2.57)$$

Solving for the fractional change in j^{th} member's stiffness, the following expression can be obtained

$$\frac{E_j}{E_j^*} = \frac{\gamma_{ij}^*/\gamma_i}{\left(\frac{dK_{ij}}{K_i}+\frac{\gamma_{ij}}{\gamma_i}\right)} \qquad (2.58)$$

where K_i is defined in Eq. (2.40) and γ_i is defined as

$$\gamma_i = \vec{\phi}_i^T\left[C_0\right]\vec{\phi}_i \qquad (2.59)$$

and $[C] = E_j [C_0]$ following the same concept as in Eq. (2.45). Here, once again it is assumed the structure have uniform stiffness in the undamaged state.

The fractional change of i^{th} modal stiffness before and after damage can be expressed as

$$\frac{dK_i}{K_i} = \frac{d\lambda_i}{\lambda_i} + \frac{dM_i}{M_i}(1 + \frac{d\lambda_i}{\lambda_i}) \tag{2.60}$$

where $\frac{dM_i}{M_i}$ is the fractional change of modal mass, and $\frac{d\lambda_i}{\lambda_i}$ is the fractional change of *i*th system eigenvalue. It is assumed that the structure is damaged in a single location, thus $dK_{ij} \approx dK_i$. Substituting this relation and Eq. (2.60) into Eq. (2.58), the index β_j can be formulated as

$$\beta_j = \frac{E_j}{E_j^*} = \frac{\gamma_{ij}^*}{\gamma_i g_i + \gamma_{ij}} \tag{2.61}$$

where $g_i = \frac{dK_{ij}}{K_i} = \frac{d\lambda_i}{\lambda_i} + \frac{dM_i}{M_i}(1 + \frac{d\lambda_i}{\lambda_i})$. The damage localization and sizing algorithm based on Eq. (2.61) was compared with results obtained from Eq. (2.48) and Eq. (2.50) using a numerical model of a two-span continuous beam. It was shown the updated algorithm gave better results both in damage localization and estimation of damage severity.

Park et al. (2002) extended the concept of the Damage Index method to truss structures, where the fraction modal strain energy of *i*th mode F_{ij} could be expressed as

$$F_{ij} = \frac{k_j \left(\Delta_{ij}\right)^2}{\sum_{j=1}^{NE} k_j \left(\Delta_{ij}\right)^2} \tag{2.62}$$

where k_j represents the stiffness of jth element, Δ_{ij} represents the deformation of j^{th} element in i^{th} mode, and NE is the number of elements. The change in fractional modal strain energy can then be expressed as

$$dF_{ij} = F_{ij}^* - F_{ij} \approx \frac{d\left(k_j \left(\Delta_{ij}\right)^2\right)}{\sum_{j=1}^{NE} k_j \left(\Delta_{ij}\right)^2} \tag{2.63}$$

Here it is assumed that $k_j \left(\Delta_{ij}\right)^2 << \sum_{j=1}^{NE} k_j \left(\Delta_{ij}\right)^2$ and only one element in the structure was damaged. Park et al. (2002) further made the implicit assumption that the change in internal force of the structure due to damage was negligible, i.e., the internal force in element j, P_j, is constant, where

$$P_j = k_j \Delta_{ij} \tag{2.64}$$

Expanding the numerator in Eq. (2.63)

$$\begin{aligned} d\left(k_j \left(\Delta_{ij}\right)^2\right) &= \left(\Delta_{ij}\right)^2 dk_j + k_j d\left(\Delta_{ij}\right)^2 \\ &= \left(\Delta_{ij}\right)^2 dk_j + k_j d\left(\frac{P_j}{k_j}\right)^2 = -\left(\Delta_{ij}\right)^2 dk_j \end{aligned} \tag{2.65}$$

Substituting Eq. (2.65) into Eq. (2.63)

$$dF_{ij} = -\frac{\left(\Delta_{ij}\right)^2 dk_j}{\sum_{j=1}^{NE} k_j \left(\Delta_{ij}\right)^2} = -F_{ij}\frac{dk_j}{k_j} = -F_{ij}\alpha_j \tag{2.66}$$

where $\alpha_j = \frac{k_j^* - k_j}{k_j}$. The damage index β_j can be then expressed as

$$\beta_j = \frac{k_j}{k_j^*} = \frac{1}{2}\left(\frac{f_{ij}^*}{f_{ij}} + 1\right) \tag{2.67}$$

in which $f_{ij} = \Delta_{ij}^2 \Big/ \sum_{j=1}^{NE}\left(\Delta_{ij}\right)^2$ and $f_{ij} = \Delta_{ij}^{*2} \Big/ \sum_{j=1}^{NE}\left(\Delta^*{}_{ij}\right)^2$. To overcome the numerical difficulties when the denominator is close to zero in Eq. (2.67), unity is added to both the denominator and numerator,

$$\beta_j = \frac{1}{2}\left(\frac{f_{ij}^* + 1}{f_{ij} + 1} + 1\right) \tag{2.68}$$

If several modes are used, Eq. (2.68) can be further written as

$$\beta_j = \frac{1}{2}\left(\frac{\sum_{i=1}^{NM} f_{ij}^* + 1}{\sum_{i=1}^{NM} f_{ij} + 1} + 1\right) \tag{2.69}$$

Park et al. (2002) verified their method using both a finite element model of a 3-D truss structure with 246 members and a laboratory model of a space truss and reported that the proposed method can accurately locate the damage under both situations.

Shi et al. (Shi et al. 1998; Shi et al. 2000) proposed using the concept of element modal strain energy for damage identification. The proposed method is a two stage

process: in which, first, the damage is located using the change of element Modal Strain Energy, and then the extent of damage is determined using an iterative procedure. For the purpose of damage localization, the modal strain energy of j^{th} element of the intact and damaged structure was defined as

$$MSE_{ij} = \Phi_i^T K_j \Phi_i \qquad MSE_{ij}^d = \Phi_{di}^T K_{dj} \Phi_{di} \tag{2.70}$$

where K_j is the element stiffness matrix of j^{th} element and Φ_i is the i^{th} mode shape. Subscript d denotes damaged structure. The Modal Strain Energy Change Ratio (MSCER) was defined as

$$MSCER_j^i = \frac{\left| MSE_{ij}^d - MSE_{ij} \right|}{MSE_{ij}} \tag{2.71}$$

Shi et al. (1998) stated that with damage occurring in an element of a system, the MSE would change little in the undamaged elements, but there would be a larger change of MSE in the damaged elements. Thus, MSCER could be a meaningful indicator for damage localization.

Writing the stiffness matrix K of damaged structure in terms of fractional change of the elemental stiffness matrix

$$K^d = K + \sum_{j=1}^{L} \Delta K_j = K + \sum_{j=1}^{L} \alpha_j K_j \quad (-1 < \alpha_j \le 0) \tag{2.72}$$

The change of modal strain energy can be expressed as

$$MSEC_{ij} = 2\Delta\Phi_i^T K_j \Phi_i + \alpha_j \Phi_i^T K_j \Phi_i \tag{2.73}$$

Since α_j is unknown, it is assumed to be very small and set to zero at the start of iteration, thus Eq. (2.73) becomes

$$MSEC_{ij} = 2\Delta\Phi_i^T \mathrm{K}_j \Phi_i \tag{2.74}$$

The value of MSEC can be determined from the damaged and undamaged mode shape and original system stiffness matrix. For a small perturbation in an undamped dynamic system, the equation of motion can be expressed as

$$\left[\left(K+\Delta K\right)-\left(\lambda_i+\Delta\lambda_i\right)M\right]\left(\Phi_i+\Delta\Phi_i\right)=0 \tag{2.75}$$

Expressing the term $\Delta\Phi_i$ as a linear combination of mode shapes of the original system

$$\Delta\Phi_i = \sum_{k=1}^{n} d_{ik}\Phi_k \tag{2.76}$$

Inserting Eq. (2.76) into Eq. (2.75) and neglecting second-order terms in Eq. (2.75), after some manipulation, d_{ir} can be determined as:

$$d_{ir} = -\frac{\Phi_r^T \Delta K \Phi_i}{\lambda_r - \lambda_i} \quad (r \neq i) \tag{2.77}$$

Inserting Eq. (2.76) and Eq. (2.77) into Eq. (2.74), an expression for MSEC can be obtained as

$$MSEC_{ij} = 2\Phi_i^T K_j \left(\sum_{r=1}^{n} -\frac{\Phi_r^T \Delta K \Phi_i}{\lambda_r - \lambda_i} \Phi_r \right) \quad (r \neq i) \tag{2.78}$$

utilizing Eq. (2.72), the above equation can be further expressed as

$$MSEC_{ij} = \sum_{p=1}^{L} 2\alpha_p \Phi_i^T K_j \left(\sum_{r=1}^{n} -\frac{\Phi_r^T K_p \Phi_i}{\lambda_r - \lambda_i} \Phi_r \right) \quad (r \neq i) \tag{2.79}$$

After determining the damage sites using the localization approach, the damage severity of the suspected damaged elements can then be evaluated with

$$\begin{Bmatrix} MSEC_{i1} \\ MSEC_{i2} \\ \vdots \\ MSEC_{iJ} \end{Bmatrix} = \begin{bmatrix} \beta_{11} & \beta_{12} & \cdots & \beta_{1p} \\ \beta_{21} & \ddots & & \vdots \\ \vdots & & \ddots & \vdots \\ \beta_{J1} & \cdots & \cdots & \beta_{Jp} \end{bmatrix} \begin{Bmatrix} \alpha_1 \\ \alpha_2 \\ \vdots \\ \alpha_p \end{Bmatrix} \tag{2.80}$$

where p is the number of suspected damaged sites and J is the number of element where MSEC is calculated. Element β_{st} is sensitivity coefficient of MSEC to damage

$$\beta_{st} = -2\sum_{r=1}^{n} \Phi_i^T K_s \frac{\Phi_r^T K_t \Phi_i}{\lambda_r - \lambda_i} \Phi_r \quad (r \neq i) \tag{2.81}$$

Solving Eq. (2.80) using experimentally measured MSEC will lead to values of fractional change of individual element stiffness change. Once the initial estimate of α_p is obtained, the values of MSEC can be updated using Eq. (2.73) and the procedure is repeated until convergence is achieved.

A numerical model of a cantilever beam and a fixed supported beam was used to verify the method discussed above by Shi et al. (1998). The method was shown to be able to correctly estimate the severity of the damage when a sufficient numbers of modes are used. However, no experimental verification was given. In addition, the method is seen to suffer from the drawback that the problem tends to be ill-conditioned.

Shi et al. (2002) further proposed an improved version of the aforementioned method, in which, the sensitivity relation between eigenvector and change in stiffness parameters are expressed as

$$d_{ir}^{(W)} = -\frac{\left(\frac{\lambda_i}{\lambda_r}\right)^W \Phi_r^T \Delta K \Phi_i}{\lambda_r - \lambda_i} \tag{2.82}$$

$$\Delta\Phi_i = K^{-1} b_W b + \sum_{r=1}^{n^*} \frac{-\left(\frac{\lambda_i}{\lambda_r}\right)^W \Phi_r^T \Delta K \Phi_i}{\lambda_r - \lambda_i} \Phi_r \quad (r \neq i) \tag{2.83}$$

in which

$$b_W = I + \lambda_i M K^{-1} + \left(\lambda_i M K^{-1}\right)^2 + \cdots + \left(\lambda_i M K^{-1}\right)^{W-1} \tag{2.84}$$

$$b = \Delta\lambda_i M \Phi_i - \Delta K \Phi_i \tag{2.85}$$

where W is a weighting factor. Shi et al. (2002) stated that the formulation in Eq. (2.82) effectively reduced the contribution from higher modes compared with Eq. (2.77). Thus a smaller number of analytical modes is required to achieved the same degree of accuracy. They again used the numerical model of a fixed-supported beam to verify the proposed algorithm and showed the improved algorithm was able to converge with fewer numbers of modes compared with the original algorithm.

2.2.4 Methods using Dynamic Flexibility

Dynamically measured flexibility is another feature often used for vibration-based damage detection of structures. Since the connection between the mode shape and

the dynamic flexibility was established in the ground-breaking paper by Berman and Flannelly (1971), a large number of papers have been published proposing damage detection methodologies utilizing dynamic flexibility.

For a recent example, Bernal and Gunes (2004) proposed a strategy for damage detection of the IASC-ASCE benchmark structure. The IASC-ASCE benchmark structure was the outcome of research performed by the IASC-ASCE SHM task group established by the dynamics committee of ASCE in 1999. The details of the benchmark structure can be found in the paper published by Johnson et al. (2004). The strategy proposed by Bernal and Gunes (2004) involved the following steps: First, flexibility matrix was extracted from measured vibrational response of the structure. The extraction was performed by using either the system realization results when the inputs were measured, or by utilizing the mass orthogonality condition to obtain a matrix that differ from the flexibility by a scalar multiplier when inputs were stochastic. Secondly, the changes in flexibility were mapped to elements whose stiffness properties have changed. This was completed by utilizing the damage locating vector technique which can be summarized as follows:

1. Compute the change in flexibility as

$$DF = F_D - F_U \tag{2.86}$$

where F_D and F_U are flexibilities of damaged and undamaged states, respectively.

2. Obtain a singular value decomposition of DF

$$DF = U\begin{bmatrix} S_1 & 0 \\ 0 & s_2 \end{bmatrix}V^T \tag{2.87}$$

where s_2 are the "small" singular values which should equal to zero for ideal conditions. The *DLV* vectors are simply the columns of *V* associated with the null space. For the noisy conditions, the values in s_2 never equal zero and a cutoff has be to established by computing the stresses in an undamaged model of the structure using the vectors in *V* as loads, and define

$$c_j = \min\left(\frac{1}{\sigma_i}\right) \tag{2.88}$$

If the svn index defined as

$$svn_j = \sqrt{\frac{s_j c_j^2}{s_q c_q^2}} \tag{2.89}$$

for a certain vector V_j is less than or equal to 0.20, the vector V_j can be treated as a DLV. In Eq. (2.89),

$$s_q c_q^2 = \max\left(s_j c_j^2\right) \quad for\ j = 1:m \tag{2.90}$$

3. Compute, for each DLV vector, the normalized stress index vector

$$nsi_j = c_j \sigma \tag{2.91}$$

4. Compute the vector of weighted stress indices (WSI) as

$$WSI = \frac{\sum_{i=1}^{ndlv} \frac{nsi_i}{svn_i}}{ndlv} \tag{2.92}$$

where $\overline{svn_i} = \max\left(svn_i, 0.015\right)$ and ndlv = number of DLV vectors. The potentially damaged elements are those having WSI<1.

Once the damaged elements are located, a model update strategy was then used to obtain quantification of damage severity. The strategy described in Eqs. (2.86) to (2.92) was applied to numerical simulation data of the IASC-ASCE benchmark structure and it was concluded that the strategy performed successfully.

Kim et al. (2002) developed a damage identification scheme utilizing the dynamically measured flexibility matrix of the structure. The calculation and physical implication of the dynamically measured flexibility matrix was first discussed in the paper. Kim et al. (2002) suggested using the well-known formula

$$K^{-1} = \sum_{i=1}^{r} \frac{1}{m_i \omega_i^2} \varphi_i \varphi_i^T \tag{2.93}$$

to calculate the flexibility matrix from dynamic measurement. Then it is pointed out that the j^{th} column of the flexibility matrix was a displacement vector due to a unit load at the j^{th} degree of freedom and hence the flexibility matrix served as a transformation from dynamic domain to static domain. For output-only measurements, the modal mass in Eq. (2.93) cannot be calculated directly. It is then suggested using the following formula to estimate modal mass

$$m_i = \int_L \rho A \varphi_i \varphi_i dx \tag{2.94}$$

where ρ and A denote the density and cross sectional area of the beam, respectively.

Kim et al. (2002) based their discussion on a simplified model of Euler-Bernoulli beam. Because it was concluded that the measurement of rotational degrees of freedom were not practical, the slope-deflection formulae was utilized to relate rotational degrees of freedom to the internal moment of transverse degrees of freedom of the beam element

$$\begin{bmatrix} \theta_1 \\ \theta_2 \end{bmatrix} = \begin{bmatrix} \frac{L}{3EI} & \frac{L}{6EI} \\ -\frac{L}{6EI} & -\frac{L}{3EI} \end{bmatrix} \begin{bmatrix} M_1 \\ M_2 \end{bmatrix} + \begin{bmatrix} \frac{1}{L} & -\frac{1}{L} \\ \frac{1}{L} & -\frac{1}{L} \end{bmatrix} \begin{bmatrix} w_1 \\ w_2 \end{bmatrix} \tag{2.95}$$

where θ_i and w_i denote rotational and transverse degrees of freedom at node i, respectively. M, EI and L denote the bending moment, the flexural rigidity and the length of the beam element, respectively. The slope continuity equation between two adjacent elements

$$\theta_2^e = \theta_1^{e+1} \tag{2.96}$$

was then utilized to yield

$$\left(M_{i-1} + 2M_i\right)\frac{1}{EI_e} + \left(2M_i + M_{i+1}\right)\frac{1}{EI_{e+1}} = 6\frac{w_{i-1} - 2w_i + w_{i+1}}{L^2} \tag{2.97}$$

Based on the assumption of small damage, Kim et al. assumed the internal moment M_i remains unchanged before and after damage. And by noticing the right-hand side of Eq. (2.97) contains the central difference formulation for curvature, Eq. (2.97) becomes

$$\left(M_{i-1} + 2M_i\right)\frac{1}{EI_i^*} + \left(2M_i + M_{i+1}\right)\frac{1}{EI_{i+1}^*} = 6\kappa_i^* \tag{2.98}$$

where again the superscript * denotes damaged structure and κ_i is the curvature. Utilizing the moment-curvature relation

$$M_i = EI_i \kappa_i \tag{2.99}$$

and assuming that the flexural rigidity of an intact structure is uniform ($EI_e = EI_{e+1} = EI_i = EI_{i+1}$), Eq. (2.98) can be further written as

$$\left(\kappa_{i-1} + 2\kappa_i\right)\beta_e + \left(2\kappa_i + \kappa_{i+1}\right)\beta_{e+1} = 6\kappa_i^* \tag{2.100}$$

where $\beta \equiv EI_e / EI_e^*$ represents the flexural damage index of e^{th} element. Assuming that the total number of nodes in the structure model is q, then total possible number of equations is $(q-2)\times(q-2)$. However, the number of unknown damage indices β_e is only q-1. Therefore, from Eq. (2.100), an over-determined system of linear equations is available and damage indices can be solved.

Kim et al. (2005) extended the previous damage identification scheme to plate structures. The slope-deflection formulae of 2D plate was expressed as

$$w_r^e = FM^e + Gw_t^e \tag{2.101}$$

where w_r^e and w_t^e are the rotational and transverse DOFs of a four-node plate element, respectively. M^e is a 8×1 vector of normal stress resultant at the four nodes. The 8×8 matrix F denotes the element flexibility matrix of rotational DOF and G denotes the relationship between the rotational DOF and the transverse DOF. Again using the slope-continuity condition at the nodes and small damage assumption, a series of formulae analogous to Eq. (2.100) can be obtained, for example,

$$\left(\kappa_y^{i-1,j-1} + 2\kappa_y^{i-1,y}\right)\beta^{e,f} + \left(2\kappa_y^{i-1,j} + \kappa_y^{i-1,j+1}\right)\beta^{e,f+1} = 6\overline{\kappa}^{i-1,j} \tag{2.102}$$

where

$$\beta^{e,f} = EI^{e,f} \big/ \overline{EI}^{e,f} \tag{2.103}$$

is the flexural damage index of the *(e, f)*th element. By solving an over-determined system of linear equations, damage indices $\beta^{e,f}$ can be obtained. Here, the authors made an implicit assumption during the deduction of the algorithm that the flexural rigidity of the undamaged structure was uniform. The authors verified their method using a finite element model and showed that the proposed method can both accurately locate and size the damage when the inherent assumptions of the method were met.

2.2.5 Methods using Other Physical Quantities

Sampaio et al. (1999) extended the concept of modal curvature to Frequency Response Functions (FRF). For each frequency, the FRF curvature is given by

$$\alpha''(\omega)_{i,j} = \frac{\alpha(\omega)_{i+1,j} - 2\alpha(\omega)_{i,j} + \alpha(\omega)_{i-1,j}}{h^2} \tag{2.104}$$

where $\alpha_{i,j}$ is the receptance FRF measured at location *i* for a force input at location *j*. The absolute difference between the FRF curvatures of the damaged undamaged structure at location *i* for an applied force at point *j* is given by

$$\Delta\alpha''_{i,j} = \sum_{\omega} \left| \alpha''_d(\omega)_{i,j} - \alpha''(\omega)_{i,j} \right| \tag{2.105}$$

The benefit of Eq. (2.104) and (2.105) compared with modal curvature method was concluded as follows: In Eq. (2.104) and (2.105), information for all frequencies within the test range can be utilized, while for modal curvature method, only information at the resonant frequencies is used. Numerical examples were then used to verify the ability of the proposed method to detect and localize damage. However, no damage severity estimation results were given although the method was claimed to be able to provide damage extent assessment as well.

Choi and Stubbs (2004) suggested that the mean strain energy of the structure during vibration be used to detect changes in the structure. The instantaneous strain energy of the structure was defined as

$$U_i^S = \frac{1}{2} V_i^T [K] V_i \tag{2.106}$$

where V_i represents the displacement configuration of the structure at time instant t_i. $[K]$ is the system stiffness matrix. The mean strain energy for a specified time interval between t_a and t_b may be defined as

$$\bar{U}_t^S = \frac{1}{2(b-a)} \sum_{i=a}^{b} V_i^T [K] V_i \tag{2.107}$$

Similarly, the mean strain energy for the *j*th element during the same time period may be given by

$$\bar{U}_t^j = \frac{1}{2(b-a)} \sum_{i=a}^{b} V_i^T [K_j] V_i \tag{2.108}$$

where $\left[K_j\right] = k_j\left[C_j\right]$, k_j is the stiffness of element *j*, and $\left[C_j\right]$ is the geometric portion of the contribution of the *j*th element to the system stiffness matrix. The ratio of the mean strain energy for the jth element to the system mean strain energy, similar to the concept of fractional modal strain energy in Eq. (2.42), can then be given by

$$F_j = \frac{\bar{U}_t^j}{\bar{U}_t^S} \quad F_j^* = \frac{\bar{U}_t^{j*}}{\bar{U}_t^{S*}} \tag{2.109}$$

where * denotes damaged structure. The author states that the change of the pre-damaged and the post-damaged fractional mean strain energy can be given by

$$dF_j = F_j^* - F_j \approx -F_j\alpha_j \tag{2.110}$$

where the fractional change in stiffness α_j, is given by

$$\alpha_j = \frac{k_j^* - k_j}{k_j} \tag{2.111}$$

then a similar damage index as the one appeared in Eq. (2.47) can be calculated as

$$\beta_j = \frac{k_j}{k_j^*} = \frac{1}{2}\left(\frac{f_j^*}{f_j} + 1\right) \tag{2.112}$$

where

$$f_j = \frac{\sum_{i=a}^{b} V_i^T\left[C_j\right]V_i}{\sum_{i=a}^{b} V_i^T\left[K\right]V_i} \quad f_j^* = \frac{\sum_{i=a}^{b} V_i^{*T}\left[C_j\right]V^*{}_i}{\sum_{i=a}^{b} V_i^{*T}\left[K^*\right]V^*{}_i} \tag{2.113}$$

Shifting the domain of interest in the problem by adding unity to the denominator and numerator in Eq. (2.112), the authors gave the final form of damage index β_j as

$$\beta_j \approx \frac{\sum_{i=1}^{NT} V_i^T [K] V_i \left(\sum_{i=1}^{NT} V_i^{*T} \left[C_j \right] V^*{}_i + \sum_{i=1}^{NT} V_i^{*T} \left[K \right] V^*{}_i \right)}{\sum_{i=a}^{b} V_i^{*T} \left[K \right] V^*{}_i \left(\sum_{i=a}^{b} V_i^T \left[C_j \right] V_i + \sum_{i=1}^{NT} V_i^T [K] V_i \right)} \tag{2.114}$$

The authors verified their method on a finite element model of three-span continuous beam. It was shown that the method can locate the damage areas relatively accurately but gives poor severity estimation.

Choi et al. (2005) proposed another damage identification method for plate structures using the concept of modal compliance. The authors utilized the relationship between bending moments and curvatures

$$M_x = -D\left(\frac{\partial^2 w}{\partial x^2} + \nu \frac{\partial^2 w}{\partial y^2} \right) \quad M_y = -D\left(\frac{\partial^2 w}{\partial y^2} + \nu \frac{\partial^2 w}{\partial x^2} \right) \tag{2.115}$$

Taking advantage of the fact that the sum of the bending moment is invariant, and defining the sum of bending moment as

$$M = \frac{M_x + M_y}{1+\nu} = -D\left(\frac{\partial^2 w}{\partial x^2} + \frac{\partial^2 w}{\partial y^2} \right) \tag{2.116}$$

For an arbitrary element *j* in the structure, using the mean value theorem for integrals

$$\bar{M}_j = \frac{1}{\Delta A_j} \iint_{\Delta A_j} M dx dy = M_j \left(\hat{x}, \hat{y} \right) \tag{2.117}$$

and integrate both sides of Eq. (2.116) over the range of element *j*, one can obtain

$$\iint_{\Delta A_j} M dA = -D \iint_{\Delta A_j} \left(\frac{\partial^2 w}{\partial x^2} + \frac{\partial^2 w}{\partial y^2} \right) dA \tag{2.118}$$

Comparing Eq. (2.118) for undamaged and damaged structure, the authors made the assumption that the pre-damage and post-damage moment sum *M* remains unchanged. Thus the damage index can be defined as (using * to denote damaged state)

$$\beta_{ij}^{c} = \frac{D_j}{D_j^*} = \frac{\iint_{\Delta A_j} \left(\frac{\partial^2 w_i^*}{\partial x^2} + \frac{\partial^2 w_i^*}{\partial y^2} \right) dA}{\iint_{\Delta A_j} \left(\frac{\partial^2 w_i}{\partial x^2} + \frac{\partial^2 w_i}{\partial y^2} \right) dA} \tag{2.119}$$

where w_i is the displacement mode shape of mode *i*. The authors used proposed method for damage localization and showed positive results. However, no result was given for damage severity estimation.

2.2.6 Summary and Comparison of Physical Model Based methods

To compare the relative merits and disadvantages of each method discussed above, a summary is presented in Table 2-1 below.

Table 2-1 Summary and Comparison of Physical Mode Based Methods

Method	Feature Used*	Merits	Disadvantages
Stubbs and Osegueda (1990)	FQ	Using sensitivity of frequency change with respect to parameter change to determine the size and location of damage.	Accurate FE model or theoretical solution needed for sensitivity matrix; numerical ill-conditioning when number of unknown parameter is larger than number of measured frequencies.
Kim and Stubbs (2003)	FQ	Sensitivity calculated theoretically without numerical perturbation.	Require system stiffness matrix to calculate sensitivity matrix; same numerical ill-conditioning problem as above.
Gudmundson (1982)	FQ	Accurate determination of crack size from frequency change.	Only applicable to crack-type damage.
Yuan et al. (1998)	FQ/MS	Utilizing both frequency and mode shape information to estimate mass and storey stiffness.	Only applicable to shear building type structure with lumped mass; damping not considered.
Chakraverty (2005)	FQ/MS	Improved accuracy over method of Yuan et al. (1998).	Same as the method of Yuan et al. (1998).
Udwadia (2005)	FQ/MS	Adopting the general form of equation of motion, does not depend on specific structural type.	Require knowledge of the form of the system stiffness matrix; full mode shape measured at all degree-of-freedoms required; also require known mass matrix.
Yoshimoto et al. (2005)	FQ/MS	Can identify both stiffness and damping of the structure.	Only applicable to shear building type of structure.

Table 2-1 Summary and Comparison of Physical Mode Based Methods (continued)

Method	Feature Used*	Merits	Disadvantages
Ren and De Roeck (2002a, 2002b)	FQ/MS	More robust parameter identification based on equation of motion using SVD and non-negative least squares.	Require knowledge of the form of the system stiffness matrix; numerical difficulty with complex structure; damping cannot be considered.
Stubbs and Kim (1996)	MSE	Utilizing more damage sensitive features such as modal strain energy and modal curvature.	Assuming element modal sensitivity unchanged; unable to accurately predict the severity of the damage.
Choi and Stubbs (1997)	MSE	Extension of MSE concept to 2D plate-like structures.	Assuming constant element modal sensitivity; unable to accurately predict the severity of damage.
Kim and Stubbs (2003)	MSE	Improved damage identification accuracy compared with Stubbs and Kim (1996).	Assuming structure having uniform stiffness at undamaged state; only applicable for single damage case.
Park et al. (2002)	MSE	Extension of MSE concept to truss type structure.	Assuming damage is small and internal force state of the structure is not changed by damage.
Shi et al. (1998, 2000)	EMSE	Correctly estimate the severity of the damage when sufficient number of modes is used.	Need relatively large number of modes to achieve convergence.
Shi et al. (2002)	EMSE	Improved convergence compared with Shi et al. (2000)	Still need sufficient number of modes to achieve numerical stability.
Maeck and De Roeck (1999, 2003)	MC	Conceptually straightforward calculation of member stiffness.	Only applicable to statically determinate structure.
Bernal and Gunes (2004)	DF	Flexibility can be extracted from ambient test data without measured input, less susceptible to noise compared with mode shape	Two stage process, flexibility only used to located damage. Damage severity estimation strategy based on mode shape.

Table 2-1 Summary and Comparison of Physical Mode Based Methods (continued)

Method	Feature Used*	Merits	Disadvantages
Kim et al. (2002)	DF	Can accurately identify location and severity of damage.	Assuming internal force remain unchanged before and after damage; also assume the flexural rigidity of intact structure is uniform
Kim et al. (2005)	DF	Extension of above Dynamic Flexibility concept to 2D plate-like structures.	Assuming internal force remains unchanged due to small damage; flexural rigidity of intact structure needs to be uniform.
Sampaio et al. (1999)	FC	Information at all frequency can be utilized	No damage severity estimation results were given
Choi and Stubbs (2004)	SE	Direct use of measured vibration signature. No need to extract modal parameters.	Can locate damage area relatively accurately but gives poor severity estimation.
Choi et al. (2005)	MCP	Applicable to 2D plate-like structures.	No result given for damage severity estimation.

* Feature used : FQ – Frequency; MS – Mode Shape; MSE – Modal Strain Energy; EMSE – Element Modal Strain Energy; MC – Modal Curvature; DF – Dynamic Flexibility; FC – FRF Curvature; SE – Strain Energy; MCP – Modal Compliance.

2.3 State-of-the-Art of Long-term Vibration-based Health Monitoring Applications of Bridge Structures

Ko (2003) presented the details of a sophisticated long-term monitoring system devised by the Hong Kong Special Administrative Region (HKSAR) Highways Department to monitor structural performance of three cable-supported bridges in Hong Kong. This integrated on-line monitoring system with more than 800 sensors permanently installed on the bridges is deemed by some as the most heavily

instrumented bridge project in the world. Accelerometers were installed on both the bridge deck and the stay cables to measure acceleration due to traffic and wind. For example, the Ting Kau Bridge was instrumented with 24 uni-axial, 20 bi-axial and 1 tri-axial accelerometers. An automated database system was developed based on existing geographic information system (GIS) technologies for data management. The feasibility of study of Level II damage detection algorithm using neural networks was also performed. However, there was no evidence in the paper that Level III structural damage identification had been performed on the structure.

Koh et al. (2003) discussed the development and application of structural health monitoring systems on bridge structures in Korea. Health monitoring systems installed on several existing bridges and new bridges were covered in the paper. Typical bridges were instrumented with different types of sensor for different monitoring purposes. For example, tiltmeter, strain gage, joint meter, thermometer, accelerometer, anemometer and laser displacement sensor were used for static and dynamic monitoring. Apart from the use of accelerometer to detect cable force in stay cables, no details were revealed about the use of vibration measurement for damage identification.

Wu (2003) presented the state-of-the-art development in the Structural Health Monitoring field in Japan. A general flow chart for SHM was presented and various technologies that can support SHM were discussed. Vibration-based monitoring of bridge structures was briefly discussed with some potential research areas pointed out.

Abe and Siringoringo (2003) presented a SHM method for long span bridge using ambient measurement. First, impulse response synthesis was performed with

ambient vibration data using Random Decrement technique. Then the Eigensystem Realization Algorithm (ERA) was employed for identifying the modal parameters. The identified modal parameters were used as inputs to structural inverse analysis to recover changes in structural properties. The changes were modeled as additional state-space matrices. A numerical model of lumped mass system was used to prove the feasibility of proposed method.

Ou (2005) presented some recent advances in structural health monitoring for civil infrastructure in mainland China. Several promising sensor technologies such as Optical fiber Bragg Grating sensors, Polyvinylidene fluoride sensors and SMA sensors were discussed. Several examples of applications on long-span bridges were presented. However, the bridge monitoring system discussed in the paper emphasized on the monitoring of such quantities as girder deformation, local strains and cable forces rather than the global vibration behavior of the bridge.

Li et al. (2003) discussed the health monitoring system for a long-span cable-stayed bridge – the Runyang Yangtse River Bridge. The authors divided the monitoring system into four subsystems: the sensory subsystem, data acquisition and transmitting subsystem, data management subsystem and data analysis and processing subsystem. They also clearly defined the function of the system including notifying structural load changes, reporting actual working condition of the principal components in the bridge and evaluating whether any potential injury exists in the bridge's principal components. Vibration characteristics were used to monitor the change in steel-cable forces and

fatigue response of the cable system. However, no details regarding how the objective could be achieved were given in the paper.

More recently, Chase (2005) discussed the role of sensing and monitoring in achieving FHWA's strategic vision for highway infrastructure. The need for health monitoring system for highway bridge structures was presented from the bridge owners' and administrators' perspective. Some technologies for bridge health monitoring including local NDE, fatigue detection and wireless networks were discussed. However, no discussion about vibration-based health monitoring was present.

Sikorsky (2005) presented a review of current practice of vibration-based health monitoring of bridge structures and pointed out several weaknesses of the current research. These weaknesses include the lack of Level IV techniques, the cost of SHM system, the mobility of the SHM system and its applicability to different structures. The author then provided a list of questions that the investigators must answer when designing a Structural Health Monitoring system to ensure success. These questions include: 1) What output does a bridge owner expect from a structural health monitoring system? 2) What algorithms are available to provide this output? 3) What measurements are needed as input to these algorithms? 4) What sensors are available to measure this response? and 5) Can the SHM system cost be reduced significantly? Based on this list of questions, the author proposed a Level IV damage assessment method and discussed two applications of the proposed method.

2.4 Summary

Based on the review of the existing literature, it can be concluded that long-term vibration-based health monitoring of bridge structures is still in its infancy. This can be clearly seen from the rarity of successful real world applications. Many different types of *Bridge Health Monitoring Systems* (BHMS) have been developed and implemented. However, it should be noted that Bridge Health Monitoring System is not equivalent to *Vibration-based Bridge Health Monitoring System* (VBBHMS). The reason for making such distinction is that current Bridge Health Monitoring Systems place more emphasis on monitoring of local structural behavior such as strain, stress and force rather than the global dynamic response of the structure. Although local structural behavior can be a useful indicator of the health condition of the structure, such monitoring system provides no information about the global behavior of the structure and will face difficulty in accomplishing Level IV tasks of estimating remaining capacity and usable life.

Ultimately, the Level IV problem must be solved in order to fulfill the requirements from bridge owners and administrators. Among the large number of papers in the literature on the topic of *Vibration-Based Damage Identification*, only a small number of papers deal with Level III and Level IV problems. The majority are limited to the modest goal of discovering the occurrence and the location of the damage. Physical model based damage identification methods seem to be a promising class of approach for accomplishing Level III and Level IV tasks. There exist a number of Level III and IV *Physical Model Based* methods proposed for the purpose of VBDI, some of

which appear to be quite promising in laboratory experiments or numerical simulations. However, in the context of integrating such techniques in the *Vibration-based Structural Health Monitoring* System, almost all the methods in their current formulation suffer from problems of one sort or another that will likely limit their application to real world structures. Some are based on theoretical assumptions and simplifications difficult to justify in real world applications, and others face numerical problems that arise from the complexity of civil engineering structures, as shown in Table 2-1. New approaches with improved performance under real world situations are thus needed. The development of such new approaches within context of VBSHM system will be discussed in the remaining part of this dissertation while the author tries to address some of the problems and difficulties associated with the current class of VBDI methodologies applied in real world conditions.

Chapter 3 Operational Modal Analysis for Civil Engineering Structures

3.1 A Brief Overview of Operational Modal Analysis

From the discussion in Section 2.1, it becomes clear that the measurement of structural dynamic properties such as modal parameters is an important step in vibration-based structural health monitoring. In this chapter, the techniques that are used to extract modal parameters from experimentally measured structural vibrational response will be described.

Modal analysis has been widely used for the task of extracting structural modal parameters from the response of structural components and systems to vibration. Traditional Experimental Modal Analysis (EMA) makes use of measured input excitation as well as output response. EMA has made substantial progress in the past three decades. Numerous modal identification algorithms, including Single-Input-Single-Output (SISO), Single-Input-Multiple-Output (SIMO) and Multiple-Input-Multiple-Output (MIMO) techniques, have been developed both in the Time Domain and the Frequency Domain. Traditional EMA has been applied in various fields such as vibration control, structural dynamic modification, and analytical model validation, as well as vibration-based structural health monitoring in mechanical, aerospace and civil applications. For large civil structures, however, it is typically very difficult to excite

the structure using controlled input. It is also impossible to measure all the inputs under operational conditions, especially those from ambient sources. In the last decade and a half or so, starting from the early 1990's, Operational Modal Analysis (OMA) has drawn significant attention in the civil engineering field as an attractive way to tackle this problem. OMA utilizes only response measurements of the structure under operational or ambient conditions to identify modal parameters. Compared with traditional EMA, OMA does not require expensive excitation sources and can be applied to structures while they are in operation. The latter attribute is particularly attractive for vibration-based bridge health monitoring applications because the target bridge does not need to be closed to traffic to perform the modal parameter identification. Due to these reasons, OMA has become the method of choice when it comes to identification of structural modal parameters in long-term Vibration-based Structural Health Monitoring applications. A brief overview of the state-of-the-art of operational modal analysis techniques is presented below.

3.1.1 Operational Modal Analysis in the Time Domain

The development of OMA in the time domain can be classified into three main approaches: Natural Excitation Technique (NExT) based approaches, Autoregressive Moving Average (ARMA) model based approaches, and Stochastic Subspace Identification (SSI) based approaches.

The Natural Excitation Technique was first proposed in the early 1990s by James III et al. (1993) to address the problem of modal identification using ambient excitations. The basic idea of NExT is that the cross-correlation function of two random

responses of the structure that result from an unknown white noise excitation can be expressed as a summation of decaying sinusoids. These sinusoids have the same characteristics as the system's impulse response function. Therefore, time domain modal identification techniques, which are typically applied to impulse response functions, can also be applied to these cross-correlation functions to estimate modal parameters. Modal identification using NExT is a two-step process: first, the correlation function is estimated using measured response data, typically by transforming the cross-spectrum function of the response from frequency domain to time domain; and then a time domain modal parameter identification technique is applied to the correlation function to estimate modal parameters. NExT has been paired with various time domain modal identification techniques, such as the Polyreference Complex Exponential (PRCE) technique (Vold et al. 1982), Extended Ibrahim Time-Domain (EITD) technique (Ibrahim and Mikulcik 1977), and Eigensystem Realization Algorithm (ERA) (Juang and Pappa 1985). A technique that is related to NExT is the Random Decrement Signature (RDS) first proposed by Cole (1973). It has been shown that the Random Decrement Signature is related to the correlation function when the excitation is stationary Gaussian white noise (Asmussen et al. 1999; Asmussen et al. 1998; Vandiver 1977). Thus, similar to NExT, RDS can be paired with various time domain modal identification techniques.

Autoregressive Moving Average (ARMA) models are typically applied to time series data. Typical system identification techniques based on ARMA models such as the Prediction-Error Method (PEM) identify the parameters by minimizing the

prediction errors. Once the model parameters are identified, modal parameters can be computed from the coefficient matrices of the AR polynomials (Anderson 1997).

The Stochastic Subspace Identification (SSI) method is based on the concept of system realization, i.e., recovery or identification of system matrices. It was developed for stochastic systems in parallel with deterministic realization algorithms such as ERA. In the Covariance-driven Stochastic Subspace Identification (SSI-COV) method (Arun 1989), stochastic realization is calculated by performing the decomposition of the covariance matrix of the response instead of the decomposition of impulse response function matrix which is typically performed in the deterministic case. Thus the procedure is in essence similar to the NExT-ERA method discussed previously. Another approach, which is usually called the Data-driven Stochastic Subspace Identification (SSI-DATA) method (Van Overschee and De Moor 1993), makes direct use of the stochastic response without the calculation of the covariance matrix.

A common difficulty in all time domain based OMA methods is the estimation of model order. Under experimental conditions, the order, or the number of vibrational modes, of the structure is not known *a priori*. Modal identification in the time domain is thus usually first performed with presumed model order much higher than the number of possible structural modes. Stabilization diagrams are then used to filter out non-structural or 'computational' modes after modal identification is completed. However, the use of a stabilization diagram has a limited effect in distinguishing true structural modes from those caused by noise. Over- or under-determination of model order results

in inaccurate estimation of modal parameters. At the same time, user-interaction is needed in order to interpret results from the stabilization diagrams.

3.1.2 Operational Modal Analysis in the Frequency Domain

The simplest method to estimate modal parameters from operation data in the frequency domain is the so-called Peak-Picking (PP) or Basic Frequency Domain (BFD) method (Maia and Montalväao e Silva 1997). In this method, the natural frequencies are simply taken from the observation of the peaks on the power spectrum plots. The method yields estimations of acceptable accuracy when the structure exhibits low damping, and structural modes are well separated in frequency. However, a violation of these conditions leads to erroneous results. Another disadvantage is that the method does not given any estimate of modal damping.

Another group of OMA methods in the frequency domain consists of methods utilizing Singular Value Decomposition of the cross-spectrum matrix. These methods are discussed in many references and are referred to as either Complex Mode Indication Function (CMIF) method (Ni et al. 2003) or Frequency Domain Decomposition (FDD) method (Brincker et al. 2000). These methods do not rely on the assumptions of low damping and well-separated modes. Damping ratios can be obtained by transforming the singular values near the peak to time domain (Brincker et al. 2001). The resulting time domain function is an approximation of the correlation function of a SDOF system and the damping ratio can be calculated by use of the logarithmic decrement technique. However, since only truncated data are used for damping calculation, the damping estimation may be biased.

A third group of frequency domain OMA methods are those based on the Least Squares Complex Frequency-domain (LSCF) approximation. Originally intended for finding initial estimates for the iterative Maximum Likelihood (ML) method (Guillaume et al. 1999), it was found these "initial estimates" yield modal parameters accurate enough with smaller computational effort. The main drawbacks of the LSCF approach, which is based on a common-denominator transfer function model, is that mode shapes and modal contribution factors are difficult to obtain.

3.1.3 Summary of the State-of-the-Art of Operational Modal Analysis

Table 3-1 summarizes time and frequency domain Operational Modal Analysis techniques in the existing literature and their limitations. Most of the existing time domain based methods rely on user interaction to select the correct model order and are clearly not suitable for long-term monitoring applications. Although some automatic model order identification algorithms have been proposed (Peeters and De Roeck 2000), the effectiveness of these algorithms in health monitoring applications is not yet fully verified. In this aspect, frequency domain based OMA techniques seem to be more promising. On the other hand, the accurate localization of damage using some vibration-based damage detection techniques such as the modal curvature method discussed in Chapter 4 require sufficient spatial resolution of the mode shape. An accurate estimation of modal parameters for higher modes also requires a higher sampling rate. In such applications, the previously discussed time domain and frequency domain OMA techniques may be computationally too intensive for continuous monitoring

applications. Techniques that are more suitable for automation and also computationally efficient are required.

Table 3-1 Comparison of Operational Modal Analysis Techniques

Domain	Technique[1]	Limitations
Time Domain	NExT based	Accurate model order estimation is difficult to obtain under noisy conditions
	ARMA model based	Accurate model order estimation is difficult to obtain under noisy conditions
	SSI based	Accurate model order estimation is difficult to obtain under noisy conditions
Frequency Domain	Peak-Picking	Only accurate for structure with low damping and well-separated modes
	FDD / CMIF	Damping estimate biased
	LSCF	Mode shape estimate hard to obtain

[1] -- NExT: Natural Excitation Technique; ARMA: Autoregressive Moving Average; SSI: Stochastic Subspace Identification; FDD: Frequency Domain Decomposition; CMIF: Complex Modal Indicator Function; LSCF: Least Square Complex Frequency-domain

3.2 Time Domain Decomposition Technique

The vibration response of a linear time-invariant dynamic system can be expressed in terms of its mode shapes and generalized coordinates as

$$\mathbf{u}(x,t) = \sum_{r=1}^{\infty} \boldsymbol{\varphi}_r(x) q_r(t) \tag{3.1}$$

where $\boldsymbol{\varphi}_r(x)$ is the r^{th} mode shape function and $q_r(t)$ is the corresponding generalized coordinate at time instant t. Assuming all modes are well separated, by applying a

bandpass filter to the system responses, it is possible to isolate the individual modal components in the response time-history (Kim et al. 2002).

$$\mathbf{u}_n(x,t) = \boldsymbol{\varphi}_n(x) q_n(t) \tag{3.2}$$

where $\mathbf{u}_n(x,t)$ is the n^{th} modal contribution to the response, and $\boldsymbol{\varphi}_n(x)$ and $q_n(t)$ is the n^{th} mode shape function and generalized coordinates, respectively.

Consider a system with N_d degrees-of-freedom and assuming the measured response quantity is an acceleration response sampled at N_s discrete time points, Eq. (3.1) can be expressed in discrete time as,

$$[U] = \sum_{r=1}^{N_d} \boldsymbol{\varphi}_r \ddot{\mathbf{q}}_r^T \tag{3.3}$$

where, $[U]$ is the $N_d \times N_s$ response matrix, $\boldsymbol{\varphi}_r$ is the $N_d \times 1$ r^{th} mode shape vector and $\ddot{\mathbf{q}}_r$ is the $N_s \times 1$ vector containing values of the r^{th} generalized coordinate at each time instant. At the same time, Eq. (3.2) can also be expressed in matrix form as

$$[U_n] = \boldsymbol{\varphi}_n \ddot{\mathbf{q}}_n^T \tag{3.4}$$

$$[U_n] = \begin{bmatrix} \ddot{u}_{1n}(1) & \cdots & \ddot{u}_{1n}(N_s) \\ \vdots & \ddots & \vdots \\ \ddot{u}_{N_d n}(1) & \cdots & \ddot{u}_{N_d n}(N_s) \end{bmatrix} = \begin{bmatrix} \phi_{1n} \\ \vdots \\ \phi_{N_d n} \end{bmatrix} \begin{bmatrix} \ddot{q}_n(1) & \cdots & \ddot{q}_n(N_s) \end{bmatrix} \tag{3.5}$$

The autocorrelation of the n^{th} mode-isolated acceleration time history is thus given by

$$[E_n] \equiv [U_n][U_n]^T = \boldsymbol{\varphi}_n \ddot{\mathbf{q}}_n^T \ddot{\mathbf{q}}_n \boldsymbol{\varphi}_n{}^T = \boldsymbol{\varphi}_n Q_n \boldsymbol{\varphi}_n{}^T = Q_n \boldsymbol{\varphi}_n \boldsymbol{\varphi}_n{}^T \tag{3.6}$$

where Q_n is a scalar. In expanded matrix form this can be expressed as:

$$[E_n] = Q_n \begin{bmatrix} \phi_{1n} \\ \vdots \\ \phi_{N_d n} \end{bmatrix} \begin{bmatrix} \phi_{1n} & \cdots & \phi_{N_d n} \end{bmatrix} = Q_n \begin{bmatrix} \phi_{1n}\phi_{1n} & \phi_{1n}\phi_{2n} & \cdots & \phi_{1n}\phi_{N_d n} \\ \phi_{2n}\phi_{1n} & \ddots & & \vdots \\ \vdots & & & \vdots \\ \phi_{N_d n}\phi_{1n} & \cdots & \cdots & \phi_{N_d n}\phi_{1n} \end{bmatrix} \tag{3.7}$$

where $[E_n]$ is a $N_d \times N_d$ symmetric matrix of rank 1.

A close examination of the structure of the $[E_n]$ matrix reveals that each column of $[E_n]$ is a proportional to the modal vector of the n^{th} mode. The Spectral Decomposition Theorem (Lay 2003) states that, the symmetry matrix $[E_n]$ can be expanded by its eigenvalues and eigenvectors,

$$[E_n] = PDP^{-1} = \begin{bmatrix} \mathbf{u}_1 & \cdots & \mathbf{u}_{N_d} \end{bmatrix} \begin{bmatrix} \lambda_1 & & 0 \\ & \ddots & \\ 0 & & \lambda_{N_d} \end{bmatrix} \begin{bmatrix} \mathbf{u}_1^T \\ \vdots \\ \mathbf{u}_{N_d}^T \end{bmatrix} = \tag{3.8}$$
$$\lambda_1 \mathbf{u}_1 \mathbf{u}_1^T + \lambda_2 \mathbf{u}_2 \mathbf{u}_2^T + \cdots + \lambda_{N_d} \mathbf{u}_{N_d} \mathbf{u}_{N_d}^T$$

where $\lambda_1 > \lambda_2 > \cdots > \lambda_{N_d}$ are the eigenvalues of matrix $[E_n]$ and $\mathbf{u}_1$, $\mathbf{u}_2$, $\cdots$, $\mathbf{u}_{N_d}$ are its eigenvectors. Comparing Eq. (3.6) with Eq. (3.8), it becomes clear that if there is no noise in the measurement response, the spectral decomposition of $[E_n]$ will generate a single non-zero eigenvalue λ_1 , and the corresponding eigenvector will be proportional to the modal vector $\boldsymbol{\varphi}_n$. Considering the fact that the modal vector can be arbitrarily scaled, the eigenvector $\mathbf{u}_1$ can be effectively treated as the modal vector.

When noise is present in the measurement, other eigenvalues of the matrix $[E_n]$ will not be equal to zero. However, the contribution to system response from the physical mode will usually dominate the response within the frequency range close to the resonance of that particular mode. Thus, with appropriate selection of band-pass

filter parameters, the largest eigenvalue λ_1 always corresponds to the physical mode and the corresponding eigenvector is same as the modal vector. The existence of noise does not affect the identification of the modal vector. It is noted that Eq. (3.8) holds true no matter what kind of motion the system is experiencing, either free vibration or forced vibration due to some external excitations.

Pre-multiplying Eq. (3.4) with the transpose of the identified n^{th} mode shape yields

$$\boldsymbol{\varphi}_n^T \left[U_n\right] = \boldsymbol{\varphi}_n^T \boldsymbol{\varphi}_n \ddot{\mathbf{q}}_n^T \tag{3.9}$$

The response of n^{th} mode in generalized coordinates can then be obtained as

$$\ddot{\mathbf{q}}_n^T = \frac{1}{\boldsymbol{\varphi}_n^T \boldsymbol{\varphi}_n} \boldsymbol{\varphi}_n^T \left[U_n\right] \tag{3.10}$$

here Eq. (3.10) represents the response of a single degree-of-freedom system corresponding to the n^{th} mode. Therefore, the natural frequency and modal damping of the n^{th} mode can be readily identified using time-domain modal identification techniques such as the Complex Exponential (CE) method or the Eigensystem Realization Algorithm (ERA).

The described technique is subsequently referred to as the Time Domain Decomposition (TDD) technique. The general steps of TDD method start with identifying the frequency region where a certain mode might be located, typically from power spectrum plots of the response signal or from the Frequency Response Function if input is measured. The second step consists of applying a band-pass filter to isolate the desired modes while eliminating the contribution from other modes. In the third step

the matrix $[E_n]$ is formed and the modal vector can be conveniently extracted using Eq. (3.8) and Singular Value Decomposition (SVD) algorithm. The last step involves the construction of SDOF response using Eq. (3.10) and the identification of natural frequencies and modal damping. The process is repeated for each mode within the frequency range of interest.

The computationally intensive part of the process, the singular value decomposition, deals with time domain data only and no Fourier transform is needed. The size of the matrix used for SVD in the TDD method is $N_d \times N_d$, with N_d equals to the number of measurement sites. If n modes are to be identified, the SVD process needs to be repeated n times for the $N_d \times N_d$ matrix. This compares favorably with the time domain based ERA technique, where SVD is also used and the size of the matrix used is $sN_d \times s$, with s equaling to the time lag in the Henkel matrix (Juang and Pappa 1985). For civil engineering applications, s is typically much larger than N_d and nN_d. The computation time required by ERA is thus significant longer than TDD when applied to problems where only a few modes are needed.

3.3 Frequency Domain NExT (FNExT) Technique

3.3.1 The Natural Excitation Technique (NExT) and Its Extension to the Frequency Domain

The Natural Excitation Technique (NExT) was first introduced by James et al. (1993) as a technique for modal testing of wind turbines utilizing natural excitation. The

basic idea is that a Multiple Input Multiple Output (MIMO) structural system excited by random input produces autocorrelation and cross-correlation functions that have the same form as the impulse response functions of the system. Although the original development presented in James et al. (1993) used the second order differential equation form of the equation of motion, a state-space formulation (Chiang and Cheng 1999) will be used below because it helps to clarify the derivation considerably.

The equation of motion of discrete linear system can be expressed in state-space form as

$$[A]\{\dot{X}(t)\}+[B]\{X(t)\}=\{F(t)\} \tag{3.11}$$

where

$$\begin{aligned}&[A]=\begin{bmatrix}[C] & [M]\\ [M] & [0]\end{bmatrix},\quad [B]=\begin{bmatrix}[K] & [0]\\ [0] & -[M]\end{bmatrix},\\ &\{X(t)\}=\begin{Bmatrix}\{x(t)\}\\ \{\dot{x}(t)\}\end{Bmatrix},\quad \{F(t)\}=\begin{Bmatrix}\{f(t)\}\\ \{0\}\end{Bmatrix}\end{aligned} \tag{3.12}$$

in which $[M]$ is the mass matrix, $[K]$ is the stiffness matrix, $[C]$ is the damping matrix, $\{f(t)\}$ is the vector of input forcing functions, $\{x(t)\}$ is the structure response vector. Introducing the modal transformation as

$$\{X(t)\}=[\Psi]\{q(t)\}=\begin{bmatrix}[\Phi]\\ [\Phi][\Lambda]\end{bmatrix}\{q(t)\} \tag{3.13}$$

where $[\Psi]$ is the $2N_d \times 2N_d$ complex modal matrix, $[\Phi]$ denotes the $N_d \times 2N_d$ system eigenvector or mode shape matrix, $[\Lambda]$ denotes the $2N_d \times 2N_d$ complex eigenvalue

matrix, $\{q(t)\}$ is the $2N_d \times 1$ vector of generalized coordinates, N_d is the number of system degree of freedom. Pre-multiplying equation (3.11) by the complex modal matrix $[\Psi]^T$ yields

$$[\Psi]^T [A][\Psi]\{\dot{q}(t)\} + [\Psi]^T [B][\Psi]\{q(t)\} = [\Psi]^T \{F(t)\} \tag{3.14}$$

Invoking the modal orthogonality condition gives

$$[a]\{\dot{q}(t)\} + [b]\{q(t)\} = [\Psi]^T \{F(t)\} \tag{3.15}$$

in which $[a]$ and $[b]$ are diagonal matrices given by

$$[\Psi]^T [A][\Psi] = [a], \quad [\Psi]^T [B][\Psi] = [b] \tag{3.16}$$

The equation of motion is thus decoupled into a series of equations in terms of each generalized or modal coordinate. For the r^{th} generalized coordinate, the decoupled equation can be expressed as:

$$a_r \dot{q}_r(t) + b_r q_r(t) = \{\phi_r\}^T \{f(t)\} \quad (r = 1, 2, \ldots, 2N_d) \tag{3.17}$$

in which a_r and b_r are the diagonal elements of diagonal matrices $[a]$ and $[b]$, respectively, and $\{\phi_r\}$ is the r^{th} mode shape.

Assuming that the system is initially at rest, the solution to Eq. (3.17) can be determined as

$$q_r(t) = \frac{1}{a_r} \int_{-\infty}^{t} \{\phi_r\}^T \{f(\tau)\} e^{\lambda_r (t-\tau)} d\tau \tag{3.18}$$

where $\lambda_r = -b_r/a_r$. The response vector $\{x(t)\}$ can then be obtained as

$$\{x(t)\} = \sum_{r=1}^{2N_d} \{\phi_r\} q_r(t) = \sum_{r=1}^{2N_d} \frac{1}{a_r} \{\phi_r\} \int_{-\infty}^{t} \{\phi_r\}^T \{f(\tau)\} e^{\lambda_r (t-\tau)} d\tau \tag{3.19}$$

The response $x_i(t)$ at the i^{th} degree of freedom (DOF) due input $\{f(t)\} = \begin{bmatrix} f_1(t) & f_2(t) & \cdots & f_{N_d}(t) \end{bmatrix}^T$ is thus given by the expression

$$x_i(t) = \sum_{r=1}^{2N_d} \frac{1}{a_r} \phi_{ir} \int_{-\infty}^{t} \{\phi_r\}^T \{f(\tau)\} e^{\lambda_r (t-\tau)} d\tau \tag{3.20}$$

in which, ϕ_{ir} and ϕ_{kr} are the i^{th} and k^{th} components of r^{th} mode shape, respectively.

The cross-correlation function between the two stationary responses from the i^{th} DOF and the j^{th} DOF can be defined following Bendat and Piersol (1996):

$$R_{ij}(T) = E\left[x_i(t+T) x_j(t) \right] \tag{3.21}$$

Substituting Eq. (3.20) into Eq. (3.21) and interchanging the order of expectation and integration and summation leads to the following expression

$$\begin{aligned} R_{ij}(T) = \sum_{r=1}^{2N_d} \sum_{s=1}^{2N_d} \frac{1}{a_r} \phi_{ir} \frac{1}{a_s} \phi_{js} \int_{-\infty}^{t} \int_{-\infty}^{t+T} e^{\lambda_r (t+T-\sigma)} e^{\lambda_s (t-\tau)} \bullet \\ E\left[\{\phi_r\}^T \{f(\sigma)\} \{\phi_s\}^T \{f(\tau)\} \right] d\sigma d\tau \end{aligned} \tag{3.22}$$

Assuming that the input $\{f(t)\}$ is uncorrelated white noise, then

$$E\left[f_i(\sigma) f_j(\tau) \right] = \begin{cases} \alpha_i \delta(\tau - \sigma) & i = j \\ 0 & i \neq j \end{cases} \tag{3.23}$$

where α_i is a constant and $\delta(t)$ is the Dirac delta function. Eq. (3.22) can then be reduced to

$$R_{ij}(T)=\sum_{r=1}^{2N_d}\sum_{s=1}^{2N_d}\frac{1}{a_r}\phi_{ir}\frac{1}{a_s}\phi_{js}\sum_{k=1}^{N_d}\alpha_k\phi_{kr}\phi_{ks}\int_{-\infty}^{t}e^{\lambda_r(t+T-\tau)}e^{\lambda_s(t-\tau)}d\tau \tag{3.24}$$

Making a change in the variable and changing the limits of integration correspondingly, Eq. (3.24) can be further reduced to

$$R_{ij}(T)=\sum_{r=1}^{2N_d}\sum_{s=1}^{2N_d}\frac{1}{a_r}\phi_{ir}\frac{1}{a_s}\phi_{js}\sum_{k=1}^{N_d}\alpha_k\phi_{kr}\phi_{ks}e^{\lambda_r T}\int_{0}^{+\infty}e^{\lambda_r\theta}e^{\lambda_s\theta}d\theta \quad (T\geq 0) \tag{3.25}$$

It is noted that the time lag T in Eq. (3.25) must be positive which is required by the causal condition of the impulse response function. Evaluating the indefinite integral yields

$$R_{ij}(T)=\sum_{r=1}^{2N_d}\sum_{s=1}^{2N_d}\sum_{k=1}^{N_d}\frac{-1}{a_r a_s(\lambda_r+\lambda_s)}\phi_{ir}\phi_{kr}\phi_{js}\phi_{ks}\alpha_k e^{\lambda_r T} \quad (T\geq 0) \tag{3.26}$$

For negative time lags $(T<0)$, the order of x_i and x_j in Eq. (3.21) can be reversed. This results in the cross-correlation function expression:

$$R_{ij}(T)=\begin{cases}\displaystyle\sum_{r=1}^{2N_d}\left[\sum_{k=1}^{N}\sum_{s=1}^{2N_d}\frac{-\alpha_k}{a_r a_s(\lambda_r+\lambda_s)}\phi_{kr}\phi_{js}\phi_{ks}\right]\phi_{ir}\cdot e^{\lambda_r T}=\sum_{r=1}^{2N_d}Q_{jr}\cdot\phi_{ir}\cdot e^{\lambda_r T} & (T\geq 0)\\ \displaystyle\sum_{r=1}^{2N_d}\left[\sum_{k=1}^{N}\sum_{s=1}^{2N_d}\frac{-\alpha_k}{a_r a_s(\lambda_r+\lambda_s)}\phi_{kr}\phi_{is}\phi_{ks}\right]\phi_{jr}\cdot e^{-\lambda_r T}=\sum_{r=1}^{2N_d}Q_{ir}\cdot\phi_{jr}\cdot e^{-\lambda_r T} & (T<0)\end{cases} \tag{3.27}$$

where Q_{jr} and Q_{ir} represent the double summation inside the bracket. Both are complex constants that are only dependent on DOF *j, i* and mode number *r*.

Comparing Eq. (3.27) with the impulse response function between DOF *i* and *j* of the original system $h_{ij}(t)$, which can be expressed as (Maia and Montalväao e Silva 1997)

$$h_{ij}(t) = \sum_{r=1}^{2N_d} W_{ir}\phi_{ir}e^{\lambda_r t} \tag{3.28}$$

where W_{ir} is the modal participation factor. It can be seen that the positive lag part of the cross-correlation function $R_{ij}(T)$, i.e., when $T \geq 0$, can be expressed as the summation of a series of complex exponentials in the same form as the impulse response function. Although the scalar constants $Q_{jr} \neq W_{jr}$ generally, they are constants for a given mode number *r* and DOF *j*. If all measured channels are correlated to a common reference channel, all the components of the cross-correlation function will then possess the common Q_{jr} component for a certain mode *r*. Thus the value of Q_{jr} will only affect the contribution of different modes to the total system response and will have no effect on the identification of modal parameters λ_r and $\{\phi_r\}$.

Eqs. (3.27) and (3.28) give the relation between the displacement response cross-correlations function and system impulse response functions and so far the derivation has followed the traditional definition of NExT technique. However, in practice it is often preferable to measure the acceleration response. Although the displacement response can be obtained from the acceleration response through numerical integration, the results are not always ideal. It is then of interest to find out if similar relations as expressed in Eqs. (3.27) and (3.28) also holds for the cross-

correlations of acceleration response. The following section extends the NExT technique to the case of acceleration response.

The acceleration response at DOF *i* due to a single input force at DOF *k* can be obtained by taking derivatives of Eq.(3.20) with respect to time

$$\ddot{x}_{ik}(t) = \sum_{r=1}^{2N_d} \frac{1}{a_r} \phi_{ir} \phi_{kr} \frac{d^2}{dt^2} \int_{-\infty}^{t} \{ f(\tau) \} e^{\lambda_r (t-\tau)} d\tau \tag{3.29}$$

The cross-correlation between two stationary acceleration responses can then be found as

$$R''_{ijk}(T) = E\left[\ddot{x}_{ik}(t+T) \ddot{x}_{jk}(t) \right] \tag{3.30}$$

in which, $R''_{ijk}(T)$ represents the cross-correlation of acceleration response. If the input is ideal white noise, theoretically the cross-correlation between acceleration responses does not exist. However, in practice ideal white noise excitation is never achieved. Assuming the input excitation is broad-band white noise such that the following equation holds

$$E\left[f_k(\sigma) f_k(\tau) \right] \approx \alpha_k \delta(t-\sigma) \tag{3.31}$$

the cross-correlation in Eq. (3.30) exists under this assumption and can be expressed as

$$R''_{ijk}(T) = \sum_{r=1}^{2N_d} \sum_{s=1}^{2N_d} \frac{1}{a_r} \phi_{ir} \phi_{kr} \frac{1}{a_s} \phi_{js} \phi_{ks} \alpha_k \frac{d^2}{dt^2} \frac{d^2}{d(t+T)^2} \int_{-\infty}^{t} e^{\lambda_r (t+T-\tau)} e^{\lambda_s (t-\tau)} d\tau \tag{3.32}$$

Evaluating the derivatives and integrals in Eq. (3.32) leads to

$$R''_{ijk}(T) = \sum_{r=1}^{2N_d}\sum_{s=1}^{2N_d} \frac{-1}{a_r a_s (\lambda_r + \lambda_s)} \phi_{ir}\phi_{kr}\phi_{js}\phi_{ks}\alpha_k \lambda_r^2 e^{\lambda_r T} \quad (T \geq 0) \tag{3.33}$$

Summing over all input locations and using notations similar to Eq. (3.27), Eq. (3.33) can be further written as

$$R''_{ij}(T) = \begin{cases} \sum_{r=1}^{2N_d} Q_{jr} \cdot \lambda_r^2 \cdot \phi_{ir} \cdot e^{\lambda_r T} & (T \geq 0) \\ \sum_{r=1}^{2N_d} Q_{ir} \cdot \lambda_r^2 \cdot \phi_{jr} \cdot e^{-\lambda_r T} & (T < 0) \end{cases} \tag{3.34}$$

Comparing Eq. (3.34) with Eq. (3.27) shows that the cross-correlation between acceleration responses shares the same form as the displacement cross-correlation function except for a constant. The constant is different for each mode but will not affect the identification of modal parameters λ_r and $\{\phi_r\}$. Taking derivatives of Eq. (3.29) with respect to *t* yields

$$\ddot{h}_{ij}(t) = \sum_{r=1}^{2N_d} W_{ir} \lambda_r^2 \phi_{ir} e^{\lambda_r t} \tag{3.35}$$

Similar reasoning as used for Eq. (3.27) and Eq. (3.28) can be applied to Eq. (3.34) and Eq. (3.35) to yield the conclusion that the acceleration cross-correlation function $R''_{ij}(T)$ can be used in place of $\ddot{h}_{ij}(t)$ for modal parameter identification purposes.

Further extension of the NExT technique can be introduced in the frequency domain. By converting both Eq. (3.34) and Eq. (3.35) from the time domain to the frequency domain, we obtain

$$G_{ij}(j\omega) = \sum_{r=1}^{2N_d} \frac{\lambda_r^2 Q_{jr}\phi_{ir}}{j\omega - \lambda_r} + \sum_{r=1}^{2N_d} \frac{\lambda_r^2 Q_{ir}\phi_{jr}}{-j\omega - \lambda_r} \tag{3.36}$$

$$H_{ij}(j\omega) = \sum_{r=1}^{2N_d} \frac{\lambda_r^2 W_{jr}\phi_{ir}}{j\omega - \lambda_r} \tag{3.37}$$

where $G_{ij}(j\omega)$ is the cross-spectral density function, or cross-spectrum, of the acceleration response. $H_{ij}(j\omega)$ is the accelerance frequency response function. The first term in Eq. (3.36) corresponds to the positive lag portion of the cross-correlation function in Eq. (3.34). The second terms corresponds to the negative lag portion. Note that the second term in Eq. (3.36) (corresponding to the negative time lag portion) has poles in the negative frequency range. Thus if we limited our discussion to the cross-spectrum function in the positive frequency range only, the second term will have little contribution to the cross-spectrum. It can be easily seen that, just like the relation between cross-correlation functions and impulse response functions, the cross-spectral density functions that correspond to the positive lag cross-correlation have the same form as the frequency response functions except for a constant. Thus, the former can be used in place of frequency response functions for modal parameter identification when input measurement is not available.

3.3.2 Modal Parameter Identification Using Cross-Spectrum Function

Eq. (3.37) is usually referred to as the partial fraction form of the frequency response function (Maia and Montalväao e Silva 1997). Correspondingly, we should

also refer to Eq. (3.36) as the partial fraction form of the cross-spectrum. Alternatively, the cross-spectrum can be expressed in rational fraction polynomial form as

$$G_{ij}(\omega) = \frac{\sum_{k=0}^{2N_d-1} \beta_k (j\omega)^k}{\sum_{k=0}^{2N_d} \alpha_k (j\omega)^k} \tag{3.38}$$

Here, for clarity, we only retain the part of cross-spectrum that corresponds to the positive lag cross-correlation. The part of cross-spectrum that corresponds to the negative time lag cross-correlation is omitted due to their insignificant contribution in the positive frequency range, as pointed out in Section 3.3.1. Further rearranging terms yields the following equation that is linear in unknown parameters α_k and β_k

$$\sum_{k=0}^{2N_d} \alpha_k (j\omega)^k G_{ij}(\omega) - \sum_{k=0}^{2N_d-1} \beta_k (j\omega)^k = 0 \tag{3.39}$$

The equation is valid at each frequency of the measured cross-spectrum function. The total number of unknowns in Eq. (3.39) is $4N_d - 1$, where N_d is the number of system degree of freedom. So as long as the cross-spectrum is measured at more than $4N_d - 1$ discrete frequencies, the unknown coefficients can theoretically be determined. In most practical conditions, the number of measured discrete frequencies is much larger than $4N_d - 1$ and thus results in a system of over-determined equations. Eq. (3.39) can also be generalized to the multiple reference case as

$$\sum_{k=0}^{2N_d} [\alpha_k](j\omega)^k \left[G_{ij}(\omega)\right] - \sum_{k=0}^{2N_d-1} [\beta_k](j\omega)^k [I] = 0 \tag{3.40}$$

where $\left[G_{ij}(\omega)\right]$ is the $N_o \times N_{Ref}$ cross-spectrum matrix, with N_o denoting the number of measured response locations and N_{Ref} denoting the number of reference locations used to calculate the cross-spectrum function. The size of the coefficient matrix $[\alpha_k]$ will normally be $N_o \times N_o$ and the size of the coefficient matrix $[\beta_k]$ will be $N_o \times N_{Ref}$.

Since Eq. (3.39) is a homogenous equation, one of the unknown coefficients can be chosen arbitrarily. It is customary to choose $\alpha_{2N_d} = 1$. The resulting basic equation is given by

$$\sum_{k=0}^{2N_d-1} \alpha_k (j\omega)^k G_{ij}(\omega) - \sum_{k=0}^{2N_d-1} \beta_k (j\omega)^k + (j\omega)^{2N_d} G_{ij}(\omega) = 0 \tag{3.41}$$

Defining the error vector $\{E\}$ for L measured discrete frequencies as:

$$\{E\} = [\Theta]\{\mathrm{A}\} - [\Xi]\{\mathrm{B}\} + \{\Gamma\} \tag{3.42}$$

where, the vectors $\{E\}$, $\{\mathrm{A}\}$, $\{\mathrm{B}\}$ and $\{\Gamma\}$ are given as

$$\{E\} = \begin{Bmatrix} e_1 \\ e_2 \\ \vdots \\ e_L \end{Bmatrix} \quad \{\mathrm{A}\} = \begin{Bmatrix} \alpha_0 \\ \alpha_1 \\ \vdots \\ \alpha_{2N_d} \end{Bmatrix} \quad \{\mathrm{B}\} = \begin{Bmatrix} \beta_0 \\ \beta_1 \\ \vdots \\ \beta_{2N_d-1} \end{Bmatrix} \quad \{\Gamma\} = \begin{Bmatrix} (j\omega)^{2N_d} G_{ij}(\omega_1) \\ (j\omega)^{2N_d} G_{ij}(\omega_2) \\ \vdots \\ (j\omega)^{2N_d} G_{ij}(\omega_L) \end{Bmatrix} \tag{3.43}$$

and the matrices $[\Theta]$, $[\Xi]$ as

$$[\Theta]=\begin{bmatrix} G_{ij}(\omega_1) & G_{ij}(\omega_1)(j\omega_1) & \cdots & G_{ij}(\omega_1)(j\omega_1)^{2N_d-1} \\ G_{ij}(\omega_2) & G_{ij}(\omega_2)(j\omega_2) & \cdots & G_{ij}(\omega_2)(j\omega_2)^{2N_d-1} \\ \vdots & \vdots & & \vdots \\ G_{ij}(\omega_L) & G_{ij}(\omega_L)(j\omega_L) & \cdots & G_{ij}(\omega_L)(j\omega_L)^{2N_d-1} \end{bmatrix} \tag{3.44}$$

$$[\Xi]=\begin{bmatrix} 1 & j\omega_1 & \cdots & (j\omega_1)^{2N_d-1} \\ 1 & j\omega_2 & \cdots & (j\omega_2)^{2N_d-1} \\ \vdots & \vdots & & \vdots \\ 1 & j\omega_L & \cdots & (j\omega_N)^{2N_d-1} \end{bmatrix} \tag{3.45}$$

The unknown coefficient vectors $\{\mathrm{A}\}$ and $\{\mathrm{B}\}$ can be found by minimizing the least squares error function *J,* defined as

$$J=\{E\}^H\{E\} \tag{3.46}$$

In Eq. (3.46), superscript $^{\mathrm{H}}$ stands for complex conjugate transpose. The minimization of *J* can be achieved by finding the derivatives of J respect to vectors $\{\mathrm{A}\}$ and $\{\mathrm{B}\}$ and setting them to zero:

$$\begin{aligned} \frac{\partial J}{\partial A} &= 2[\Xi]^H[\Xi]\{A\}-2\,\mathrm{Re}\left([\Xi]^H[\Theta]\right)\{B\}-2\,\mathrm{Re}\left([\Xi]^H\{\Gamma\}\right)=\{0\} \\ \frac{\partial J}{\partial B} &= 2[\Theta]^H[\Theta]\{B\}-2\,\mathrm{Re}\left([\Theta]^H[\Xi]\right)\{A\}-2\,\mathrm{Re}\left([\Theta]^H\{\Gamma\}\right)=\{0\} \end{aligned} \tag{3.47}$$

or, in matrix form:

$$\begin{bmatrix} [\mathrm{O}] & [P] \\ [\mathrm{P}]^H & [\Lambda] \end{bmatrix}\begin{Bmatrix} \{A\} \\ \{B\} \end{Bmatrix}=\begin{Bmatrix} \{\Delta\} \\ \{\mathrm{Z}\} \end{Bmatrix} \tag{3.48}$$

where,

$$
\begin{aligned}
[\mathrm{O}] &= [\Xi]^H [\Xi] \\
[P] &= -\mathrm{Re}\left([\Xi]^H [\Theta]\right) \\
[\Lambda] &= [\Theta]^H [\Theta] \\
\{\Delta\} &= \mathrm{Re}\left([\Xi]^H \{\Gamma\}\right) \\
\{Z\} &= \mathrm{Re}\left([\Theta]^H \{\Gamma\}\right)
\end{aligned}
\tag{3.49}
$$

In Eqs. (3.47) and (3.49), Re( ) denotes the real part of a complex number. By solving Eq. (3.48), which is essentially the normal equations of the least square problem in Eq. (3.46), the unknown coefficients α_k and β_k can be found.

Matrices $[\Theta]$ and $[\Xi]$ in Eq. (3.42) are of the Vandermonde form (Allemang 1999) and are known to be numerically ill-conditioned for cases involving wide frequency range (Maia and Montalväao e Silva 1997). To solve this problem, Richardson and Formenti (1982) proposed rewriting the complex polynomials in Eq. (3.38) in the following form:

$$
G_{ij}(\omega) = \frac{\sum_{k=0}^{2N_d-1} d_k \phi_k(\omega)}{\sum_{k=0}^{2N_d} c_k \phi_k(\omega)} \tag{3.50}
$$

where, $\phi_k(\omega)$ are orthogonal Forsythe Polynomials given by

$$
\begin{aligned}
&\phi_0(\omega) = a_0 \\
&\phi_1(\omega) = a_1(j\omega) \\
&\phi_2(\omega) = a_2 + a_3(j\omega)^2 \\
&\phi_3(\omega) = a_4(j\omega) + a_5(j\omega)^3 \\
&\phi_4(\omega) = a_6 + a_7(j\omega)^2 + a_8(j\omega)^4 \\
&\quad\vdots
\end{aligned}
\tag{3.51}
$$

Once the coefficients c_k and d_k in Eq. (3.50) are found by minimizing error function J, values of coefficients α_k and β_k of the ordinary polynomial equation can be recovered. Following same procedure as Eq. (3.39) through Eq. (3.49), a new set of normal equations can be formed. Solving the equations leads to the values of c_k and d_k. Natural frequencies and modal damping can then be calculated by finding the roots of the characteristic polynomial in the denominator of Eq. (3.38). Modal vectors can be found by rewriting Eq. (3.38) in partial fraction form.

The computationally intensive part of the modal parameter identification process outlined above involves solution of the systems of linear equations (3.48). There exist many efficient algorithms for the solution of such system of equations (Lay 2003). Compared with NExT based techniques discussed in Section 3.1.2, the FNExT method does not require the transformation of cross-spectrum functions into time domain, which might introduce error in the calculated cross-correlation functions. At the same time, FNExT technique also does not involve singular value decomposition of a large matrix as utilized in the ERA and FDD method, which can be computationally intensive.

3.4 Experimental Validation of FNExT Method

A case study was investigated employing experimentally measured vibration data from a reinforced concrete bridge deck specimen in order to verify the validity of the FNExT modal parameter identification method outlined in Sections 3.3.

3.4.1 Description of the Test Structure and Test Procedures

The dimension of the bridge deck specimen is 4.58 m in length and 3.20 m in width (Figure 3-1). The deck consists of three girders equally spaced at 1.68 m and connected on the top by a deck slab 0.15 m in thickness. The structure rests on six supports, one at each end of the girder.

A MB Dynamics SL500 electromagnetic shaker was used to provide excitation to the structure. The shaker is capable of producing force with peak amplitude of 222.4 N. The shaker mounting scheme was designed to produce a single vertical excitation force to the deck at location 7 (Figure 3-1b). A flexible push-rod was used to attach the shaker to the structure, ensuring minimal rotational moment transmission to the structure. Random excitation in the form of Gaussian white noise was applied to simulate the ambient excitation typically experienced by bridges under operational conditions. A PCB 208C02 load cell was used measure the excitation force applied by the shaker to the structure.

To measure the acceleration response of the bridge deck due to random excitations, twenty-five PCB 3701G3FA20G capacitive accelerometers were mounted on the top of the deck. Their locations are marked by the black dots in Figure 3-1b. The

accelerometers have an amplitude range of ± 20 g and frequency range of 0~500 Hz. Accelerometers are screw-mounted to aluminum mounting plates that are adhesively bonded to the deck surface (Figure 3-2).

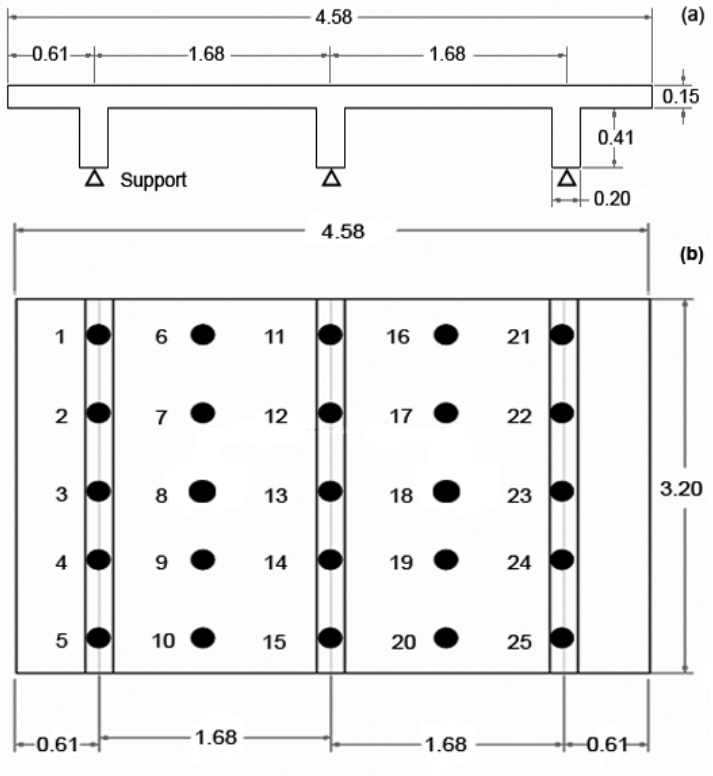

Figure 3-1 Schematic of Test Structure: (a) Elevation (b) Plan View and Location of Accelerometers (Unit: m)

Both the excitation force and the response were measured during the experiment. The signal was sampled at 2000 Hz and filtered with an anti-aliasing filter to reduce the effect of aliasing. Random input and response approximately 250 seconds in length was recorded during each experiment. Typical traces of the time history of the random input force and its power spectrum are presented in Figure 3-3. It can be seen that the power spectrum of the random input force remains approximately constant over a wide frequency range, matching very well with the white noise assumption. The input and

response was divided into multiple sections of equal length and converted to the frequency domain to calculate the frequency response functions. A Hanning window (Ewins 2000) was used to reduce the effect of leakage. The resulting frequency response functions from each section were then averaged to reduce the random error in the measurement. A typical averaged frequency response functions is shown in Figure 3-4a. The cross-spectrum functions between each response and the reference response at location 7 was also calculated. The cross-spectral density function $G_{ij}(j\omega)$ in Eq. (3.36) is estimated using the Welch's averaged periodogram method (Welch 1967):

$$G_{ij}(j\omega) = \frac{1}{N_{avg}T}\sum_{k=1}^{N_{avg}} X_i^*(j\omega)X_j(j\omega) \tag{3.52}$$

in which, $X_i(j\omega)$ and $X_j(j\omega)$ are the discrete Fourier transforms of the time domain response $x_i(t)$ and $x_j(t)$. The time domain response is divided into N_{avg} number of sections and discrete Fourier transform is calculated for each section. T is the time duration of each section of the response. A typical cross-spectrum function within the frequency range of interest is plotted in Figure 3-4b. It is clear that the cross-spectrum function does has same form as the frequency response function, as proved in Section 3.3 by Eqs. (3.36) and (3.37). One important point that should be noted is that cross spectrum function in Figure 3-4b shows more variance than the frequency response function when calculated using the same number of averages. In order to reduce the variance of the cross-spectrum function, more averages are usually needed.

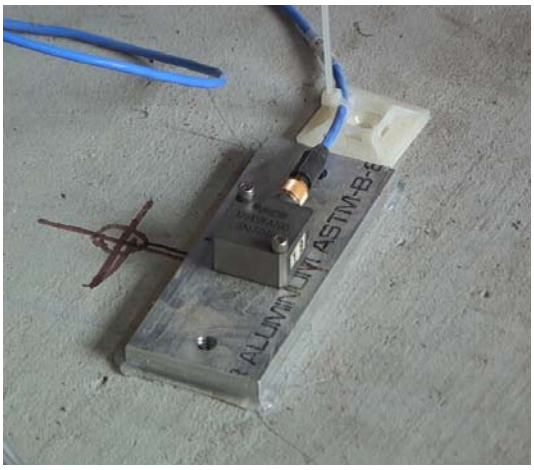

Figure 3-2 Sample Mounting of Accelerometer Mounting on Concrete Surface

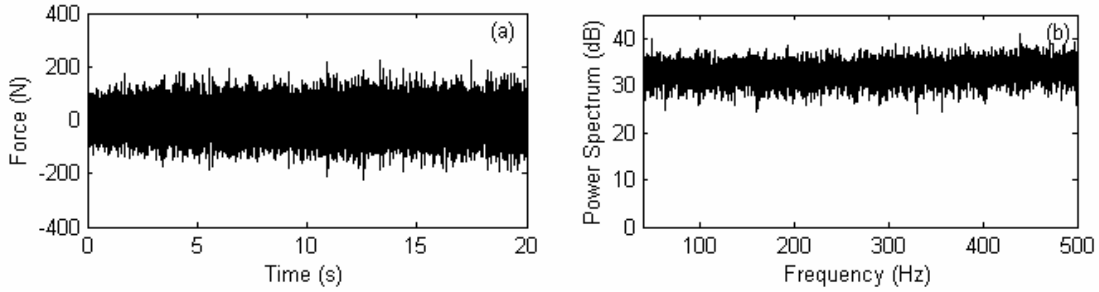

Figure 3-3 Excitation Force Time History and Power Spectrum: (a) Time history (b) Power spectrum

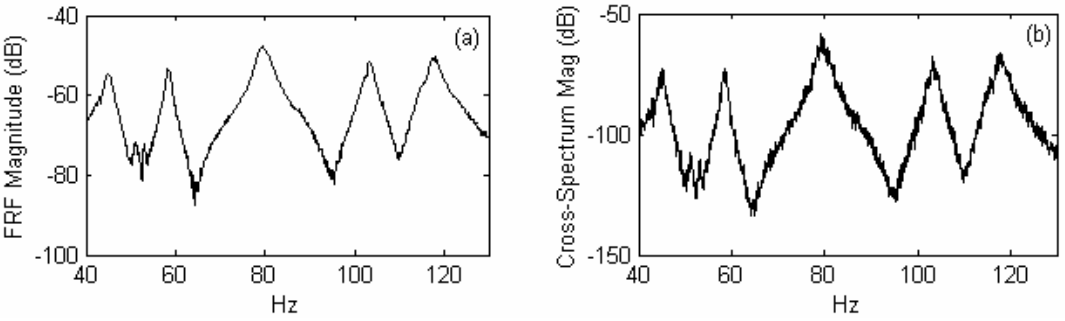

Figure 3-4 Typical Frequency Response Function (FRF) and Cross-Spectrum Function: (a) FRF (b) Cross-Spectrum

3.4.2 Discussion of Test Results

The FNExT technique outlined in Section 3.3 is implemented in MATLAB programming environment (MATLAB 2004) and is used to identify modal parameters from the measured cross-spectrum functions. Figure 3-5 presents a comparison between the measured and synthesized (using identified modal parameters) cross-spectrum functions in the frequency range of 40-130 Hz. All five modes within the frequency range are correctly identified. The mode shapes of the five identified modes are plotted in Figure 3-6.

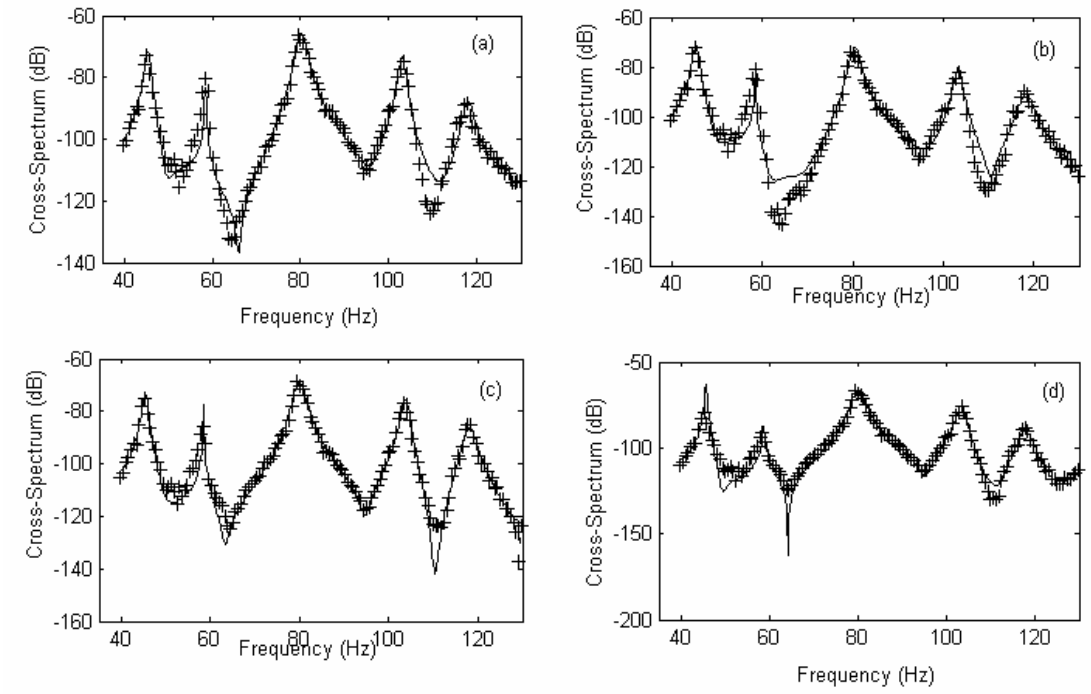

Figure 3-5 Comparison between the measured (+) and synthesized (—) cross-spectral density functions: (a) Cross-spectrum between point 1 and point 7 (b) Cross-spectrum between point 2 and point 7 (c) Cross-spectrum between point 4 and point 7 (d) Cross-spectrum between point 5 and point 7

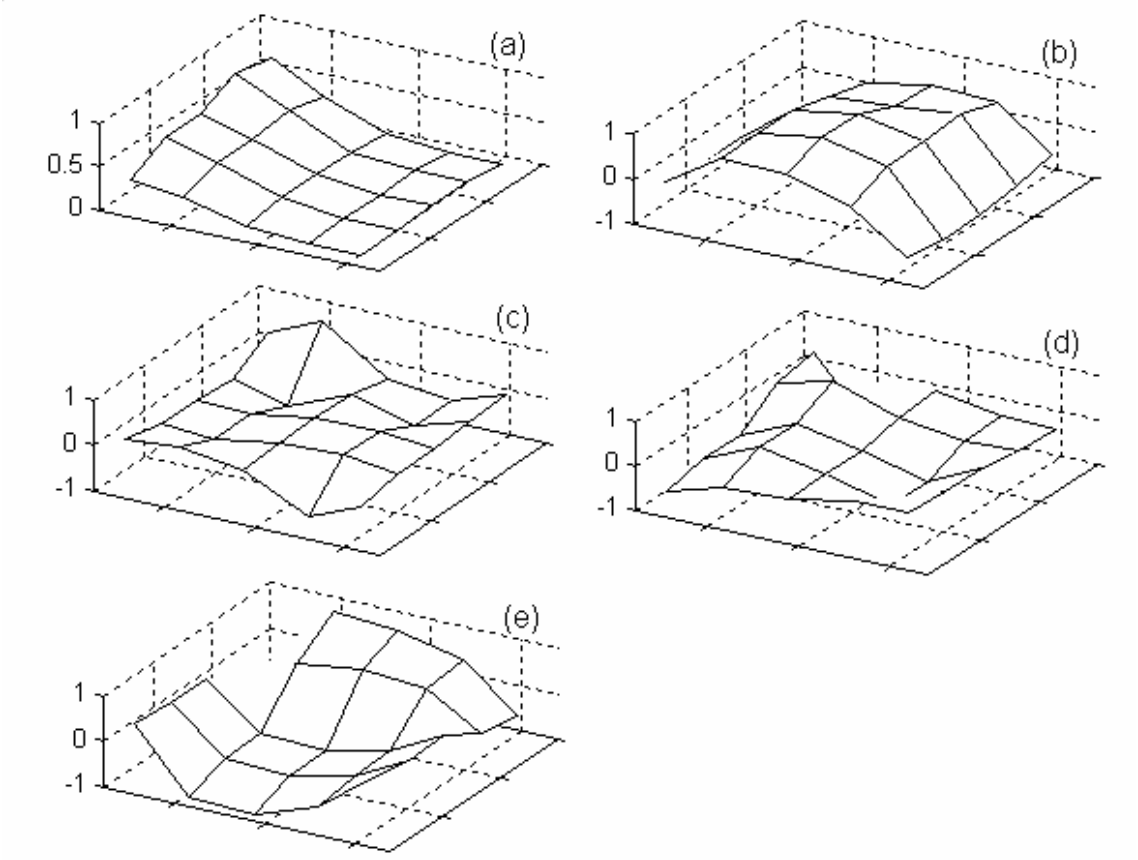

Figure 3-6 Mode Shapes Identified using FNExT Method: (a) First mode (b) Second mode (c) Third mode (d) Fourth mode (e) Fifth mode

Modal parameters were also identified using the Complex Exponential (CE) method (Maia and Montalväao e Silva 1997) which utilizes both the input and response information. Modal parameters identified using Complex Exponential method were used for comparison purpose. Table 3-2 gives values of natural frequency and modal damping identified by the FNExT method and CE method. The frequencies identified by the two methods have a very good agreement. But damping ratios show significant differences for some of the modes. It appears that accurate identification of damping ratios from operational data is difficult and remains a problem to be solved.

Table 3-2 Comparison of Modal Parameters from Two Different Methods

Mode no.	Frequency Domain NExT		Complex Exponential Method		Freq. Diff. $\left(\frac{F-C}{F}\times 100\%\right)$
	Freq. (Hz)	Damping (%)	Freq. (Hz)	Damping (%)	
1	45.4	1.9	45.1	2.1	0.7
2	53.2	1.2	53.1	1.0	0.2
3	79.5	2.4	79.2	1.5	0.4
4	103.5	0.6	103.4	0.8	0.1
5	117.8	2.2	117.5	1.8	0.3

3.5 Applications to Highway Bridges

In this section, the two Operational Modal Analysis techniques discussed in Section 3.2 and Section 3.3 – the Time Domain Decomposition technique and the Frequency Domain NExT technique – are applied to the real world cases of two highway bridges. It will be shown that both methods are successful in identifying modal parameters from measured ambient excitation induced vibrations.

3.5.1 Watson Wash Bridge

3.5.1.1 Description of the Bridge

The Watson Wash Bridge is a reinforced concrete T-girder bridge located on the California section of Interstate Highway 40. The bridge site is west of the city of Needles and approximately 10.3 km east of Essex Road in the Mojave Desert. Figure 3-7 shows the location of the bridge. Figure 3-8 provides an aerial view of the bridge site. Figure 3-9 shows a photograph of the bridge structure. The superstructure consists of a cast-in-place reinforced-concrete deck and girder system with sixteen central spans of 12.8 m each and two shorter end spans of 10.5 m each. Each span consists of five bays separated by six girders at 2.13 m center. The spans are further grouped into five frames connected with shear transfer hinges.

A series of modal tests was performed on the bridge in between July 2001 and June 2003. The purpose of these tests was to monitor the change of dynamic characteristics, such as modal parameters, of the structure resulting from FRP

rehabilitation performed on the bridge during the same time period. The resulting modal parameters are then used as the inputs for Vibration-based Damage Detection algorithms to provide quantitative evaluation the effect of FRP rehabilitation. The current discussion only concerns the ambient vibration modal test performed on June 2003. Detailed discussion of the FRP rehabilitation and monitoring of the Watson Wash Bridge can be found in Lee (Lee 2005). All modal tests were conducted in the Frame S-3 consisting of spans 8 through 12, as shown in Figure 3-10.

Figure 3-7 Location of the Watson Wash Bridge

Figure 3-8 Aerial Photo of the Watson Wash Bridge

Figure 3-9 Watson Wash Bridge

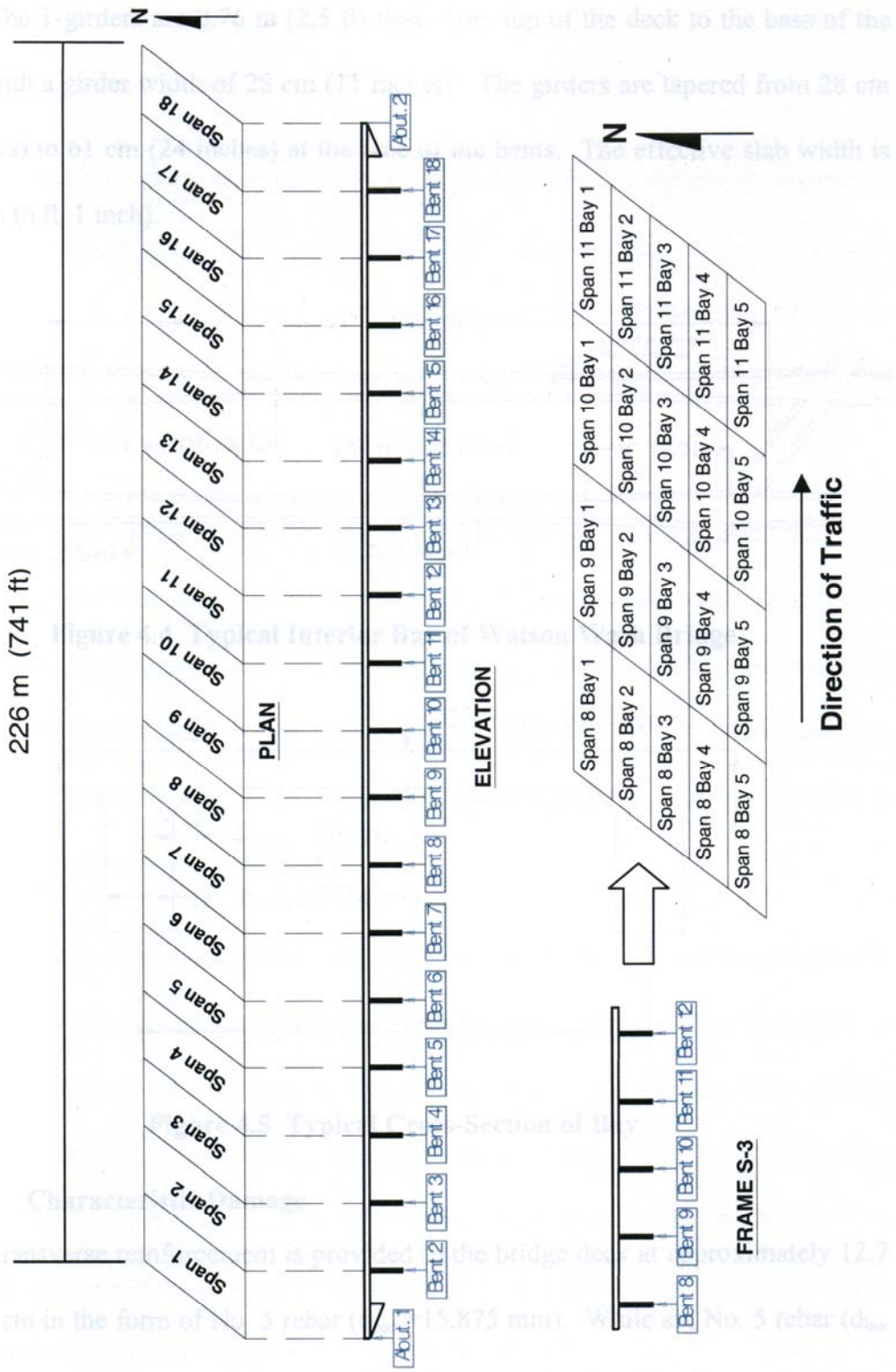

Figure 3-10 Overview of Watson Wash Bridge and Numbering of Spans

3.5.1.2 Ambient Vibration Modal Test

During the test carried out in June 2003, normal traffic over the bridge structure was used as the source of ambient excitation. The use of traffic induced ambient excitation was mainly dictated by the physical constraint that the bridge must remain open to traffic during the test. Since input force was not measured, the use of Operational Modal Analysis to identify modal parameters was warranted.

PCB 3701G2FA3G capacitive accelerometers were used to measure the vertical acceleration of the structure during the modal test. The usable frequency range of the accelerometers is 0~100 Hz and amplitude range is ± 3g. Accelerometers were mounted on the bridge structure using aluminum mounting plates attached to the soffit of longitudinal girders. A sensor grid of six lines in the longitudinal deck directions and eleven lines in the transverse deck direction is used. For girder lines 1, 2, 5 and 6, accelerometers are attached at the hinges, at bent locations, and at mid span of Spans 8, 9, 10 and 11. For girder lines 3 and 4 accelerometers are only applied at hinge and mid span locations but not the bent. Therefore, lines 1, 2, 5, 6 consist of 11 sensor locations each, while line 3 and 4 are composed of 6 sensor locations. The total number of sensor locations is 56, as shown in Figure 3-11.

Due to limited availability of sensors and data acquisition equipment, only 15 sensor locations could be monitored simultaneously. Decision was then made to perform the modal test in multiple setups. For each setup, 15 accelerometers were used. Among the 15 accelerometers, 3 were used as ‘Reference’ accelerometers and their location remained unchanged throughout the test. The locations of the Reference

accelerometers are marked by the red squares in Figure 3-11. The rest of the 12 accelerometers were used as 'Roving' accelerometers and were moved from setup to setup in order to cover all sensor locations.

Figure 3-11 shows each setup of the Roving locations with a different color. The test procedure starts with installing the accelerometers at sensor locations for the current setup. Measurement of the structure response due to ambient traffic excitation is then performed for a duration of approximately 2 minutes. The Roving accelerometers are then detached from their current location and moved to the next set of locations. A total of five setups were needed to cover all sensor locations.

Ambient vibration response data were collected with a sampling rate of 200 samples/sec. The total number of data points collected for the duration of one setup is approximately 24000 points/channel. Typical acceleration time histories recorded during the modal test are plotted in Figure 3-12. A significant amount of noise can be observed on several channels of the time history. Five ambient vibration modal tests were carried out during the period between June 7th and June 10th, 2003. The date and time when each test was carried out is listed as follows: Test 1 was carried out in the morning of June 7th. Test 2 and 3 were carried out in the morning of June 8th. Test 4 and 5 were performed in the afternoon and evening of June 10th, respectively. Each test consists of all five setups and takes approximately 3~4 hours to finish.

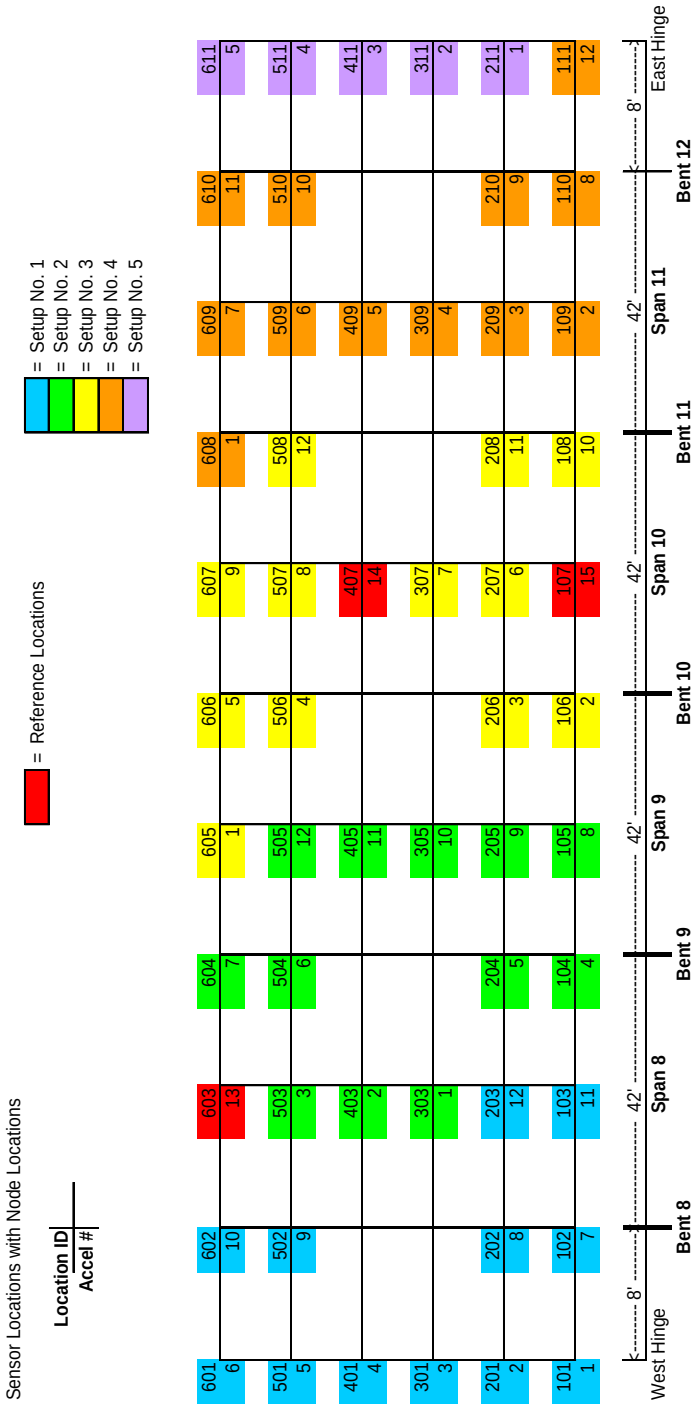

Figure 3-11 Schematic of Accelerometer Locations

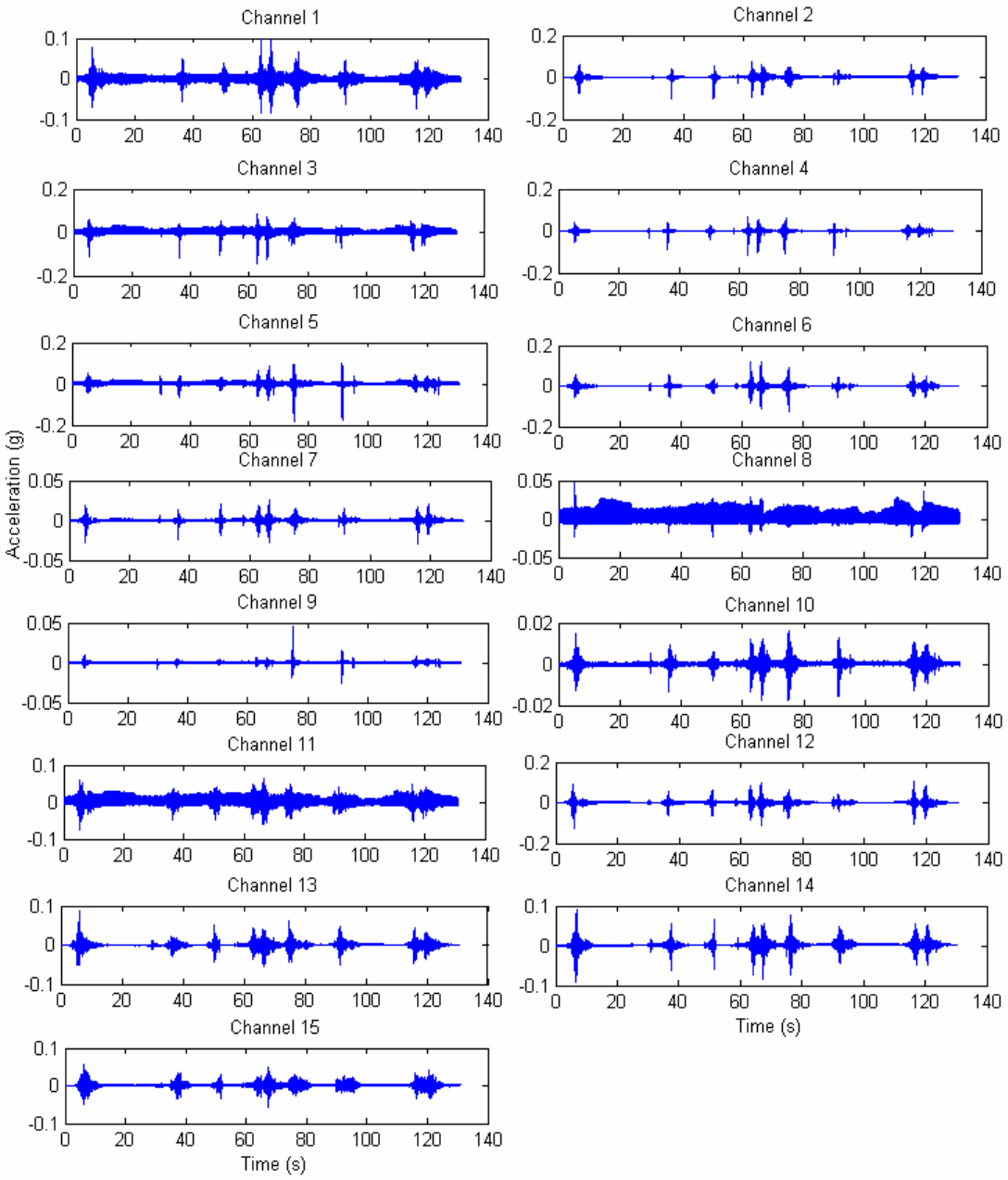

Figure 3-12 Typical Acceleration Time History Recorded During the Modal Test

3.5.1.3 Operational Modal Analysis and Discussion of Results

The Time Domain Decomposition technique presented in Section 3.2 is implemented in MATLAB and used for the identification of modal parameters of the Watson Wash Bridge during the ambient vibration modal test. The Graphical User Interface (GUI) of the program used during the test is presented in Figure 3-13. Data from each setup are analyzed independently using the TDD method to retrieve natural frequency and mode shape information. The frequencies from each setup are then averaged to obtain the natural frequencies of the entire structure. The partial mode shapes obtained during each setup are normalized with respect to one reference sensor location. Therefore, the modal amplitude at the chosen reference location is always unity for every setup. The partial mode shapes for different setups are then 'glued' back together based on the information of the common reference location.

As discussed in Section 3.2, the first step of the TDD method involves the isolation of the modal response of each mode using a digital bandpass filter. A 3rd order Butterworth filter (Roberts 2004) is chosen for the present investigation due to its sharp roll off outside the passband. The selection of the initial estimates of the passband frequencies is carried out by inspecting the power spectral density plots of the measured response and noting respective peaks within the frequency range of interest. Typical power spectral density of the response signal is plotted in Figure 3-14 for the frequency range of 0~10 Hz. Three distinctive peaks are immediately observed in the frequency range between 5 and 5.5 Hz, 5.5 and 6 Hz, and 7 and 8 Hz. These frequency ranges are thus selected as the initial estimate of passband ranges. A closer examination of the

PSD plot reveals that a number of other frequency bands contain peaks which may correspond to vibration modes of the bridge structure. However, only the first two modes are identified consistently throughout all tests.

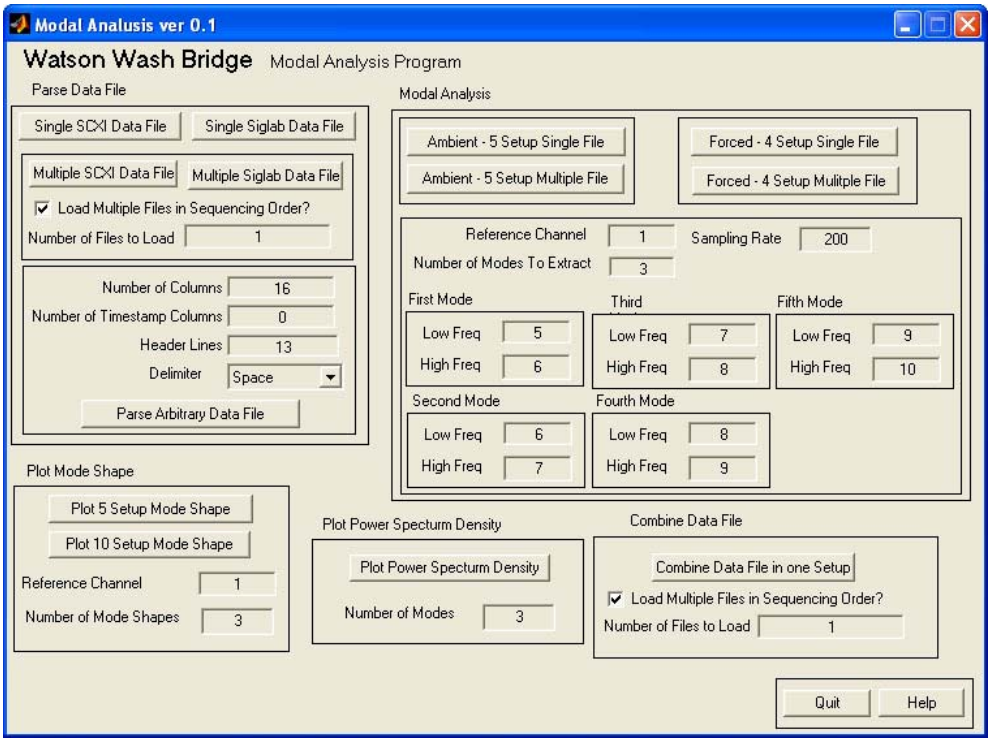

Figure 3-13 Graphical User Interface of the Modal Analysis Program

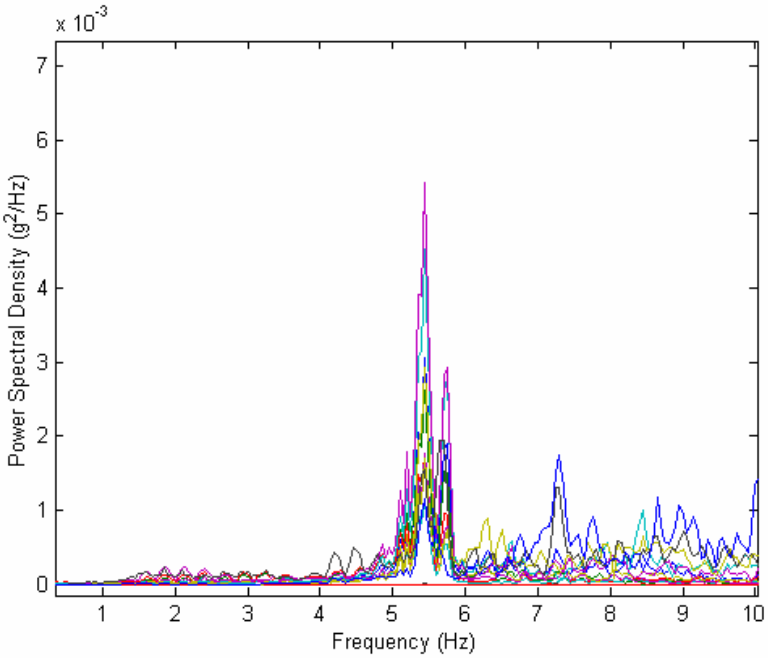

Figure 3-14 Typical Power Spectral Density of the Response

Table 3-3 lists the identified modal frequencies for the first and second mode. Figure 3-15 through Figure 3-18 plot the identified mode shape for test 1, 2, 4 and 5. Data from test 3, carried out on June 8th, contains bad data on several channels and thus was not used for modal analysis. The first mode is dominated by longitudinal bending of the bridge where the vibration of adjacent spans is out-of-phase. The second mode is a combined bending and torsion mode. It should be noted that although the ambient vibration data exhibit strong non-stationary feature, TDD method is still able to consistently identify both modes in all four tests. Both the identified natural frequencies and mode shapes show very good consistency.

Results from field tests of Watson Wash Bridge show that the TDD method is a fast and efficient way to extract modal parameters from ambient vibrations in situations where the natural modes of the structure is well separated. Although each modal test

took about 3 to 4 hours to complete, most of the testing time is accounted for by the time spent on moving roving sensors and necessary cables from one location to another, which was made necessary by the multiple setup nature of the test. The task of modal parameter calculation took less than a minute for each test when performed using the pervious mentioned Matlab program on a Pentium III 1.0 GHz laptop computer. It is also noted that the process of modal parameter identification using the TDD method does not involve the estimation of model order once the initial frequency bands are determined. Also, the TDD method seems to perform reasonably well in the presence of noise and non-stationary data. Combined, these features make the TDD method very attractive for long-term monitoring applications.

Table 3-3 Natural Frequencies of Ambient Vibration Tests

Test no.	Frequency (Hz)	
	Mode 1	Mode 2
1	5.33	5.76
2	5.44	5.69
4	5.39	5.71
5	5.44	5.74

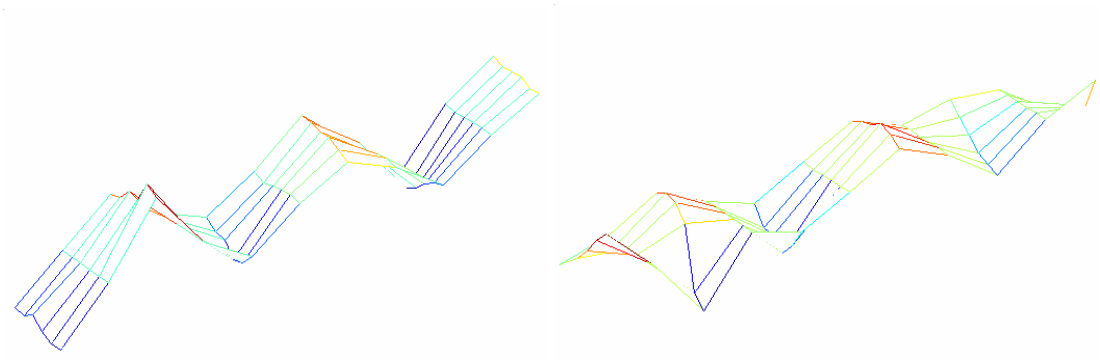

(a) (b)

Figure 3-15 Mode Shapes from Ambient Vibration Test 1: (a) First Bending Mode (b) Second Bending Mode

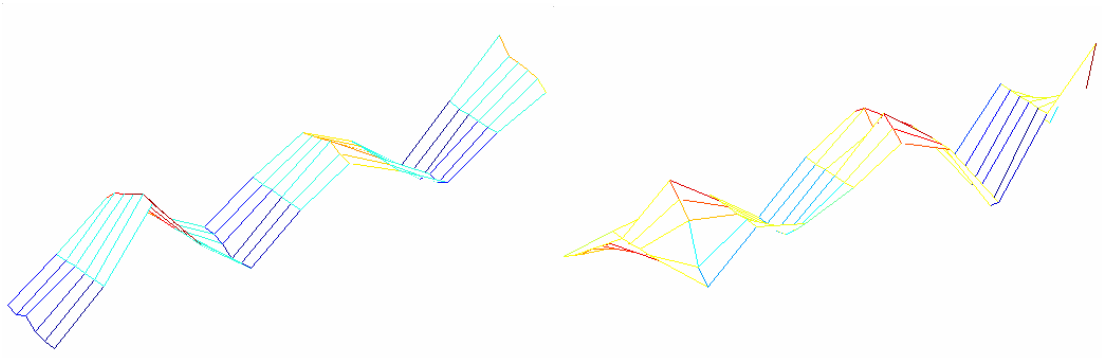

(a) (b)

Figure 3-16 Mode Shapes from Ambient Vibration Test 2: (a) First Bending Mode (b) Second Bending Mode

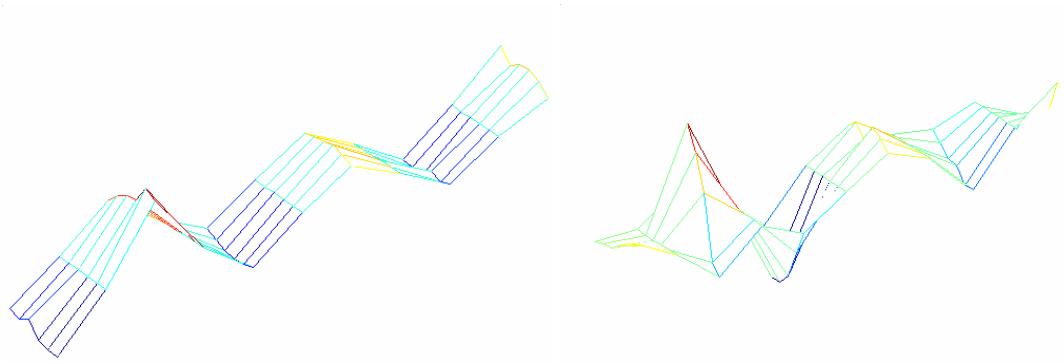

(a) (b)

Figure 3-17 Mode Shapes from Ambient Vibration Test 4: (a) First Bending Mode (b) Second Bending Mode

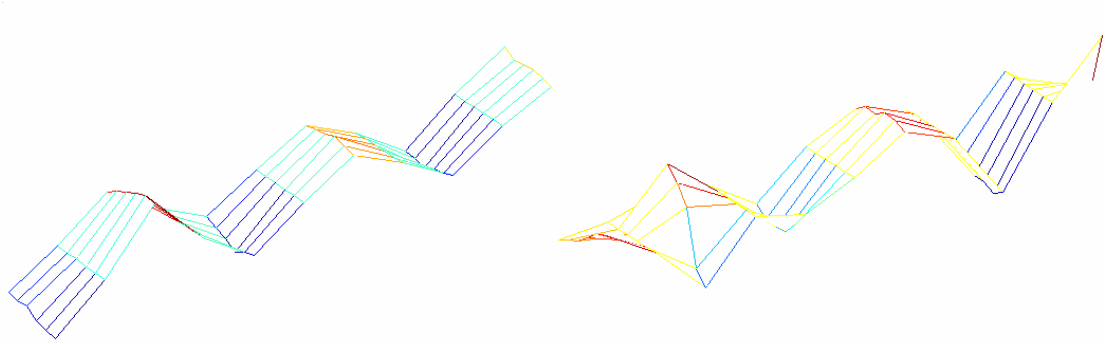

(a) (b)

Figure 3-18 Mode Shapes from Ambient Vibration Test 5: (a) First Bending Mode (b) Second Bending Mode

3.5.2 Vincent Thomas Bridge

3.5.2.1 Description of the Bridge

The Vincent Thomas Bridge is a suspension bridge located in Los Angeles Harbor, San Pedro, California. The bridge superstructure consists of a main span of

approximately 457 m, two suspended side spans of 154 m each, and a 10-span approach of approximately 545 m length on either end. The total bridge length is approximately 1850m. The bridge was completed in 1964, and in 1980 was instrumented with 26 accelerometers as part of a seismic upgrading project. The strong-motion instrumentation was installed and is maintained by the California Division of Mines and Geology. Figure 3-19 shows the elevation and plan view of the sensor locations. A summary of the sensor locations and numbering is presented in Table 3-4.

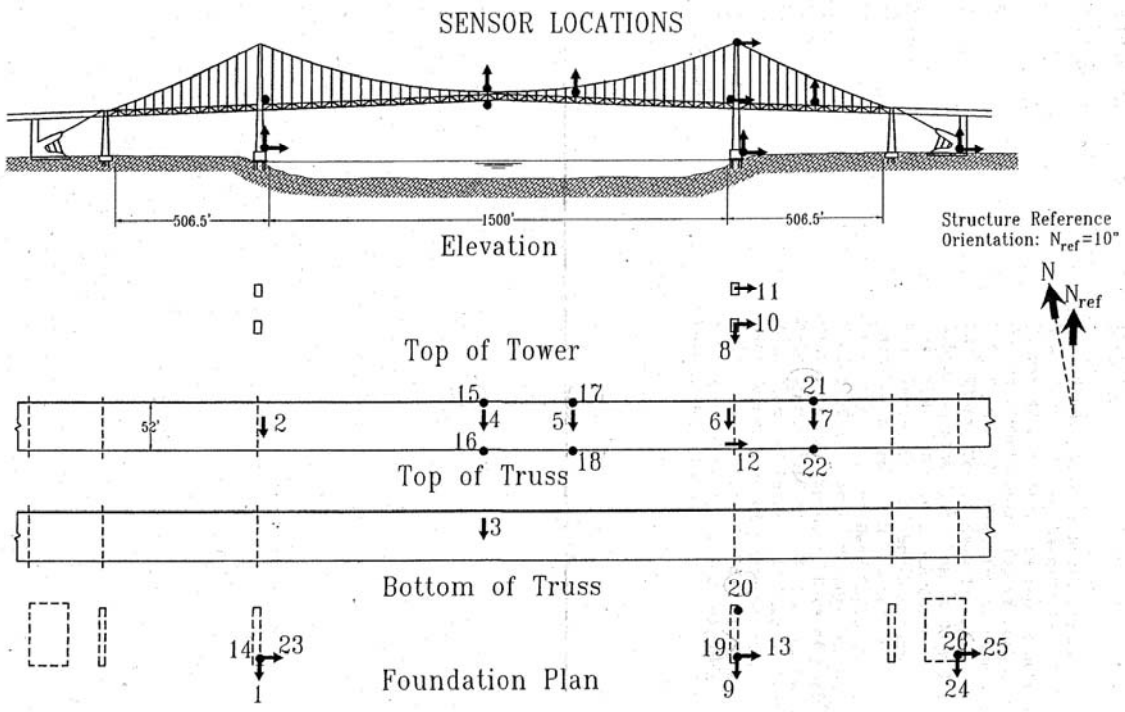

Figure 3-19 Elevation and Plan View of Sensor Locations

Table 3-4 Sensor Numbering and Locations

Sensor No.	Location
1, 14, 23	West Tower, Base of South Column
2	West Tower, Top of Deck Truss
3	Center of Main Span, Bottom of Deck Truss
4	Center of Main Span, Top of Deck Truss
5	Main Span, 1/3rd Pt., Top of Deck Truss
6	East Tower, Top of Deck Truss
7	Center of Side Span, Top of Deck Truss
8, 10	East Tower, Top of South Column
9,13, 19	East Tower, Base of South Column
11	East Tower, Top of North Column
12	East Tower, Top of Deck Truss
15	Center of Main Span, N. Edge of Deck
16	Center of Main Span, S. Edge of Deck
17	Main Span, 1/3rd Pt., N. Edge of Deck
18	Main Span, 1/3rd Pt., S. Edge of Deck
20	East Tower, Base of North Column
21	Side Span, Center, N. Edge of Deck
22	Side Span, Center, S. Edge of Deck
24, 25, 26	East Anchor, Base

3.5.2.2 Ambient Vibration Data for Deck Vertical Vibration Analysis

On April 18th, May 28th and June 1st of 2003, three sets of acceleration data were collected on the bridge to measure the response due to ambient excitations. Ambient excitations to the bridge are mainly caused by wind load and traffic load. The 26 accelerometers installed on the bridge measure accelerations in three different directions, namely, vertical, lateral and longitudinal directions. For the purpose of current discussion, it was surmised that deck vertical vibration is of the primary concern. Six sensors measuring the deck vertical acceleration are thus chosen for analysis. The six

sensors chosen are sensors 15, 16, 17, 18, 21, and 22. Their relative locations on the bridge deck are shown in Figure 3-20.

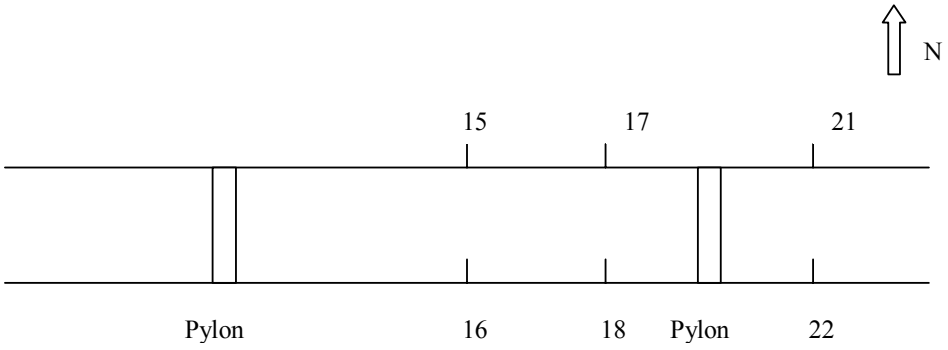

Figure 3-20 Positions of Selected Sensors Used for Deck Vertical Vibration Analysis

After a close examination of collected acceleration time history, it is found that the data set from May 28th contains a bad channel (channel 22) and will not be used in the subsequent analysis. The time history of April 18th and June 1st are plotted in Figure 3-21 and Figure 3-22 respectively. The total length of the time history is 380 seconds for April 18th and 360 seconds for June 1st. It should be noted that the time histories shown in Figure 3-21 and Figure 3-22 exhibit strong non-stationary feature. DC shift is also observed on some of the channels. After detrending the data, the cross spectrum between sensor 15 and sensors 16, 17, 18, 21, 22 together with 15 itself are calculated and plotted in Figure 3-23 and Figure 3-24.

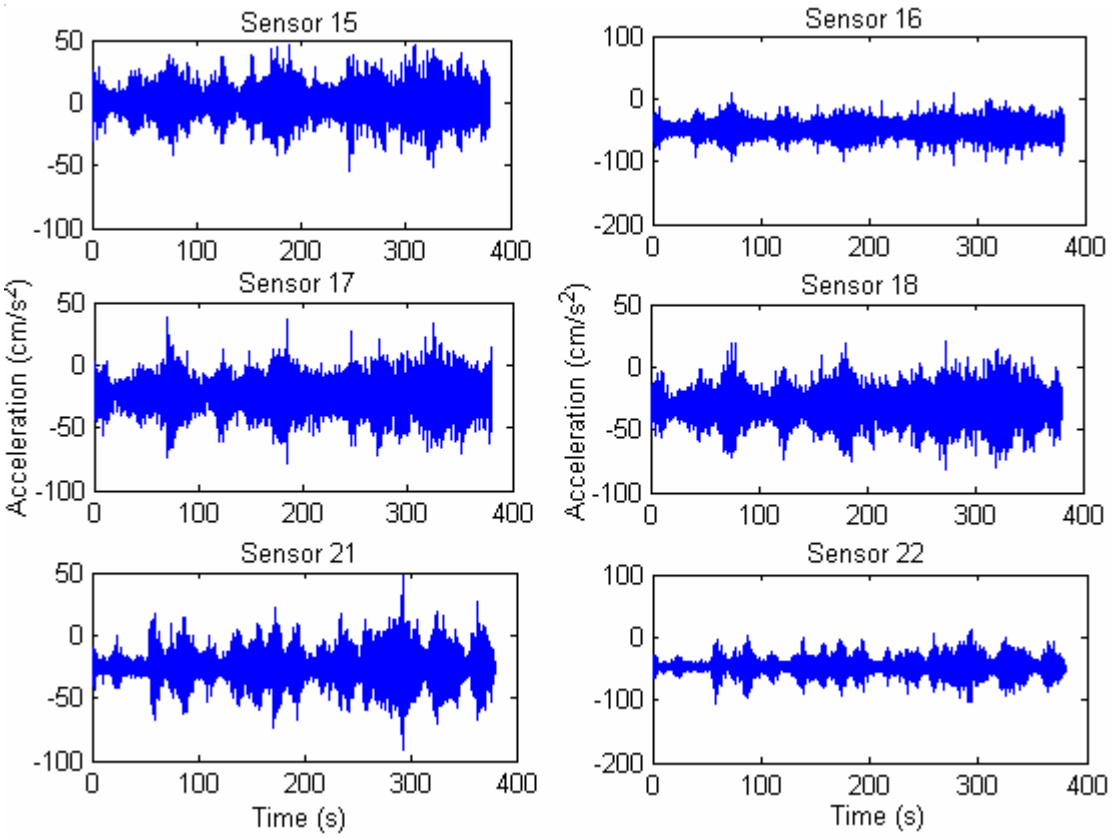

Figure 3-21 Acceleration Time History from the April 18th, 2003 Data Set

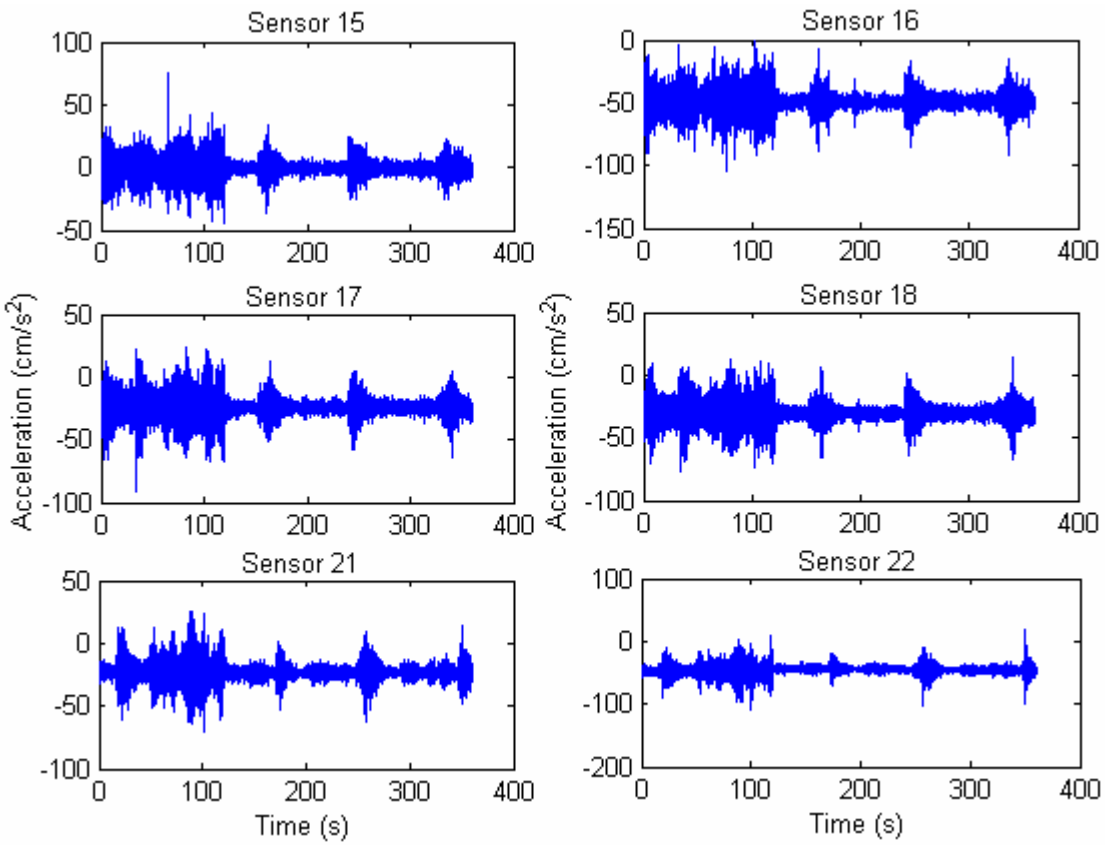

Figure 3-22 Acceleration Time History from the June 1st, 2003 Data Set

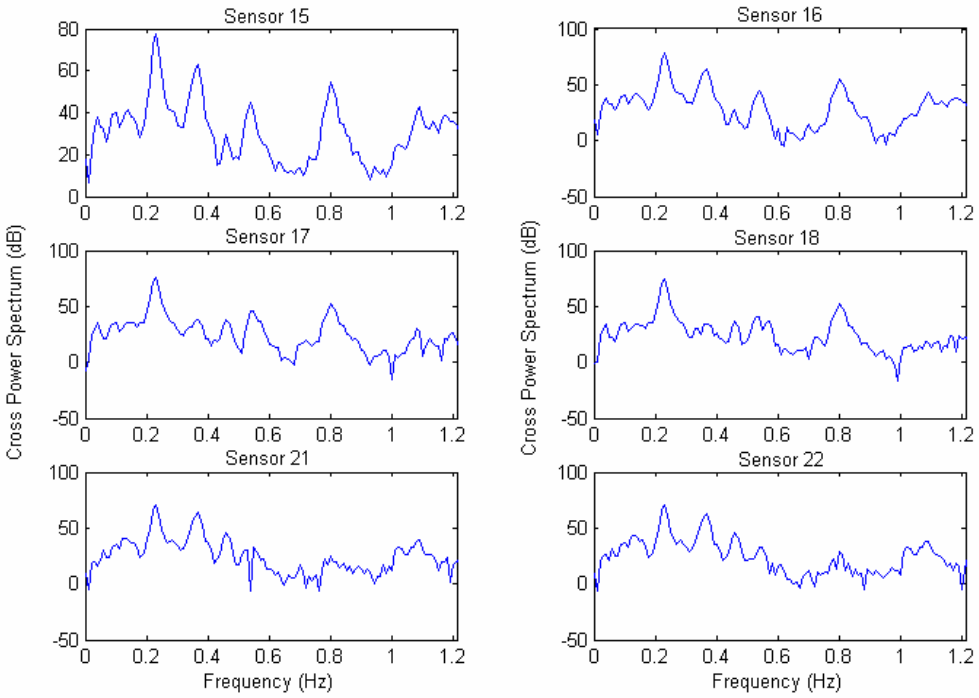

Figure 3-23 Cross Spectrum between Sensor 15 and Other Sensors from the April 18th, 2003 Data Set

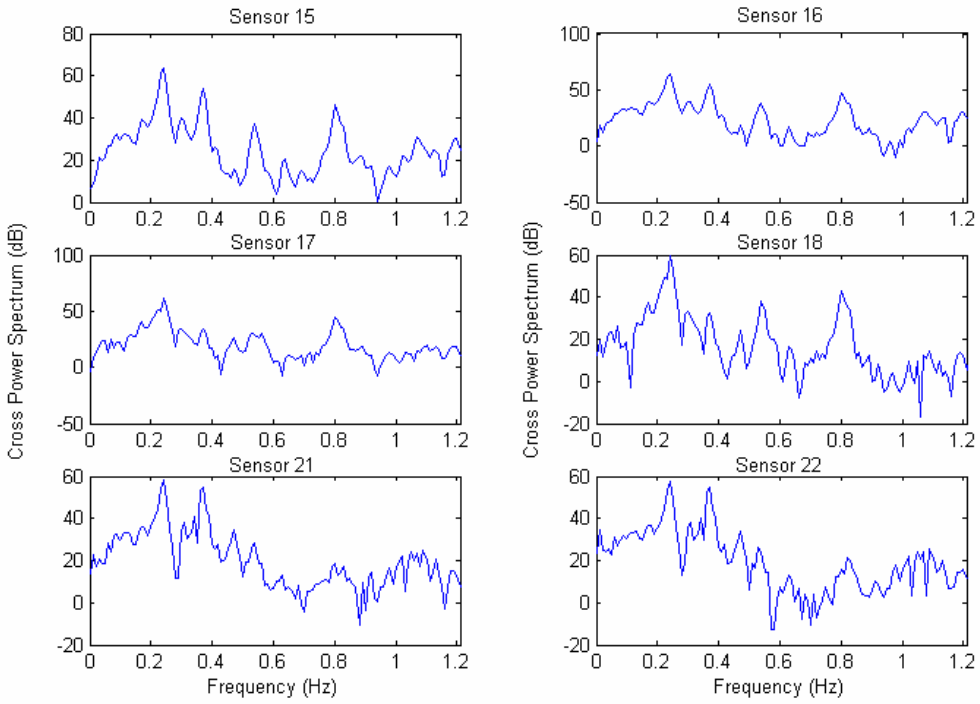

Figure 3-24 Cross Spectrum between Sensor 15 and Other Sensors from the June 1st, 2003 Data Set

3.5.2.3 Identification Results

FNExT technique described in Section 3.3 is used to identify modal parameters from ambient vibration data. Previous studies have shown that the dominant modes of vibration of the bridge concentrate in the frequency range between 0.2 Hz and 1.1 Hz. Focus is thus placed on this frequency range during the FNExT technique identification process. The selection of model order in FNExT technique can be facilitated by directly observing the peaks in cross-spectrum plots or by using more sophisticated frequency domain indicators such as the Modal Indicator Function and Complex Modal Indicator Function (Allemang 1999). The identified modal parameters are presented in Table 3-5.

It can be seen that the identified modal frequencies from two data sets show very good consistency. Only one mode that is identified in the April 18th data set is not identified in the June 1st data set.

Table 3-5 Modal Frequencies of Vertically Dominant Modes as Reported by Niazy (1991) and Luş et al. (1999) and Identified by FNExT Technique Using Only Deck Vertical Response (Unit: Hz)

FNExT Ambient[1]	FNExT Ambient[2]	Luş et al. – Whittier Earthquake	Luş et al. – Northridge Earthquake	Niazy – Ambient	Niazy – FEM
0.226	0.227	0.234	0.225	0.216	0.201
0.242	0.242	-	-	0.234	0.223
0.366	0.369	0.388	0.304	0.366	0.336
-	-	-	-	-	0.344
0.464	-	0.464	0.459	0.487	0.422
0.537	0.540	0.576	0.533	0.579	0.526
-	-	0.6170	0.600	-	-
0.637	0.637	0.6174	0.632	-	-
0.773	0.767	0.769	0.791	-	0.772
0.804	0.805	0.804	0.811	0.835	
0.853	0.859	0.857	-	-	-
0.974	0.965	0.947	0.974		
1.088	0.068	-	1.110	-	1.065

[1]: April 18th, 2003 data set [2]: June1st, 2003 data set

For comparison, identified modal parameters from two previous studies are also presented in Table 3-5. Niazy (1991) studied the dynamics of the Vincent Thomas Bridge in his doctoral dissertation. Both FEM predicted modal parameters and identified modal parameter from ambient vibrations were reported. Luş et al. (1999) used Observer/Kalman filter Identification (OKID) technique to identify modal parameters of the Vincent Thomas Bridge using earthquake response data. Responses

measured on the bridge during the 1987 Whittier earthquake and 1994 Northridge earthquake were studied. Only the vertically dominant modes reported in the two previous studies are used for comparison, as shown in Table 3-5. The results from FNExT technique show good agreement with previous results. In particular, all modes identified using ambient vibration reported by Niazy (1991) is identified using FNExT technique with good accuracy with the exception of one mode around 0.579 Hz. The number of modes identified using FNExT technique is 11, larger than the number reported by Luş et al. (1999) and Niazy (1991). This is an indication that some weakly excited modes that are overlooked by other methods are also identified by the FNExT technique.

Figure 3-25 and Figure 3-26 show the measured and synthesized (using identified modal parameters) cross spectrum function of sensor 15, 16, 17, 18, 21 and 22. The agreement between the measured and synthesized cross spectrum function is excellent.

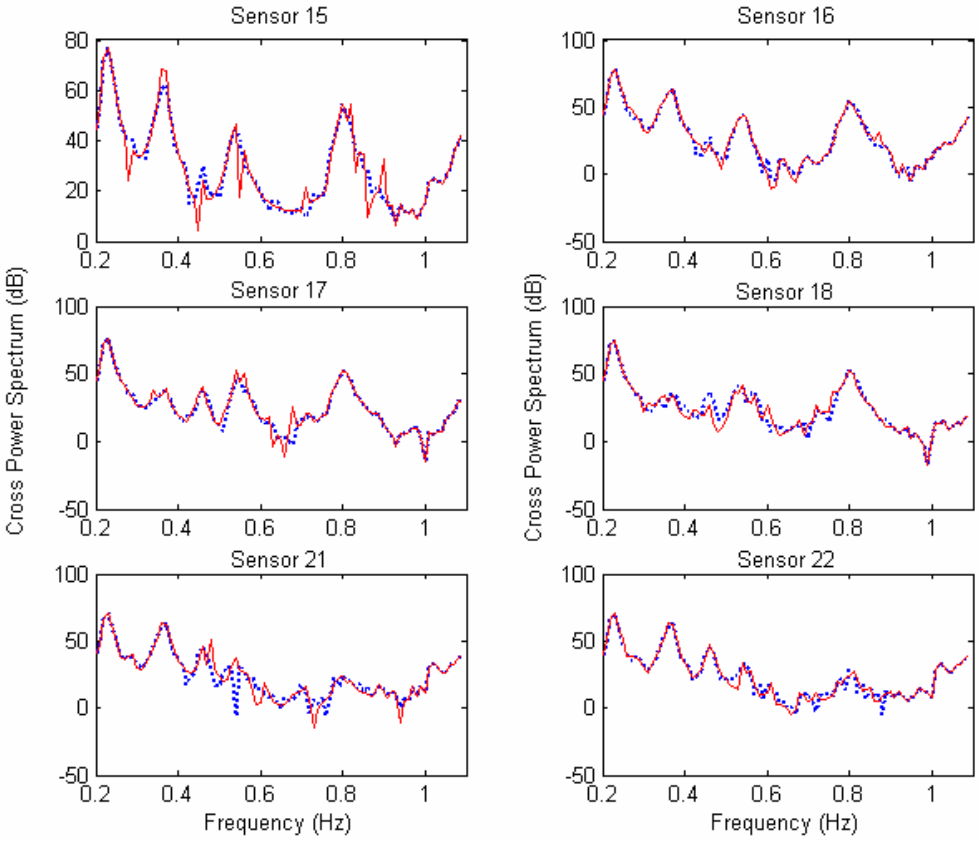

Figure 3-25 Measured and Synthesized Cross Spectrum Function (April 18th Data Set): Blue Dashed Line – Measured; Red Solid Line – Synthesized

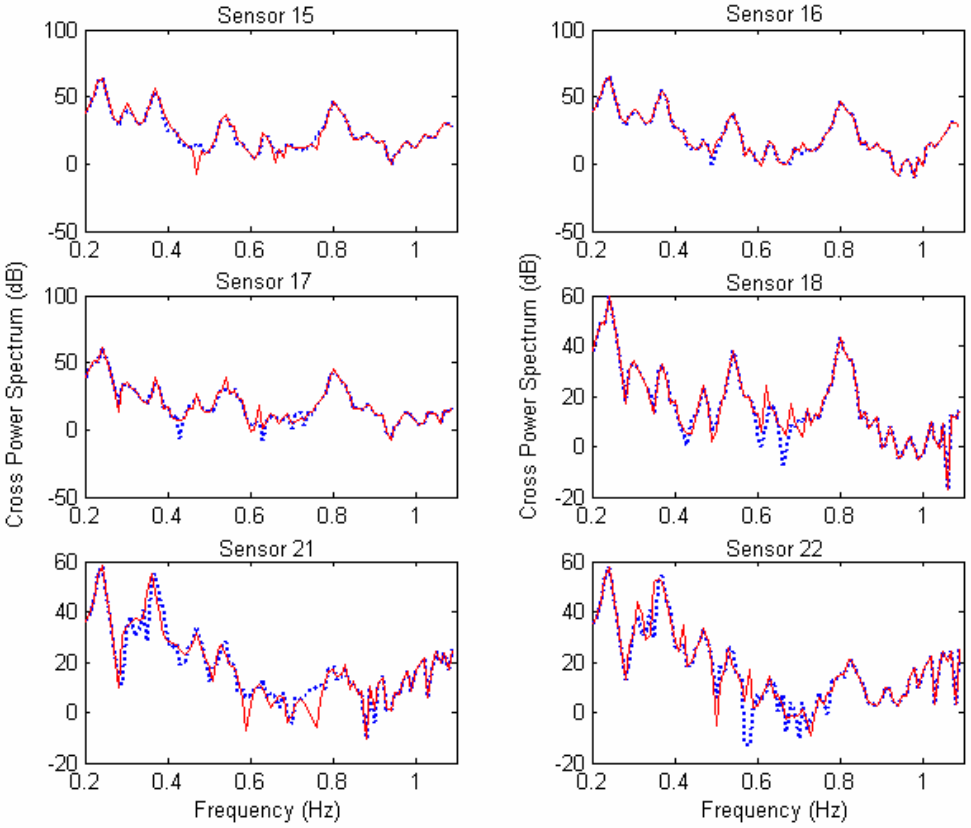

Figure 3-26 Measured and Synthesized Cross Spectrum Function (June 1st Data Set): Blue Dashed Line – Measured; Red Solid Line – Synthesized

3.6 Summary

In this chapter, two methods to identify modal parameters from ambient vibrations of civil engineering structures are investigated. The TDD method, first proposed by Kim et al. (Kim et al. 2002), was shown to be a fast and efficient method to extract modal parameters. Application in the modal test of Watson Wash Bridge showed that it is possible to obtain reasonably accurate modal parameter estimates using TDD method with significantly less amount of computation requirement compared with some other time domain techniques.

The FNExT technique is a new development in frequency domain. Based on the time domain Natural Excitation Technique, the author extended the approach to frequency domain and to the cases where acceleration responses are measured instead of displacement responses. The transformation into frequency domain allows the utilization of more computationally efficient modal parameter estimation techniques such as the Rational Fraction Polynomial method which is not available in time domain. The FNExT technique was applied to the ambient vibration data of Vincent Thomas Bridge and the results compare favorably with those from other time domain techniques adopted in previous research.

In summary, both the TDD method and the FNExT method are shown to be computationally efficient modal parameter identification technique and their performance compare favorably with modal identification methods discussed in Section 3.1. Due to these reasons they are potentially ideal candidates for automatic modal identification algorithm in long term vibration-based health monitoring system. The utilization of identified modal data in the vibration-based health monitoring system is outlined in Chapter 1 and will be discussed in detail in Chapter 4.

Chapter 4 Vibration-based Damage Detection using Element Modal Strain Damage Index Method

4.1 Introduction

As having been pointed out in Chapter 1 and Chapter 2, it is a well established fact that structural damage results in a change in mass, stiffness and/or damping of the structure. These changes in turn exhibit themselves in the dynamic characteristics of the structure as changes in natural frequencies, mode shapes and modal damping. There have been many attempts in the past three decades making use of measured changes of modal parameters to localize and quantify damage. In fact, the modal approach can be considered as the main stimulus for the growth of the field of vibration-based structural health monitoring and damage detection. The attractiveness of this approach can be attributed to the fact that dynamic characterization of the structure is in many cases easier to perform in the field than static characterization. Due to the advances in sensor technology, low input energy levels are usually sufficient to produce sets of measurable dynamic response. Hence ambient sources can be used as the excitation for structures eliminating the need for expensive excitation devices. Technologies such as Experimental Modal Analysis (EMA) and Operational Modal Analysis (OMA) have been developed to levels whereby relatively accurate results of natural frequencies, mode shapes and modal damping can be extracted from vibration based measurements.

The success of such vibration-based damage detection approaches intrinsically depends on the damage producing measurable changes in the structural modal parameters.

Early attempts to use frequency shifts to detect and localize damage include those by Lifshitz and Rotem (1969), Vandiver (1977) and Adams et al. (1978) . At about the same time, researchers started using mode shape changes for damage detection purposes (West 1984; Yuen 1985). Since then, many techniques have been developed utilizing frequency and mode shape changes to locate and quantify damage. These techniques have been well documented in the extensive literature reviews published by Salawu (1997) and Doebling et al. (1996) and hence will not be repeated herein. A major limitation of such damage detection techniques, is that natural frequencies and mode shapes are generally not very sensitive to local and moderate level of damages.

Pandey et al. (1991) first proposed using curvature mode shapes as a means to locate structural damage. In their research, curvature mode shape, also referred to as mode shape curvature or modal curvature, was shown to be able to correctly locate damage in cases where traditional damage localization techniques, such as the modal assurance criterion (MAC) and the coordinate modal assurance criterion (COMAC), had failed. Curvature mode shapes can be obtained from transverse displacement mode shapes through numerical differentiation procedures such as the central difference approximation. Abdo and Hori (2002) pointed out that for localized damage in beam like structures, the curvature at a damage location suffers a sudden jump while the displacement, bending moment and shear force remain relatively smooth. Thus,

curvature mode shapes are more sensitive to localized damage compared to displacement mode shapes. Yam et al. (2002) compared the damage sensitivity of curvature with those of out-of-plane deflection and slope in the context of static analysis of plate-like structures and concluded that because curvature is the most sensitive parameter of the three, curvature mode shape be used for damage detection using dynamic measurement.

Stubbs and Kim (1996) presented the "Damage Index Method" using the concept of modal strain energy. For an Euler-Bernoulli beam model, modal strain energy can be computed by integrating the product of bending stiffness and modal curvature along the length of the beam. The damage index was then defined as the ratio of normalized modal energy of the pristine and damaged states of the structure. They applied this technique to the numerical model of a continuous beam test specimen and showed that the damage index can provide accurate information about the location of damage. Cornwell et al. (1999) further extended the concept to plate-like structures where the calculation involves double integration of modal curvature along two coordinate axes. Farrar and Jauregui (1998a; 1998b) compared the mode shape curvature method and the damage index method with three other damage identification methods using data from a damaged bridge and concluded that the damage index and mode shape curvature methods were better using both experimental and numerical simulation data. Studies from other researchers (Alvandi and Cremona 2006; Ndambi et al. 2002) also seem to support this conclusion.

Although damage identification methods based on modal curvature or modal strain energy have been used successfully in a number of cases, there is one serious limitation associated with the application of such methods in the field. In all the aforementioned papers, modal curvatures were obtained from displacement mode shapes via numerical differentiation procedures which are essentially approximations. For example, the error introduced by the central difference approximation increases with the square of the spacing of measurement sites, where two adjacent mode shape measurement are taken. In the case of experimentally measured displacement mode shape data, the spacing of measurement sites is dictated by the structural configuration and availability of equipment and often cannot be easily modified in the field. It will be shown later in this paper that when there is only a limited number of spatial points that can be measured dynamically, which is often the case during field applications, the errors associated with numerical differentiation can have a masking effect over the change caused by damage. Perhaps more importantly, noise in the mode shape measurements tend to propagate through the numerical differentiation process and cause the final results to deteriorate significantly. It is noted that this has been raised as a concern by previous researchers. For example, Abdel Wahab and De Roeck (1999) applied a modal curvature based method to an actual bridge damage scenario and concluded that an extensive measurement grid was required in order to get a good estimation for modal curvature. They also introduced a new parameter called “CDF” in which the difference in modal curvature was averaged over all modes to improve results. Maeck and De Roeck (1999) pointed out that direct calculation of first and second derivatives from measured mode shapes (i.e., by using the central difference

approximation), results in oscillating and inaccurate values and hence proposed the use of a weighted residual penalty-based smoothing procedure to account for the inherent inaccuracies of the measured mode shapes.

In some of the aforementioned studies, mode shapes at sparse measurement locations obtained from experiment were first expanded to a denser array of locations using interpolation. This approach reduced the error introduced by large spacing of data sites. However, the problem associated with propagated noise was still not solved. Sazonov and Klinkhachorn (2005) showed in the case of computing the modal curvature from a displacement mode shape using central difference method, that merely reducing the spacing between sensors did not always improve results. In fact, when the sensor spacing is relatively small, the error due to propagated noise from the displacement mode shape starts to dominate the result. One hence is forced to find a compromise between errors introduced by central difference approximation and errors from propagated noise.

In this chapter, an improved damage identification technique based on the concept of Element Modal Strain Damage Index (EMSDI) is presented. The proposed method shares some common aspects with some of the previous studies (Abdel Wahab and De Roeck 1999; Cornwell et al. 1999; Maeck and De Roeck 1999; Pandey et al. 1991; Stubbs and Kim 1996) in that the displacement mode shape extracted from vibration measurements is used as the starting point of the approach. The proposed method, however, attempts to address some of the weaknesses of the numerical differentiation procedures noted in previous research in the calculation of modal

curvature and strain energy. Numerical simulation results as well as experimental validation results are presented to demonstrate the potential of the formulation and its relative advantages over currently existing approaches.

4.2 Theoretical Formulation of EMSDI Method

4.2.1 Errors Associated with the Calculation of Modal Curvature through Numerical Differentiation

For beam-like structures, modal curvature κ is defined as the second derivative of the corresponding transverse displacement mode shape ϕ, i.e., $\kappa \equiv \phi''$. When an analytical representation of the mode shape is not available, as is the case of experimentally measured mode shapes, the calculation of modal curvature has to be performed numerically. If $\phi(x_i)$ is the mode shape value at a measurement site x_i, $\phi(x_{i+1})$ and $\phi(x_{i-1})$ can be expressed in terms of $\phi(x_i)$ using a Taylor series expansion as:

$$\begin{aligned}\phi(x_{i+1}) &= \phi(x_i) + \phi'(x_i)h + \frac{\phi''(x_i)}{2!}h^2 + \cdots \\ \phi(x_{i-1}) &= \phi(x_i) + \phi'(x_i)(-h) + \frac{\phi''(x_i)}{2!}(-h)^2 + \cdots\end{aligned} \tag{4.1}$$

The summation of the two equations in Eq. (4.1) and reorganize gives

$$\begin{aligned}\phi''(x_i) &= \frac{\phi(x_{i+1}) - 2\phi(x_i) + \phi(x_{i-1})}{h^2} + O(h^2) \\ &= \frac{\phi(x_i + h) - 2\phi(x_i) + \phi(x_i - h)}{h^2} + O(h^2)\end{aligned} \tag{4.2}$$

in which, x_i, x_{i-1}, x_{i+1} are the current, previous, and next measurement sites where displacement mode shapes are available. $\phi''(x_i) = \kappa(x_i)$ is the modal curvature at data site x_i, and h is the spacing between measurement sites. It should be noted that the spacing between measurement sites must remain constant in order for Eq. (4.2) to be valid. Eq. (4.2) is called the *second central finite divided difference*, or in short, *central difference*. It is apparent that Eq. (4.2) is an approximation due to the truncation error term $O(h^2)$. The accuracy of Eq. (4.2) can be further improved following Chapra and Canale (2001) by including additional terms in the Taylor series expansion, leading to an expression where the truncation error is of order h^4:

$$\kappa(x_i) = \frac{-\phi(x_{i+2}) + 16\phi(x_{i+1}) - 30\phi(x_i) + 16\phi(x_{i-1}) - \phi(x_{i-2})}{12h^2} + O(h^4) \qquad (4.3)$$

Sazonov and Klinkhachorn (2005) demonstrated that the maximum error bound of Eq. (4.2) considering both truncation error and measurement error in $\phi(x)$ can be expressed as :

$$\left| E\left[\kappa(x_i)\right] \right| \le \frac{\varepsilon\left(|\phi_{i+1}| + 2|\phi_i| + |\phi_{i-1}|\right)}{h^2} + \frac{M_4}{12}h^2 \qquad (4.4)$$

where $E\left[\kappa(x_i)\right]$ is the modal curvature error bound, ε is the maximum relative random multiplicative error of mode shape ϕ, and M_4 is a constant term determined by the maximum value of the 4th derivative of ϕ. The first term on the right hand side of Eq. (4.4) corresponds to the noise in mode shape data. The second term corresponds to the truncation errors. When the spacing between measurement sites, h, is relatively

large, the second term tends to dominate Eq. (4.4). With a reduction in h, the first term tends to grow larger and gradually become the dominant factor in the error.

In most practical cases, modal testing experiments are carried out using accelerometers. The extracted mode shape sites correspond to the location of accelerometers in a one-to-one fashion. The number of available sensors thus becomes the main controlling factor for the number of sites that can be measured. Even with approaches such as multiple set-ups during testing, the number of measurement sites is often still very limited. Under these conditions, as will be shown later in this paper, the truncation error term in Eq. (4.4) will be the dominant factor. In order to reduce the effects of this concern some researchers have proposed the use of sensing equipment with high spatial resolution such as laser vibrometers (Khan et al. 1999; Pai et al. 2004). However, in modal testing experiments mode shapes are always prone to be contaminated by noise. With a reduction of measurement spacing, the first term in Eq. (4.4) will increase and gradually become the dominate error factor. Thus it appears that, contrary to common belief, the results of damage detection method may not be able to benefit from high-spatial resolution measurements if it depends on modal curvature computed using a numerical differentiation procedure.

4.2.2 Damage Identification using Element Modal Strain Damage Index

The bending strain energy of an Euler-Bernoulli beam can be expressed as:

$$U_s = \int_L \frac{1}{2} M(x) d\theta = \frac{1}{2} \int_L \frac{M^2(x)}{EI(x)} dx = \frac{1}{2} \int_L EI(x) \cdot \left(v''(x) \right)^2 dx \tag{4.5}$$

where $M(x)$ is the internal bending moment, $EI(x)$ is the bending stiffness, and $v''(x)$ is the 2nd derivative of the beam transverse displacement. Replacing $v(x)$ with modal transverse displacement $\phi(x)$ gives the expression for modal strain energy of the beam as:

$$U_{ms} = \frac{1}{2} \int_L EI(x) \cdot \left(\phi''(x) \right)^2 dx \tag{4.6}$$

For simplicity we consider a single beam element **I** with uniform stiffness EI and length l_e as shown in Figure 4-1, where ϕ_i and ϕ_j are the mode shape amplitude at transverse degree-of-freedom of node i and j respectively, and θ_i and θ_j are the mode shape amplitude at the rotation degree-of-freedom at node i and j. For purposes of clarity in the current discussion, ϕ_i and ϕ_j will be referred to as nodal modal displacements and θ_i and θ_j nodal modal rotations. Assuming cubic displacement shape functions, the transverse modal displacement at any point on this beam element can be expressed in terms of the nodal modal displacement and rotation as:

$$\phi_I(\tilde{x}) = \phi_i \cdot N_1(\tilde{x}) + \theta_i \cdot N_2(\tilde{x}) + \phi_j \cdot N_3(\tilde{x}) + \theta_j \cdot N_4(\tilde{x}) \tag{4.7}$$

where $N_1(\tilde{x})$ through $N_4(\tilde{x})$ are the cubic shape functions shown in Figure 4-2. The ~ symbol above coordinate x indicates Eq. (4.7) is expressed in the local element coordinate system shown in Figure 4-2 as opposed to the global coordinate system of

the whole structure which will be defined later. The reason for this distinction will soon become clear. An expansion of Eq. (4.7) gives

$$\begin{aligned}\phi_I(\tilde{x}) = &\left(1-\frac{3}{l_e^{\,2}}\tilde{x}^2+\frac{2}{l_e^{\,3}}\tilde{x}^3\right)\phi_i+\left(-\tilde{x}+\frac{2}{l_e}\tilde{x}^2-\frac{1}{l_e^{\,2}}\tilde{x}^3\right)\theta_i \\ &+\left(\frac{3}{l_e^{\,2}}\tilde{x}^2-\frac{2}{l_e^{\,3}}\tilde{x}^3\right)\phi_j+\left(\frac{2}{l_e}\tilde{x}^2-\frac{1}{l_e^{\,2}}\tilde{x}^3\right)\theta_j\end{aligned} \tag{4.8}$$

Collecting terms of the same order gives

$$\begin{aligned}\phi_I(\tilde{x}) &= \phi_i+(-\theta_i)\tilde{x}+\left(-\frac{3}{l_e^2}\phi_i+\frac{3}{l_e^2}\phi_{i+1}+\frac{2}{l_e^2}\theta_i+\frac{1}{l_e}\theta_{i+1}\right)\tilde{x}^2 \\ &\quad+\left(\frac{2}{l_e^3}\phi_i-\frac{2}{l_e^3}\phi_{i+1}-\frac{1}{l_e^2}\theta_i-\frac{1}{l_e^2}\theta_{i+1}\right)\tilde{x}^3 \\ &= c_{1,I}+c_{2,I}\tilde{x}+c_{3,I}\tilde{x}^2+c_{4,I}\tilde{x}^3\end{aligned} \tag{4.9}$$

in which, c_1, c_2, c_3, c_4 are the coefficients of 4th order polynomial $\phi_I(\tilde{x})$. Similarly the 2nd derivative of transverse modal displacement can be written as

$$\phi_I''(\tilde{x}) = [B]\{D\} \tag{4.10}$$

wherein

$$[B] = \begin{bmatrix}\dfrac{d^2N_1}{d\tilde{x}^2} & \dfrac{d^2N_2}{d\tilde{x}^2} & \dfrac{d^2N_3}{d\tilde{x}^2} & \dfrac{d^2N_4}{d\tilde{x}^2}\end{bmatrix} \quad \{D\} = \begin{Bmatrix}\phi_i \\ \theta_i \\ \phi_j \\ \theta_j\end{Bmatrix} \tag{4.11}$$

Substituting Eq. (4.10) into Eq. (4.6) and integrating over the length of the element yields

$$
\begin{aligned}
U_{ms} &= \frac{1}{2}\int_{l_e} EI(\tilde{x})\cdot\left(\phi_I''(\tilde{x})\right)^2 d\tilde{x} \\
&= \frac{1}{2}\int_{l_e} EI\cdot\{D\}^T\left[B\right]^T\left[B\right]\{D\}\,d\tilde{x} \\
&= \frac{1}{2}EI\cdot\{D\}^T\cdot\int_{l_e}\left[B\right]^T\left[B\right]d\tilde{x}\cdot\{D\}
\end{aligned}
\tag{4.12}
$$

which can then be solved as

$$
U_{ms} = \frac{1}{2}EI\cdot\{D\}^T\cdot\left[N_e\right]\cdot\{D\} \tag{4.13}
$$

where the matrix $\left[N_e\right]$ is given by

$$
\left[N_e\right] = \begin{bmatrix}
\frac{12}{L^3} & -\frac{6}{L^2} & -\frac{12}{L^3} & -\frac{6}{L^2} \\
-\frac{6}{L^2} & \frac{4}{L} & \frac{6}{L^2} & \frac{2}{L} \\
-\frac{12}{L^3} & \frac{6}{L^2} & \frac{12}{L^3} & \frac{6}{L^2} \\
-\frac{6}{L^2} & \frac{2}{L} & \frac{6}{L^2} & \frac{4}{L}
\end{bmatrix} \tag{4.14}
$$

It is noted that the elements in $\left[N_e\right]$ only rely on the geometric configuration of the element. The Element Modal Strain Damage Index (EMSDI) can then be defined as

$$
A_m^e = \{D\}^T\cdot\left[N_e\right]\cdot\{D\} \tag{4.15}
$$

Since equations (4.13) and (4.15) provide an alternative means of calculating element modal strain energy and EMSDI without calculating modal curvature, the problems associated with the numerical differentiation procedure required in the conventional

determination of modal curvature can be avoided. A comparison of Eq. (4.13) with Eq. (4.6) shows that

$$A_m^e = \{D\}^T \cdot [N_e] \cdot \{D\} = \frac{1}{2}\int_{l_e} \left(\phi_I''(\tilde{x})\right)^2 d\tilde{x} \tag{4.16}$$

From Eq. (4.16) it can be seen that, for an element of length l_e, EMSDI is physically equivalent to the area under the curve denoted by the integrand. If the structure is damaged at a particular element, it can be expected that $\phi_I''(\tilde{x})$ in Eq. (4.16) will show a sudden increase at the damage location. Correspondingly, A_m^e of the element will show an increase in comparison to its value in the undamaged state. Based on this the quantity A_m^e can be used for the purpose of damage identification. It should be noted that the uniform stiffness assumption in the formulation of Eq. (4.7) through Eq. (4.15) does not signify that the damage has to be uniform within the element. Rather, it reflects the fact that the observation made at measurement locations will only be able to reveal information about the damage that occurred in between two measurement locations in an averaged, integral sense.

It should be noted that the vector $\{D\}$ in Eq. (4.13) includes both modal displacement and modal rotation. Modal displacement is the most common quantity measured in most experiments in which modal tests are conducted and hence it is important that a reliable method to estimate the modal rotation from measured modal displacement is used. A proposed formulation to calculate modal rotation using modal displacement measurement is discussed in the next section.

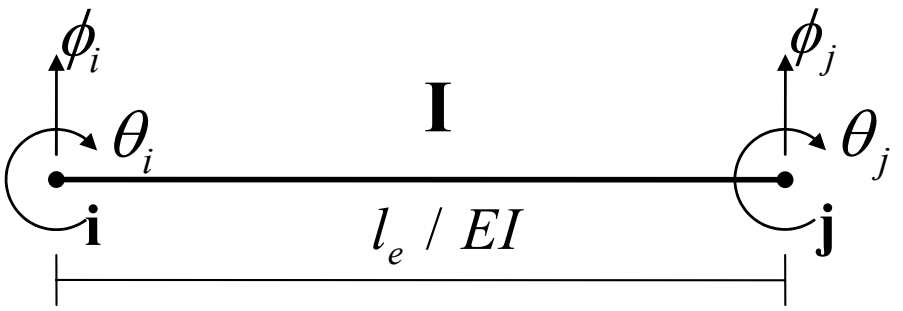

Figure 4-1 Modal Displacement of Beam Element

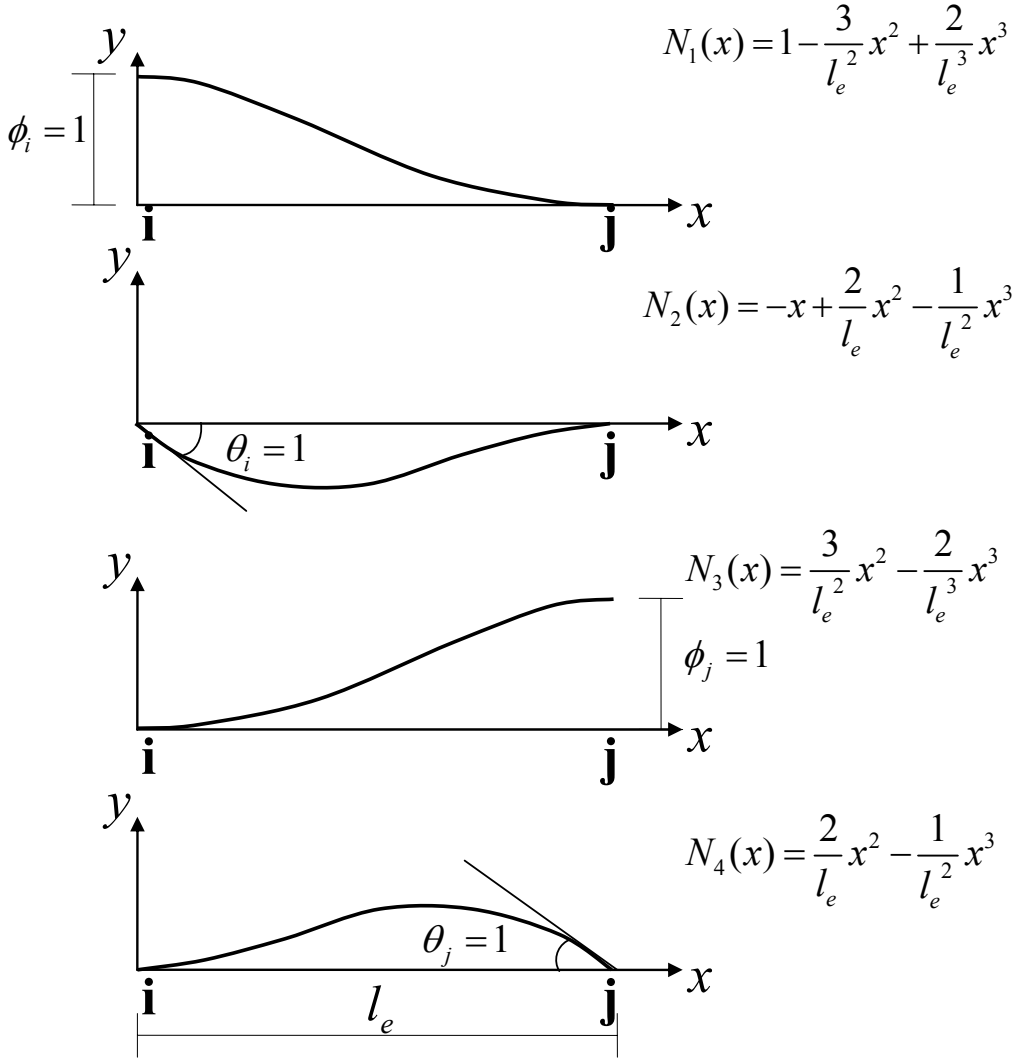

Figure 4-2 Element Shape Function

4.2.3 Calculation of Modal Rotation using Modal Displacement

4.2.3.1 Calculation of Modal Rotation using noise-free Modal Displacement Measurement

Consider a beam-like structure that can be discretized into N elements ($I = 1,\ldots,N$) and $N+1$ nodes ($i = 1,\ldots,N+1$), as shown in Figure 4-3. Using the same mode shape estimation function for each element in the form of Eq. (4.7), an estimated mode shape function $\phi(x)$ of the entire structure can be expressed using a piecewise polynomial of order 4, i.e.,

$$\phi(x) = \phi_I(x) \quad for\ x_i \le x \le x_{i+1} \quad for\ some\ \phi_I(x) \in \Pi_{<4}, i, I = 1,\ldots,N \tag{4.17}$$

in which, $\Pi_{<4}$ is the linear space of the polynomials of order 4, and x_i is the location of the node i separating two adjacent elements. The relation between the global coordinate x and local element coordinates $\tilde{x}$ of element I is expressed by:

$$\tilde{x} = x - x_i \quad for\ x_i \le x \le x_{i+1} \tag{4.18}$$

The expression of polynomial $\phi_I(x)$ can then be obtained from Eq. (4.9):

$$\phi_I(x) = c_{1,I} + c_{2,I}(x - x_i) + c_{3,I}(x - x_i)^2 + c_{4,I}(x - x_i)^3 \tag{4.19}$$

Using the displacement continuity condition, the Ith polynomial piece $\phi_I(x)$ should satisfy the conditions:

$$\phi_I(x_i) = \phi_i, \quad \phi_I(x_{i+1}) = \phi_{i+1} \quad i, I = 1,\ldots,N \tag{4.20}$$

where ϕ_i and ϕ_{i+1} are the measured modal displacements at node i and $i+1$, respectively. Because $\phi_I(x)$ is a polynomial of order 4, two additional conditions are needed to determine all the coefficients. A commonly used condition is one proposed by De Boor (2001):

$$\phi_I'(x_i) = s_i, \quad \phi_I'(x_{i+1}) = s_{i+1} \quad i, I = 1, \ldots, N \tag{4.21}$$

in which s_i, s_{i+1} are free parameters that have to be determined. The resulting $\phi(x)$ can be shown to agree with transverse modal displacements ϕ_i at the nodes. Also, $\phi(x)$ is continuous and has a continuous first derivative. Furthermore, the relation

$$\theta_i = -\phi_I'(x_i), \quad \theta_{i+1} = -\phi_I'(x_{i+1}) \quad i, I = 1, \ldots, N \tag{4.22}$$

exists between $\phi_I'(x)$ and the modal rotations at each node. Once the free parameters are determined, the form of the element mode shape functions $\phi_I(x)$ and its first derivative $\phi_I'(x)$ can be uniquely determined, and modal rotations at nodes can be calculated.

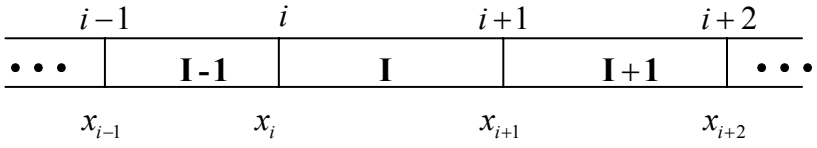

Figure 4-3 Discretization of Beam-like Structure

One possible choice of s_i is to use the slope of at x_i of the 3rd order polynomial which agrees with $\phi(x)$ at x_{i-1}, x_i and x_{i+1}. This choice leads to the representation of s_i as:

$$s_i = \frac{(x_{i+1} - x_i)\, g[x_{i-1}, x_i] + (x_i - x_{i-1})\, g[x_i, x_{i+1}]}{x_{i+1} - x_{i-1}} \tag{4.23}$$

where $g[x_i, x_{i+1}]$ is the second divided difference of a function g that agrees with nodal modal displacements $\phi_1, \ldots, \phi_i, \phi_{i+1}, \ldots, \phi_{N+1}$ at the sequence $(x_1 \ldots x_i, x_{i+1}, \ldots, x_{N+1})$ which is given by

$$g[x_i, x_{i+1}] = \frac{g(x_i) - g(x_{i+1})}{x_i - x_{i+1}} \tag{4.24}$$

The form of s_i given in Eq. (4.23) is theoretically similar to the one used in the piecewise cubic Bessel interpolation of functions. It should be noted that the conditions leading to Eq. (4.23) is an approximation, and thus the modal rotation calculated using Eq. (4.23) generally will not be exact.

Another possible choice of s_i is based on the condition that $\phi(x)$ should be twice continuously differentiable. This gives the conditions that, for $i, I = 2, \ldots, N$

$$\phi''_{I-1}(x_i) = \phi''_I(x_i) \tag{4.25}$$

Or, after substituting in Eq. (4.19),

$$2c_{3,I-1} + 6c_{4,I-1}(x_i - x_{i-1}) = 2c_{3,I} \tag{4.26}$$

It can be shown (De Boor 2001) that the coefficients $c_{3,I-1}$, $c_{3,I}$ and $c_{4,I-1}$ in Eq. (4.26) can be expressed as

$$\begin{aligned} c_{3,I-1} &= \left(g\left[x_{i-1},x_i\right]-s_{i-1}\right)\Big/\left(x_i-x_{i-1}\right)-c_{4,I-1}\left(x_i-x_{i-1}\right) \\ c_{3,I} &= \left(g\left[x_i,x_{i+1}\right]-s_i\right)\Big/\left(x_{i+1}-x_i\right)-c_{4,I}\left(x_{i+1}-x_i\right) \\ c_{4,I-1} &= \left(s_{i-1}+s_i-2g\left[x_{i-1},x_i\right]\right)\Big/\left(x_i-x_{i-1}\right)^2 \end{aligned} \tag{4.27}$$

Substituting in Eq. (4.20), (4.21), (4.27) and after some manipulation, Eq. (4.26) leads to the linear system

$$\begin{aligned} s_{i-1}(x_{i+1}-x_i)+s_i\cdot 2\left(x_{i+1}-x_{i-1}\right)+s_{i+1}\left(x_i-x_{i-1}\right)= \\ 3\left((x_{i+1}-x_i)g\left[x_{i-1},x_i\right]+\left(x_i-x_{i-1}\right)g\left[x_i,x_{i+1}\right]\right) \end{aligned} \tag{4.28}$$

$for \quad i=2,\ldots,N$. Given boundary conditions s_1 and s_{N+1}, Eq. (4.28) represents a linear system of *N-1* equations for the *N-1* unknowns, $s_2,\ldots,s_N$. It can be shown that this system has a unique solution which can be found without any difficulty using the Gauss elimination technique (De Boor 2001). In general, Eq. (4.28) represents a more realistic prediction of free parameters s_i (and thus of modal rotations θ_i) as compared to Eq. (4.23). This is because the curvature continuity condition in Eq. (4.25) holds true for any beam-type structure as long as there is no sudden change of stiffness at the nodes. This can be proved by referring to the moment curvature relation of the beam $\kappa=\phi''=M/EI$. For a typical beam used in engineering structures, the internal moment M is generally continuous within its boundary. If the stiffness EI has no singularity at the nodes, the curvature ϕ'' will also remain continuous across the nodes. As will be discussed later in this paper, the discretization of the structure can be based on a one-to-

one correspondence between the measurement sites and the nodes. Due to the use of limited measurement points in experiments, it is assumed as unlikely that one of the nodes will coincide exactly with a damage location that could cause a sudden change of stiffness.

4.2.3.2 Calculation of Modal Rotation using noisy Modal Displacement Measurement

When noise is present in the modal displacement measurement, the use of either Eq. (4.23) or Eq. (4.28) to calculate modal rotations can sometimes cause unacceptable errors. This can be highlighted by considering the true modal displacement of node *i* to be ϕ_i, and the noisy measured modal displacement to be $\phi_i^m = \phi_i + \varepsilon_i$, where ε_i is the normally distributed random error. The direct application of Eq. (4.20) will make the mode shape function $\phi(x)$ follow the small deviations caused by random errors ε_i in the measurement. This is clearly not a desired result. This problem can be solved by reformulating Eq. (4.25) and Eq. (4.28) into a minimization problem expressed as:

$$\min f(x) = p\sum_{i=1}^{N+1}\left(\frac{\phi(x_i)-\phi_i^m}{\sigma_\phi}\right)^2 + (1-p)\int_{x_1}^{x_{N+1}}\left(\phi''(x)\right)^2 dx \qquad (4.29)$$

in which, σ_m is the standard deviation of measured noisy modal displacements ϕ^m and p is a weighting constant. The first term in Eq. (4.29) is the normal least-squares term and second term is a penalty term used to express the roughness of the mode shape estimate $\phi(x)$. The minimization of the function $f(x)$ in Eq. (4.29) using an appropriate value of p will establish a balance between the goal of maintaining a close

fit to the measured modal displacement data and the goals of maintaining the smoothness of the function $\phi(x)$ and avoiding 'kinks' caused by random errors in the data.

Reinsch (1967) reported that the solution of the problem formulated in Eq. (4.29) can take the form of a natural cubic smoothing spline. It is pointed out that smoothing splines are piecewise polynomials which have a form similar to Eq. (4.17). Both Reinsch (1967) and Green and Silverman (1994) presented efficient algorithms to calculate the coefficients of these polynomials. However, the problem of finding the appropriate choice of weighting parameter *p* still exists.

The mean-squared error (MSE) can be defined as

$$MSE(p) = \frac{1}{N+1}\sum_{i=1}^{N+1}\left(\phi_p(x_i) - \phi_i\right)^2 \tag{4.30}$$

where ϕ_i is the true modal displacement value and $\phi_p(x)$ is the smoothing spline estimate of mode shape function determined using Eq. (4.29) and value *p*. The *MSE* is an indicator of the goodness of the fit by the estimation function $\phi(x)$. Thus, minimizing *MSE(p)* gives the optimal weighting parameter *p*. The formulation of MSE in Eq. (4.30) relies on the unknown modal displacements ϕ_i. This problem can be avoided by using the cross validation score as an estimate of MSE (Green and Silverman 1994):

$$CV(p) = \frac{1}{N+1}\sum_{i=1}^{N+1}\left(\phi_i^m - \phi_p^{(-i)}(x_i)\right)^2 \tag{4.31}$$

in which, $\phi_p^{(-i)}(x)$ is the smoothing spline estimate of the mode shape function using the value p with the ith observation ϕ_i left out. The minimization of *CV(p)* instead of *MSE(p)* gives an estimation of the optimal weighting parameter p.

4.3 Numerical Simulation

4.3.1 Description of the Numerical Model

The purpose of the numerical simulation provided herein is to validate the proposed method and assess its comparative advantages with respect to the previously discussed numerical differentiation techniques in the context of damage detection. The test structure selected here is a theoretical model of a two-span continuous beam. The material and sectional properties of the model are identical to a beam specimen tested in the laboratory, as detailed in later Section 4.5. The aluminum beam specimen has a section of 76.2 mm (3 in) in width and 6.35 mm (1/4 in) in height. The theoretical model was built using the general purpose finite element analysis software package ANSYS (2004). The continuous beam has two spans of equal length of 0.8636 m (34 in), as shown in Figure 4-4. The support conditions were modeled as being pinned at the left-end support and having a slider at the middle and right-end supports. The beam was modeled using a total of 544 3D linear elastic beam elements of 3.175 mm in length. The important element properties are: (1) Cross-sectional area $A = 4.84 \times 10^{-4}\ m^2$. (2) Moment of inertia in y direction $I_{yy} = 1.63 \times 10^{-9}\ m^4$. (3) Moment of inertia in z direction $I_{zz} = 2.34 \times 10^{-7}\ m^4$. (4) Young's modulus E = 6.964×10^{10} Pa. (5) Poisson's ratio $\nu = 0.35$, and (6) Test specimen mass density of $\rho = 2700\ kg/m^3$.

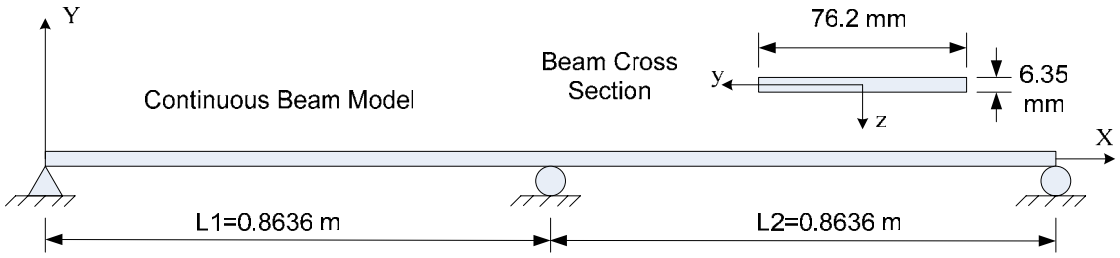

Figure 4-4 Schematic of Continuous Beam Model

The first six modes of the beam model were extracted using the subspace algorithm in ANSYS. Results of natural frequencies, transverse modal displacements in the Y direction and modal rotations around the Z axis at each node were obtained for each mode. The extracted mode shapes of the first 6 modes are plotted in Figure 4-5.

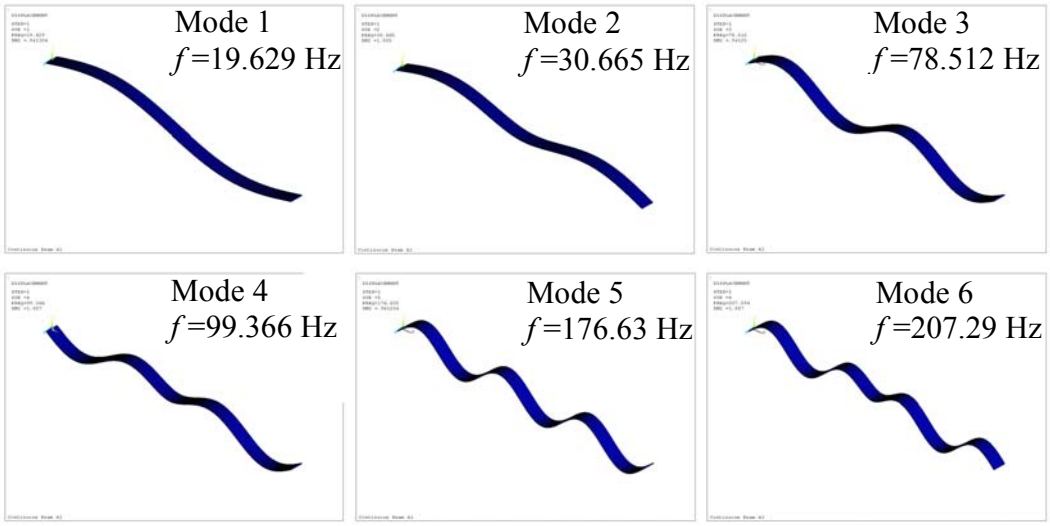

Figure 4-5 Mode Shapes of Mode 1-6

4.3.2 Errors Associated with Numerical Differentiation Procedures

While values for modal displacement and modal rotations are available at every node in theoretical or numerical simulations, this is typically not the case in experiments. In experiments not only is the number of instrumented points generally limited, but it is also very difficult to accurately measure modal rotations using current available sensor technology. Under these conditions, both modal curvature and the Element Modal Strain Damage Index (EMSDI) in Eq. (4.15) must be estimated using sparse measurement of modal displacements only. In order to simulate the situation where only sparse measurements are available, the full FEM modal displacement is sampled at three sets of intervals. The first set is composed of 35 sample points, with the distance between each pair of adjacent sample points roughly equals to 0.0508 m. corresponding to the case where only 18 measurement sites are available on one span of the continuous beam. The second and third sets are composed of 17 and 7 sample points respectively. with the distance between sample points being 0.108 m and 0.289 m respectively.

Figure 4-6 presents the modal curvature calculated using the numerical differentiation procedure in Eq. (4.2). Only results from first four modes are presented. Results from other modes show similar trend and are thus omitted. The locations of sample points, or measurements sites, are represented by the small circles, triangles and stars in the figure. It is evident that with the decrease in the number of measurement sites, the curvature calculated using Eq. (4.2) deviates farther from the true curvature value as represented by the solid dark lines. The true curvature value is approximated by curvature calculated using all 545 measurement site, which can be shown to be very

close to the true curvature value calculated by differentiating analytical mode shape functions. The error introduced by numerical differentiation also increases with higher modes. This can be explained by noting the second term in Eq. (4.4) . The value M_4 is associated with the amplitude of the 4th derivative of the mode shape and tends to grow larger in higher modes.

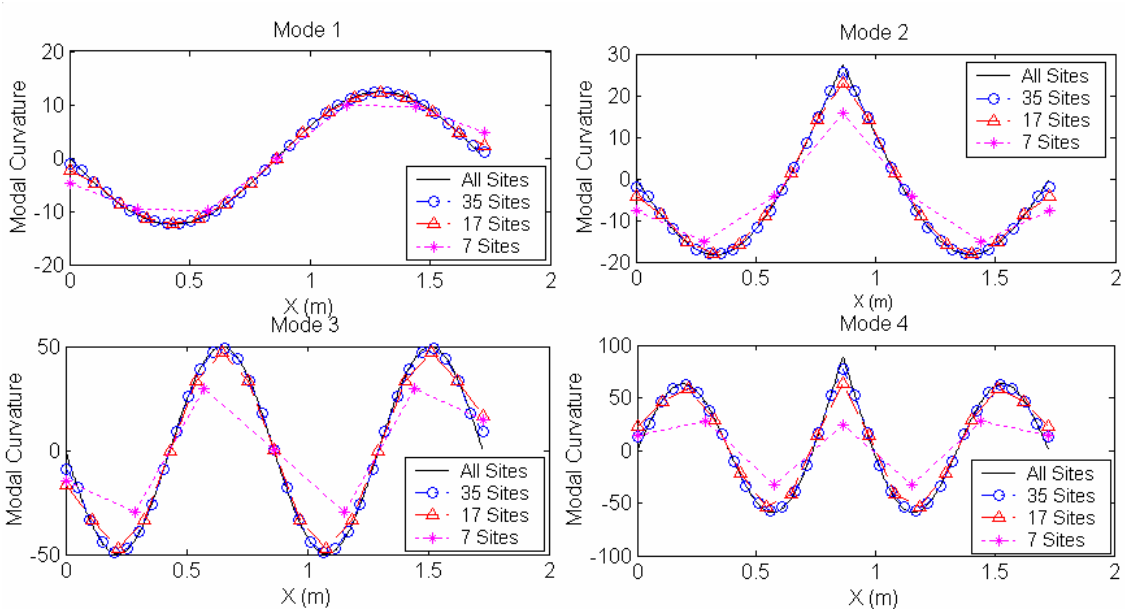

Figure 4-6 Effect of Sparse Measurement on Modal Curvature Calculation using Numerical Differentiation

Figure 4-7 shows the comparison of results between two different numerical differentiation procedures: 1) Central Difference (CD) equation of Eq. (4.2) and 2) Eq. (4.3), which will be referred to as the High Accuracy Difference (HAD) equation. For clarity, only the calculated modal curvature from modes 2 and 3 are plotted. Results from other modes show similar trend and are thus omitted. In general, results from HAD are closer to the true curvature values. For relatively dense measurement sites, i.e.,

35 sites and 17 sites, the difference between CD and HAD is insignificant. However, in the situation where 7 measurement sites are available HAD performs significantly better than CD. Although both procedures produce estimates of modal curvature that are far from ideal under this situation.

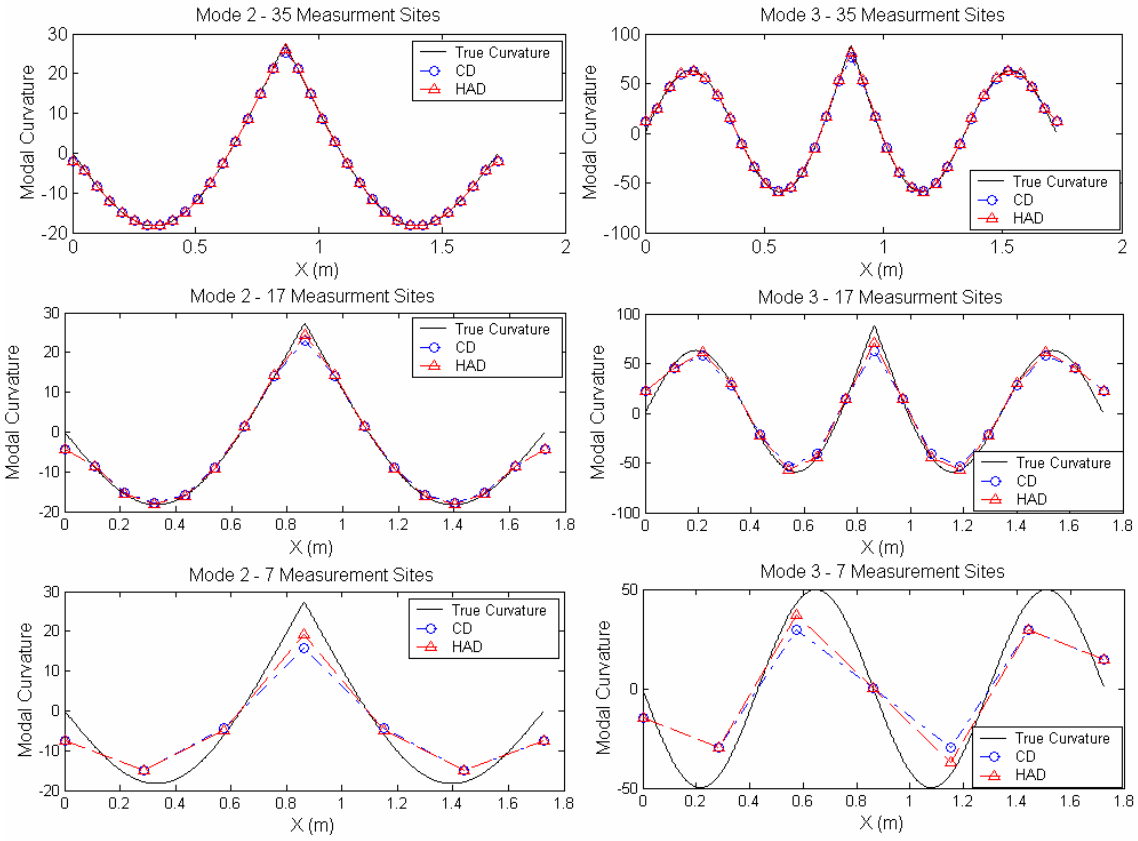

Figure 4-7 Effect of Different Numerical Differentiation Procedure on Modal Curvature Calculation

In order to assess the effect of measurement noise on the performance of numerical differentiation procedures, simulated noise was added to FEM generated mode shapes. Three different levels of uniformly distributed random noise were added, with their maximum magnitude equal to 1%, 2% and 5% of the maximum magnitude of

the respective mode shapes. Numerical differentiation procedures involving both CD and HAD, were applied to the noise-augmented mode shapes. The results are shown in Figure 4-8 using the modal curvatures of the first mode as an example. It can be seen that, for both numerical differentiation procedures, the magnitude of propagated noise in the modal curvature results is large compared to the true, noise-free modal curvature. In the case of 35 measurement sites, it is likely that the propagated noise in the modal curvature will mask any change caused by a moderate level of damage, even when the noise level is only 1%. Perhaps more significantly, the level of propagated noise in the modal curvature results increases with the number of measurement sites. This result has the important implication that numerical differentiation procedures are not able to take advantage of the increased spatial resolution in mode shape offered by advanced sensor technologies in cases when noise is present.

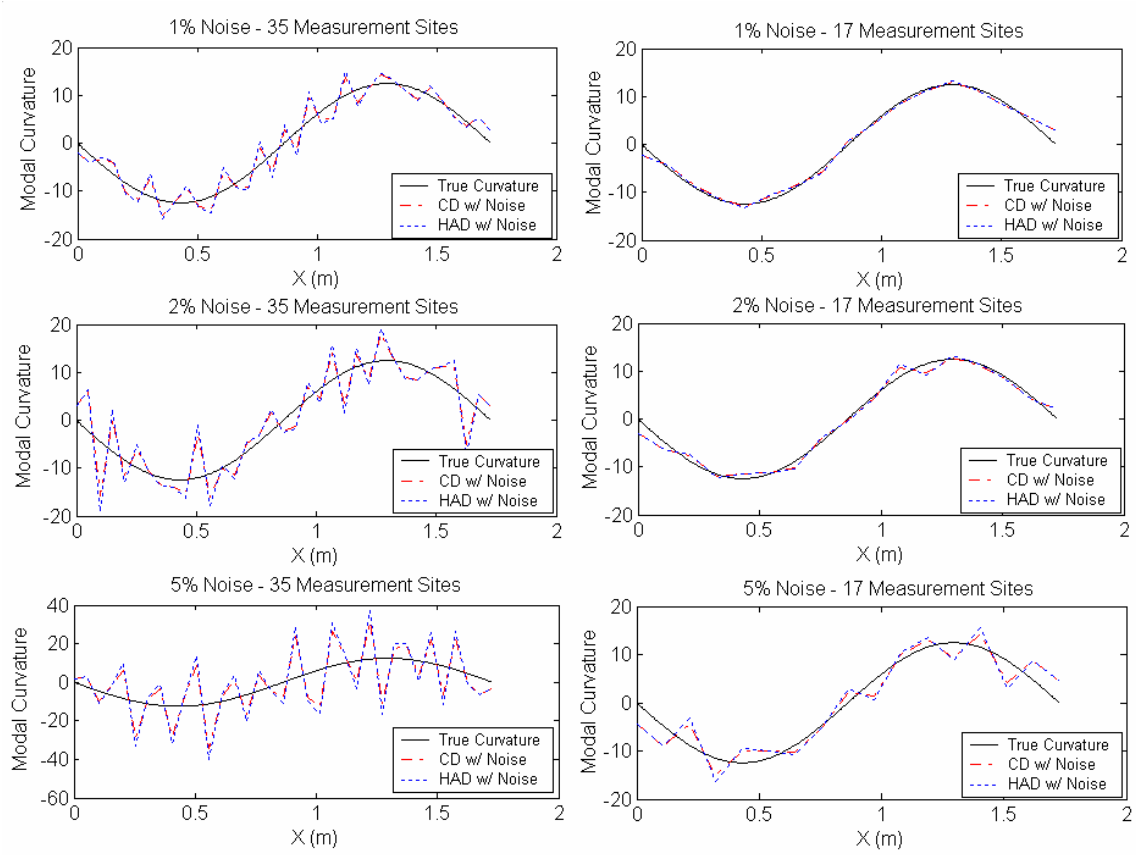

Figure 4-8 Effect of Measurement Noise on Modal Curvature Calculation

4.3.3 Damage Identification using Element Modal Strain Damage Index with Sparse Modal Displacement Measurement

In order to demonstrate capability of the proposed EMSDI method to identify damage, simulated damage was introduced in the finite element model. Two damage scenarios were simulated: (1) a 6% reduction in bending stiffness on a 0.102 m (4 in) section of the left span of the beam and (2) a 49% reduction in bending stiffness on a 0.152 m (6 in) section of the right span of the beam. These two damage scenarios were chosen to represent small and medium levels of damage, respectively. The two damage

scenarios are illustrated in Figure 4-9. The natural frequencies of the first 6 modes for both damage cases are listed in Table 4-1.

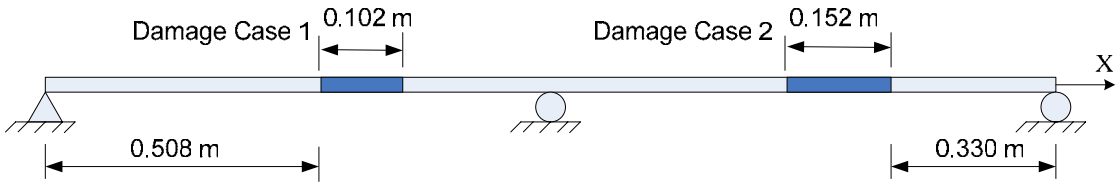

Figure 4-9 Damage Scenarios

Modal displacements are again obtained through modal analysis and are resampled to simulate the condition of sparse measurement. Figure 4-10 plots the modal displacement comparison of the first two modes between the undamaged state and Damage Case 1 for the case of 35 measurement sites. The modal displacement of Damage Case 1 is overlaid on the undamaged modal displacement in the figures (a) and (b). Figures (c) and (d) depict the modal displacement differences calculated by subtracting modal displacements of the damaged state from those of the undamaged states. It can be seen that modal displacements from the two states were barely discernible for Damage Case 1, which represents a damage pertaining to a 6% stiffness reduction over a section of approximately 10% of the beam span length. The difference between modal displacements does not provide a good indication for damage location either, with results from the two modes indicating maximum differences at different locations.

Figure 4-11 plots the results of Damage Case 2. In this case, due to the larger magnitude of damage the change in mode shape is more discernible. Results from sparse measurements of 17 and 7 measurement sites also show similar trends.

Table 4-1 Natural Frequency Comparison between Undamaged State and Damage Case 1 and 2 (Unit: Hz)

Mode	Undamaged	Damage Case 1	Damage Case 2
1	19.629	19.575	18.124
2	30.665	30.647	29.290
3	78.512	78.340	77.705
4	99.366	99.088	98.247
5	176.63	176.56	166.80
6	207.29	207.17	200.16
7	313.96	313.10	303.59
8	354.43	353.82	345.76

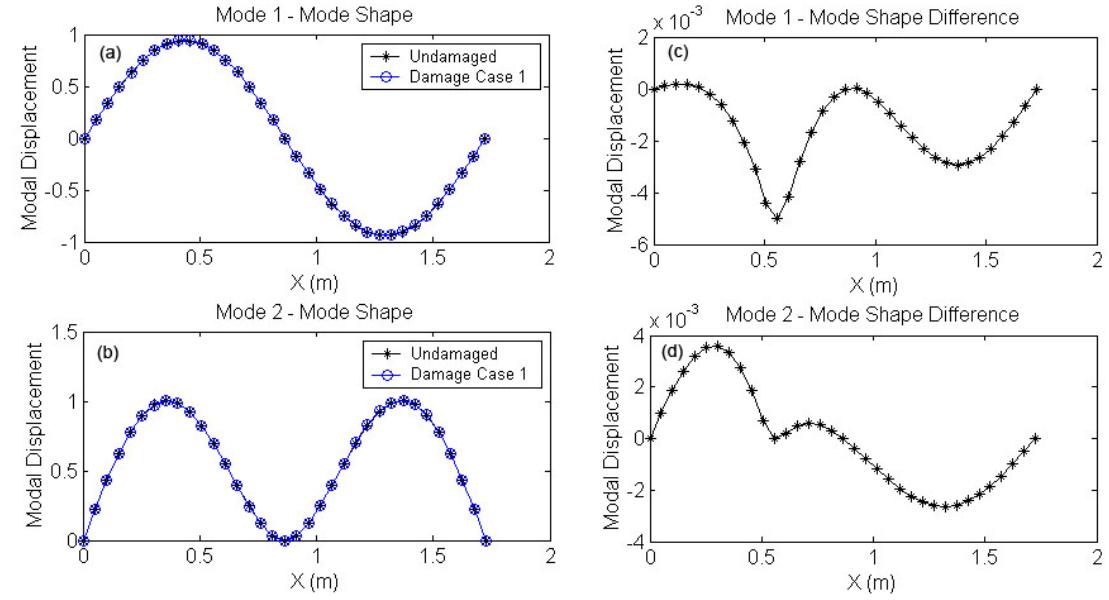

Figure 4-10 Modal Displacement Comparison and Modal Displacement Difference between Undamaged State and Damage Case 1

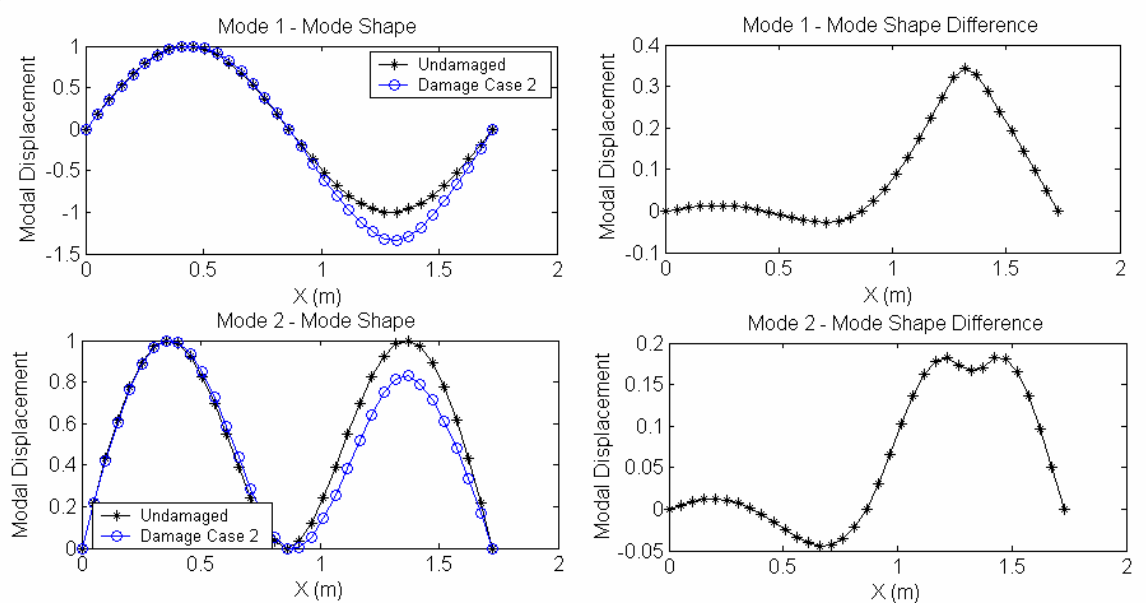

Figure 4-11 Modal Displacement Comparison and Modal Displacement Difference between Undamaged State and Damage Case 2

The Element Modal Strain Damage Index can then be calculated using equation (4.15) using all three sets of sparse measurements. The measurement sites are taken as the nodes and the beam section between adjacent sites are treated as single elements in the calculation of EMSDI. Modal rotations are first determined by solving Eq. (4.28). The modal displacements and modal rotations at each node can then be substituted into Eq. (4.15) to calculate EMSDI for each element. The results are presented in Figure 4-12 to Figure 4-16.

Figure 4-12 presents the EMSDI difference of each element between the undamaged state and Damage Case 1 for the case of 35 measurement sites. For all three modes selected, EMSDI difference plots show a clear peak at the location of the damage, which is between 0.5m to 0.6m from the left support. As a comparison, the

modal curvature difference calculated using numerical differentiation is plotted in Figure 4-13. The results show that modal curvature is also able to correctly locate the damage for the case of 35 measurement sites. Results for the case of 17 measurement sites are plotted in Figure 4-14 and Figure 4-15. Only results for mode 1 and mode 3 are plotted, since the results from other modes are similar. Again, the EMSDI is seen to correctly indicate the damage location for both modes. For the purposes of comparison, modal curvature difference is also plotted in Figure 4-14 and Figure 4-15. It appears that for mode 1, modal curvature calculated using the numerical difference procedure is also able to correctly indicate the damage location. But in the case of mode 3, the results of modal curvature difference appear to be ambiguous and hard to interpret. This trend compares well with the conclusion drawn from Eq. (4.4) and Figure 4-7 in that the error introduced by numerical differentiation increases in the higher modes. A similar comparison is given in Figure 4-16 for the case of 7 measurement sites. For this case, neither method is able to give a clear indication of the location of the damage.

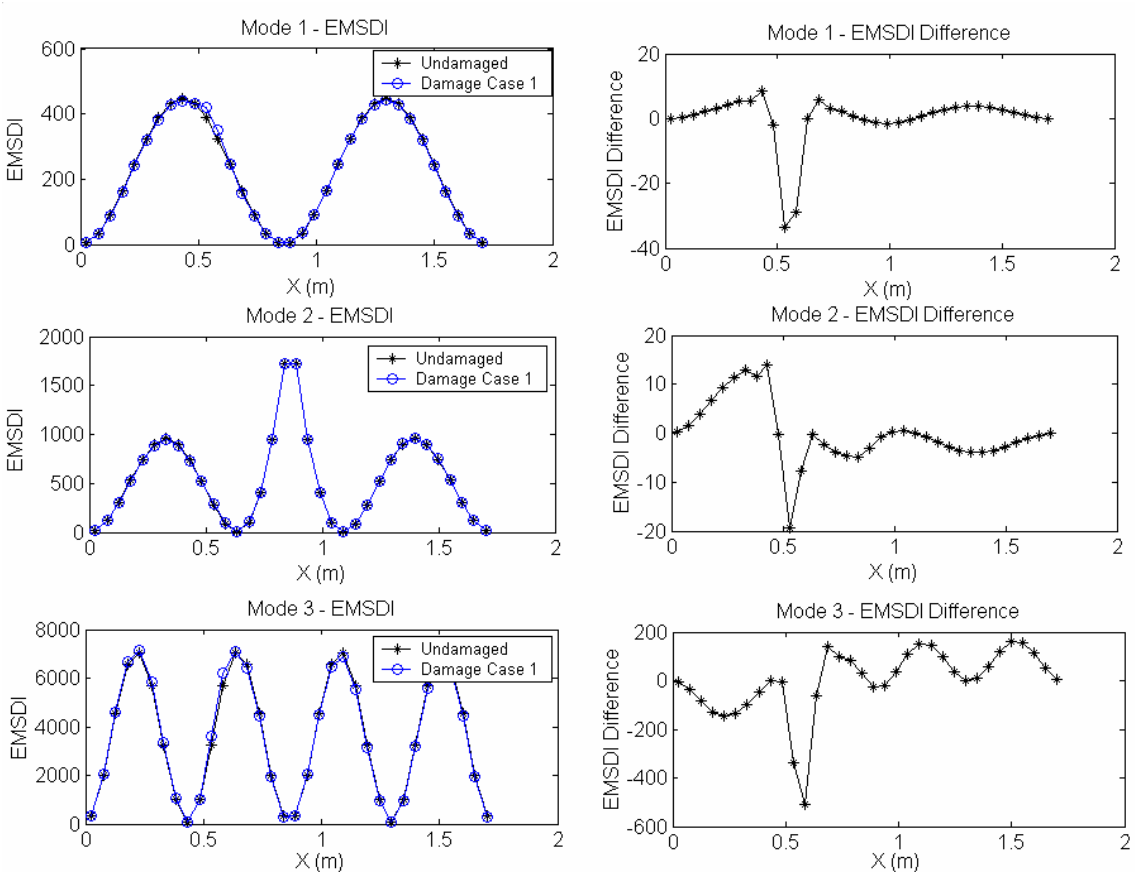

Figure 4-12 EMSDI and EMSDI Difference: Undamaged State vs. Damage Case 1 (35 Measurement Sites)

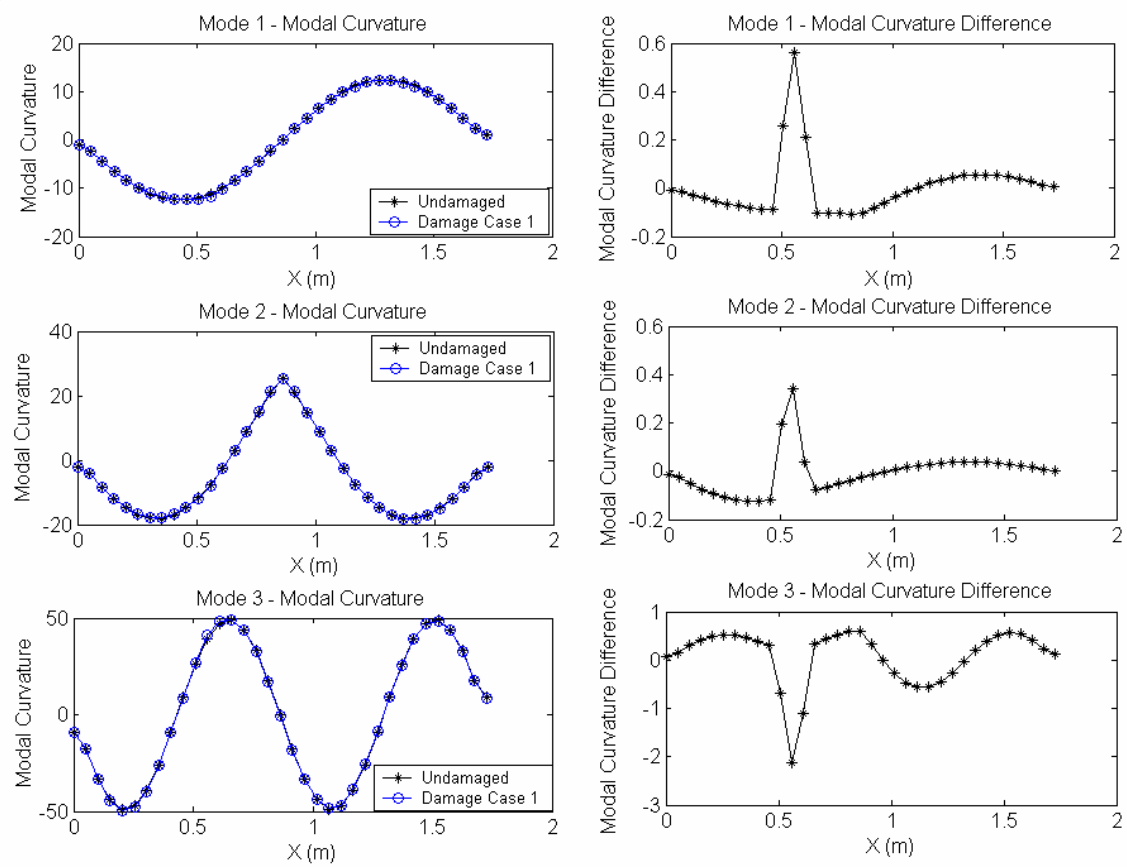

Figure 4-13 Modal Curvature and Modal Curvature Difference: Undamaged State vs. Damage Case 1 (35 Measurement Sites)

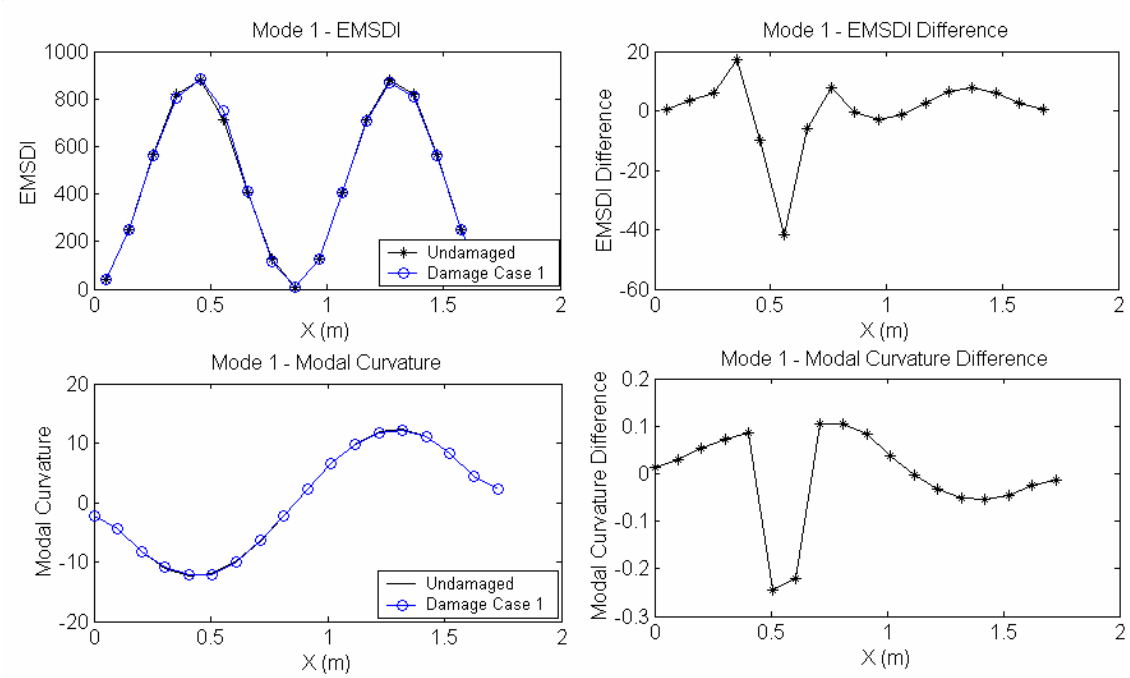

Figure 4-14 EMSDI Difference and Modal Curvature Difference: Undamaged State vs. Damage Case 1 (17 Measurement Sites – Mode 1)

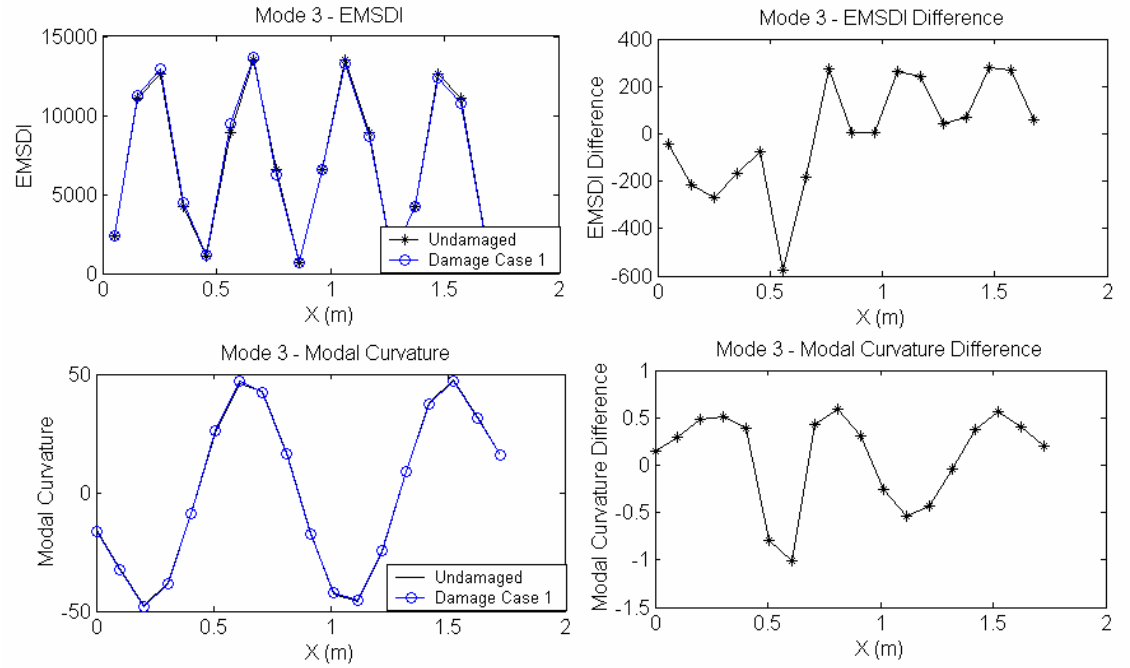

Figure 4-15 EMSDI Difference and Modal Curvature Difference: Undamaged State vs. Damage Case 1 (17 Measurement Sites – Mode 3)

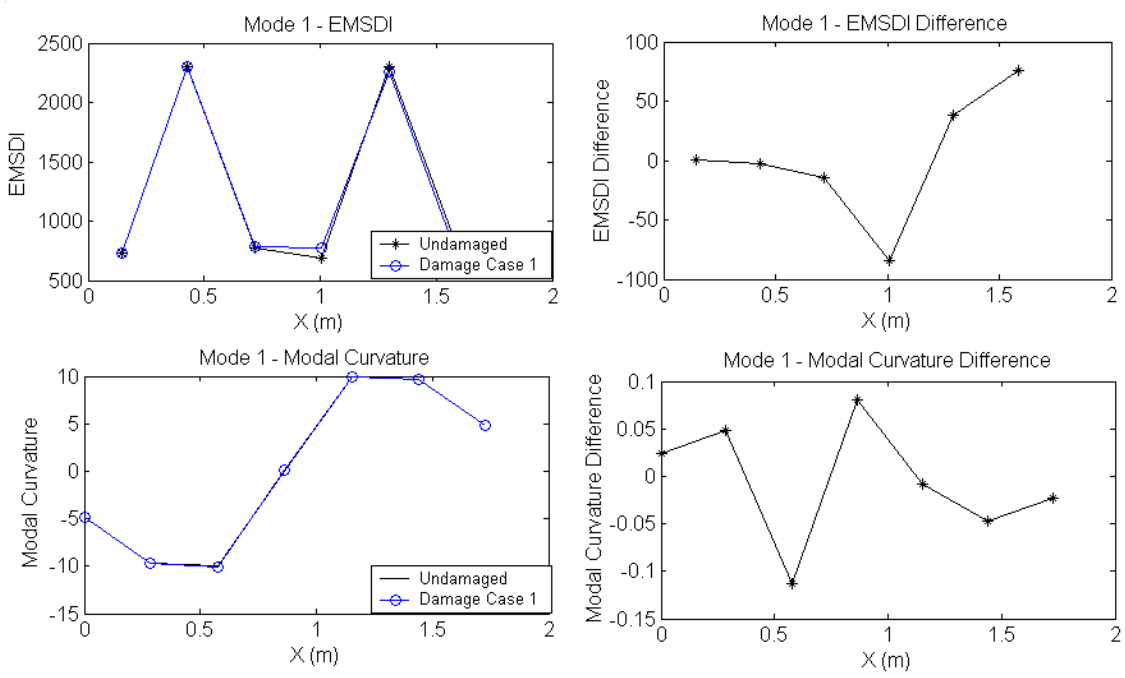

Figure 4-16 EMSDI Difference and Modal Curvature Difference: Undamaged State vs. Damage Case 1 (7 Measurement Sites)

Results from Damage Case 2 are presented in Figure 4-17 through Figure 4-20. Figure 4-17 and Figure 4-18 show a comparison between the EMSDI method and modal curvature in the case of 35 measurement sites. Similar to Damage Case 1, both methods are seen to be able to locate the damage region correctly. However, in the case of mode 2, the use of the EMSDI difference presents a more distinctive peak at the location of damage, which is about 0.33m – 0.38m from the right support. Results from the case of 17 measurement sites are plotted in Figure 4-19. Again similar to Damage Case 1, both methods are able to identify the damaged region correctly. Figure 4-20 presents the results obtained from the consideration of only 7 measurement sites. For this case, the EMSDI method clearly outperforms the modal curvature method and shows a clear peak at the correct location in the difference plot.

Overall it is concluded that the EMSDI method generally shows better performance in comparison to the modal curvature method using numerical differentiation procedures. The advantage of the EMSDI method is highlighted when the mode number increases and the number of measurement sites decreases.

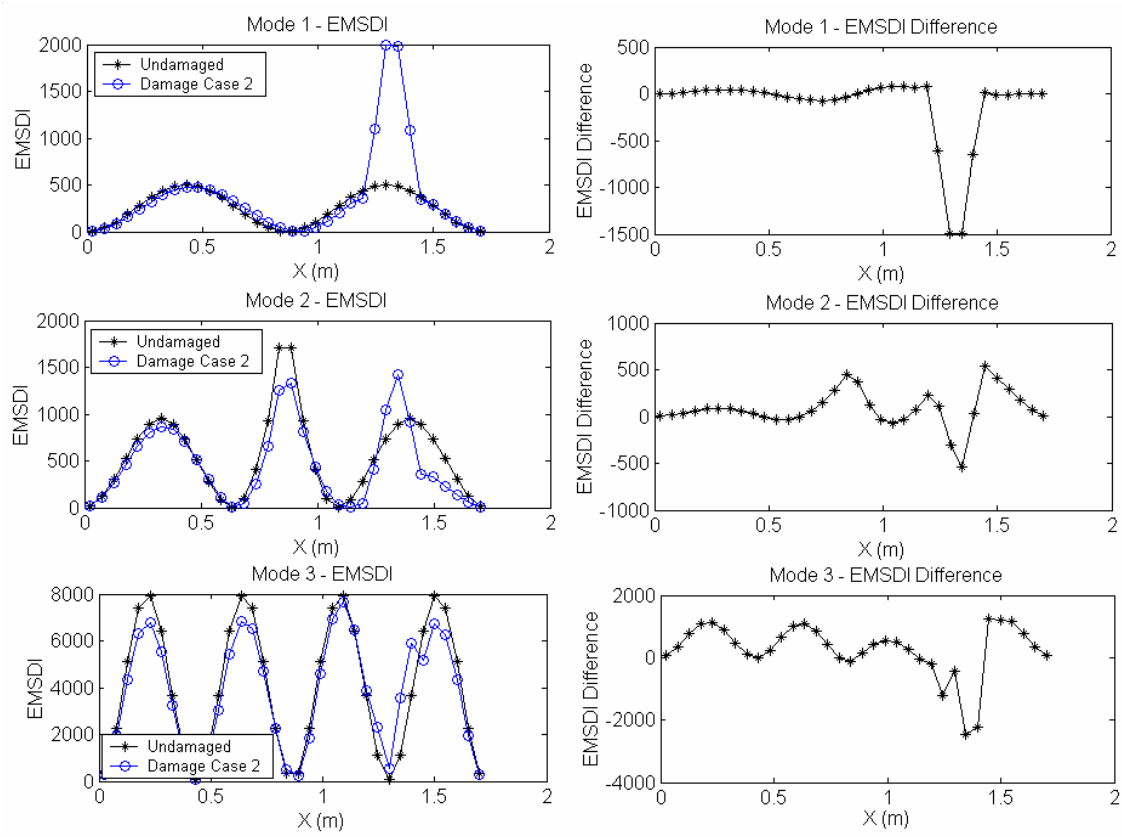

Figure 4-17 EMSDI and EMSDI Difference: Undamaged State vs. Damage Case 2 (35 Measurement Sites)

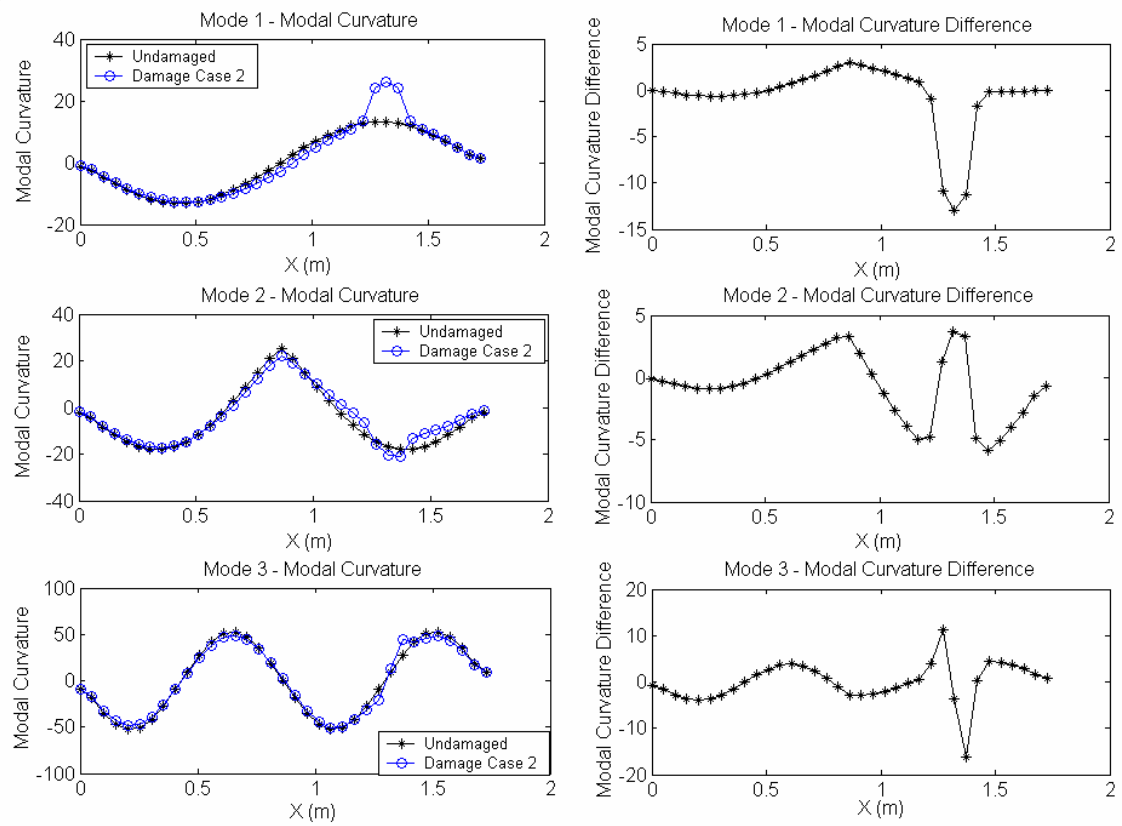

Figure 4-18 Modal Curvature and Modal Curvature Difference: Undamaged State vs. Damage Case 2 (35 Measurement Sites)

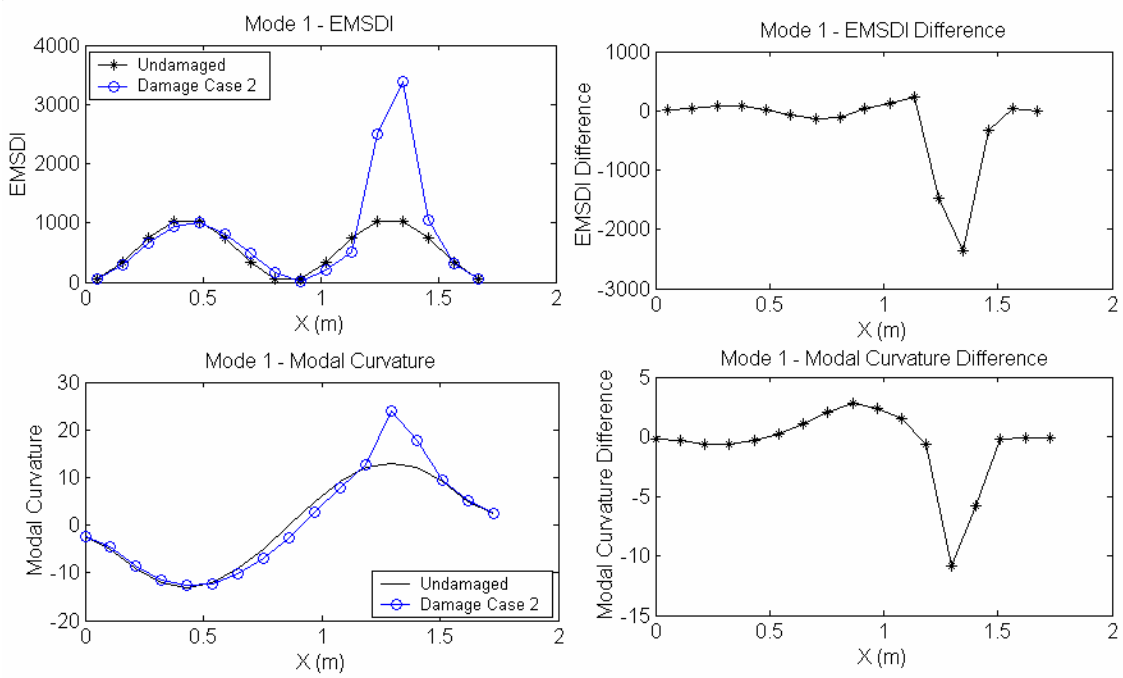

Figure 4-19 EMSDI Difference and Modal Curvature Difference: Undamaged State vs. Damage Case 2 (17 Measurement Sites)

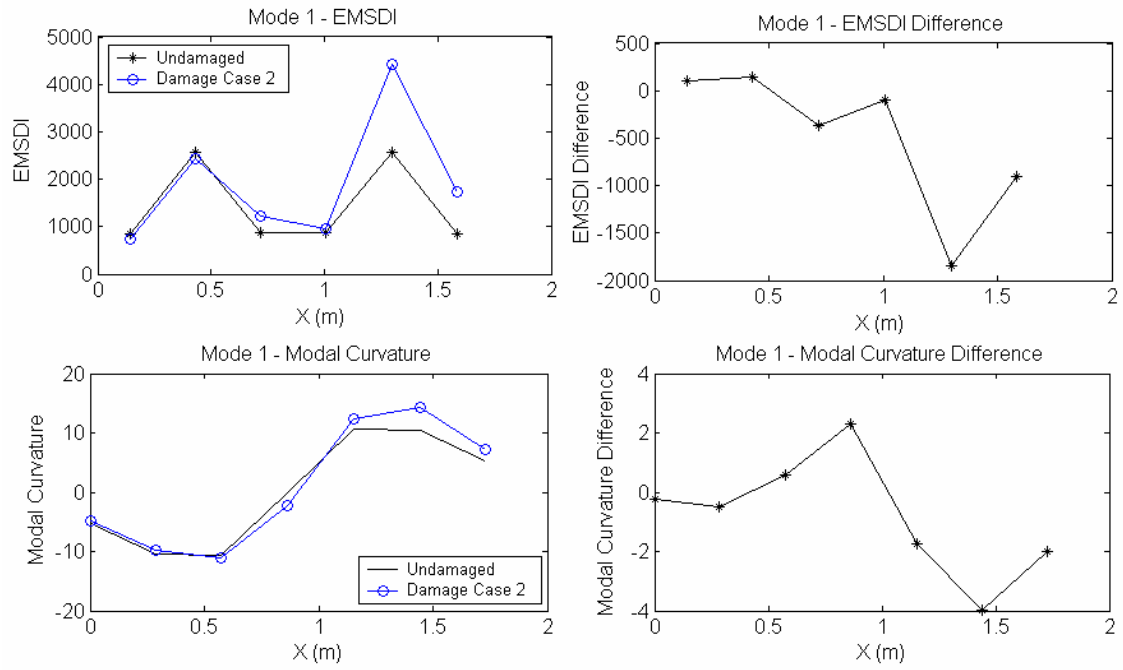

Figure 4-20 EMSDI Difference and Modal Curvature Difference: Undamaged State vs. Damage Case 2 (7 Measurement Sites)

4.3.4 Damage Identification using Element Modal Strain Damage Index with Noisy Modal Displacement Measurements

To compare the performance of the proposed EMSDI method with the commonly used modal curvature method under conditions where measurement noise is present, three different realistic levels of noise were added to both the damaged and undamaged simulated modal displacements as discussed in Section 4.3.2. The difference between the undamaged mode shape and that of Damage Case 1 was too small compared with simulated noise, thus only Damage Case 2 will considered in the following study. Modal curvature differences for mode 1 between the undamaged state and Damage Case 1 for both noisy and noise-free measurements are plotted in Figure 4-21. In each figure, curvature difference calculated using noise-free measurements are represented by the solid lines marked with stars. Curvature difference calculated using noisy measurements are represented by dashed lines marked with triangles. It can be seen that for the case of 35 measurement sites, the unevenness caused by the propagated noise due to use of a numerical differentiation procedure is comparable in size to the change caused by damage even for the lowest noise level. For higher noise levels, numerical errors in curvature completely mask the change caused by damage. For the case of 17 measurement sites, due to the larger spacing between sites, the peak caused by damage is still quite discernible for lower noise levels. However, for the highest noise level, the numerical errors also start to dominate.

The corresponding EMSDI difference results of mode 1 are plotted in Figure 4-22**.** EMSDI for both undamaged and damaged states were calculated using Eq. (4.28),

i.e., no measure was specially taken to deal with the problem of measurement noise. For this case, EMSDI showed slightly better performance compared with the modal curvature method under the same situations. The damage location was correctly indicated in the case of two lower noise levels for both the 35 and 17 measurement sites cases but not for the highest noise level.

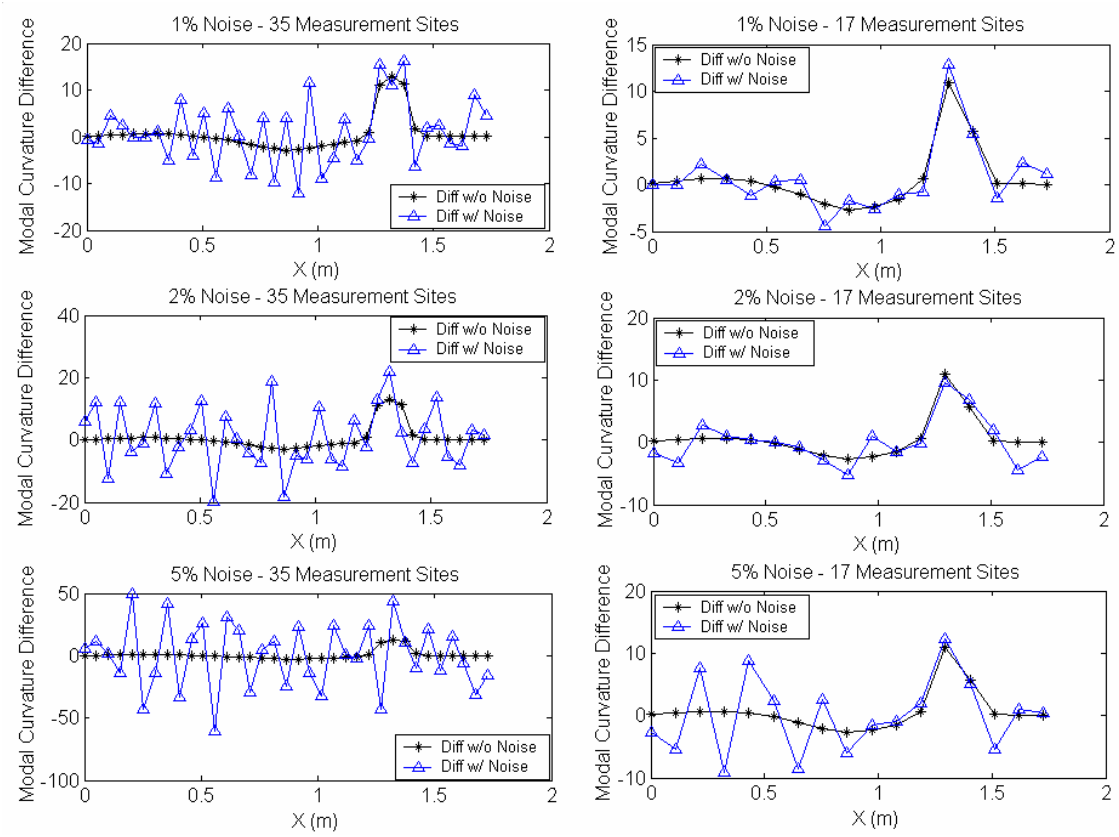

Figure 4-21 Modal Curvature Difference of Mode 1: Noisy Measurement vs. Noise-free Measurement

The EMSDI difference computed using Eq. (4.29) is presented in Figure 4-23, from which it can clearly be seen that the inclusion of the penalty term in Eq. (4.29) drastically improve the performance of EMSDI method under noisy conditions. The

damage location was correctly indicated for all noise levels and for both 35 and 17 measurement sites. For higher noise levels, the base of the peak indicating the damage region is seen to widen. This is expected since higher noise content in the measurement will no doubt affect the preciseness by which the damage region can be located. Nevertheless, the number and the center location of the damage region are both identified correctly. The results for 7 measurement sites are plotted in Figure 4-24. Again, the improved EMSDI method using Eq. (4.29) is able to correctly locate the damage region for all three noise levels although the result for the highest noise level seems somewhat ambiguous.

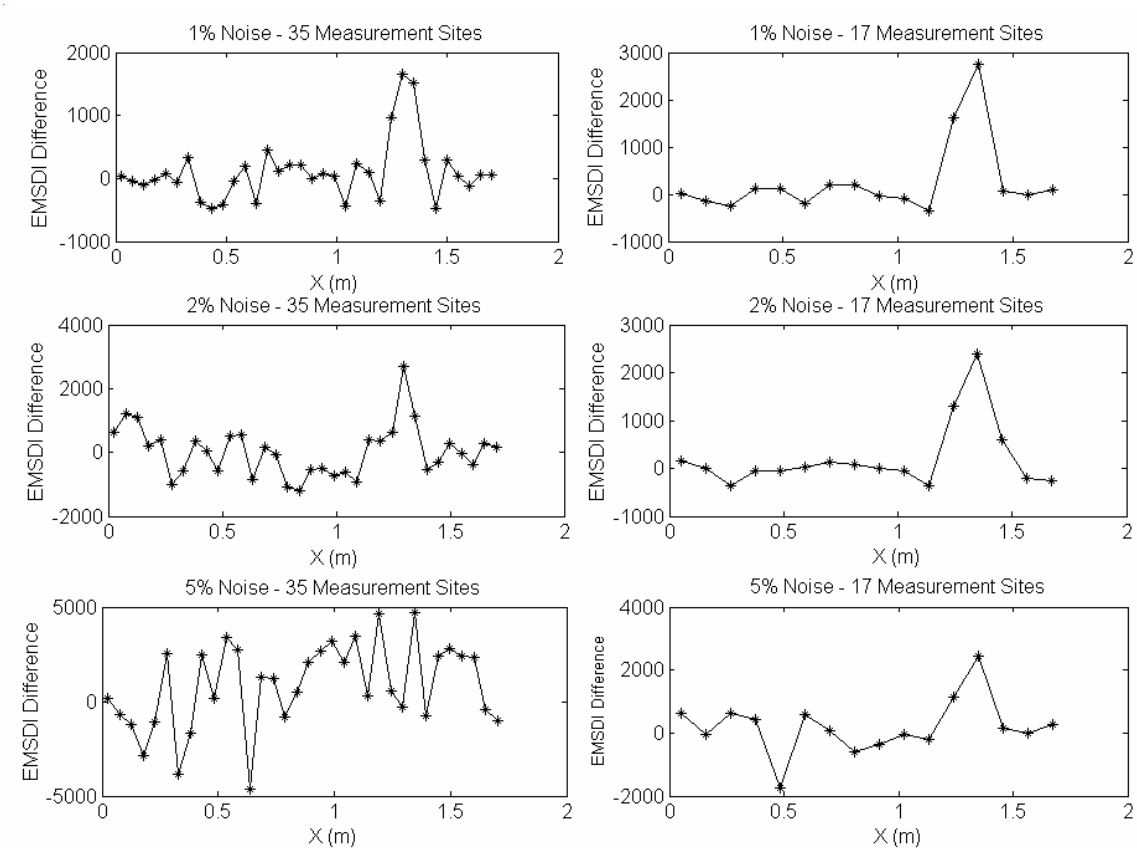

Figure 4-22 EMSDI Difference of Mode 1 - Eq. (4.28) – 35 and 17 Measurement Sites

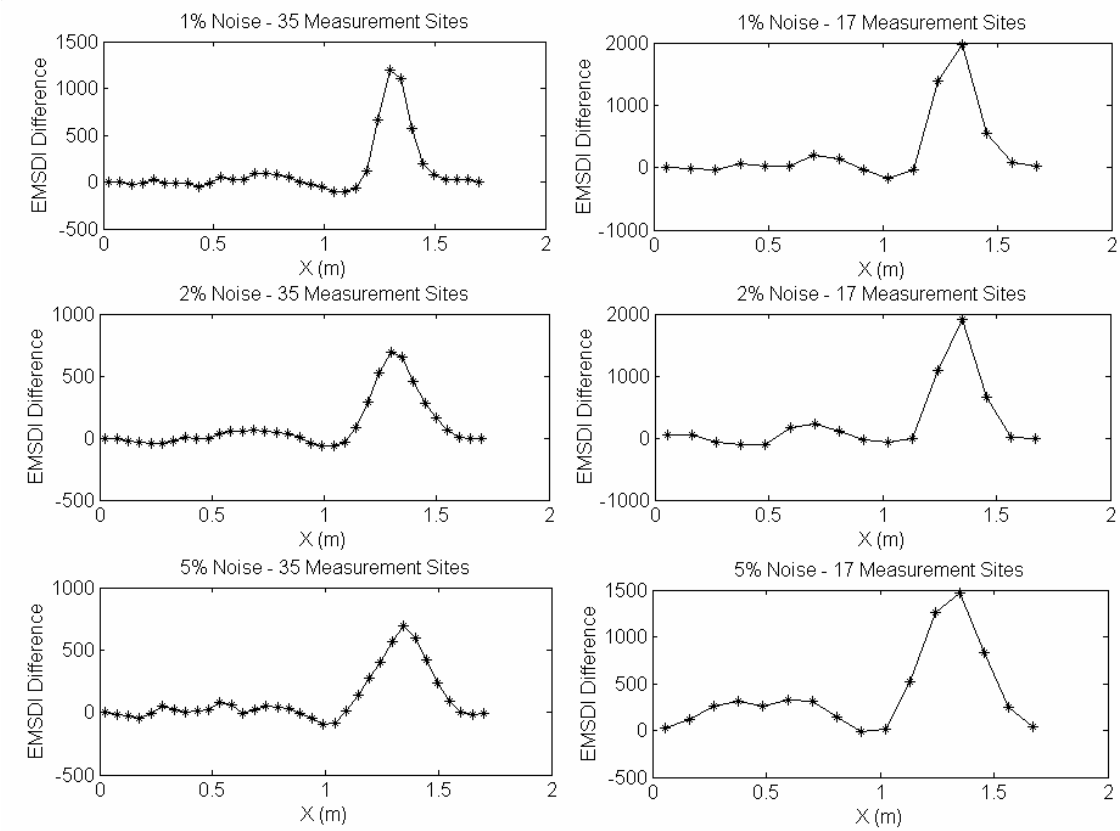

Figure 4-23 EMSDI Difference of Mode 1 - Eq. (4.29) – 35 and 17 Measurement Sites

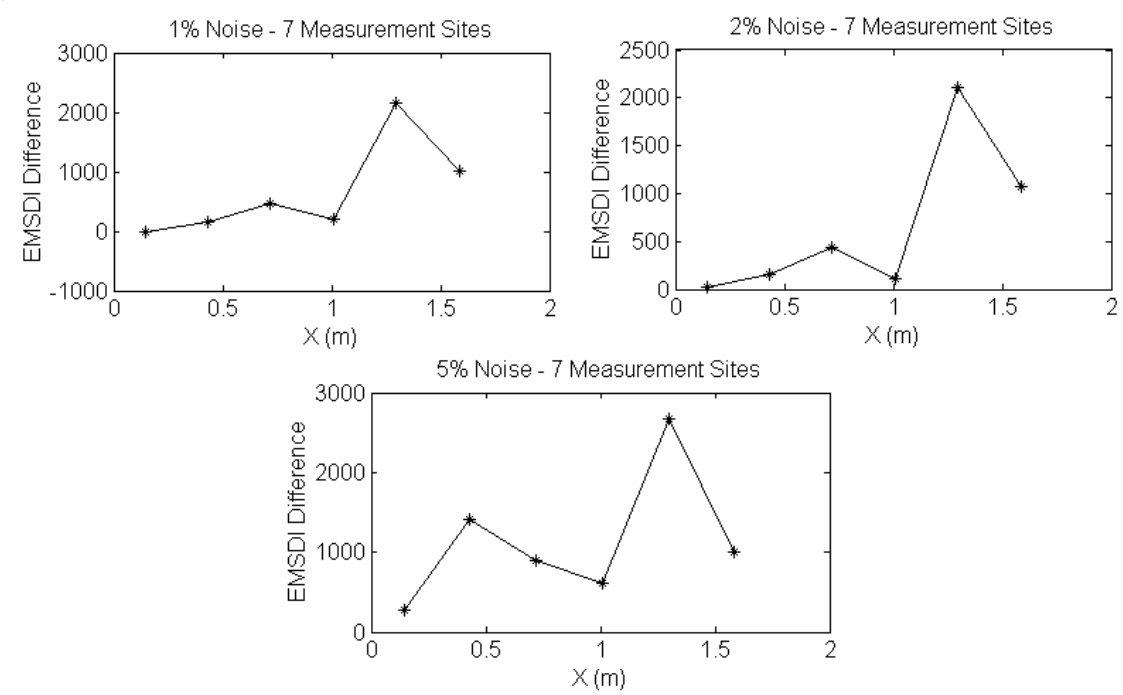

Figure 4-24 EMSDI Difference of Mode 1 – Eq. (4.29) – 7 Measurement Sites

4.4 Extension of EMSDI Method to Two Dimensional Structures

4.4.1 Extension to Two Dimensional Structures

There are several ways to extend the theoretical formulation of the EMSDI method laid out in Section 4.2 to two dimensional structures. One approach, which was adopted in the current research, is described below.

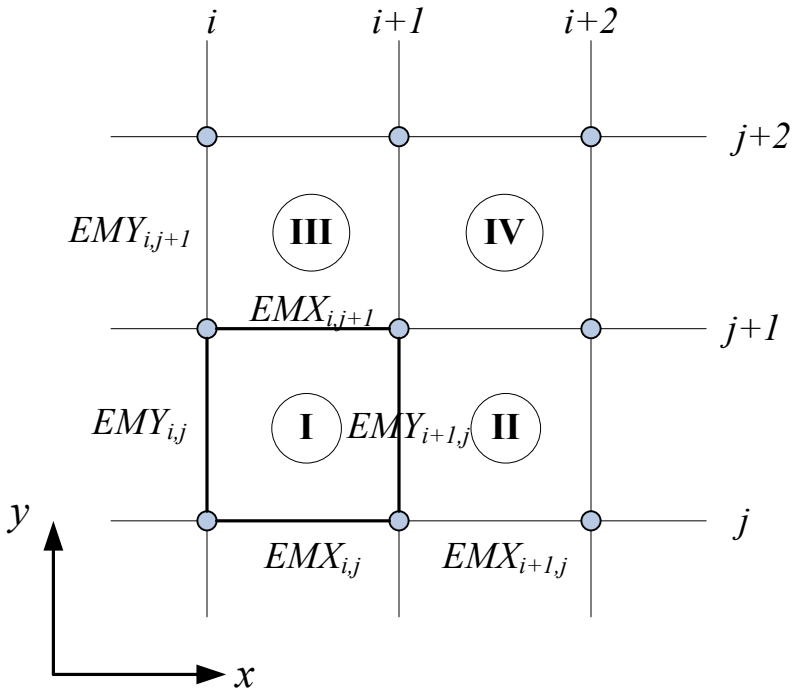

Figure 4-25 Grid Division for Two Dimensional Case

Consider a subsection of a two dimensional structure with sensor locations laid out in a rectangular grid, as shown in Figure 4-25. Sensors are arranged in lines along

the x direction denoted by the sequence *j, j+1, j+2,* …, etc. Correspondingly, the sensor lines along the y direction are denoted by the sequence *i, i+1, i+2*, …, etc. One can calculate the EMSDI index along line in x direction as well as lines in y direction. The EMSDI indexes calculated are named based on the direction they are aligned to and the location of the sensors they are associated with. For example, the value of the EMSDI index on line *j* along the x direction between two sensors located on line *i* and line *i+1* is denoted as $EMX_{i,j}$, as shown in Figure 4-25. Similarly, one can define the EMSDI values $EMX_{i,j+1}$, $EMY_{i,j}$, $EMY_{i+1,j}$ around area I. The nominal EMSDI values for area I can be then defined as the average of these values, i.e.,

$$EMSDI_I = \left(EMX_{i,j} + EMX_{i,j+1} + EMY_{i,j} + EMY_{i+1,j} \right) \Big/ 4 \tag{4.32}$$

In Eq. (4.32), $EMSDI_I$ represents the average of EMSDI in two direction around the subsection of the area defined by the sensor grid.

4.4.2 Numerical Example

For the purpose of comparison, a numerical example used in Kim et al. (2005) was adopted to show the effectiveness of the EMSDI technique extended to two dimensional structures. The numerical example considered is a simply supported plate-like structure shown schematically in Figure 4-26. All dimension and material properties of the numerical model are identical to those used in Kim et al. (2005). The structure represents a simply supported reinforced concrete slab of the dimension 16.0m by 10.0m, with a thickness of 0.15m, a Young's modulus of 28.6 GPa and a density of 2400 kg. The Poisson's ratio of the material was taken to be 0.15. The damage location

is indicated by the shaded area in Figure 4-26. The damage is simulated by a 10% uniform reduction of Young's modulus.

For the current analysis, the model is built using the finite element software ANSYS (2004). Assuming that only the transverse degrees of freedom are measured at each sensor location, the first six natural frequencies and displacement mode shapes are extracted for the undamaged structure and the damaged structure. There are a total of 231 sensor locations where displacement mode shapes are extracted, with a spacing of 0.8m in the X direction and 1.0m in the Y direction. In Kim et al. (2005), the Flexural Damage Index Equation (FDIE) approach was used to locate the damage. The details of the FDIE method were reviewed in Section 2.2.4 of the dissertation and hence will not be repeated here. Only results from the FDIE method will be given below for comparison. However, one noteworthy point that will be mentioned here is that Kim et al. (2005) compared the FDIE method with other methods based on modal curvature and the damage index method. It was shown that the FDIE method performs better than other and hence the FDIE method was considered as representing the state-of-the-art of vibration-based damage detection methods.

To simulate the actual conditions of measurement, Kim et al. (2005) considered the following model to model measurement noise: the accelerometers were considered to be tilted by an inaccurate installation. It was assumed that the accelerometers could not be installed exactly perpendicular to the surface of the plate and their tilt angles were randomly distributed from -5 degrees to +5 degrees in the perpendicular direction. The error in measurement caused by this random tilt angle was numerically considered

by taking the cosine function for the range of random angles and multiplying the original noise-free mode shape by this cosine function. This random multiplication factor is plotted in Figure 4-27. The maximum amplitude error in the mode shape caused by this random tilt noise is approximately 0.4%. Results of the FDIE method using noisy mode shapes is plotted in Figure 4-28. Many spurious peaks can be observed which greatly hinders the effort to identify the location of the true damage area. Without any prior knowledge of the damage location, one might reach the wrong conclusion that the slab was damaged in multiple locations.

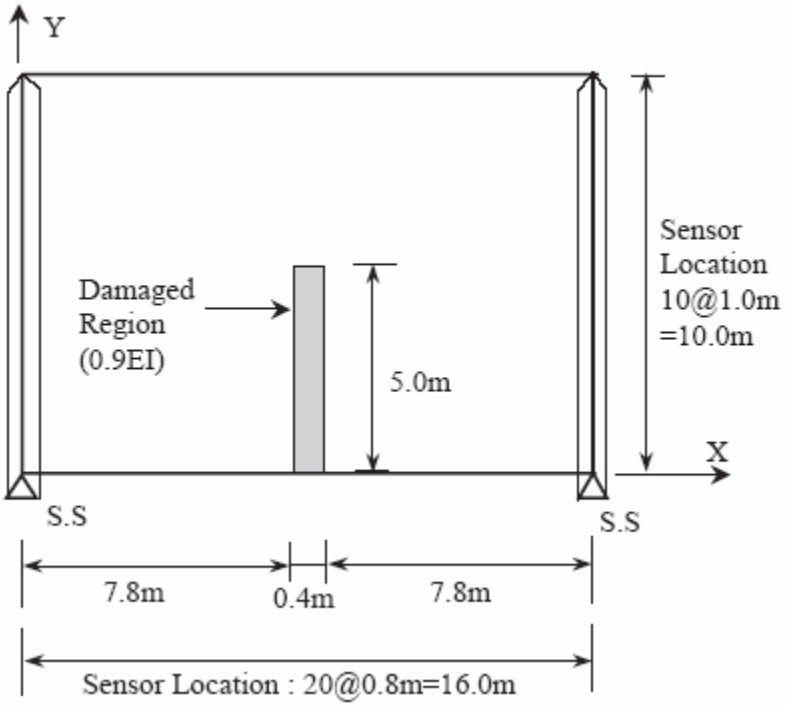

Figure 4-26 Schematic of Simply Supported Plate (Kim et al. 2005)

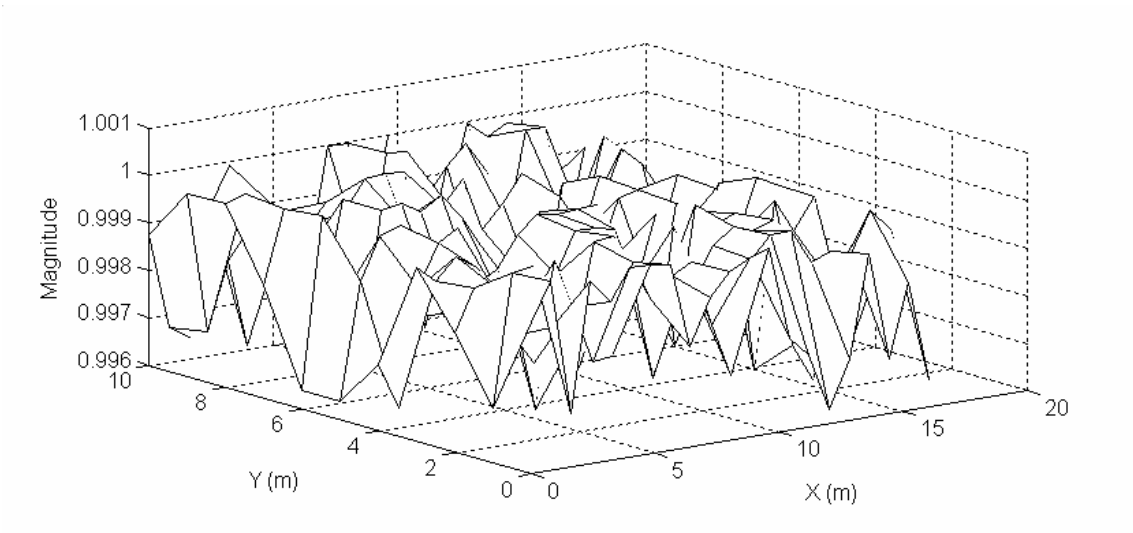

Figure 4-27 Random Tilt Noise

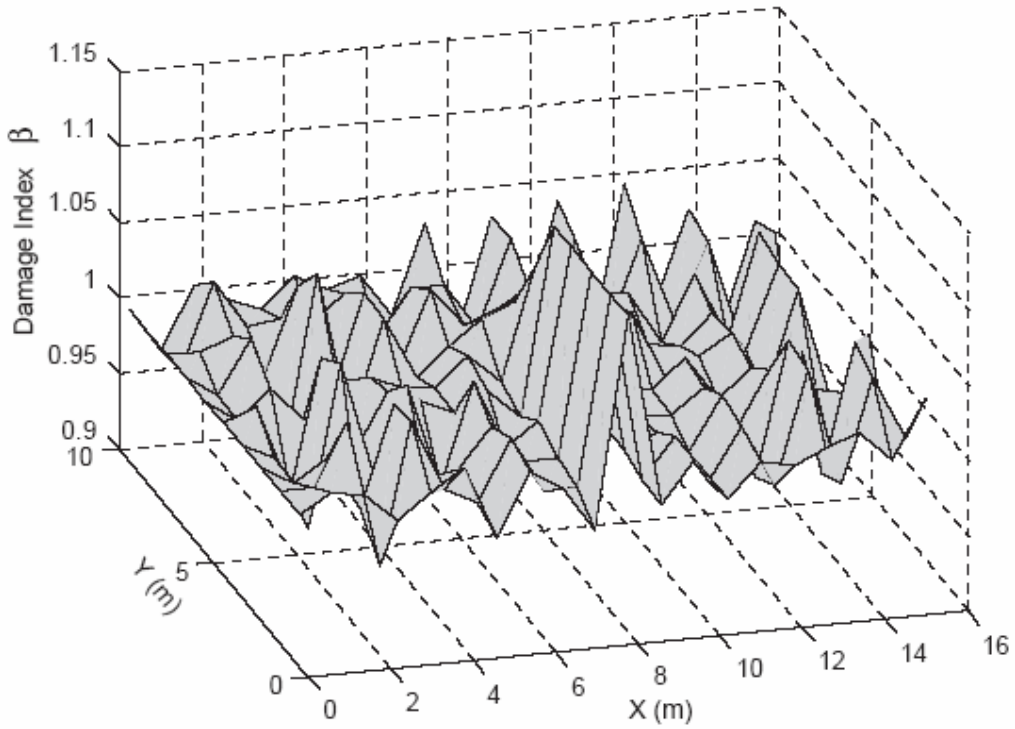

Figure 4-28 FDIE Result using Noisy Mode Shapes

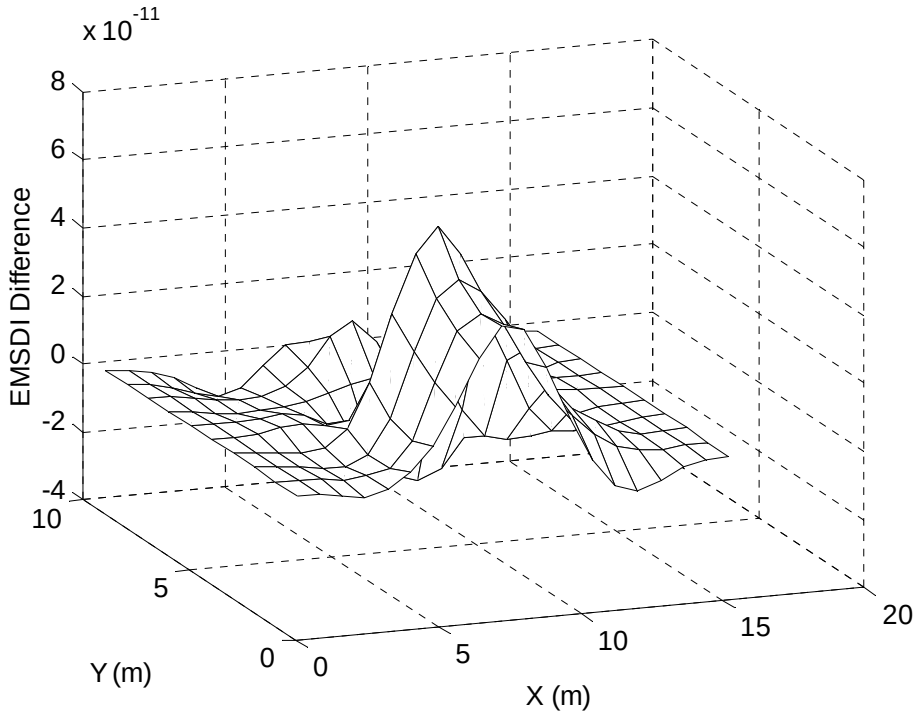

Figure 4-29 EMSDI Result using Noisy Mode Shapes

The result from the application of the two dimensional EMSDI method (Eq. (4.32)) is shown in Figure 4-29. It can be seen that result from the EMSDI method contains significantly less spurious peaks than the result from FDIE method, which greatly reduces the chance of misidentifying the damage location. It is also noted that due to the presence of noise, the base of the peak in the EMSDI result is wider than the actual damage area. However, the peak itself still correctly pinpoints the damage location. In conclusion, it seems the EMSDI method performs significantly better than the FDIE method when applied to same noisy mode shapes.

4.5 Experimental Validation

4.5.1 Experiment Setup

To evaluate the performance of the proposed EMSDI technique under actual experimental conditions, a series of tests were performed on small scale beam specimens in the laboratory. The aluminium beams tested have a length of 914.4 mm (36 in) and a section of 76.2 mm (3 in) by 6.35 mm (1/4 in). The geometry of the cross-section was identical to the one used for the numerical analysis depicted in Figure 4-4. The beams were set up in to simulate a simply-simply supported boundary condition, frequently encountered in modal testing of bridges (Figure 4-30a). A special support fixture was used on both ends of the beam to ensure that a close approximation of the idealized boundary condition was achieved. The span of the beam is 863.6 mm (34 in).

(a) Test Setup (b) DAQ System

Figure 4-30 Experiment Setup and Data Acquisition System

4.5.2 Experimental Determination of Modal Parameters

Damage was introduced in the beam in the form of saw cuts in the direction perpendicular to the longitudinal axis of the beam. Three damage cases were considered during the experiment. In all three cases, full width saw cuts of 3 mm thickness were made on both sides of the beam symmetric to the longitudinal axis. The first damage case involved saw cuts at location D1 (431.8mm from left support, as shown in Figure 4-31) with a depth of 6.35 mm (1/4 inch) at each side. The second damage case involved saw cuts at the previous location but with a depth of 12.7 mm (1/2 inch). In the third damage case, additional saw cuts were made at location D2 (177.9 mm from left support) with a depth of 12.7 mm. The reduction in Equivalent bending stiffness at the damaged locations due to loss of sectional area and sectional moment of inertia can be calculated for each of the three cases and is list in Table 4-2.

A PCB 086C03 Impact Hammer was used to apply an impulsive force on the beam at a pre-determined location. The response of the beam was measured by the accelerometers at a sampling rate of 1000 Hz. The response acceleration signal was first passed through an anti-aliasing filter to filter out high frequency noise. Acceleration Frequency Response Functions (FRFs) were then calculated using the measured impact force and the acceleration response. Multiple impact tests were carried out to obtain averaged FRFs.

A typical FRF and its corresponding coherence function are shown in Figure 4-32. The coherence value was close to 1 for most of the frequency range indicating a low noise level during the experiment. The rational Fractional Polynomial (RFP)

method (Formenti and Richardson 1982) was applied on FRFs in the frequency domain to obtain estimates of modal parameters, including natural frequencies, modal damping and mode shapes.

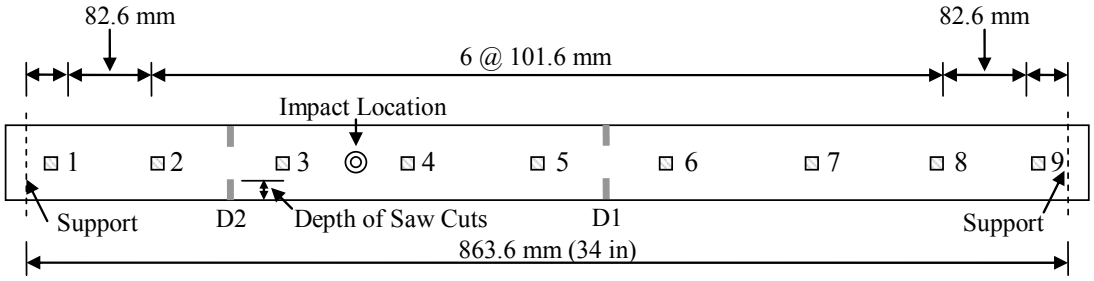

Figure 4-31 Accelerometer Locations

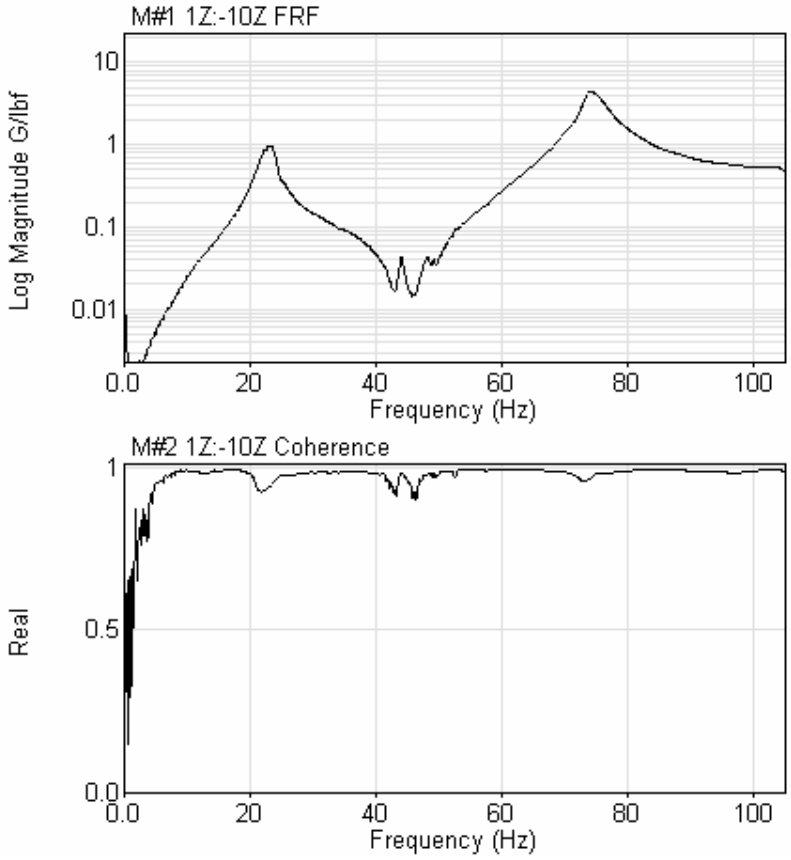

Figure 4-32 Typical Frequency Response Function and Coherence Function

4.5.3 Damage Cases

Damage was introduced in the beam in the form of saw cuts in the direction perpendicular to the longitudinal axis of the beam. Three damage cases were applied during the experiment. In all three cases, saw cuts were made on both sides of the beam symmetric to the longitudinal axis. The width of the saw cuts was uniform and approximately equals to 3mm. The saw cuts completely cut through the thickness of the beam but their depth in the beam width direction vary. The first damage case involved saw cuts at location D1 (431.8mm from left support, as shown in Figure 4-31) with a depth of 6.35 mm (1/4 inch) at each side. The second damage case involved saw cuts at the previous location but with a depth of 12.7 mm (1/2 inch). In the third damage case, additional saw cuts were made at location D2 (177.9 mm from left support) with a depth of 12.7 mm. Equivalent bending stiffness reduction at the damaged locations due to loss of sectional area and sectional moment of inertia can be calculated for each of the three cases and was list in Table 4-2.

Table 4-2 Damage Cases - Location and Magnitude

Damage Case	Location	Depth (mm)	Equivalent Reduction in EI
Case 1	D1 (431.8mm from left support)	6.35	16.7%
Case 2	D1 (431.8mm from left support)	12.7	33.3%
Case 3	D1 and D2 (177.9 mm from left support)	12.7 (both)	33.3% (both)

4.5.4 Damage Identification using EMSDI Method

Displacement mode shapes were obtained for the undamaged structure and all three damage cases using techniques described previously in Section 4.2. Within the measurement frequency range, two modes were identified. The first mode is a symmetric bending mode with its frequency around 23 Hz. The second mode is an anti-symmetric bending mode with a natural frequency of approximately 75 Hz. A closer examination of the curve fitting process used in the Rational Fractional Polynomial method reveals that the mode shape of the second mode is susceptible to a distortional effect for some of the damage cases. However, the cause for this distortion could not be identified, and it was hence decided to use only the first mode in the damage identification process.

Amplitudes of displacement mode shape for undamaged and damaged states are plotted in Figure 4-33 as well as the difference between the modal displacements of three damage cases and that of the undamaged state. The X axis indicates the distance on the beam from the left support. From Figure 4-33 it can be seen that the changes in modal displacements caused by damage were small and very difficult to discern from the original mode shape. The maximum difference in mode shape between the undamaged state and Damage Case 3 amounts to about 1.7% of the largest modal displacement. The difference in modal displacements clearly does not give a good indication of damage location in all three damage cases.

Modal curvature calculated using the central difference approximation for all cases is plotted in Figure 4-34. It is apparent that modal curvature is not effective in

locating damage in this case due to the use of a small number of measurement points. The random variation of measurement mode shape may also contribute to the failure of modal curvature method in this case although the modal testing was carried out in a laboratory environment and measurement noise was considerably better controlled than in a field application condition.

The EMSDI results using Eq. (4.29) are presented in Figure 4-35. The beam was divided into 8 elements separated by sensor locations. Damage locations D1 and D2 are situated at elements 5 and 2, respectively. For Damage Case 1, EMSDI was not able to locate the damage correctly, with two false indications at elements 2 and 3. For both Damage Case 2 and Damage 3, the saw cut at location D1 was identified correctly. Damage was also indicated on the adjacent element 4, which is consistent with the behavior observed in numerical analysis when measurement noise was present. Damage location D2 was again identified correctly in Damage Case 3.

In summary, during the experimental validation the EMSDI method was able to identify damage correctly in most cases when the damage is sufficiently large. Although a false indication of damage can occur at low levels of damage, such indications almost non-existent with higher damage levels. It should be kept in mind that the above results were obtained using a very limited set of measurement sites under field simulated experimental conditions where noise influence was present. Within the experimental constraints, the EMSDI method shows a superior performance as compared to the more commonly used modal curvature method.

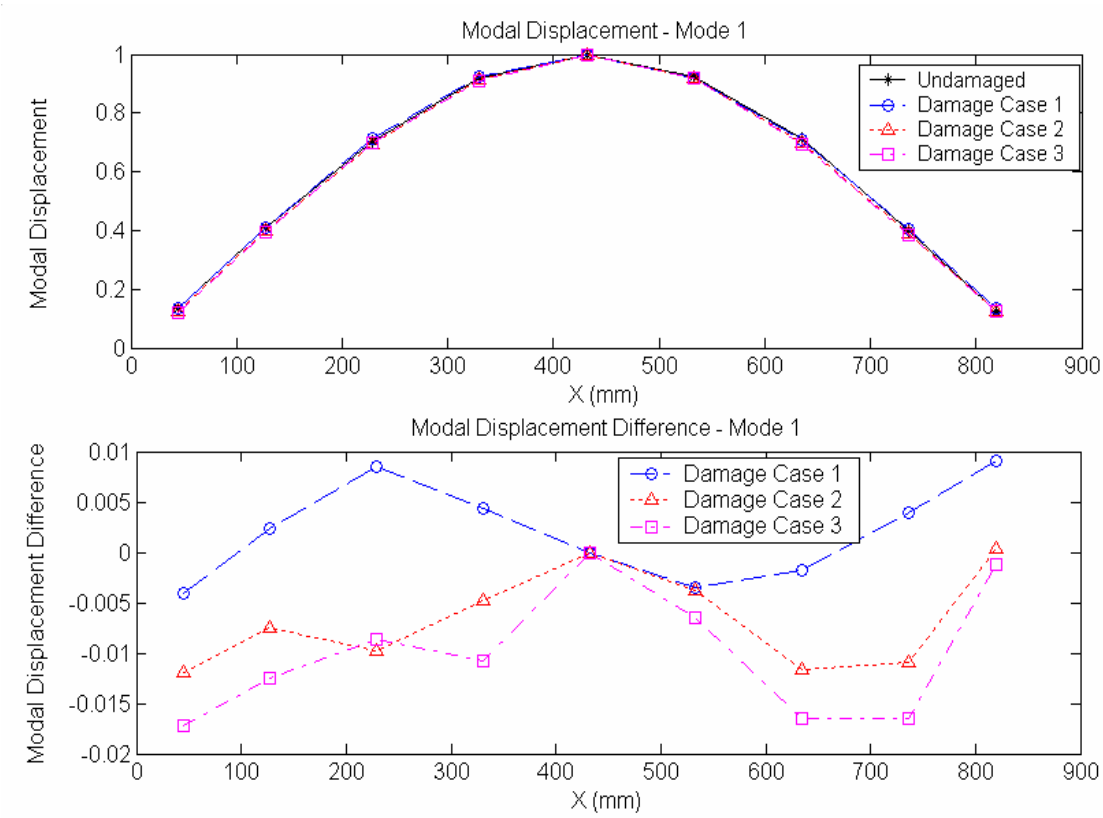

Figure 4-33 Modal Displacement and Modal Displacement Difference

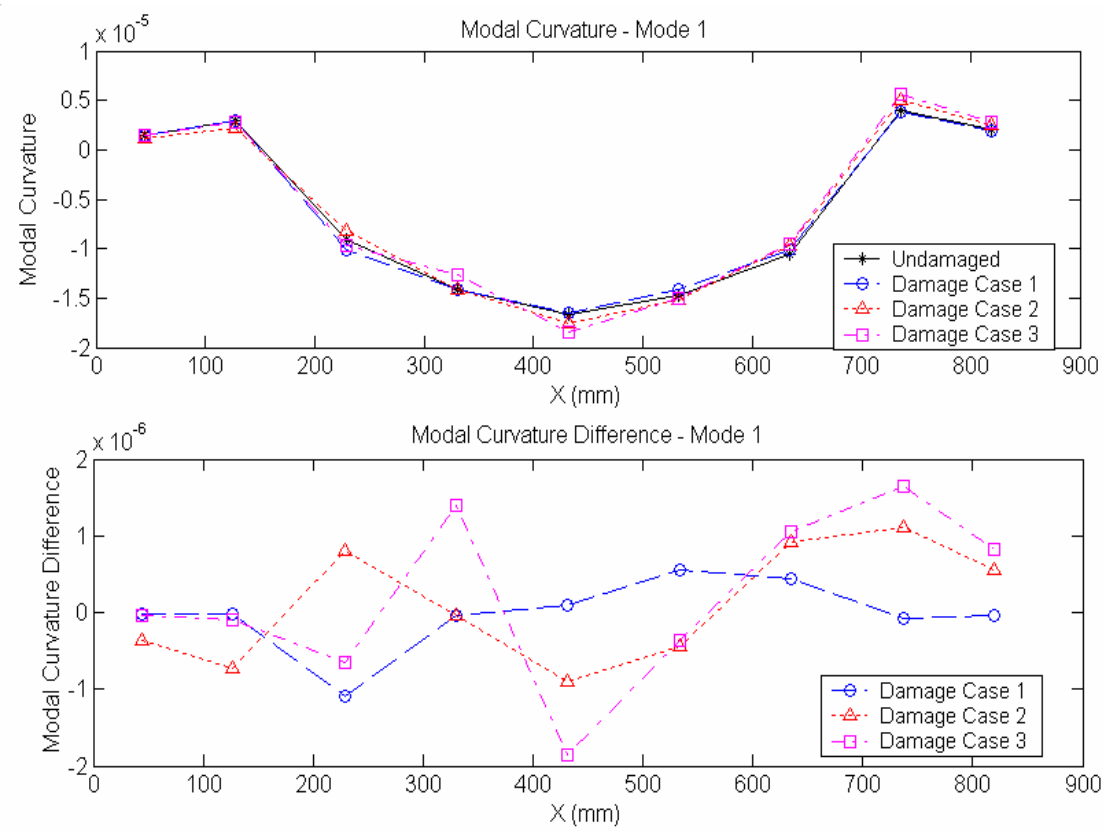

Figure 4-34 Modal Curvature and Modal Curvature Difference

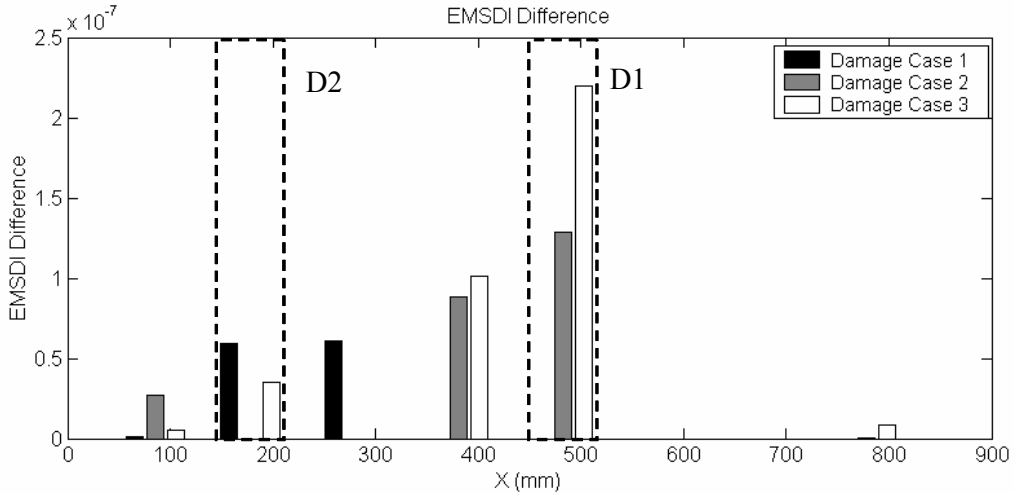

Figure 4-35 EMSDI Difference of Experimental Beam

4.6 Conclusions

On the basis of a careful review of the methods adopted in the existing literature, it is concluded that there are some major weaknesses associated with the computation of modal curvature from experimentally measured displacement mode shapes. First of all, the errors introduced by the use of the central difference approximation used commonly to compute modal curvature increase with the square of the spacing of measurement sites. When only relatively sparsely spaced measurements are available, which is often the case during field experimentation, the errors could hinder the damage identification process. Secondly, when noise is present in the measurement mode shape, computed modal curvatures tend to be polluted by noise propagated through the numerical differentiation process. Thus the damage detection methods based on modal curvature are not be able to take advantage of the increased mode shape spatial resolution offered by advancing sensor technology when noise is present.

In order to address the aforementioned problems, a new damage identification method based on the concept of Element Modal Strain Damage Index is proposed in this Chapter. By employing an element shape function technique, the Element Modal Strain Damage Index can be directly computed from measured modal displacements without the need for numerical differentiation, thus avoiding the problems associated with numerical differentiation procedures. The unmeasured modal rotation is computed from modal displacement using a penalty based method, improving performance even under noisy conditions. It is demonstrated through the use of numerical simulation

examples that the proposed method is able to correctly locate a damage region using only noisy sparse measurement even in cases when the modal curvature method fails.

This chapter, in part, has been submitted for publication in the Journal of Sound and Vibration under the title "Improved Damage Detection Method Based on Element Modal Strain Damage Index Using Sparse Measurement" in 2006. The dissertation author was the principle researcher/author on this paper.

Chapter 5 Finite Element Model Updating for Vibration Based Damage Detection

5.1 Introduction

The Element Modal Strain Damage Index technique presented in Chapter 4 provides a means to detect and locate damage in the structure. However, an absolute magnitude of the damage can not be obtained using the EMSDI technique. On the other hand, in order to evaluate the effect of the damage on the structure and predict the remaining structural capacity, a model able to predict structural behavior is needed.

Structures such as bridges, highways and buildings etc., which show vibrational response, are distributed parameter systems with infinite degrees of freedom. The modeling of such structure in engineering practice, however, is usually accomplished by discretizing the structure into a matrix second order differential equation of the form:

$$[M]\{\ddot{x}(t)\}+[C]\{\dot{x}(t)\}+[K]\{x(t)\}=\{F(t)\} \tag{5.1}$$

The matrices $[M],[C],[K]$ are, respectively, the mass, stiffness and damping matrices. $\{x(t)\}$ and $\{F(t)\}$ are vectors of structural response and external force at each degree-of-freedom. The single and double dots stand for orders of differentiation. The mathematical model of the structure represented by Eq. (5.1) is usually referred to as a Finite Element (FE) model. The process of solving this mathematical model in order to

analyze the physical behavior of the original structure is referred to as (Bathe and Bathe 1996) Finite Element Analysis (FEA).

It is easily understood that an initial finite element model is often a poor representation of the real structural behavior, particularly as related to in-field structural dynamics, because a number of simplifying assumptions have to made in order to reach the mathematical model of Eq. (5.1). Experimentally measured vibration data are generally assumed to be a better reflection of how the structure behaves than the prediction from the initial FE model. The FE model therefore needs to corrected in order to better predict the structural behavior. Such a procedure has been referred to as Test-Analysis Correlation (TAC) or Finite Element Model Updating (FEMU) by different researchers (Friswell and Mottershead 1995; Hemez 1993; Maia and Montalväao e Silva 1997; Teughels 2003). The work in this field has various levels of goals. Some try to modify the model in order to reproduce exactly all the measured modal properties in terms of natural frequencies and mode shapes. Others try to reproduce all the measured frequency response function properties in addition to modal parameters. For civil engineering structures, the first approach is usually adopted because modal parameters, instead of frequency response functions, can be identified from output only data obtained from ambient vibrations (as shown in Chapter 3).

According to their mathematical framework, the most popular FEMU methods belong to one of the two categories: 1) Optimum Matrix Updating (OMU) methods or direct methods and 2) Sensitivity-based Matrix Updating methods (SBMU) or sensitivity-based methods. The former, as defined by Friswell and Mottershead (1995),

computes a closed-form solution for the global stiffness, mass and/or damping matrices using the equation of motion and orthogonality conditions. In general, methods based on stiffness and/or mass matrices are prevalent and little attention is paid in the literature to the adjustment of the damping matrix due the lack of an appropriate model to represent damping for complex structures. The updating problem consists of a finding correction matrices $[\Delta M]$, $[\Delta C]$ and $[\Delta K]$ such that the adjusted model minimizes a given error criterion $J(\Delta M, \Delta C, \Delta K)$. Direct solution, i.e., without iteration, can then be achieved by solving Euler's equations. However, it was observed that the adjusted model could lose some of its fundamental properties such as the symmetry, the positivity or the sparse pattern in the stiffness and mass matrices. Various constraints (Berman and Nagy 1983; Kaouk and Zimmerman 1994) are added using Lagrange multipliers or penalty techniques to ensure that the fundamental properties of the original model are preserved. But the success of such constraints for large complex structures is not guaranteed. In addition, Friswell and Mottershead (1995) state that forcing the model updating procedure to reproduce measured modal data exactly causes the measurement errors to propagate to the updated model. And since the number of measured degrees of freedom (DOFs) is generally much smaller than the number of analytical DOFs, it is necessary to expand the measured mode shape to full analytical model size or reduce the analytical model to match the measured DOFs. The expansion or reduction process introduces an additional source of error.

The Sensitivity-Based Model Updating methods seek the minimization of an objective function $\mathbf{J}(\mathbf{p})$ containing the differences between experimental and analytical

vibration data by adjusting a pre-selected set of physical parameters $\{\mathbf{p}\}$. The optimal solution is obtained in an iterative procedure by using sensitivity-based optimization methods such as the Newton's iteration (Hemez 1993) in the form:

$$\mathbf{J}(\mathbf{p})^{(n+1)} \approx \mathbf{J}(\mathbf{p})^{(n)} + \frac{\partial \mathbf{J}}{\partial \mathbf{p}} \delta \mathbf{p}^{(n+1)} = \mathbf{0} \tag{5.2}$$

where the superscripts represent the number of iterations. The adjusted parameters are given as

$$\{\mathbf{p}\}^{(n+1)} = \{\mathbf{p}\}^{(n)} + \{\boldsymbol{\delta}\mathbf{p}\}^{(n+1)} \tag{5.3}$$

The sensitivity matrix $\left[\frac{\partial \mathbf{J}}{\partial \mathbf{p}}\right]$ in Eq. (5.3) can be calculated by using either finite difference schemes or by finding the exact analytical formulae of $\frac{\partial \mathbf{M}}{\partial \mathbf{p}}$ and $\frac{\partial \mathbf{K}}{\partial \mathbf{p}}$. Parameters $\{\mathbf{p}\}$ may represent structural parameters, boundary conditions, or entries in the mass and stiffness matrices. In the particular case where $\{\mathbf{p}\}$ represents a set of structural parameters, the adjusted mass and stiffness matrices automatically retain the fundamental properties of the original FE model such as positivity, symmetry and sparse patterns because the update is carried out at the elemental level. Also, by employing this method, one may acquire an immediate physical interpretation of the updated results. Thus, the Sensitivity-Based Model Updating method is the choice in the present study.

The procedure of FEMU can also be applied for damage identification. By treating structural parameters subject to the effect of damage as unknown parameters,

the damage identification problem can be considered as a special case of the FEMU. Not only can FEMU indicate and locate damage but it can also be used to predict the magnitude of damage in terms of changes in structural parameters or changes in stiffness and/or mass matrices entries. The use of FEMU as a damage identification method also has the advantage that an updated FE model would be available at the end of the process that can be utilized for the prediction of remaining capacity and for further damage prognosis.

5.1.1 Ill-Conditioning of The Finite Element Model Updating Problem

Finite Element Modal Updating can be considered as a special case of the general System Identification (SI) or Parameter Estimation (PE) problem, where the model of system to be identified is a FE model expressed in terms of mass, damping and stiffness matrices. Experimentally measured data, in this case vibration data, are used to update the estimated parameters in the original model. This process is in essence an inverse problem where the following error function Π_E must be minimized (Yeo et al. 2000):

$$\underset{x}{\text{minimize}} \quad \Pi_E = \frac{1}{2}\left\|\tilde{u}(x) - \bar{u}\right\|^2 \quad \text{subject to } R(x) \le 0 \tag{5.4}$$

where $\tilde{u}(x)$, $\bar{u}$ and $R(x)$ are analytically calculated vibration response, experimentally measured vibration response, and constraint function of system parameters x, respectively, and $\|\bullet\|$ denotes the Euclidean norm of a vector. A structural system may have many potentially damaged areas while the number of measurements is usually

limited due to practical constraints. Thus, in most practical cases for damage identification, FEMU procedures are ill-conditioned because the number of independently measured vibration data sets, e.g., natural frequencies and mode shapes, is smaller than the number of system parameters to be identified. This causes the FEMU procedure to suffer from two types of instabilities: nonuniqueness and discontinuity of solutions. Yeo et al. (2000) explained the cause of the two types of instabilities by considering two vector spaces of the system parameters and measured vibration responses, X and υ, as shown in Figure 5-1. υ^c is a subspace of υ consisting of vibration responses corresponding to the entire domain of system parameters X. The minimization problem in Eq. (5.4) can find at least one solution in X for a measured vibration response vector in υ^c. However, the uniqueness of the solution cannot be guaranteed because different sets of system parameters may yield the same set of responses at discrete locations of a structure. Furthermore, when measured displacements contain random noise, measured vibration response $\bar{u}$ generally do not lie in υ^c, and are not associated with any vector of system parameters in X. In this case, Eq. (5.4) finds a vector of system parameters that yield a compatible vibration response vector u in υ^c closest to the measured vibration response vector. Such a vector u might not be unique and a slight perturbation of $\bar{u}$ (e.g., to $\bar{u}^*$) could yield dramatically different parameter estimations x and x^*, thereby causing discontinuity in the solution.

Similarly, Berman (Berman 2000) also concluded that there can be no unique updated dynamic model of a structure as long as the model has fewer DOFs than the actual structure. Baruch (1997) showed that changes in the mass and stiffness matrices

could not be identified simultaneously using modal data alone. Gola et al. (2001) examined the number of parameters identifiable in sensitivity based updating methods and concluded that the maximum number of parameters identifiable is equal to the total number of measured resonant frequencies plus the number of modes times the number of degrees of freedom measured when frequency and mode shape data are utilized.

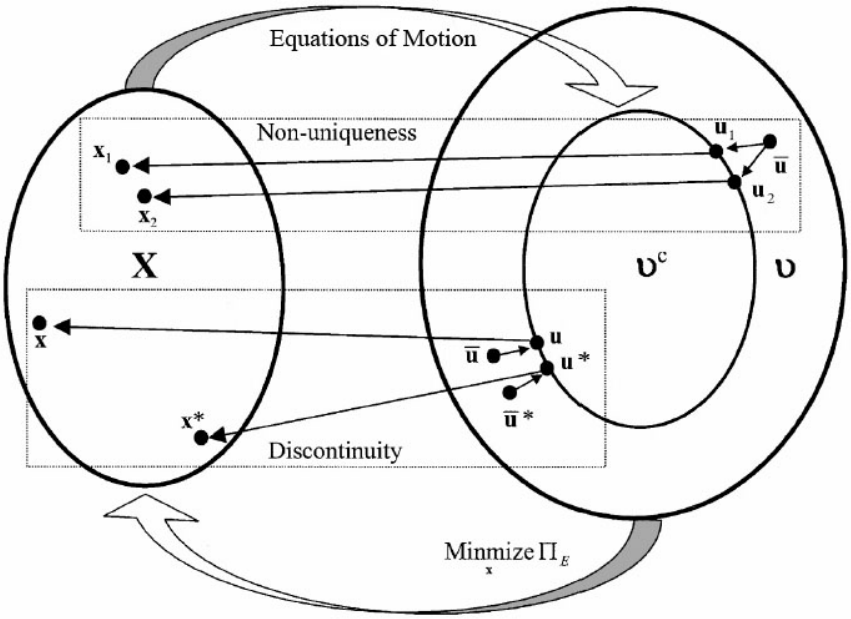

Figure 5-1 Ill-conditioning of the FEMU Procedures (Yeo et al. 2000)

There may be three possible remedies to alleviate the ill-conditioning of the FEMU problem (Yeo et al. 2000): (1) modification of measured data; (2) modification of the space of the system parameters; and (3) modification of the error function defined in Eq. (5.4). Along the direction of the first approach, attempts have been made to increase the number of independent vibration responses measured (Zang 2006) by utilizing high spatial resolution vibration measurement technique such as Laser Vibrometry or by testing the structure in different configurations (Li and Brown 1995).

However, for the majority of practical cases, the number of independent vibration responses measured is still rather limited and is smaller than the number of unknown system parameters.

The second remedy, i.e., modification of the space of system parameters, calls for reduction of the number of parameter to be identified. The most straight forward approach involves grouping similar elements together and using one unknown parameter for all elements in a specific group (Zhang et al. 2000). This approach can effectively reduce the number of unknown parameters in the FEMU process. But the choice of grouping is rather subjective and depends heavily on engineering judgment. More sophisticated grouping schemes can also be adopted, for example, Hjelmsted and Shin (1996) proposed an adaptive parameter grouping approach where the number of system parameters are reduced by grouping similar elements together. The main idea of the scheme is to isolate damaged parts of the finite element model by sequentially subdividing parameter groups, starting from a baseline grouping. At each stage the best candidate for subdivision is determined by finding the group that results in the largest reduction in the error function Π_E when subdivided. The parameters associated with the grouping at each stage are determined by solving the constrained least-squares problem. However, multiple subdivision cases must be evaluated and the process can be quite computationally intensive. Araki and Miyagi (2005) proposed a general formulation of the above parameter grouping, or subset selection, problem. They recast the problem as a combinatorial optimization problem and developed a mixed integer nonlinear least-squares solution procedure. They also pointed out that the method

appears only suitable for identifying a limited number of damaged sites and that the computational time increases exponentially as the problem size becomes larger.

Another approach that has been proposed for the reduction of unknown parameters involves the use of a damage function (Abdel Wahab et al. 1999; Maeck et al. 2000; Teughels et al. 2002). In the first two papers, a damage function characterized by three parameters is proposed to describe the damage pattern of reinforced concrete beams. Instead of treating the bending stiffness of each element in the FE model as independent parameters, the reduction of bending stiffness of each element in the FE model is uniquely determined by the damage function. Thus, the number of effective unknown parameters is reduced from thirty, which is the number of elements, to three. The selection of the particular damage function was justified by the visually observed crack pattern of the reinforced concrete beams during the experiment. However, the extension of the approach to general types of damage is questionable. In the third paper (Teughels et al. 2002), the idea is further generalized to the expression of a damage function as the sum of a set of shape functions. Shape functions are constructed from simple polynomial functions which usually span several finite elements. A few parameters determine the characteristics of the shape function and hence its contribution to the damage function over the spatial domain covered. This approach provides more flexibility in the damage function but the selection of proper shape functions still depends on engineering judgment and prior knowledge of the damage.

The third remedy, often referred to as the regularization technique, has been applied to various inverse problems (Lee et al. 2000; Schnur and Zabaras 1990; Yeo et

al. 2000). In the regularization technique, the error function in Eq. (5.4) is modified to provide additional constraints to the minimization problem based on prior information. The assumption is made that unknown parameters are close to known nominal values. For example, the solution space X is reduced directly by setting the upper bounds near the baseline properties. This assumption is often adequate in updating parameters of structures without any damage. However, it is questionable whether the assumption would still be valid in the context of a damage detection.

Based on the discussion above, it suffices to conclude that the ill-conditioning of the FEMU problem is the major difficulty hindering its deployment for the purpose of Vibration-Based Damage Identification. However, when considering the FEMU problem within the context of VBDI framework, it becomes apparent that the ill-conditioning of the SI problem can be greatly alleviated if use can be made of the information about the damage location. Such information can be obtained from damage localization procedures such as the EMSDI technique described in Chapter 4. If damage can be located within a small segment of the structure, the unknown parameter to be identified can be greatly reduced without making subjective assumptions about the damage pattern. In this chapter, the theoretical procedure based on this approach is presented. The general flow of the procedure is explained first. The formulation of the objective function is described next. The difference between analytical and experimentally measured modal parameters is chosen to compute the objective function. The selection of structural parameters and the solution procedure of the minimization problem are then discussed. Finally, a numerical example of FEMU using the proposed procedure is presented.

5.2 Procedure of Finite Element Model Updating

The general procedure of the proposed Finite Element Model Updating method is shown in Figure 5-2. In the first step, appropriate parameters are selected for updating. For the undamaged structure, selection of parameters is based on the prior knowledge of the structure in its pristine condition. For a damaged structure, damage localization is performed first in order to locate the potential damage regions. Information provided by the damage localization process is then used to facilitate the parameter selection process. Initial parameter values are set based on prior knowledge about the undamaged, or baseline, structure. Next, FE analysis is performed to obtain the analytical vibration response of the model in the form of modal parameters. The difference between the analytical and experimental modal data is used to formulate the objective function of the minimization problem. Experimental modal parameters can be identified for operational civil engineering structures using the procedures described in Chapter 3. Numerical procedures are then used to solve the minimization problem resulting in updated parameter values. These updated parameter values are then substituted into the FE model and steps 2 to 4 of the process are repeated iteratively until convergence is reached. The final identified parameters from the undamaged and damaged structure are then compared to yield information about damage location and severity.

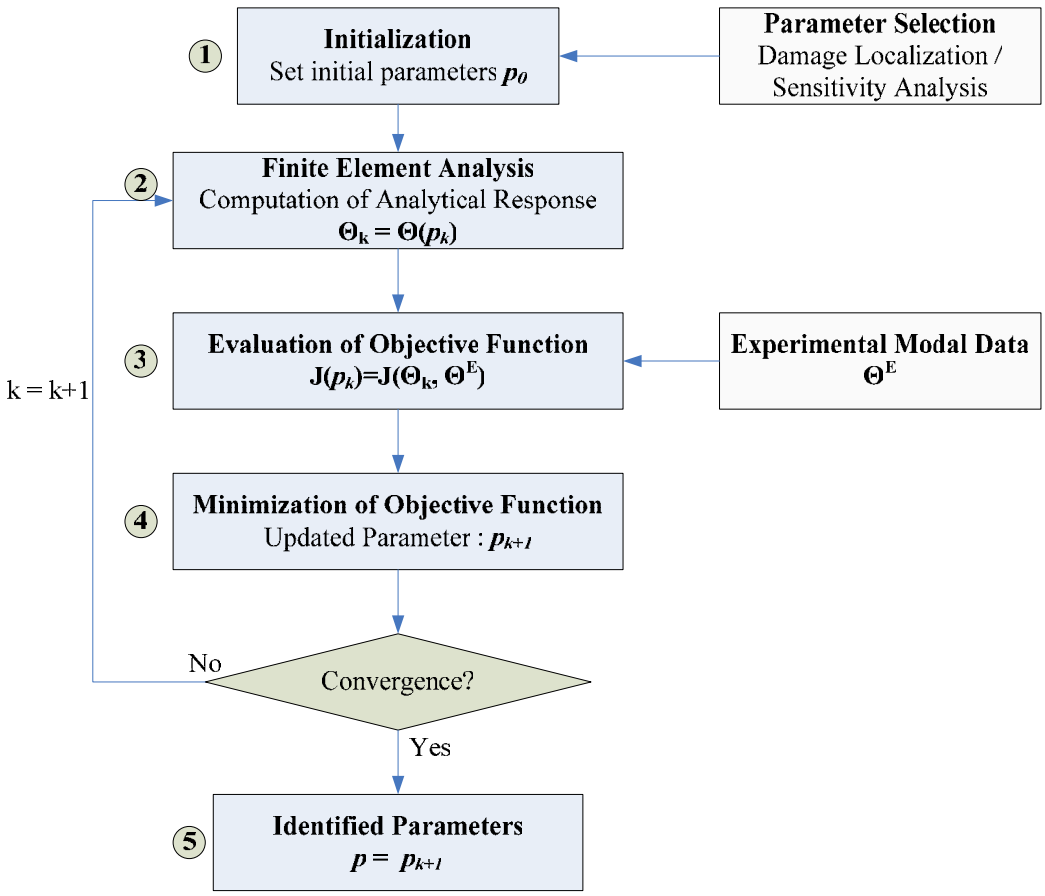

Figure 5-2 Flowchart of the FEMU Procedure

5.2.1 Correlation between Analytical and Experimental Data

In order to measure how well the FE model predicts the structure behavior, the correlation between analytical and experimental vibration response must be defined. For civil engineering structures, the correlation is usually defined by the difference between the analytical and experimental modal parameters (Friswell and Mottershead 1995; Maia and Montalväao e Silva 1997).

The objective function in Eq.(5.2) is defined as a sum of squared differences between analytical and experimental modal parameters:

$$\mathrm{J}(\mathbf{p}) = \frac{1}{2}\sum_{j=1}^{n}\left|\Theta_j^A(\mathbf{p}) - \Theta_j^E\right|^2 \tag{5.5}$$

where $\Theta_j^A(\mathbf{p})$ represents an analytical modal parameter obtained from FE analysis, and Θ_j^E is the experimental counterpart of $\Theta_j^A(\mathbf{p})$. It should be noted that $\Theta_j^A(\mathbf{p})$ is in general a nonlinear function of the unknown parameters $\mathbf{p}$. Eq. (5.5) can also be written in terms of the residual vector $\mathbf{R}$

$$\mathrm{J}(\mathbf{p}) = \frac{1}{2}\left\|\mathbf{R}(\mathbf{p})\right\|^2 \tag{5.6}$$

where

$$\mathbf{R}(\mathbf{p}) = \begin{Bmatrix} r_1(\mathbf{p}) \\ r_2(\mathbf{p}) \\ \vdots \\ r_n(\mathbf{p}) \end{Bmatrix} = \begin{Bmatrix} \Theta_1^A(\mathbf{p}) - \Theta_1^E \\ \Theta_2^A(\mathbf{p}) - \Theta_2^E \\ \vdots \\ \Theta_n^A(\mathbf{p}) - \Theta_n^E \end{Bmatrix} \tag{5.7}$$

and $\|\bullet\|$ represents the Euclidean norm.

The first part of the residual vector contains the differences between the analytical and experimental natural frequencies

$$r_\omega(\mathbf{p}) = \frac{\omega_k^A(\mathbf{p}) - \omega_k^E}{\omega_k^E} \qquad k = 1\cdots N_\omega \tag{5.8}$$

where $\omega_k^A(\mathbf{p})$ is the k^{th} analytical natural frequency, ω_k^E is the corresponding experimental natural frequency, and N_ω is the total number of natural frequencies compared. The differences are normalized with respect to the experimental natural

frequencies in order to give similar weight for modes with low natural frequencies and those with high natural frequency values.

Natural frequencies provide global information of the structure. But they provide little information about the location of the damage. In order to obtain spatial information about the damage, the second part of the residual vector contains the differences between the analytical and experimental mode shapes:

$$r_{\phi}(\mathbf{p}) = \phi_{lj}^{A}(\mathbf{p}) - \phi_{lj}^{E} \qquad l = 1 \cdots N_{\phi}, \quad j = 1 \cdots N_{d} \tag{5.9}$$

where $\phi_{lj}^{A}(\mathbf{p})$ and ϕ_{lj}^{E} are analytical and experimental mode shapes of l^{th} mode at DOF j, respectively. N_{ϕ} represents the number of modes used in the correlation process and N_d represents the number of degrees of freedom in analytical and experimental mode shape data. The mode shapes obtained from use of the operational modal analysis procedure as described in Chapter 3 cannot be absolutely scaled. Therefore, the analytical and experimental mode shapes are both normalized with respect to a common reference degree of freedom. The mode shape amplitude, or modal displacement, at the reference DOF is thus always equal to 1 in both analytical and experimental data.

The vibration data (e.g., natural frequencies and mode shapes) measured experimentally from a structure are often incompatible with that obtained from its FE model. Firstly, because of the limited bandwidth of the data acquisition system and the increased modal density at higher frequencies, modal parameter extraction is often problematic beyond moderately low frequencies. This leads to the incompleteness of the measured data in the frequency domain. Secondly, the measurement can usually only be

made at a subset of the degrees of freedom of the finite element model and hence the data is also incomplete in the spatial domain. It is therefore appropriate to limit the goal of FEMU to modifying the parameters of the model so that the predicted response best matches the experimental response at the measured degrees of freedom within the measured frequency range. The total number of terms in the residual vector **R** is thus equal to $N_R = N_\omega + N_\phi \times N_d$.

The Modal Assurance Criterion (MAC) is used ensure the correct pairing between analytical and experimental modes. MAC is defined as:

$$MAC\left(\boldsymbol{\Phi}_i, \boldsymbol{\Phi}_j\right) = \frac{\left|\boldsymbol{\Phi}_i^T \boldsymbol{\Phi}_j\right|^2}{\left(\boldsymbol{\Phi}_i^T \boldsymbol{\Phi}_i\right)\left(\boldsymbol{\Phi}_j^T \boldsymbol{\Phi}_j\right)} \tag{5.10}$$

in which $\boldsymbol{\Phi}_i$ and $\boldsymbol{\Phi}_j$ are analytical and experimental mode shapes, respectively. The value of MAC always lies between 0 and 1. A MAC value close to 1 indicates a good correlation while a value of 0 indicates a bad correlation. The optimum pairing between analytical and experimental modes is found by searching for the highest MAC value between each pair.

Weighting factors can be applied to the terms in the residual vector **R** to account for the importance of different residues and their measurement accuracy. In that case, the objective function of Eq. (5.6) can be modified as

$$\mathrm{J}\left(\mathbf{p}\right) = \frac{1}{2}\mathbf{R}^T\left(\mathbf{p}\right)\mathbf{W}\mathbf{R}\left(\mathbf{p}\right) = \frac{1}{2}\left\|\mathbf{W}^{\frac{1}{2}}\mathbf{R}\left(\mathbf{p}\right)\right\|^2 \tag{5.11}$$

in which **W** is the weighting matrix. The appropriate choice of **W** is largely an issue of engineering judgment. However, a few general rules apply when considering the formulation of weighting matrix. First, the experimental natural frequencies are usually measured with high accuracy. The experimental mode shapes, on the other hand, tend to be much more sensitive to measurement noise. Higher weighting should thus be given to the frequency residues. Second, natural frequencies and mode shapes of lower modes are usually measured with higher accuracy compared with higher modes, and thus higher weights given to lower mode residues are appropriate. It is also possible that some degrees of freedom within a given mode shape contain more uncertainty compared with other degrees of freedom. In that case, a lesser weight should be given to those DOFs with high uncertainty.

Alternatively, the weighting matrix can also be defined based on the statistical properties of the measurements. For example, Friswell and Mottershead (Friswell and Mottershead 1995) proposed to use the diagonal weighting matrix whose elements are given by the reciprocals of the variance of the corresponding measurements:

$$W = \begin{bmatrix} \frac{1}{\sigma_1^2} & & & \\ & \frac{1}{\sigma_2^2} & & \\ & & \ddots & \\ & & & \frac{1}{\sigma_n^2} \end{bmatrix} \qquad n = N_\omega + N_\phi \times N_d \tag{5.12}$$

in which $\sigma_1^2, \sigma_2^2, \cdots, \sigma_n^2$ are the variances of the measured quantity in residue $\mathbf{R}$.

5.2.2 Structural Parameters in the Model Updating Process

The principle causes of the discrepancies between the FE model and the actual structure can be summarized as (Maia and Montalväao e Silva 1997): 1) approximation of boundary conditions; 2) discretization of distributed parameter systems; 3) estimation of the physical properties of structure; 4) approximation of damping representation; and 5) inadequate modeling of joints. The second cause, i.e., discretization error, is inherent to FE analysis and can only be improved through proper modeling of the structure. Similarly, the fourth cause, approximation of damping representation, will not be included in the current discussion due to due the lack of a proper model to model damping for complex structures. The remaining three causes, i.e., approximation of boundary conditions, estimation of physical properties and the modeling of joints, can all be treated within the framework of finite element model updating. By treating the uncertainty in the modeling of material or geometrical properties, boundary conditions and joints as unknown structural parameters, the goal of the FEMU procedure is to yield updated parameter values that allow better prediction of the actual structural behavior using the numerical model.

Not all parameters in the initial set of candidate parameters should be used for the process of model updating. Figure 5-3 presents the flowchart of the parameter selection process. As discussed in Section 5.1.1, the number of potential structural parameters to be updated is typically far larger than the number of independent measurements. The resulting ill-conditioning of the identification problem must be addressed in order for the updating process to yield any physically meaningful results.

The solution to this problem requires the utilization of prior information obtained during the damage localization process to reduce the number of unknown structural parameters, as presented in Section 5.1.1. On the other hand, parameters that influence the modal parameters significantly should be selected for updating. Inclusion of insensitive parameters is likely to lead to poor parameter estimates. The process of identifying proper parameters for model updating is also referred to as subset selection (Friswell and Mottershead 1995) and the resulting set of structural parameters, the number of which is in general significantly smaller than the number of candidate structural parameters, forms the parameters to be identified of the updating process.

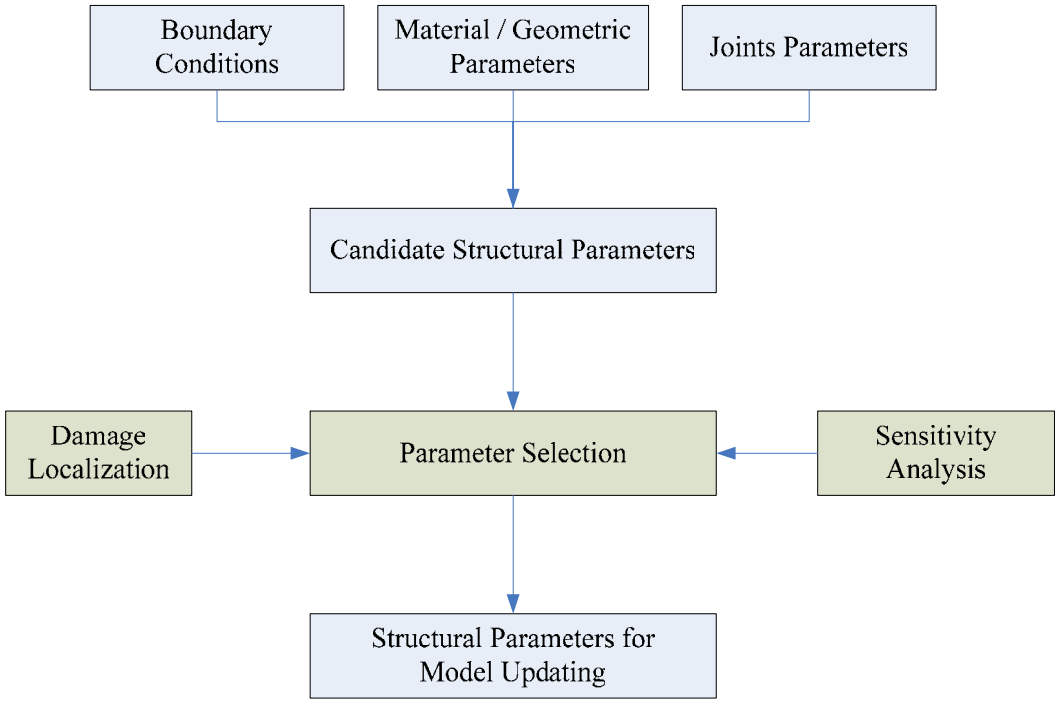

Figure 5-3 Parameter Selection Process

The various physical parameters in the model updating process can have drastically different orders of magnitude. A dimensionless correction factor is thus defined to represent the change of each parameter with respect to its reference value:

$$\alpha_k = -\frac{p_k - p_k^{ref}}{p_k^{ref}} \qquad k = 1 \cdots N_p \tag{5.13}$$

and the updated parameter p_k is expressed by

$$p_k = p_k^{ref}\left(1 - \alpha_k\right) \qquad k = 1 \cdots N_p \tag{5.14}$$

where p_k^{ref} is the reference value of k^{th} parameter, and N_p is the number of parameters to be updated. The correction factor α_k in Eq. (5.13) is a positive number between 0 and 1 when the updated parameter is smaller than its reference value. p_k^{ref} and p_k are physical parameter that are, in general, positive.

In the case where the element mass and stiffness matrix depend linearly on the structural parameter, the updated mass and stiffness matrices may be written as

$$M = M_0 + \sum_{j=1}^{N_E}\left(1 - \alpha_j\right)M_j^E \tag{5.15}$$

$$K = K_0 + \sum_{j=1}^{N_E}\left(1 - \alpha_j\right)K_j^E \tag{5.16}$$

where M and K are updated mass and stiffness matrices. M_0 and K_0 are portion of the mass and stiffness that remain unchanged before and after the updating. M_j^E and

K_j^E are the element mass and stiffness matrix for element j. N_E is the number of elements with updated parameters.

5.2.3 Solution Procedure

5.2.3.1 Solution of the Least Squares Problem

The solution of the FEMU problem can be stated as a nonlinear least squares problem in which the objective function of Eq. (5.6) is to be minimized:

$$\underset{\mathbf{p}}{\text{minimize}} \quad \mathrm{J}(\mathbf{p}) = \frac{1}{2}\left\|\mathbf{R}(\mathbf{p})\right\|^2 \tag{5.17}$$

A linear approximation to Eq. (5.17) leads to the linear least square problem

$$\underset{\mathbf{p}}{\text{minimize}} \quad \mathrm{J}_l(\mathbf{p}) = \frac{1}{2}\left\|\mathbf{S}_k \delta\mathbf{p} + \mathbf{R}_k\right\|^2 \tag{5.18}$$

at each iteration. In Eq. (5.18), $\mathbf{S}_k$ represents the sensitivity matrix (or Jacobian) at iteration k defined as the $N_R \times N_P$ matrix of the first-order partial derivatives of the residual function **R** with respect to the parameter **p:**

$$S_{ji} = \frac{\partial R_j(\mathbf{p})}{\partial p_i} \tag{5.19}$$

$\mathbf{R}_k$ is the residual function vector at iteration k, and $\delta\mathbf{p}$ is the change of parameters at k^{th} iteration. The solution of Eq. (5.18) is obtained by taking the derivatives of the objective function in Eq. (5.18) with respect to $\delta\mathbf{p}$ and setting the result equal to zero (Friswell and Mottershead 1995; Teughels 2003), which gives the equation:

$$\delta \mathbf{p}_k = -\left(\mathbf{S}_k^T \mathbf{S}_k\right)^{-1} \mathbf{S}_k^T \mathbf{R}_k \tag{5.20}$$

provided $\mathbf{S}_k$ has full column rank. Alternatively, the solution can also be found via the solution of normal equations of the linear least square problem (5.18)

$$\mathbf{S}_k^T \mathbf{S}_k \delta \mathbf{p}_k = -\mathbf{S}_k^T \mathbf{R}_k \tag{5.21}$$

using algorithms such as Cholesky factorization, QR factorization or SVD-based algorithms (Golub and Van Loan 1996).

In the case where a weighting matrix is applied to the residual function, as in Eq. (5.11), the solution to the least square problem can be written as

$$\delta \mathbf{p}_k = -\left(\mathbf{S}_k^T \mathbf{W}_R \mathbf{S}_k\right)^{-1} \mathbf{S}_k^T \mathbf{W}_R \mathbf{R}_k \tag{5.22}$$

And the updated parameters are given as

$$\mathbf{p}_{k+1} = \mathbf{p}_k - \left(\mathbf{S}_k^T \mathbf{W}_R \mathbf{S}_k\right)^{-1} \mathbf{S}_k^T \mathbf{W}_R \mathbf{R}_k \tag{5.23}$$

The nonlinear least squares problem (5.17) can also be solved using the iterative Gauss-Newton method (Lange 2004). Each iteration of the Gauss-Newton method consists of two major steps: In the first step, a search direction, $\mathbf{d}_k$, is obtained that is the solution of the linear least-squares problem

$$\underset{\mathbf{p}}{\text{minimize}} \quad \mathrm{J}_D(\mathbf{p}) = \frac{1}{2}\left\|\mathbf{S}_k d_k + \mathbf{R}_k\right\|^2 \tag{5.24}$$

It should be noted that Eq. (5.24) has the same form as Eq. (5.18) and the solution is given by solving the system of equations:

$$\mathbf{S}_k^T \mathbf{S}_k \mathbf{d}_k = -\mathbf{S}_k^T \mathbf{R}_k \tag{5.25}$$

Direction $\mathbf{d}_k$ is also known as the Newton direction. Once the search direction is determined, a line search is performed along the search direction $\mathbf{d}_k$ in an attempt to decrease the objective function by repeatedly minimizing polynomial interpolation models of the objective function. The parameter values of the next iteration are found by:

$$\mathbf{p}_{k+1} = \mathbf{p}_k + \alpha \cdot \mathbf{d}_k \tag{5.26}$$

where α is the step size determined in the line search process.

5.2.3.2 Ill-Conditioning and Regularization Techniques

For the set of equations in (5.21) to have a unique solution, the equation need to be overdetermined ($N_R > N_P$) and $\mathbf{S}_k$ has full rank, or alternatively, the matrix $\mathbf{S}_k^T \mathbf{S}_k$ is nonsingular:

$$\det\left(S_k^T S_k\right) \neq 0 \tag{5.27}$$

The determinant in Eq. (5.27) equals zero when some insensitive parameters are included in the updating process. At the same time, if some of the columns in $\mathbf{S}_k$ are linearly dependent, the determinant in Eq. (5.27) also equals zero and no unique solution can be obtained. If some columns are close to being linearly dependent, which happens when two parameters have very similar effects on the dynamics of structure, a unique solution can be obtained but is highly susceptible to noise in the measurement. Thus, in order to avoid the ill-conditioning of the updating process, it is desirable that

small changes in parameters cause large changes in the residues, i.e., the residues are highly sensitive to structural parameters. Insensitive parameters should not be included in the identification process. Parameters that have similar effects on structural dynamics should be grouped together and treated as a single independent parameter.

When Eq. (5.21) is ill-conditioned, the resulting parameter changes $\delta\mathbf{p}_k$ tend to show large variations. Regularization techniques can be applied in this case by requiring the parameter changes to be kept small. The objective function in Eq. (5.18) can be modified to include a weighted norm of the parameter changes:

$$\underset{\mathbf{p}}{\text{minimize}} \quad \mathrm{J}_\lambda(\mathbf{p}) = \frac{1}{2}\left\|\mathbf{W}_R^{1/2}\mathbf{S}_k\delta\mathbf{p} + \mathbf{W}_R^{1/2}\mathbf{R}_k\right\|^2 + \lambda\left\|\mathbf{W}_p^{1/2}\delta\mathbf{p}\right\| \tag{5.28}$$

in which λ is known as the regularization parameter, $\mathbf{W}_p$ is a diagonal weighting matrix of the parameters, and $\mathbf{W}_R$ is the weighting matrix of residues. The regularization technique in the form of Eq. (5.28) was first introduced to solve the problem of ill-conditioned system of equations and is usually referred to as Tikhonov regularization (Teughels 2003). The difficulty in the application of the regularization technique is the selection of a regularization parameter such that Eq. (5.28) is suitably well-conditioned while the solution $\delta\mathbf{p}_k$ does not depart significantly from the original solution of the problem. The solution of Eq. (5.28) can be found using similar procedures as in Eq. (5.22):

$$\delta\mathbf{p}_k = -\left(\mathbf{S}_k^T\mathbf{W}_R\mathbf{S}_k + \mathbf{W}_p\right)^{-1}\mathbf{S}_k^T\mathbf{W}_R\mathbf{R}_k \tag{5.29}$$

Further regularization of the problem can be achieved by imposing inequality constraints for the structural parameters as follows:

$$\mathbf{P}_L \le \mathbf{p} \le \mathbf{P}_U \tag{5.30}$$

where $\mathbf{P}_L$ and $\mathbf{P}_U$ are vectors of lower and upper bounds for the structural parameters.

The method outlined in 5.2.3.1 is effective in seeking minima that are reasonably well defined, provided the initial estimates of parameters are in the general region of the function minimum. However, the possibility that multiple local minima exist can not be completely excluded. Global optimization algorithms are needed to deal with such situations. Several efficient algorithms have already been developed for this purpose, such as the Genetic Algorithm (Au et al. 2003), Simulated Annealing (Janzra and Nielsen 2006), and multiple coupled local minimization (Teughels et al. 2003). The detailed discussion of the utilization of global optimization, however, is not within the scope of this dissertation.

5.2.3.3 Constrained Minimization Problem

Alternatively, Eq. (5.17) can also be treated as a general constrained minimization problem. The general form of the constrained minimization problem can expressed as minimizing a nonlinear function $J(\mathbf{p})$ subject to nonlinear constraints $g_i(\mathbf{p})$:

$$\begin{aligned} &\underset{\mathbf{p}}{\text{minimize}} \quad J(\mathbf{p}_k) \\ &\text{subject to} \quad \begin{cases} g_i(\mathbf{p}) = 0 & i = 1, \cdots, m_e \\ g_i(\mathbf{p}) = 0 & i = m_e + 1, \cdots, m \end{cases} \end{aligned} \tag{5.31}$$

in which m_e is the number of equality constraints and *m* the number of total constraints, including equality and inequality constraints. A particularly efficient algorithm to solve such problems is the Sequential Quadratic Programming (SQP) method (Biggs 1975). The principle idea of the SQP method is the formulation of a QP subproblem based on a quadratic approximation of the Lagrangian function:

$$L(\mathbf{p}, \lambda) = J(\mathbf{p}) + \sum_{i=1}^{m} \lambda_i \cdot g_i(\mathbf{p}) \tag{5.32}$$

in which λ_i is the Lagrange multiplier and $g_i(\mathbf{p})$ is the corresponding constraint. The QP subproblem is stated as

$$\begin{aligned} \underset{d_k}{\text{minimize}} \quad & \frac{1}{2}\mathbf{d}_k^T H_k \mathbf{d}_k + \nabla J(\mathbf{p}_k)^T \mathbf{d}_k \\ \text{subject to} \quad & \nabla \mathrm{g}_i(\mathbf{p}_k)^T \mathbf{d}_k + \mathrm{g}_i(\mathbf{p}_k) = 0 \qquad i = 1, \cdots, m_e \\ & \nabla \mathrm{g}_i(\mathbf{p}_k)^T \mathbf{d}_k + \mathrm{g}_i(\mathbf{p}_k) \le 0 \qquad i = m_e + 1, \cdots, m \end{aligned} \tag{5.33}$$

where H_k represents the Hessian of objective function:

$$H_k = \nabla^2 J(\mathbf{p}_k) = \left[\frac{\partial^2 J}{\partial p_i \partial p_j} \right]_{\mathbf{p}_k} \tag{5.34}$$

The solution of Eq. (5.33) gives search direction d_k which is incorporated in the line search algorithm to obtain the parameter value of the next iteration

$$\mathbf{p}_{k+1} = \mathbf{p}_k + \alpha \cdot \mathbf{d}_k \tag{5.35}$$

5.3 Numerical Example

In order to demonstrate the effectiveness of the proposed FEMU method for damage detection, the two span continuous aluminum beam model discussed in Section 4.3 is used as an example. The undamaged and damaged beam models in Section 4.3 are treated as target structures to be identified. Numerically generated modal parameters of the target structures are used in lieu of experimentally measured values (i.e., as Θ_j^E in Eq. (5.5)). The FEMU problem is formulated in the following two steps: (1) Identification of the baseline, i.e., undamaged structure properties, and (2) Identification of damage location and severity in two damage cases.

5.3.1 Calibration of the Baseline Model

As in a typical situation in the FEMU process, the geometry of the baseline target structure is assumed to be measured accurately, while the uncertainty mainly lies in the estimation of material properties. The beam model used to identify baseline structural properties, i.e., the updating model, consists of 544 beam elements each of 3.175mm in length. The beam element has a cross-sectional area of $A = 4.84 \times 10^{-4}\ m^2$ and moment of inertia in z direction $I_{zz} = 2.34 \times 10^{-7}\ m^4$, same as the target structure. The material properties of the updating model are assumed to be: Young's modulus E = 4.875×10^{10} Pa, Poisson's ratio $\nu = 0.35$, and mass density $\rho = 2700\ kg/m^3$. Accurate estimation of Young's modulus is usually considered to be difficult to achieve in the modeling of structures. At the same time, it is assumed that the Young's modulus is

uniform in all elements in the updating model. Thus Young's modulus is treated as the only unknown structural parameter in this problem.

The Subspace algorithm in the finite element package ANSYS (2004) is used to extract modal parameters of the first six modes from the updating model. Only natural frequencies of each mode are used in the FEMU process to form the residues. The solution procedure discussed in Section 5.2.3 is implemented in MATLAB (MATLAB 2004) and ANSYS (ANSYS 2004) and the flowchart is shown in Figure 5-2. The natural frequencies of the initial updating model are listed in Table 5-1 together with the natural frequencies of the target structure and the results from the updated model. A perfect match is achieved between the target structure and the updated model in all six natural frequencies. Figure 5-4 presents the variations of natural frequencies with respect to updating iterations. The identified Young's modulus equals to 6.961×10^{10} Pa and also closely matches the true value of the target structure.

Table 5-1 Natural Frequencies of Target Structure, Initial Model and Updated Model

	Natural Frequencies (Hz)		
Mode	Target Structure	Initial Model	Updated Model
1	19.629	16.423	19.629
2	30.665	25.656	30.665
3	78.512	65.689	78.512
4	99.366	83.137	99.366
5	176.63	147.78	176.63
6	207.29	173.44	207.29

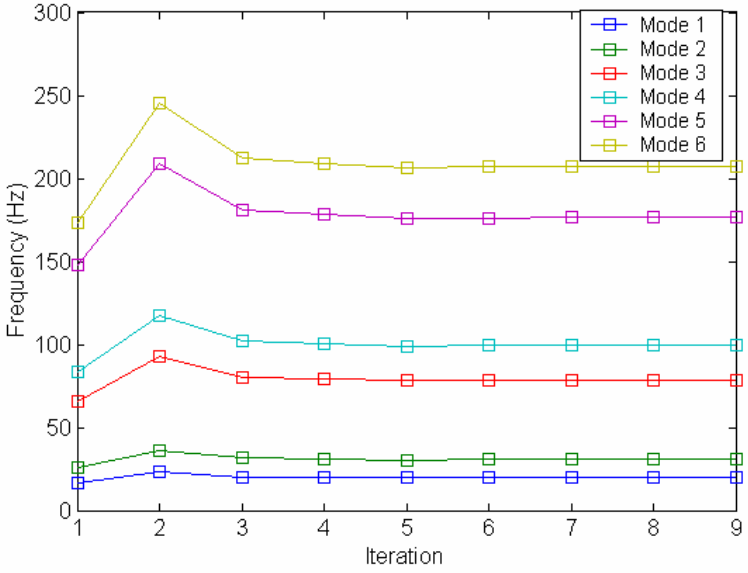

Figure 5-4 Variation of Natural Frequencies during Model Updating Process

5.3.2 Finite Element Model Updating for Damage Identification

5.3.2.1 Parameter Selection

Once the baseline structural parameter is established, FEMU is used to identify the severity of the damage in the two damage cases, D1 and D2. The two damage cases are described in Section 4.3.3 and also depicted in Figure 4-9. The first damage case involves a 6% reduction in bending stiffness on a 0.102 m section of the left span of the beam and the second damage case involves a 49% reduction in bending stiffness on a 0.152 m section of the right span of the beam. Finite element models of the two damage cases are treated as the damaged target structure. The identified baseline model from the previous step is used as the initial model to be updated. The initial model consists of elements of uniform geometric and material properties. The purpose of the FEMU process is to identify, by comparing modal data from the updating model and the target

structure, the variations in geometric and material properties that minimize the difference between the updating model and the damaged target structure.

The parameter selection phase of the FEMU process is aided by the damage localization results presented in Section 4.3.3. It is assumed that the damage is caused by reduction of Young's modulus in some of the elements, but the location and the magnitude of this reduction is unknown prior to model updating. If the Young's modulus of all the elements is allowed to vary independently, this will lead to 544 parameters. From the discussion of available residues in the next paragraph, it will become clear that such a number of independent parameters will lead to an ill-conditioned problem with no unique solutions. Thus, in order to reduce the number of independent parameters, the adjacent elements in the model are grouped into element groups, each comprising 8 elements (Figure 5-5). Young's modulus are considered to be uniform within each element group while can vary between groups. The number of independent structural parameters is thus reduced to 68. The length of such an element group is approximately 0.0254 m which is considered to provide a sufficient resolution in terms of locating and quantifying damage. Based on the damage localization results from Section 4.3.3, the possible damage regions are located between group 17~28 for damage case 1, and between group 48~55 for damage case 2, as shown in Figure 5-6. If only the Young's modulus of these groups are taken as independent structural parameters, the number of parameters to be updated can be further reduced to 12 and 8, for damage case 1 and 2, respectively.

Finally, the unknown structural parameters to be identified in the updating process are defined as

$$E_j = E_j^{ref}\left(1-\alpha_j\right) \tag{5.36}$$

in which E_j is the updated Young's modulus of element group j, E_j^{ref} is the baseline Young's modulus of element group j, and α_j is the correction factor for the Young's modulus to be identified.

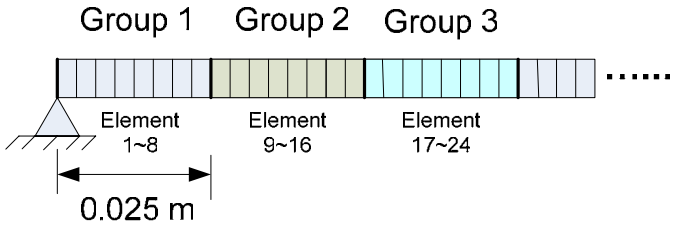

Figure 5-5 Grouping of Elements

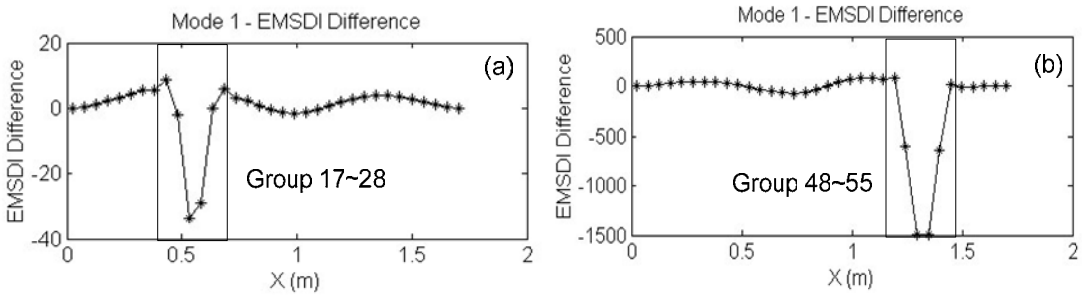

Figure 5-6 Parameter Selection via Damage Localization: (a) Damage Case 1 (b) Damage Case 2

5.3.2.2 Modal Data Correlation and Formulation of the Objective Function

Residues are formed from differences in frequencies and mode shapes between the target structure and the updating model. The first six modes are selected to calculate the difference. In most experimental cases, not all degrees of freedom can be measured.

For the current case, mode shapes are assumed to be only measured at 35 evenly spaced measurement sites in the vertical direction on the beam, the location of which is described in Section 4.3.

There are 6 frequency residues, which can be calculated using Eq. (5.8), and 210 mode shape residues, calculated using Eq. (5.9). The total number of residues is 216. Mode shapes are first normalized to a common degree of freedom before residues are calculated. In order to account for the fact that frequencies are usually measured with higher accuracy compared to mode shapes, a weighting factor of 10 is applied on the frequency residues. This results in a weighting matrix $\mathbf{W}_R$ with its first 6 elements along the diagonal equal to 10 and the rest of the diagonal elements equal to 1. Random noise is added to the residual vector in order to simulate measurement noise. For damage case 1, the magnitude of the random noise is 0.1% for frequency residues and 0.3% for mode shape residues, relative to the average magnitudes of the corresponding residues. For damage case 2, the magnitude of the random noise is 0.1% for frequency residues and 1% for mode shape residues. The initial residue values of both damage cases are plotted Figure 5-7.

MAC values are calculated in order to pair the modal data from updating model with those from the damaged target structure. The constrained minimization problem is solved using the SQP method described in Section 5.2.3.3.

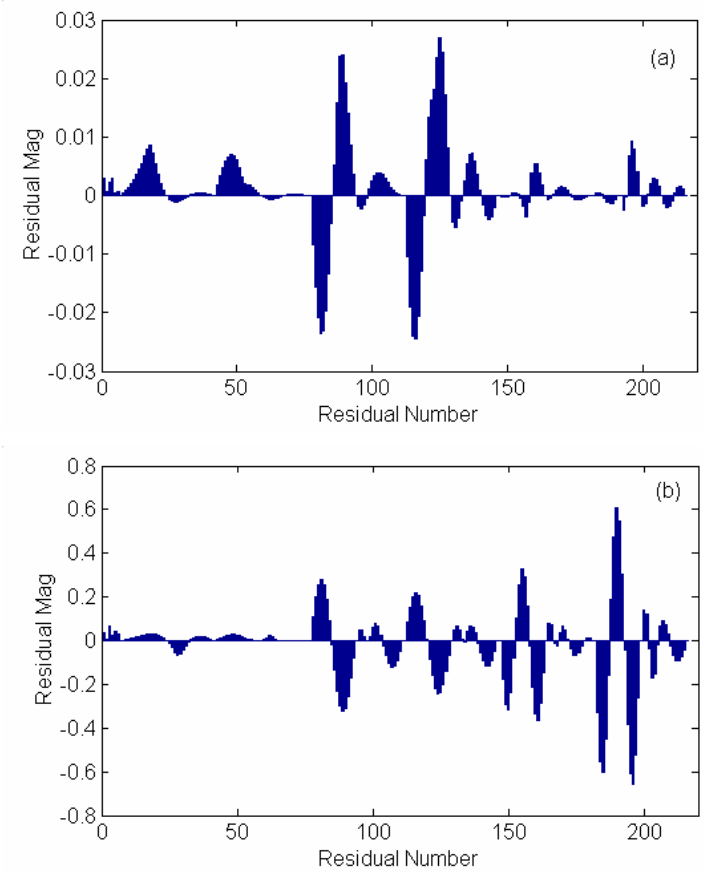

Figure 5-7 Initial Residues: (a) Damage Case 1 (b) Damage Case 2

5.3.2.3 Model Updating Results

Table 5-2 lists the initial and updated eigenfrequencies of the updating model compared with that of the target structures for both damage case 1 and damage case 2. The relative difference between the eigenfrequencies is plotted in Figure 5-8 and Figure 5-9. MAC values between the mode shapes of the initial model and that of the target structure and between the mode shapes of the updated model and that of the target structure are listed in Table 5-3. MAC values are calculated using Eq. (5.10). It can be seen that in both cases the correlation of the updating model with target structure are greatly improved by the FEMU process. The natural frequencies of the updated model

match very well with that of the target structure. The differences in terms of the natural frequencies between the target structure and the initial model are almost completed eliminated by the updating process. For damage case 1, the MAC values between the target structure and the initial and updated model are both very close to one, indicating high correlation between the two sets of data. In this case, the improvement in terms of mode shape correlation brought by the FEMU process is not obviously seen. For damage case 2, the increase in MAC values are more obvious. For the modes 4~6, the MAC values increase from between 96% to 98% to almost 1. This indicates that very good mode shape correspondence is achieved through the FEMU process. The above observation is further confirmed by inspecting the mode shapes of the target structure and that of the initial and updated model plotted in Figure 5-10 and Figure 5-11 respectively.

Table 5-2 Natural Frequencies of Target Structure, Initial Model and Updated Model

Mode	Natural Frequency (Hz)		
	Target Structure	Initial Model	Updated Model
Damage Case 1			
1	19.571	19.629	19.571
2	30.646	30.665	30.646
3	78.328	78.512	78.329
4	99.070	99.366	99.070
5	176.55	176.63	176.55
6	207.16	207.30	207.16
Damage Case 2			
1	18.988	19.629	18.983
2	30.452	30.665	30.445
3	73.681	78.512	73.669
4	97.085	99.366	97.064
5	169.63	176.63	169.59
6	201.20	207.30	201.19

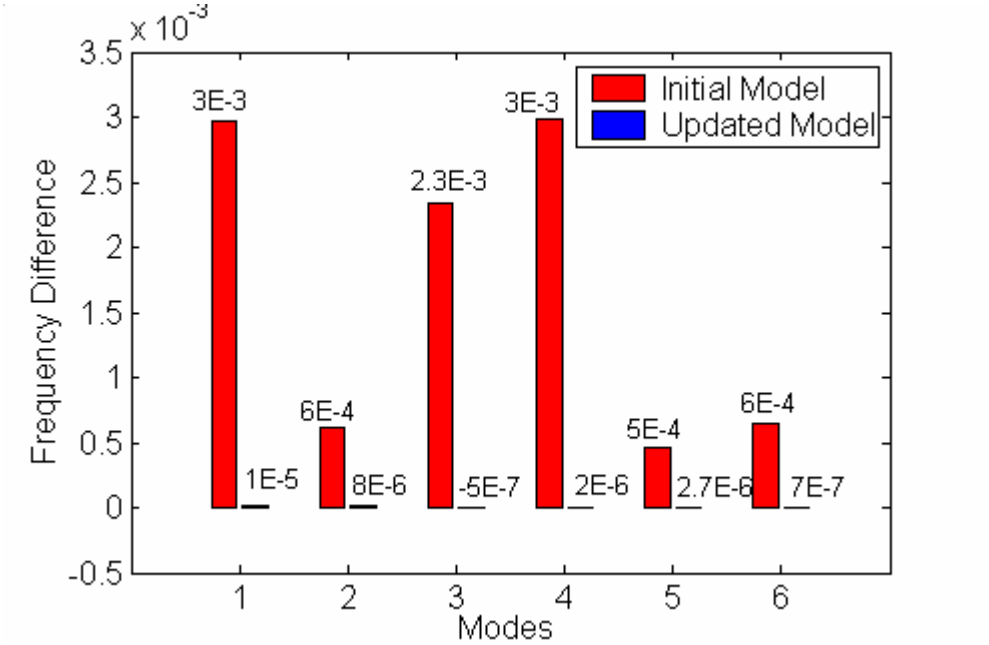

Figure 5-8 Relative Frequency Differences with Respect to Target Structure $\frac{\omega_k^A(\mathbf{p}) - \omega_k^E}{\omega_k^E}$ – Damage Case 1

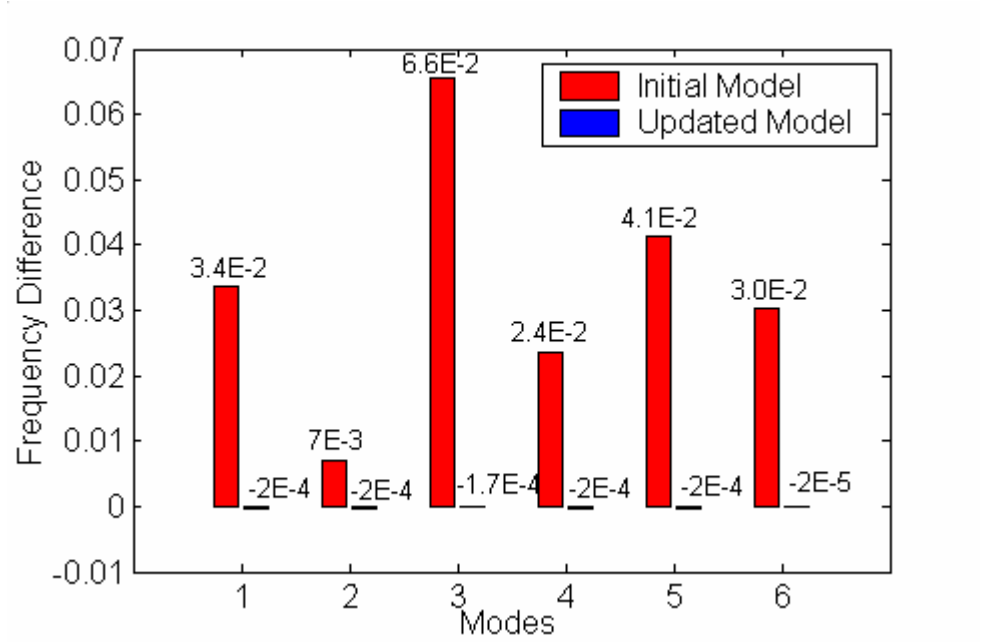

Figure 5-9 Relative Frequency Differences with Respect to Target Structure $\frac{\omega_k^A(\mathbf{p}) - \omega_k^E}{\omega_k^E}$ – Damage Case 2

Table 5-3 MAC Values between the Initial and Updated Model and the Target Structure

Mode	MAC Values (%)	
	Initial vs. Target	Updated vs. Target
	Damage Case 1	
1	100.00	100.00
2	100.00	100.00
3	99.99	100.00
4	99.99	100.00
5	100.00	100.00
6	100.00	100.00
	Damage Case 2	
1	99.91	100.00
2	99.98	100.00
3	97.78	100.00
4	98.05	99.99
5	95.89	100.00
6	96.10	100.00

The residues before and after model updating are plotted in Figure 5-12 and Figure 5-13. In both damage cases, the residues are reduced significantly during the updating process.

Table 5-4 Identified Structural Parameters for Damage Case 1

Element Group j	Correction Factor α_j	Young's Modulus E ($\times 10^{10}$ Pa)
17	-0.0024	6.9808
18	0.0037	6.9383
19	-0.0064	7.0085
20	0.0140	6.8668
21	0.0401	6.6848
22	0.0736	6.4515
23	0.0721	6.4622
24	0.0239	6.7974
25	0.0215	6.8140
26	0.0127	6.8754
27	-0.0183	7.0912
28	0.0053	6.9272

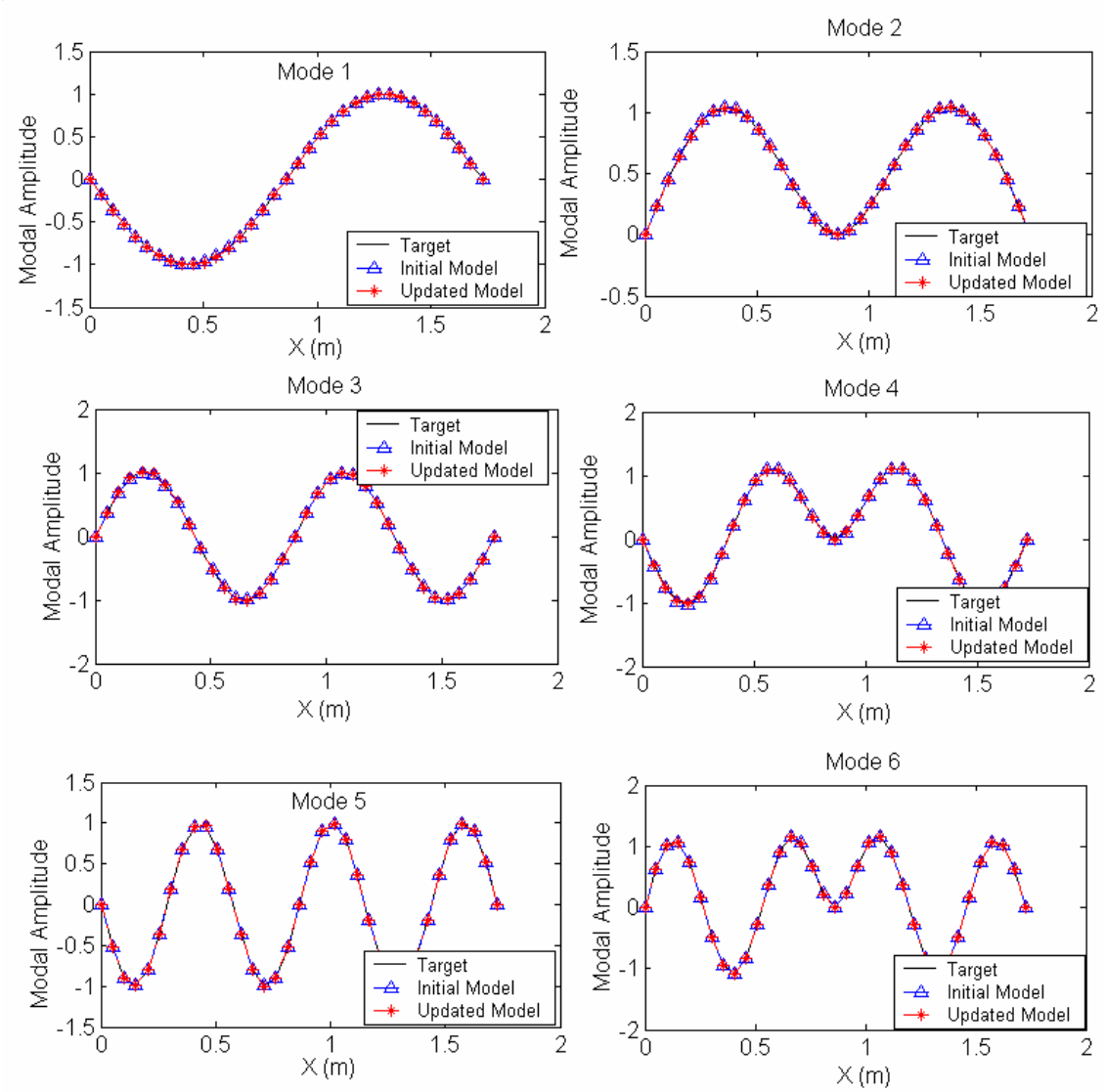

Figure 5-10 Mode Shapes of Damage Case 1: Target Structure vs. Initial and Updated Model

The identified structural parameters are listed in Table 5-4 and Table 5-5. The identified structural parameters are also plotted in Figure 5-14 and Figure 5-15. For the current case, the true correction factors $\bar{\alpha}_j$ for each element group are known. For damage case 1, $\bar{\alpha}_j$ equal to 0.06 for element groups 21~24 and 0 for other element groups. For damage case 2, $\bar{\alpha}_j$ equal to 0.49 for element groups 49~54 and 0 for other

element groups. It is noted that for both cases, although noise is present in the measured modal vectors, α_j s are identified relatively accurately.

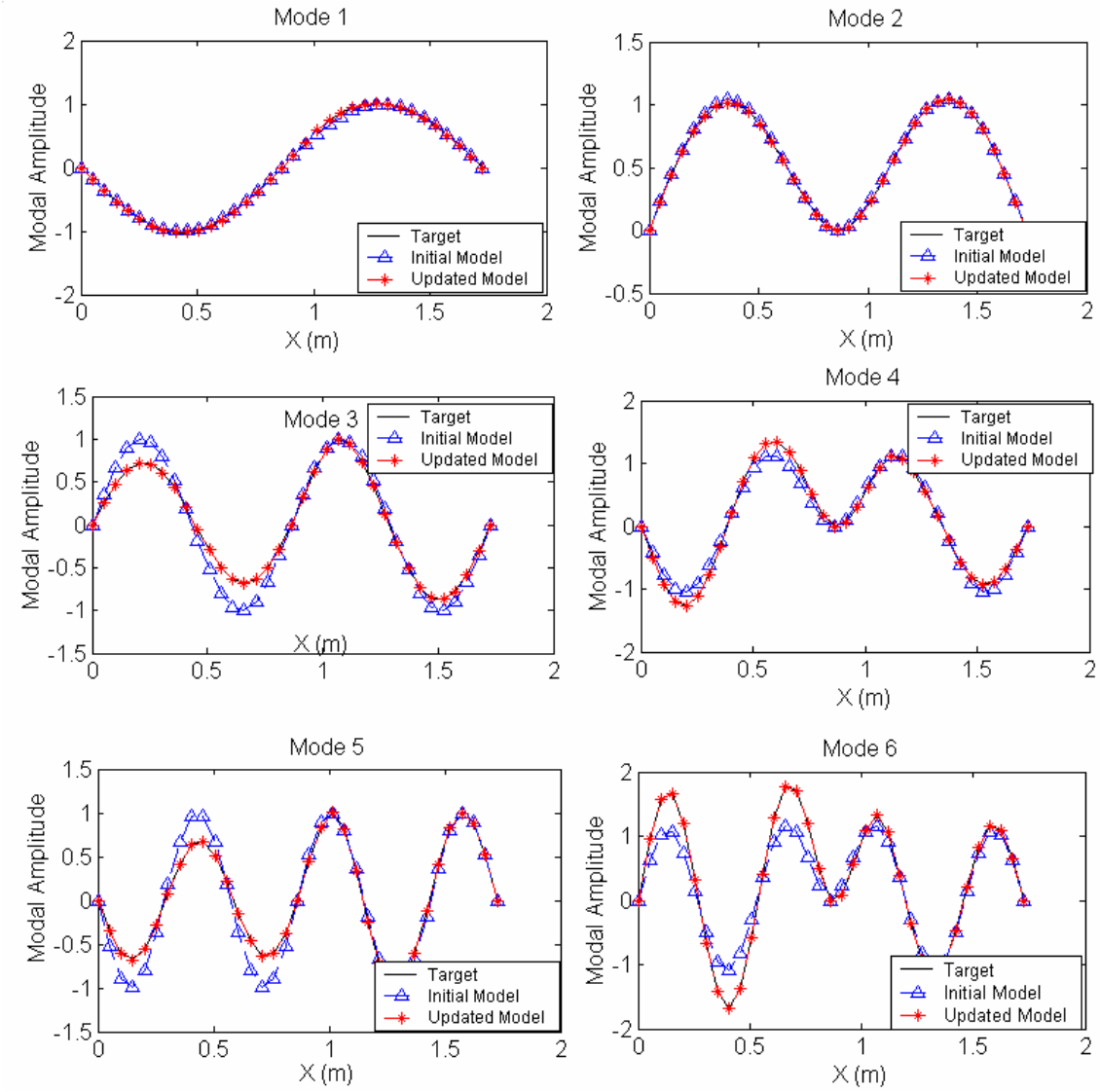

Figure 5-11 Mode Shapes of Damage Case 2: Target Structure vs. Initial and Updated Model

Table 5-5 Identified Structural Parameters for Damage Case 2

Element Group j	Correction Factor α_j	Young's Modulus E ($\times 10^{10}$ Pa)
48	0.0539	6.589
49	0.4631	3.739
50	0.5239	3.315
51	0.4252	4.003
52	0.5569	3.086
53	0.4284	3.981
54	0.4970	3.503
55	0.0492	6.622

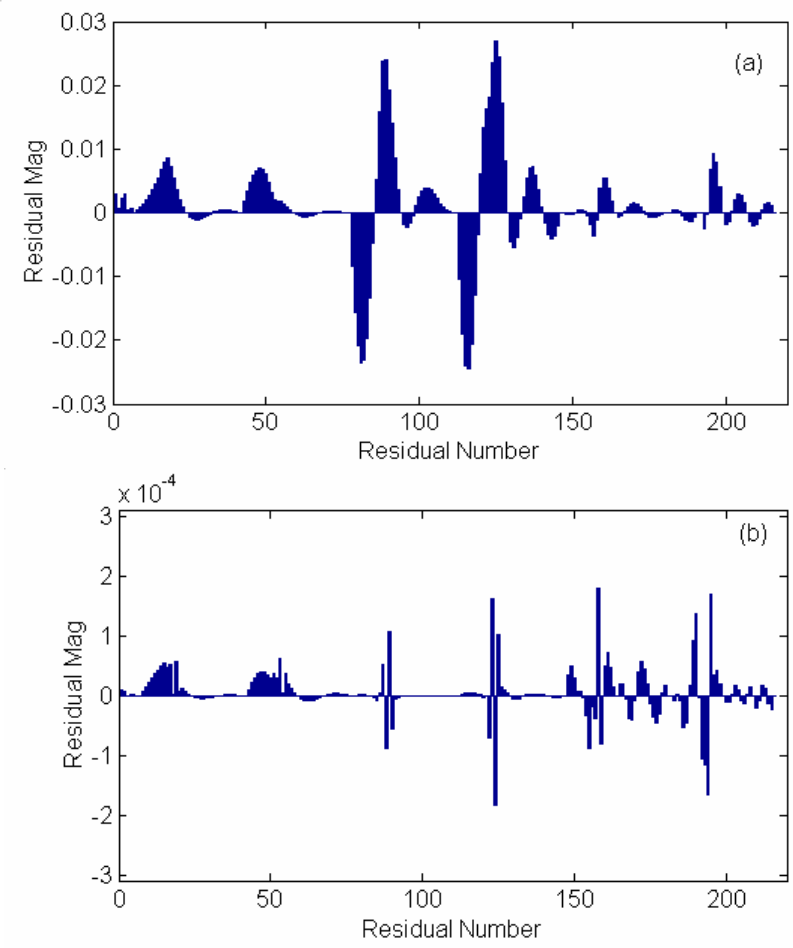

Figure 5-12 Damage Case 1 Residues: (a) Initial (b) Updated. (Initial and updated Residual Plotted in Different Scale)

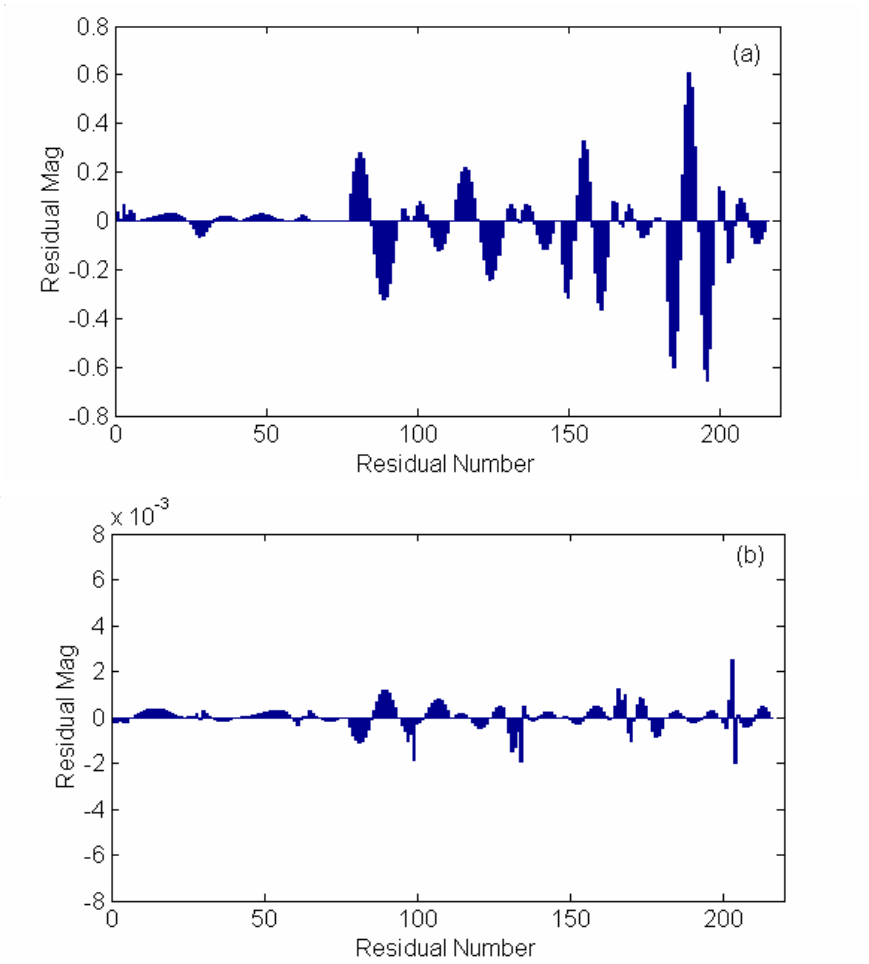

Figure 5-13 Damage Case 2 Residues: (a) Initial (b) Updated. (Initial and updated Residual Plotted in Different Scale)

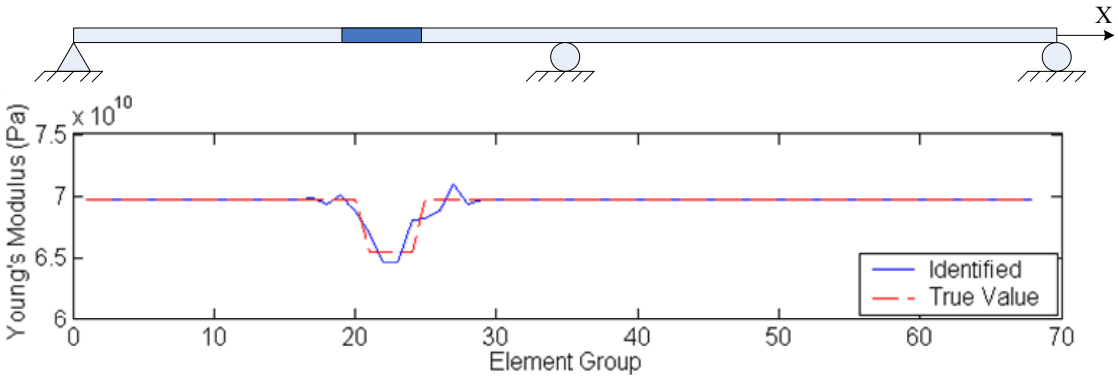

Figure 5-14 Identified Structural Parameters for Damage Case 1

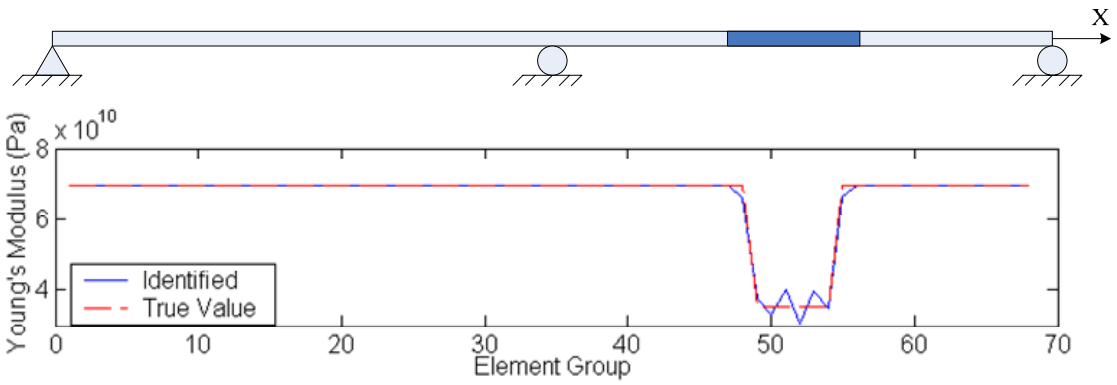

Figure 5-15 Identified Structural Parameters for Damage Case 2

5.4 Summary

A Finite Element Model Updating (FEMU) based damage identification procedure is explained in this chapter. In the FEMU process, the unknown structural parameters in the FE model are first identified. The difference between the analytical and experimental modal data is then used to formulate the minimization problem. FE analysis is performed to obtain the analytical modal parameters. Experimental modal parameters can be identified for operational civil engineering structures using the procedures described in Chapter 3. Numerical procedures are then used to solve the minimization problem resulting in updated parameter values. These updated parameter values are then substituted into the FE model and the process is repeated iteratively until convergence is reached. As a result, a finite element model more representative to the actual physical structure is achieved. The FEMU process is carried out for both the undamaged structure and the damage structure resulting two sets of identified

parameters. The identified parameters from undamaged and damaged structure are then compared to yield information about the damage location and severity.

After reviewing some of the current literature, it is concluded that the choice of proper structural parameters to update is one of the main difficulties of finite element model updating. Careless choice of parameters usually leads to ill-conditioned identification problem. It is suggested that the ill-conditioning of the FEMU problem can be greatly alleviated if use can be made of the information about the damage location. Such information can be obtained from damage localization procedures such as the EMSDI technique described in Chapter 4.

The correlation between experimental and analytical modal data is discussed in order form the residue vector for the FEMU. The formulation of both frequency and mode shape residues are explained. Regularization techniques such as weighting matrix and penalty function is utilized to improve the condition of the identification problem. Two solutions procedures are laid out: first formulating the problem as a nonlinear least squares problem and then formulating the problem as general constrained minimization problem.

A numerical example is used to demonstrate the effectiveness of the proposed FEMU based damage detection technique. The results show that the proposed method is able to accurately determine the location and severity of the damage under conditions when noise is present. The resulting updated model is considered as a good representation of the target structure in the dynamic sense and can be used for evaluating the effect of the damage on the structural capacity.

Chapter 6 Implementation of Health Monitoring System on the Kings Stormwater Channel Composite Bridge

6.1 Description of the Bridge

The Kings Stormwater Channel Composite Bridge is a two-span highway bridge with a total length of approximately 20.1 m and a width of approximately 13.0 m. It carries two north-bound lanes on state highway 86 in Riverside County, California. The bridge crosses a channel where storm water from mountains drains into a lake (Figure 6-1). The superstructure is of slab-on-girder type, with two equal spans of 10.0 m, and a cap beam connecting two adjoining spans. Five precast prestressed concrete piles 343 mm in diameter support the cap beam from the river bed, as shown in Figure 6-2. Abutments on both ends separate the bridge from the road approach. The bridge was opened to traffic in May 2001.

The design and construction of the bridge utilizes a unique structural design named the Carbon Shell System (CSS) developed at the University of California, San Diego (Karbhari et al. 2000). The 6 main girders are composed of 10 mm thick prefabricated filament-wound carbon/epoxy shells filled on-site with light-weight concrete (Figure 6-3a). The carbon/epoxy shell serves both as the reinforcement and

stay-in-place formwork for the concrete core during construction. The girders support six modular E-glass (GFRP) deck panels which perform as the bridge deck and transfer vehicular loads to the girders and also act as the transverse connections between girders. A typical cross section of the GFRP deck panel are shown in Figure 6-3b. The deck panels are placed in such a way that the pultruded tubes are in perpendicular to the carbon shell girders. A polymer concrete wearing surface is casted on top of the decks.

Steel reinforcing cages that extend from the girders into the cap beam and abutments are used to provide longitudinal connectivity between the carbon shell girders and the abutment and the cap beam (Figure 6-4a). The connection between the girders and the deck system is achieved by steel dowels extending from concrete filled carbon shell girders into locally grouted cells of fiberglass deck panel, as shown in Figure 6-4b. On either side of the bridge there is a concrete road barrier connected to the deck through steel rebars that extend from the barrier into the deck panels.

Figure 6-1 Kings Stormwater Channel Composite Bridge

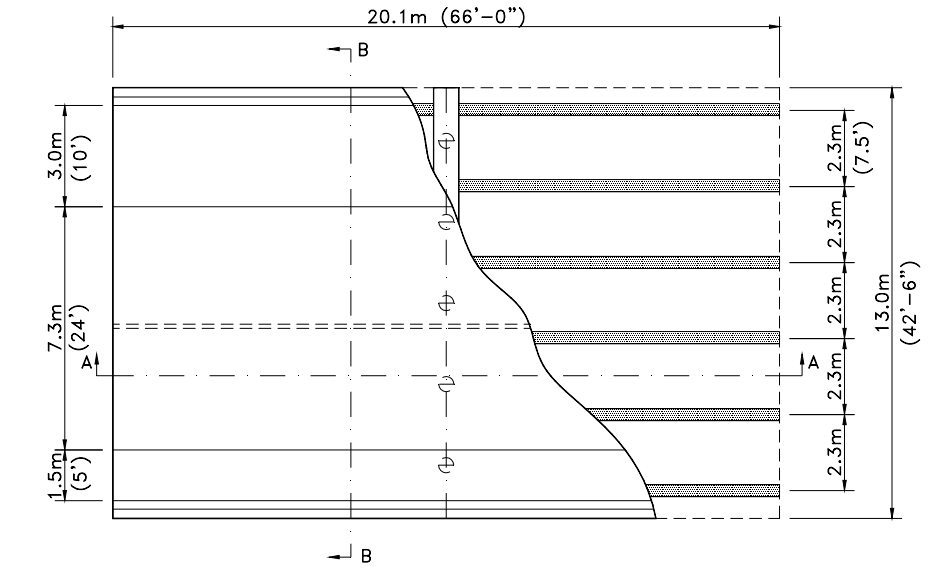

Plan view

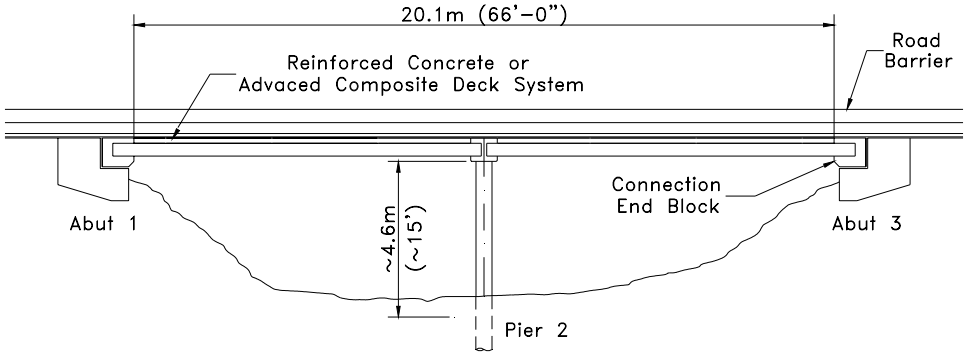

b) Longitudinal section A-A

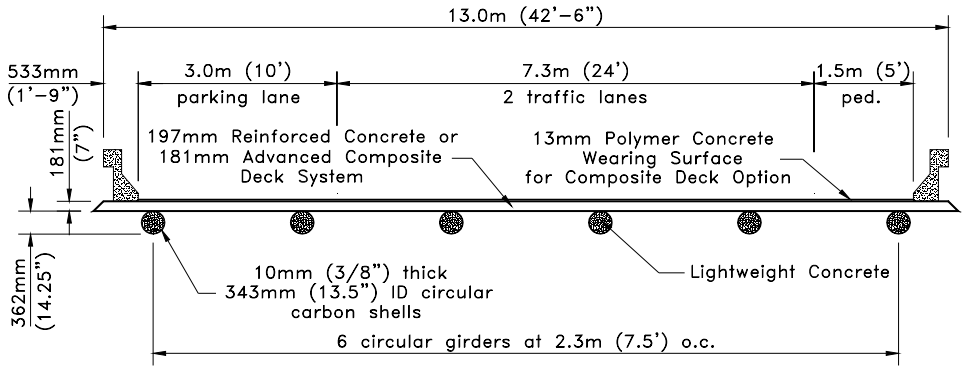

c) Cross section B-B

Figure 6-2 Geometry of Kings Storm Water Channel Advanced Composite Bridge

(a) Carbon Shell Girder (b) E-glass deck panels

Figure 6-3 Carbon Shell Girder and E-glass Deck Panel

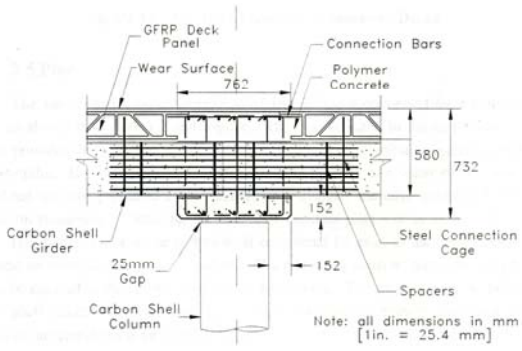

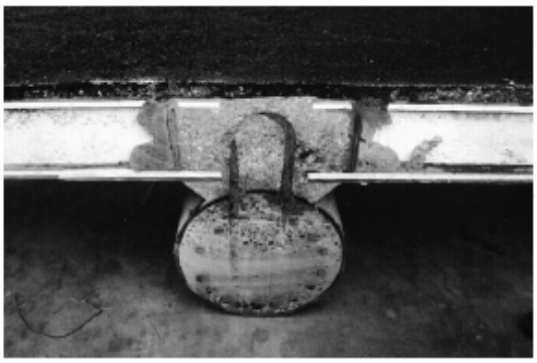

(a) Girder-Capbeam connection detail (b) Cross section of girder-deck connection

Figure 6-4 Girder-Cap Beam and Girder-Deck Connection

6.2 Initial Static Characterization

To ensure the bridge was performing according its design criteria and to study the long-term performance of this novel fiber-reinforced polymer structural system, it was planned that static tests would be performed on the bridge at a routine interval. As a

initial step, two static tests were performed prior to the opening of the bridge in order to establish the baseline performance level of the bridge.

Before the completion of the construction of the barriers on the bridge, a concrete paver (42.6 tons) traveled over the bridge (Figure 6-5). The test results, details of which can be found in Zhao et al. (Zhao et al. 2001a), indicated a maximum mid-span deflection of 8 mm (0.32 in) under a load of approximately 50% that of three AASHTO design trucks. The maximum strain recorded was approximately 16% of the strain allowable under service load, and substantial strength reserves existed. It should be noted that the concrete barrier is designed to add overall stiffness to the bridge system and therefore its absence causes higher deflections.

A second test, designed as a Proof Test, was conducted after the construction of the bridge, including barriers, was fully completed (Zhao et al. 2001b). The test utilized three fully loaded water trucks, as shown in Figure 6-6. The loading case represented approximately the same flexural demand on the superstructure as that applied by three AASHTO design trucks. The maximum mid-span deflection observed was 9 mm (0.36 in) and the maximum strain response was approximately 18% of the strain allowable under Service I condition (i.e. 25% of the ultimate of 1%).

Figure 6-5 Paver Test

Figure 6-6 Proof Test

6.3 Initial Dynamic Characterization

A forced vibration test was carried out on the Kings Stormwater Channel Composite Bridge on May 3rd, 2001, shortly before the bridge was opened to traffic. The purpose of the test was to obtain information regarding the natural frequencies and mode shapes of the pristine structure. These information sets will serve as a baseline for the Vibration-based Damage Detection algorithm.

Five PCB 393A03 ICP accelerometers were used to record the response time histories. Roving sensor technique was used to cover a total of 42 response locations, as shown in Figure 6-7. A custom-made drop hammer was used to excite the structure. The hammer tip was instrumented with a 9.09 kN PCB 200C20 piezoelectric load cell. Data were acquired with an eight-channel Zonic Model 2300 signal analyzer. The sampling rate was set at 1280 Hz.

A total of nine vibration modes were identified, with their corresponding natural frequencies and modal damping listed in Table 6-1.

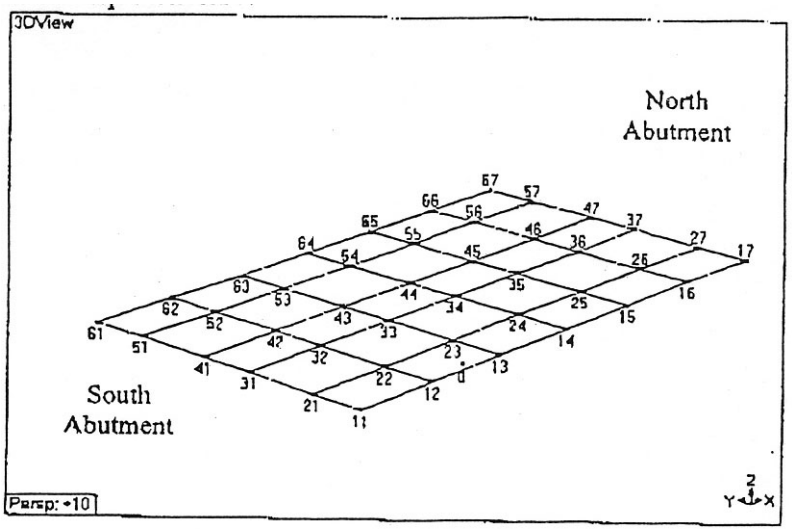

Figure 6-7 Response Location Layout for the Modal Test

Table 6-1 Natural Frequencies and Modal Damping from the Forced Vibration Test

Mode	Frequency (Hz)	Damping (%)
1	11.033	2.8
2	13.11	2.9
3	15.36	1.7
4	16.921	0.5
5	19.005	2.1
6	25.585	3.4
7	26.39	2.7
8	34.941	3.1
9	35.834	2.7

6.4 In-Service Static Characterization

Approximately one year after the bridge's completion, another static load test was jointly performed by the Department of Structural Engineering at University of California, San Diego and the California Department of Transportation (Caltrans). Extensive instrumentation was installed on the bridge prior to the load test, including strain gages, accelerometers and displacement sensors (linear potentiometers). These instruments serve the dual purpose of facilitating measurement of response during the load test and as an integral part of the long-term health monitoring system for the bridge. The installation of the instrumentation system was initiated on August 26th, 2002 and the load test was carried out on September 5th, 2002.

Caltrans had experienced difficulties in obtaining 3 trucks with exactly the same axle spacing and axle weight as the AASHTO design truck, and were also unable to provide 3 trucks for the test. Instead, two fully loaded water trucks with known axle weights and axle spacing, albeit different, were employed in the test, as shown in Figure 6-8 and Figure 6-9.

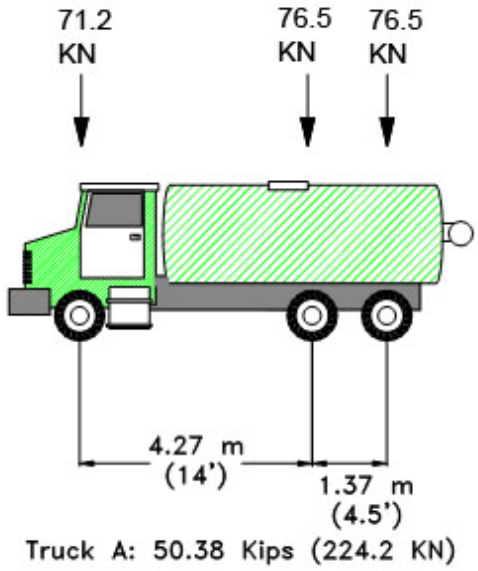

Figure 6-8 Axle Weight and Spacing of Truck A

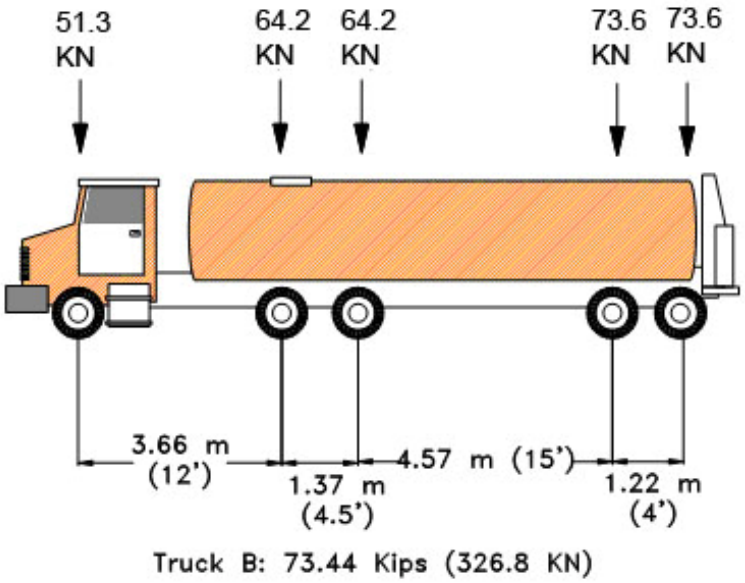

Figure 6-9 Axle Weight and Spacing of Truck B

6.4.1 Loading

6.4.1.1 Vehicle Loading

Two water trucks, designated as Trucks A and B, provided by the Caltrans field office at Coachella with known axle spacing and axle weight were utilized in the test. Normal traffic on the highway, consisting of trucks and cars, was also used as an auxiliary method of loading.

Truck A is a 3-axle water truck with a total weight of 50.38 kips (224.2 kN). The load on the front axle of Truck A is 16 kips and the two rear axles have a load of 17.19 kips each, as shown in Figure 6-8. Truck B is a 5-axle water truck with a total weight of 73.44 kips (326.8 kN). The load on the front axle is 11.52 kips. The load on the two middle axles are 14.42 kips each and the rear axle has a weight of 16.54 kips, as shown in Figure 6-9. The axle weight of the trucks was determined using a weigh station in the vicinity of the bridge. It is assumed that the load is evenly distributed between the two middle axles and the rear axle.

Since it as not possible to test under the AASHTO design truck loading, alternative strategies were devised to provide an assessment of overall bridge response. Due to constraints on traffic control it was also not possible to block both lanes, although the amount of traffic during the period of the test was such that it was possible to regulate traffic restricting it to single lanes loaded at times. 7 different test regimes were considered as part of the overall load scheme.

6.4.1.2 Lane Assignment

The bridge carries two northbound lanes on Highway 86S, as shown in Figure 6-10. The west lane was designated as Lane 1 and the east lane as Lane 2. There is a shoulder to the east of two traffic lanes and a pedestrian walkway to the west of traffic lanes.

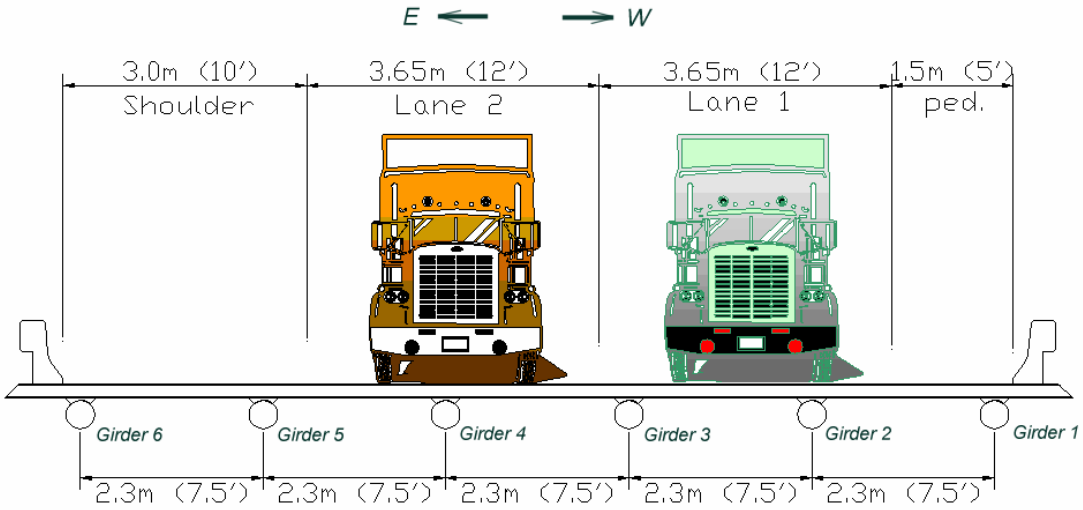

Figure 6-10 Lane Assignment

6.4.2 Instrumentation Layout

The instrumentation layout is shown in Figure 6-11. A total of 67 channels of sensors were deployed on the bridge. This includes 42 accelerometers, 4 linear potentiometers, 19 strain gages, one temperature sensor and an additional gage for temperature compensation. Linear potentiometers were attached to the bottom of Girder 3 and Girder 4 at mid-span in both the southern and northern spans. The two linear potentiometers attached to the bottom of Girder 3 are designated as G3N and G3S. The

two attached to the bottom of Girder 4 are designated as G4N and G4S. Steel frames as shown in Figure 6-12 were used to support the potentiometers. Strain gages were attached at the bottom of the girder, mid-height of the girder and bottom of the deck, as shown in Figure 6-11 and Figure 6-13. Strain gages attached to the bottom of the girder are marked in red in Figure 6-11. Those attached at the mid-height of the girder and bottom of the deck are marked in blue and green respectively.

As part of the long-term monitoring system, each strain gage was enclosed in a small plastic box and sealed. The signal cables for the strain gages, placed in PVC conduits, were also sealed to prevent water intrusion, as shown in Figure 6-13. Girders 2 and 4 were more heavily instrumented based on the fact that they are subjected to direct wheel loads when vehicles are on Lane 1 or 2.

The data acquisition system comprised of a National Instruments SCXI-1000 Data Conditioning Module, a National Instruments PXI-6070 Data Acquisition Pad and a Pentium IV notebook computer. During all the tests, data was taken at a sampling rate of 25 samples/second.

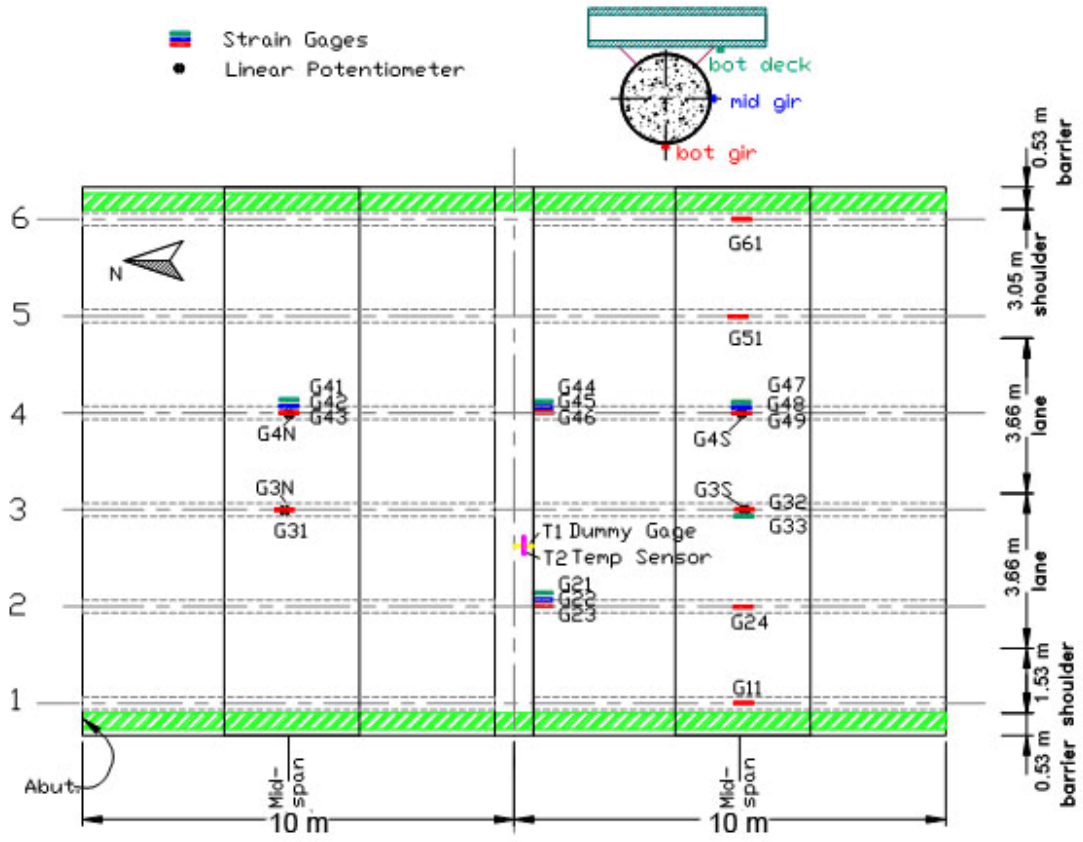

Figure 6-11 Instrumentation Layout

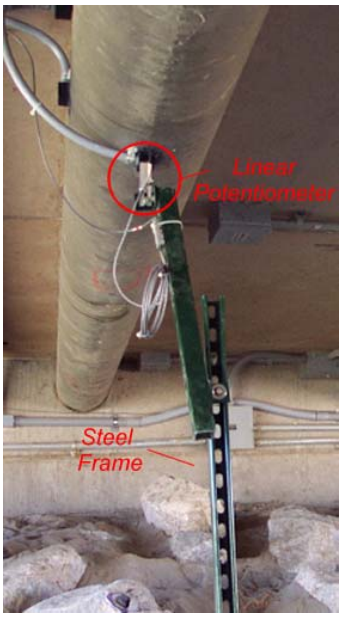

Figure 6-12 Linear Potentiometer & Supporting Frame

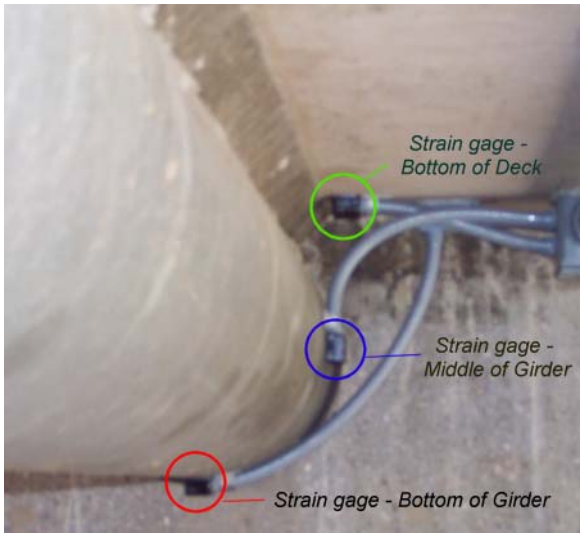

Figure 6-13 Strain Gage Locations

6.4.3 Test Program

The first part of the load test consisted of a set of rolling load tests carried out on the bridge from 7:30 AM to 10:00 AM. Truck A and Truck B were driven at a speed of approximately 5 mph from the southern end of the bridge to the northern end. The dynamic impact factor was considered to be insignificant at such speeds. Lane 2 was first closed, with Lane 1 still open to normal traffic. Great care was taken to ensure there was no traffic traveling on the bridge when the test vehicle was crossing and data was taken. Truck A and Truck B both made 5 runs each before the lanes were switched and the procedure repeated.

A full-lane loading test was then carried out with both trucks parked on the bridge. Truck B was first parked on Lane 1 on the southern span with its rear axles as close to the southern abutment as possible. Truck A was then parked on the same lane

on the northern span with rear axles as close to the front axle of Truck B as possible, as shown in Figure 6-14. Lane 2 was open to traffic during the test.

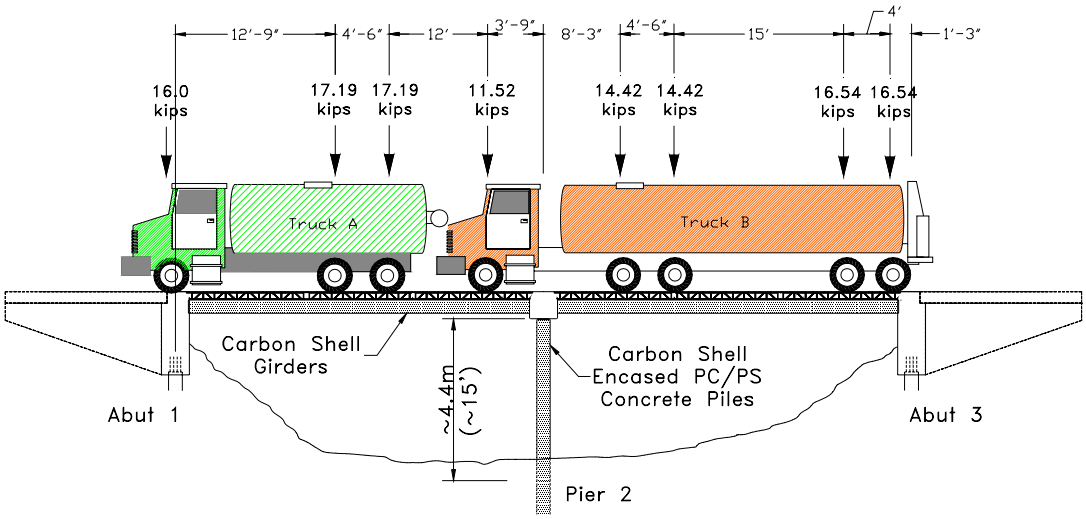

Figure 6-14 Loading Configuration of Test 21

A "brake" test was also carried out with Truck B braking suddenly at the middle of the bridge while traveling at approximately 30 mph. The test was carried out on Lane 2. The choice of lane was based on the fact that the girder under lane 2 had been reported by Caltrans personnel to show the maximum distress on the basis of a "tap" test.

The last test carried out was a rolling test with Truck A and B traveling side by side at a speed of approximately 5 mph. Truck A traveled on Lane 2 with Truck B traveling on Lane 1, both from southern end of the bridge to the northern end.

The entire test took approximately 3 hours. Based on observations it was concluded that effects of environmental variation (temperature changes) during this

period of time were insignificant and would not affect the overall results. A list of all the tests and their description is also provided in Table 6-2.

Table 6-2 Test Program

Test No.	Description
1	Truck A – Lane 2 @ 5mph, 1st Run
2	Truck B – Lane 2 @ 5mph, 1st Run
3	Truck A – Lane 2 @ 5mph, 2nd Run
4	Truck B – Lane 2 @ 5mph, 2nd Run
5	Truck A – Lane 2 @ 5mph, 3rd Run
6	Truck B – Lane 2 @ 5mph, 3rd Run
7	Truck A – Lane 2 @ 5mph, 4th Run
8	Truck B – Lane 2 @ 5mph, 4th Run
9	Truck A – Lane 2 @ 5mph, 5th Run
10	Truck B – Lane 2 @ 5mph, 5th Run
11	Truck A – Lane 1 @ 5mph, 1st Run
12	Truck B – Lane 1 @ 5mph, 1st Run
13	Truck A – Lane 1 @ 5mph, 2nd Run
14	Truck B – Lane 1 @ 5mph, 2nd Run
15	Truck A – Lane 1 @ 5mph, 3rd Run
16	Truck B – Lane 1 @ 5mph, 3rd Run
17	Truck A – Lane 1 @ 5mph, 4th Run
18	Truck B – Lane 1 @ 5mph, 4th Run
19	Truck A – Lane 1 @ 5mph, 5th Run
20	Truck B – Lane 1 @ 5mph, 5th Run
21	Full-Lane Loading Test, both trucks parked on Lane 1
22	Brake Test, Truck B brake on Lane 2
23	Two-Lane Loading Test, Two trucks side-by-side @ 5 mph, Truck A on Lane 1, Truck B on Lane 2

6.4.4 Summary of Test Results

A complete list of test results can be found in Guan et al. (Guan et al. 2002) hence only the important results are summarized here. All test results show very good consistency and repeatability among different runs. Typical mid-span deflection and strain profile measured during the rolling tests (Test 1 ~ Test 20) are presented in Figure

6-15 to Figure 6-18. Figure 6-15 plots the typical mid-span deflection time history during the rolling tests. Figure 6-16 shows the mid-span deflection at the southern span of girder 4, where the largest deflection among all rolling tests was recorded. The maximum deflection recorded at this location is 7.16 mm during load condition 2, i.e., Truck A traveling on Lane 2. This value provides a deflection/span ratio of approximately L/1400. Figure 6-17 and Figure 6-18 shows the mid-span strain time-history measured during the same test condition. Only the strain gages at the bottom of the girder were seen to show any significant values of strain. Strain gages at the mid-height of the girder and at bottom of the deck only saw strains of approximately 25% of that seen by the strain gages at the bottom of the girder. The maximum tensile strain occurred at the bottom of Girder 2, at mid-span, which is directly under wheel load during Load Condition 3 (Truck B traveling on Lane 1). The value is 306 microstrain. The maximum compressive strain of 276 με occurred at the bottom of Girder 4, close to the bent, under Load Condition 4. Truck B was traveling on Lane 2, which is right above Girder 4, in this Load Condition. The maximum peak strain (306 με) observed through all rolling tests was only about 12% of the strain allowable for the Service I condition, which is 25% of the ultimate strain of 1%.

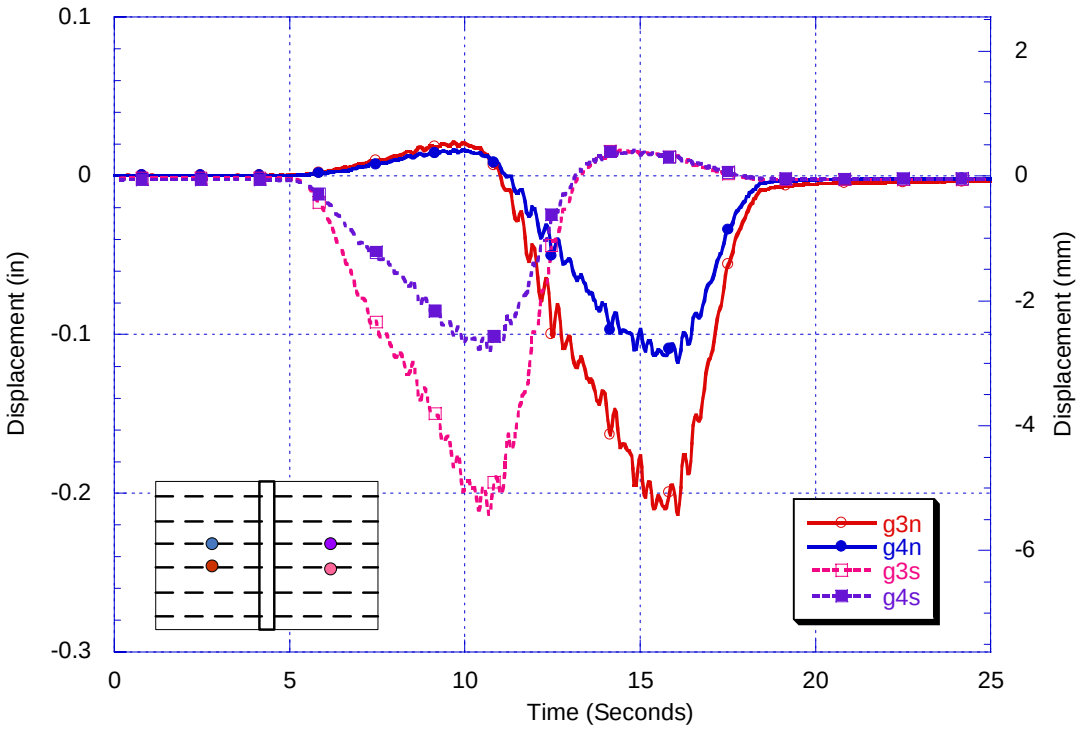

Figure 6-15 Mid-span Deflection (Truck A – Lane 1 – 1st Run)

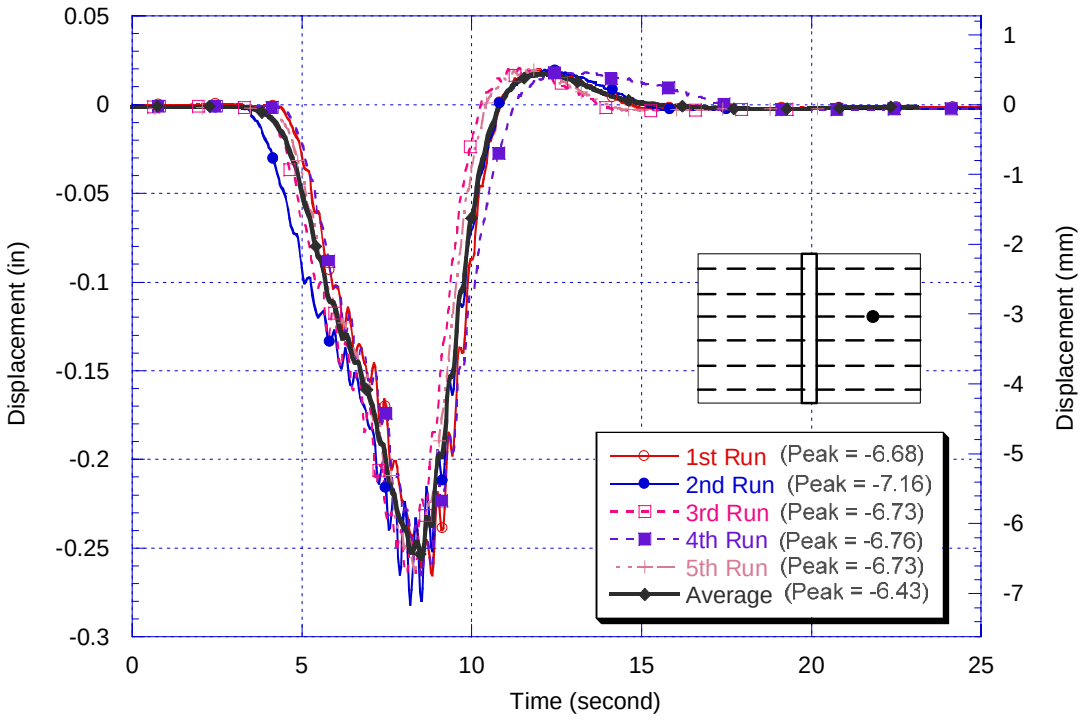

Figure 6-16 Mid-span Deflection (Girder 4 – Southern Span – Truck A – Lane 2)

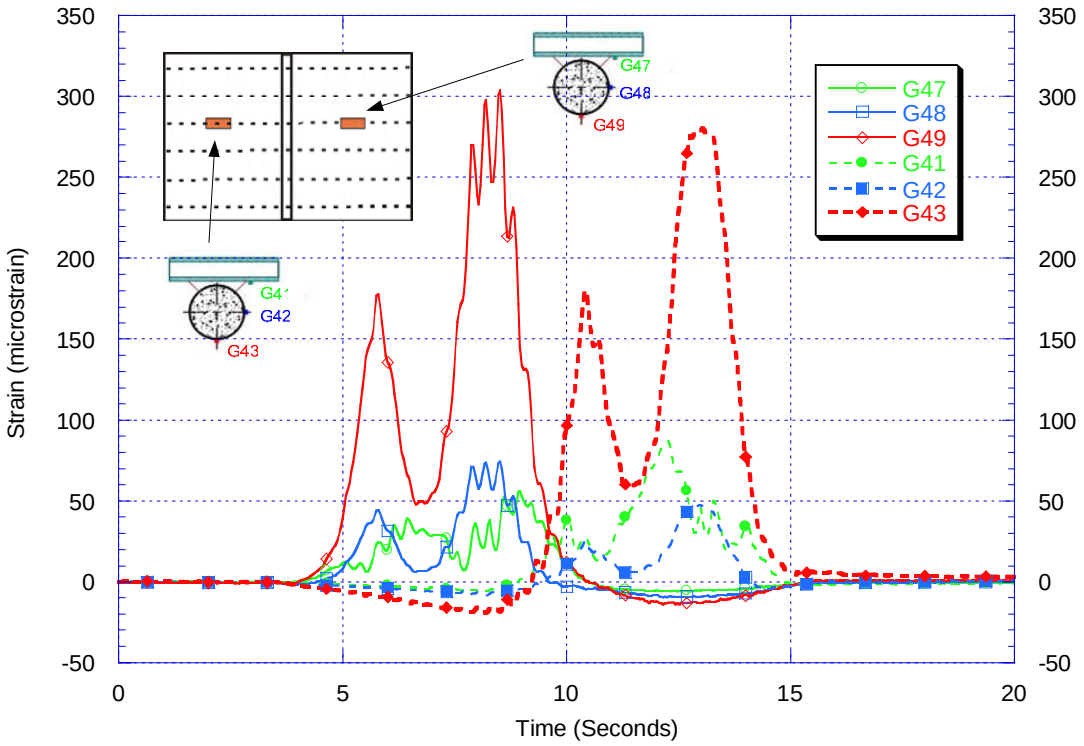

Figure 6-17 Strain Time-history at Mid-span Section (Truck A, Lane 2, 2nd Run)

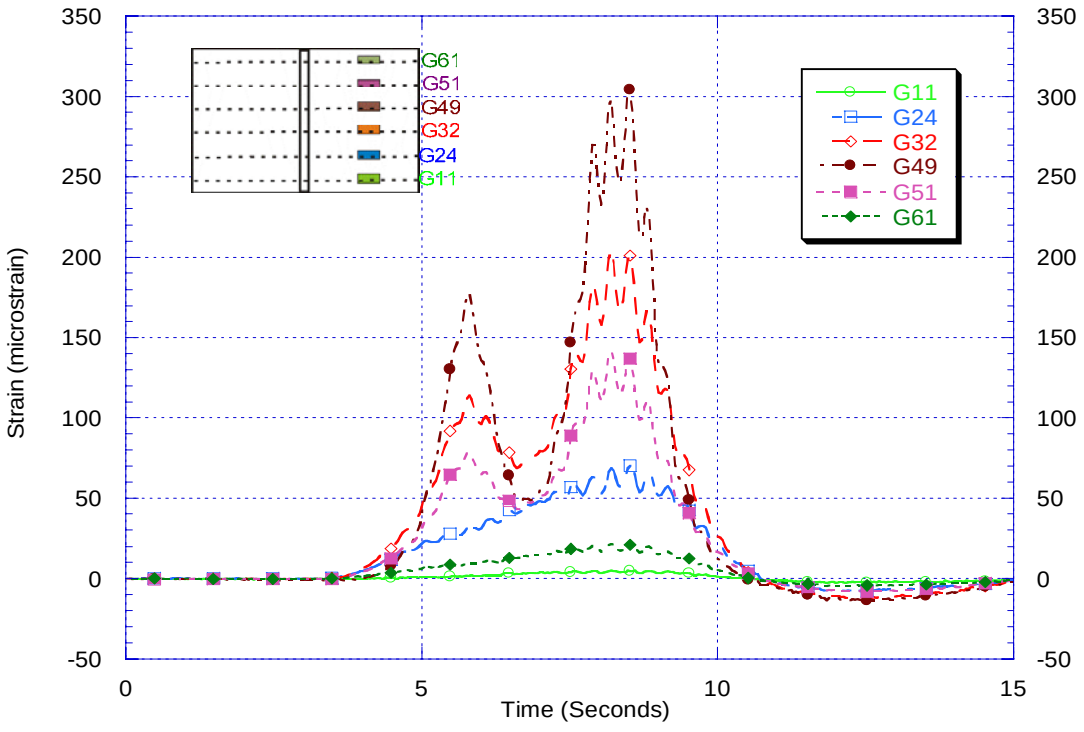

Figure 6-18 Mid-span Strain Time-history – Girder 1-6 (Truck A, Lane 2, 2nd Run)

The results of the full lane loading test (Test 21) are similar to that of the rolling test. During the full lane loading test, all 5 axles of Truck B were on the bridge. Two rear axles of Truck A were on the bridge and the front axle was on the northern abutment. Lane 2 was open to traffic during the test. The weights of passing vehicles were unknown. It should be noted that the normal traffic was traveling at approximately 60~70 mph across the bridge, and thus a dynamic impact factor must be taken into account when considering their load effect. Using a dynamic impact factor of 1.33 as specified in the AASHTO Bridge Design Specifications (AASHTO 1998), the dynamic load effect of passing traffic can be converted to an equivalent static load effect. The equivalent static load effect was then added to create an equivalent total effect. This method is a very rough approximation of the maximum mid-span deflection when both lanes are loaded. The final value is 8.28 mm, which is about 15.6% larger than the maximum mid-span deflection observed during the rolling test. However, the deflection/span ratio is still a relatively low value of L/1215. The maximum strain (403 με) observed during the full lane loading test was about 16% of the allowable strain for the Service I condition.

The brake test was intended to create a larger load effect by sudden braking of the vehicle. As shown by the results, the sudden braking did create an impact magnifying the load effect by a value from 0.6% to 16.5%, depending on the location. However, while Truck B is heavier than Truck A, its load was distributed over 5 axles instead of 3. That created a per axle load smaller than that of Truck A. It was also not possible for the middle axles and rear axles of Truck B to both contribute significantly to the mid-span deflection of one span. Either the middle axles and the rear axles are at

different spans or they are at same span but both at locations with very small contribution to the deflection. So generally the load effect created by Truck A alone on either span is larger than that created by Truck B. Due to that fact, the maximum peak deflection observed during the brake test (7.34 mm) was only slightly higher than the maximum peak deflection of the rolling test (7.16 mm), which was created by Truck A.

The last test carried out was two-lane load test. Truck A and Truck B were driven side-by-side from the south end of the bridge to the north end. Truck A traveled in Lane 1 and Truck B traveled in Lane 2. The mid-span deflection history is plotted in Figure 6-19. The maximum mid-span deflection of 8.20 mm is about 1/1225 of the span length. This value matches very well with the Equivalent Total deflection reported from the full lane loading test. The maximum peak strain of 377 με is about 15% of the allowable strain for the Service I condition.

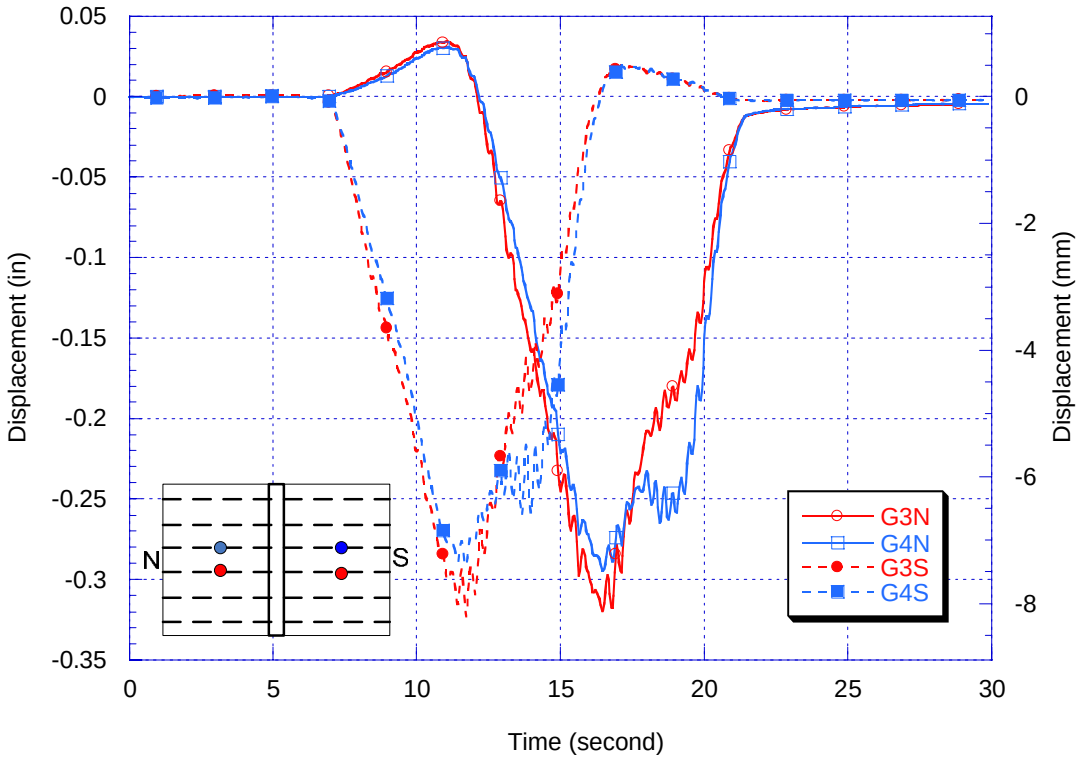

Figure 6-19 Mid-span Deflection – Two-Lane Load Test

6.4.5 Evaluation of Static Characterization Results

As mentioned in Section 6.4, trucks that exactly match the AASHTO design truck axle load were unavailable at the time of test. In order to predict the structural behavior under AASHTO design truck load, a 2-D frame finite element model was built using finite element package SAP2000 (SAP2000 2004), as shown in Figure 6-20. The geometry and material properties of the model were obtained from previous studies on bridge components (Burgueño 1999; Burgueño et al. 2001; Davol 1998; Zhao 1999). The carbon shells of the girders were embedded 9 in (229 mm) into the abutment wall. A steel cage embedded both into the girders and the abutment wall provided the

connection mechanism. A 13mm elastomer strip was placed between the carbon shells and abutment wall at the location of connection to avoid damage due to bearing. It is expected that the connection between the girder and the abutment will only provide partial moment transfer. Considering these facts, a modification to the boundary conditions of the model was made using spring constraints instead of fixed constraints at both ends. The parameters of the finite element model were calibrated according the measured static response obtained during the characterization test.

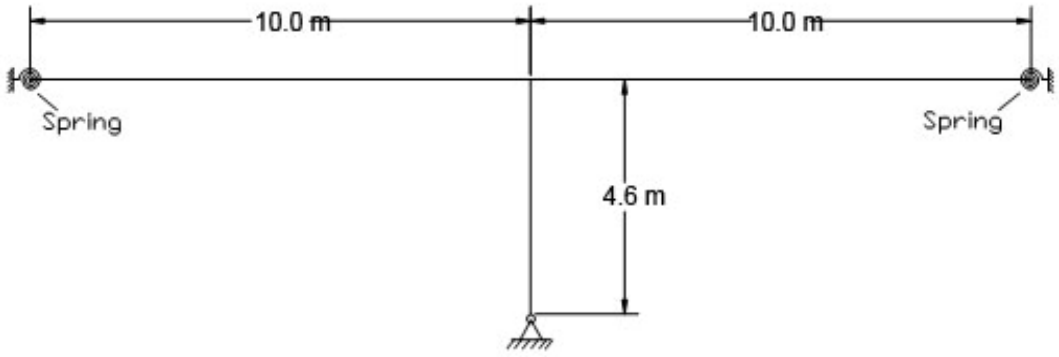

Figure 6-20 2-D Frame Model

In addition to the four load configurations used during the test (Truck A, Truck B, Full Lane Loading, Two Lane Loading), two additional load configurations were applied to the model. The first load configuration is the same as the 3 Truck Configuration used in the previous Proof Test (Zhao et al. 2001b). The second load configuration simulates the effect of three AASHTO design trucks, as shown in Figure 6-21. The procedure of calculating the load effect of three AASHTO design trucks was presented in Zhao et al. (Zhao et al. 2001b). The values outside the brackets are the

static loads of 3 AASHTO Design Trucks, the value inside the brackets are the results considering a dynamic impact factor of 1.33. The comparison of the results was given in Figure 6-22 and Table 6-3. It can be seen that finite element predictions generally match well with test results, with finite element results tending to be on the conservative side. Also, the blue dashed line in Figure 6-22 indicates the 3 truck test was carried out at a different time to other tests, i.e., during the Proof Test. Thus, structural behavior could have changed during this period.

The predicted maximum mid-span deflection of 3 AASHTO Design Trucks with and without the Dynamic Factor is 11.8 mm and 8.89 mm, respectively. The predicted peak strain under 3 AASHTO Design Trucks with Dynamic Impact Factor will be 831 με, which is about 33% of the allowable limit for Service I condition.

A final summary of test results and predictions are given in Table 6-4. Based on these results, it can be concluded that strain levels of the structural components, even after direct extrapolation to levels of design truck load, are well within the allowable limits of Service I condition. Some stiffness change was observed in the structure based on an approximate FEM analysis. However, no significant changes in the global structure behavior can be found based on the test results.

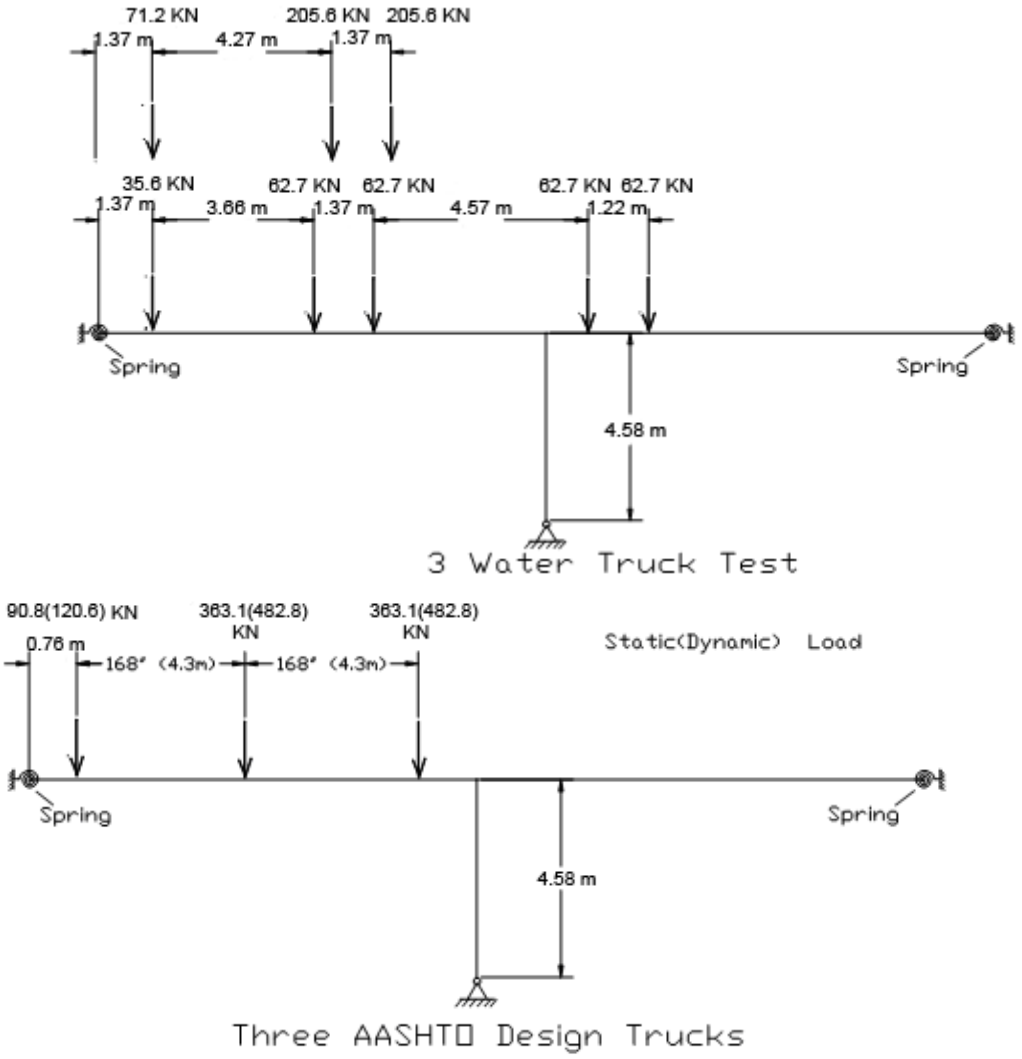

Figure 6-21 Schematic Drawing of FEM Model (3 Water Truck Test and 3 AASHTO Design Trucks)

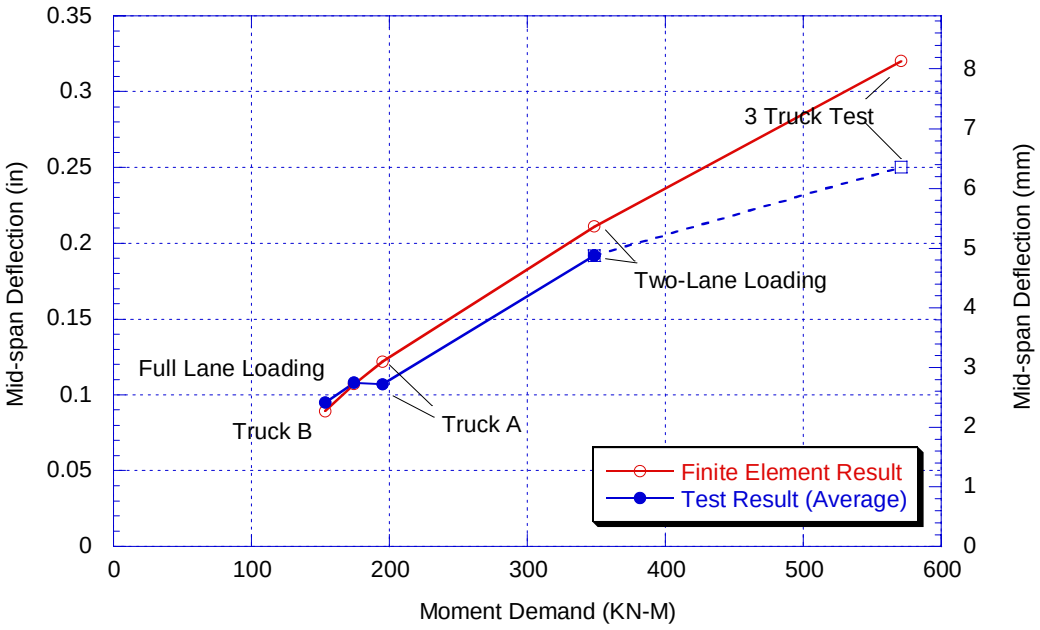

Figure 6-22 Comparison of Finite Element and Experimental Results

Table 6-3 Comparison of Mid-span Deflection of Two-Lane Loading, 3 Water Truck & 3 Design Truck Configurations

	Mid-span Deflection (mm)			Peak Strain (με)
	FEM	Test Average	Test Maximum	
Two-Lane Loading Test	5.36	4.88	8.10	377
3 Water Truck Test	9.91	6.35	9.91	450
3 AASHTO Design Trucks (w/o Dynamic Impact Factor)	8.89	/	/	625[1]
3 AASHTO Design Trucks (w/ Dynamic Impact Factor)	11.8	/	/	831[1]

[1] Predicted based on the measured peak strain of Two-lane loading test and displacement ratio between Two-Lane Loading Test and 3 AASHTO Design Trucks

Table 6-4 Summary of Test Results

	Maximum Mid-Span Deflection (mm)	Deflection-Span Ratio[1]	Peak Strain (με)	% of Allowable Strain under Service I Condition
Rolling Test	7.16	L/1400	300	12%
Full-Lane Loading Test	9.25	L/1088	403	16%
Brake Test	7.34	L/1370	291	12%
Two-Lane Loading Test	8.20	L/1226	377	15%
Predicted 3-AASHTO Design Trucks (w/o Dynamic Impact Factor)	11.1	L/906	625	25%
Predicted 3-AASHTO Design Trucks (w/ Dynamic Impact Factor)	14.8	L/682	831	33%

[1] Deflection-to-Span Ratio calculated based on the maximum mid-span deflection and a span length of 33 ft (396 in).

6.5 Implementation of a Health Monitoring System

A long-term Structural Health Monitoring System was installed on the Kings Stormwater Channel Composite Bridge shortly after it was opened to traffic. The system was designed and implemented according to the Vibration-Based Structural Health Monitoring paradigm outlined in Chapter 1. The primary purpose of the system is to monitor the changes in performance of the structure, caused by vehicular loading and environmental effects, and to provide early warning of conditions that might affect structural integrity. The system also serves the purpose of rapid condition evaluation after major events such as earthquakes and floods.

The instrumentation to measure the dynamic response of the bridge is described in this section. The initial static and dynamic tests that were used to calibrate the baseline bridge model are described in Section 6.2 and Section 6.3 respectively. The algorithms used to extract vibrational signatures and perform operational modal analysis as well as damage localization are discussed in detail in Chapter 3 and Chapter 4 of this thesis and will not be repeated herein. Similarly, methods used to update the finite element model of the structure are presented in Chapter 5 and only results that obtained are discussed in Section 6.6.

6.5.1 Instrumentation

A schematic diagram of the Kings Stormwater Bridge Health Monitoring System is shown in Figure 6-23. The dynamic response of the structure is collected by a data sensing system composed of sensors and a data acquisition system. The measured dynamic response is then transmitted, wirelessly, from the bridge site to a central data server located at the University of California, San Diego. Software that resides on the data server performs data processing, analysis and archiving in an automatic manner. The results are then provided to end users through and an user friendly, web-based user interface. The details of each subsystem are discussed in the following sections.

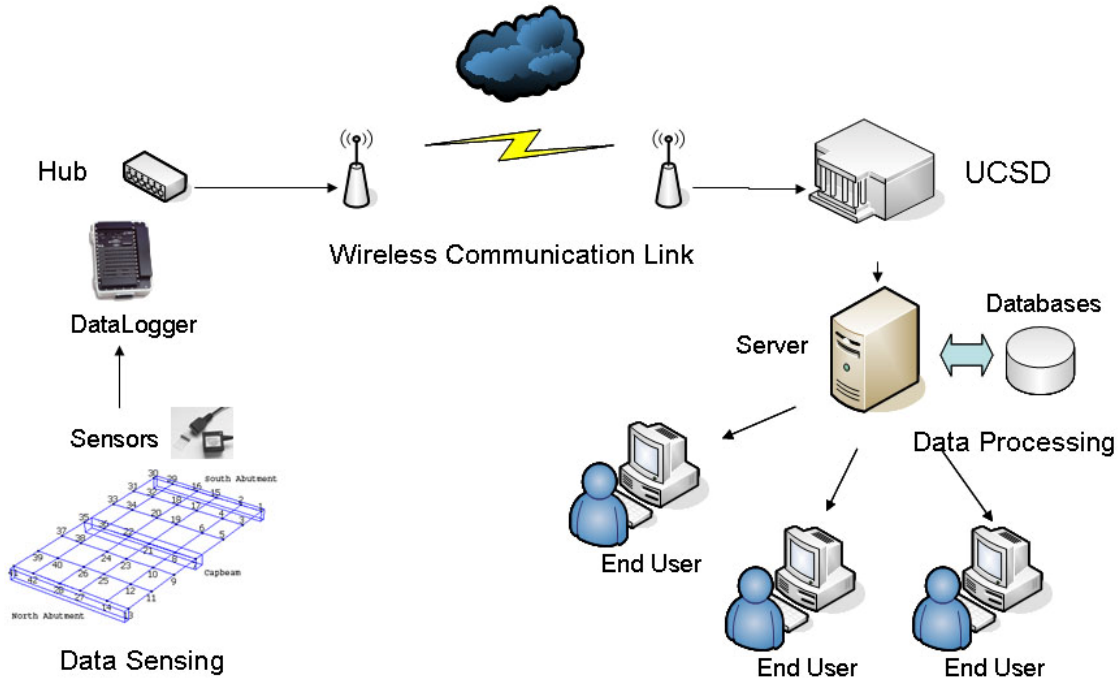

Figure 6-23 Schematic System Diagram

6.5.1.1 Sensors

A total of 63 ICSensors Model 3140 single axis accelerometers with a dynamic range of ± 2g, a sensitivity of 1 V/g and a usable frequency response of 0-200 Hz were installed on the bridge. Accelerometers were installed in protective housings attached to the bottom of the deck, as illustrated in Figure 6-24a. Accelerometers themselves are mounted by screws on metal mounting blocks that are glued to the bottom of the deck using high-strength epoxy, shown in Figure 6-25. Signal cables leading to the accelerometers are protected by steel conduits that are also mounted to the bottom of the deck using epoxy. The mounting locations of accelerometers are carefully selected to form an evenly distributed 7-by-6 measurement grid (7 in the bridge longitudinal direction and 6 in the bridge transverse direction), as shown in Figure 6-26. In half of

the protective housings, two accelerometers were mounted to the same mounting block, one in the vertical direction, and the other in the horizontal direction. These are used to measure the vertical and horizontal vibration of the bridge correspondingly.

(a) (b)

Figure 6-24 Instrumentation Housing and Conduit: (a) Accelerometer Housing (b) Strain Gage Housing and Conduits

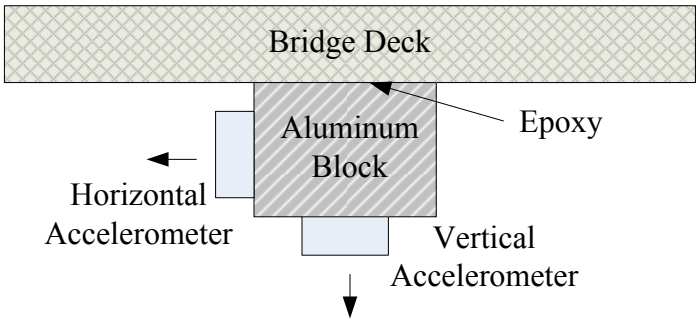

Figure 6-25 Illustration of Accelerometer Mounting

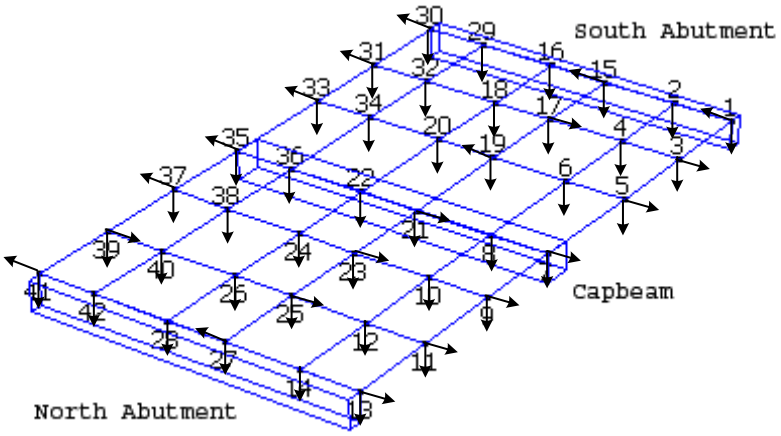

Figure 6-26 Accelerometer Locations (Arrows indicating measurement direction)

Twenty resistive strain gages were also installed on the bottom of the deck and on the surface of carbon shell girders, as illustrated in Figure 6-24b. The locations of the strain gages are described in Section 6.4.2 and also given in Figure 6-11. Like the accelerometers, the strain gages are also located in protective housings that are water sealed. Location of the strain gages are selected so that high strain regions on the deck panel and carbon shell girders, determined through previous experiment and analysis (Burgueño 1999), are monitored. Four linear potentiometers were used to measure the maximum deflection at the middle of each span, shown in Figure 6-12. Temperature drift is monitored by a LM35 precision integrated-circuit temperature sensor located on the center capbeam, shown in Figure 6-11.

6.5.1.2 Data Acquisition System

Multipair shielded cables are used to carry signals from sensors to the data acquisition system. The data acquisition system is located in a separate enclosure

approximately 40 m from the composite bridge. The longest cable run from the sensors to the data acquisition system measures approximately 65 m. All signal cables are protected by PVC conduits that run from the bridge to the data acquisition system enclosure.

Signals from accelerometers, strain gages and potentiometers are first denoised with hardware low-pass filter, removing high frequency noise from the measurement. The low-pass filter also serves as anti-aliasing filter to prevent aliasing effects when the analog signal is digitized. The signals from accelerometers are also detrended to remove any constant DC drift that may be present. The signals are then digitized using a Campbell Scientific CR9000C high speed data logger, shown in Figure 6-27. The CR9000 datalogger is capable of making measurements at an aggregate sampling rate of 100K Hertz for up to 200 channels. A TCP/IP interface enables communication and data collection via standard wired or wireless networks. The datalogger has a CPU and internal flash memory and can be programmed to sample the data when certain conditions are met. All signal conditioning units and the datalogger are housed in an equipment cabinet located in the data acquisition enclosure (Figure 6-28).

Utility power (120VAC, 60Hz) is provided at the bridge site and connected to a circuit breaker to electrically isolate the bridge system and protect the power wiring. In case of a power outrage, backup battery units are installed in the data acquisition enclosure. The signal conditioning units and the datalogger will be powered by battery whenever the voltage of the utility power line reduces to a specified threshold. During

normal working conditions, the backup battery units are charged through two battery chargers connected to the utility power line.

6.5.1.3 Wireless Data Transmission System

To transmit digitized data from the bridge site to the University of California, San Diego, a 2.4 GHz band wireless link was utilized. The wireless data link is part of the High Performance Research and Education Network (Vernon 2001) which serves research and education users in the southern California area. The data acquisition is connected through a wireless Modem to a wireless antenna, shown in Figure 6-29. The antenna was erected at the bridge site where it has direct line-of-sight communication to a mountain top relay station. From there it passes through several more relay stations until it reaches the central network node at the San Diego Super Computer Center, located within the University of California, San Diego campus. Figure 6-30 shows the Network Topo map as of December 2004. The central network node at SDSC was connected through high-speed campus network with data processing server located at the Department of Structural Engineering. The total range that data was transmitted was approximately 307 km (190 miles). During real world speed test, the link was shown to be capable of a data rate as fast as 4 Mbps.

Figure 6-27 CR9000 Datalogger

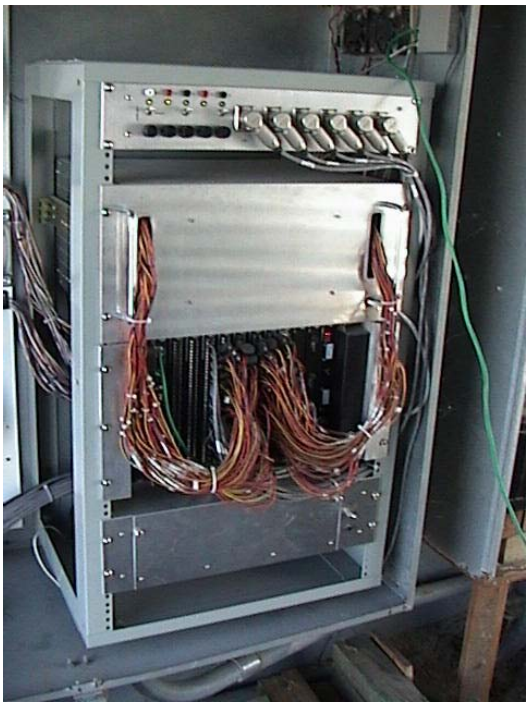

Figure 6-28 Data Acquisition Equipment Cabinet

(a) Wireless Antenna (b) Wireless Modem

Figure 6-29 Wireless Antenna and Wireless Modem on the Bridge

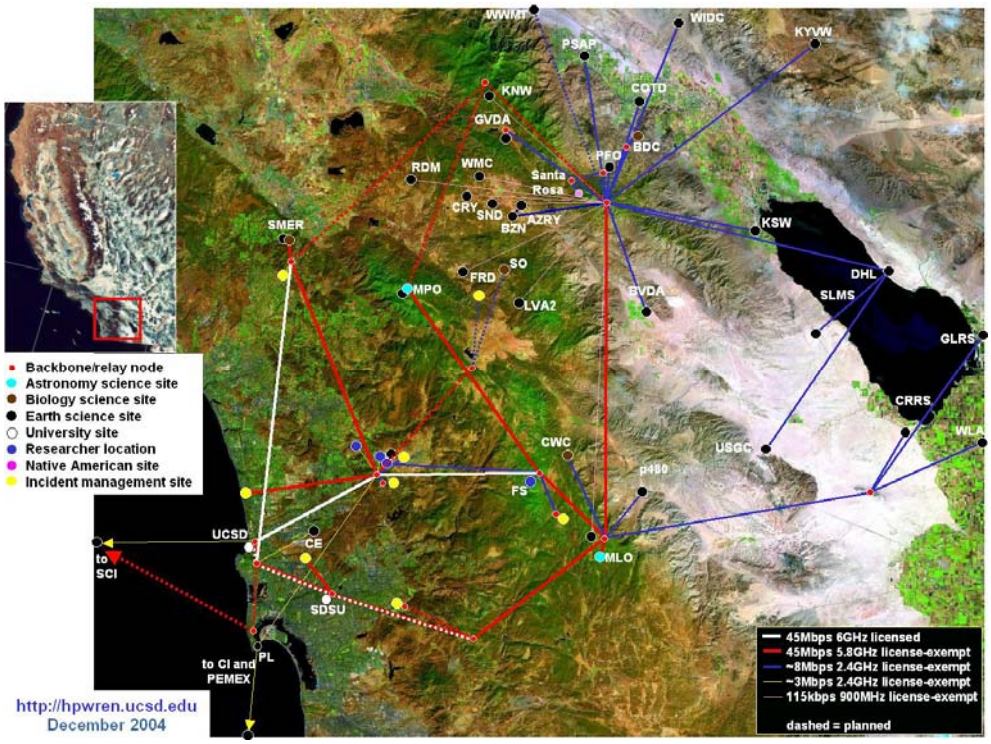

Figure 6-30 Network Topo Map of HPWREN (HPWREN 2003)

6.5.2 Data Processing and Archiving

The automated collection, digitization and transmission of data are controlled by two collaborating programs, as shown in Figure 6-31. The first program, running on the CR9000 datalogger and written in CRBASIC, which is a BASIC like programming language specially tailored for running on CR9000 dataloggers, serves the collection and digitization function. It enables data from all channels to be collected at preset intervals and when triggered either by an extreme event, such as an earthquake, or when a preset response threshold is exceeded, such as deflection or acceleration from extremely heavy traffic or permit loads. It also allows for data from a selected number of channels, denoted as "streaming channels" to be collected and transmitted continuously in real-time.

The second program, written in Visual Basic, is housed on a dedicated data server at a central location at the University of California, San Diego, and serves both data transmission and analysis functions. Streaming data from the datalogger are parsed at the data server, reduced, and fed into a data-redirect program where authorized users can view and download the data in real time from their own computer with an internet connection. A screen capture of the real-time streaming data display is shown in Figure 6-32. The data-redirect program uses a special data transmission protocol named DataSocket (National Instruments 1999). Once collected, event-based data are analyzed to extract vibrational signatures of the structure. All raw event-based data and the extracted signatures are then archived in a database for future reference.

In order to enable secure access of data and to reduce computational requirements at the user's end, a specially designed client-server architecture using Active-X controls is implemented. This embedded program runs within a user's web browser and enables access to the main server by multiple users at the same time. The setup facilitates rapid acceptance of a user's input, subsequent communication with the server and then transfer of the requested data and analysis results to the user. The analysis is thus carried out on the central server, although a user can still request access to the data itself for subsequent analysis.

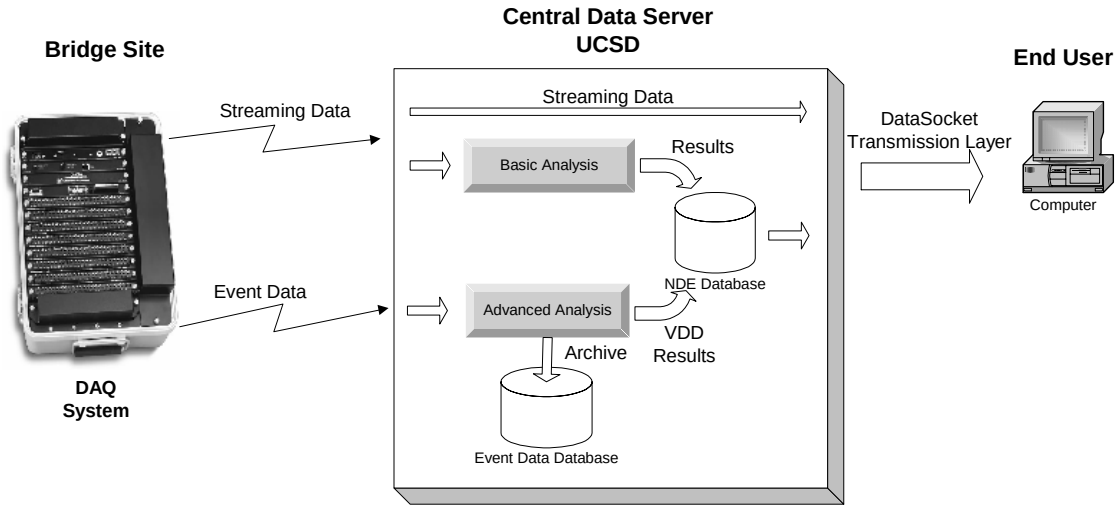

Figure 6-31 Data Processing and Archiving Flow Chart

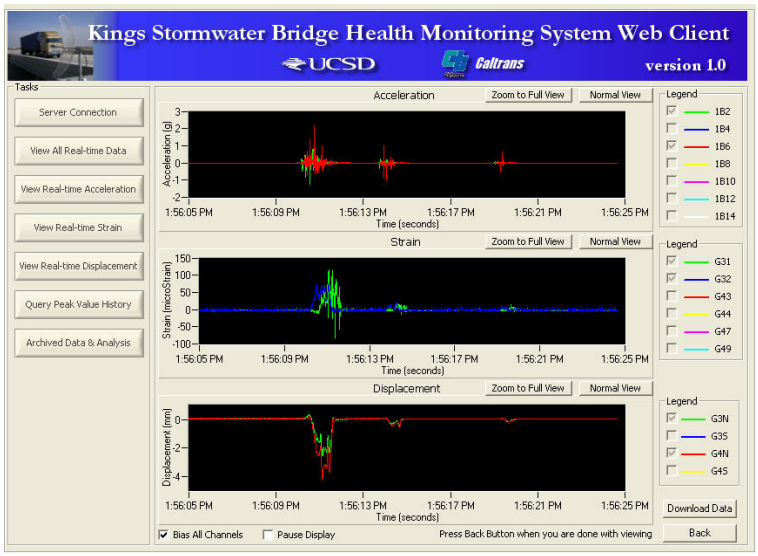

Figure 6-32 Real Time Streaming Data Display

6.6 Vibration-Based Health Monitoring Results

A tremendous amount of data was recorded by the health monitoring system since its implementation in 2001. For example, acceleration data collected during this period of time amounts to approximately 26 GB. It is impossible to present the details of all data collected within the scope of this dissertation. Thus, only some important results observed from the data are summarized in this section.

6.6.1 Ambient Acceleration Data

One major source of ambient excitation to the bridge structure is vehicular traffic. An example of the typical vertical acceleration time history due to vehicular traffic is plotted in Figure 6-33. Under vehicular excitation, the magnitude of vertical acceleration is much larger (at least one order of magnitude larger) than the magnitude of horizontal acceleration and provides significantly better signal-to-noise ratio. Thus,

most of the vibration-based health monitoring results presented below is based on vertical accelerations. It should be noted that, due to the high damping nature of the structure, the vibration response die out very rapidly after the vehicle leaves the bridge. The corresponding power spectral density of the vertical acceleration is given in Figure 6-34.

Another major source of ambient excitation is due to wind or other environment transmitted vibrations, such as vibrations caused by vehicular traffic close to, but not traveling on the bridge. A typical example of this type of ambient acceleration recorded by the monitoring system is plotted in Figure 6-35.

Wind induced ambient vibrations have much smaller amplitude compared with those caused by vehicular traffic. However, the duration of wind induced ambient vibration is much longer, as can be seen in Figure 6-35. Longer duration means higher frequency resolution can be achieved when the natural frequencies of the structure needs to be identified. The power spectral density of wind induced ambient vibration is plotted in Figure 6-36.

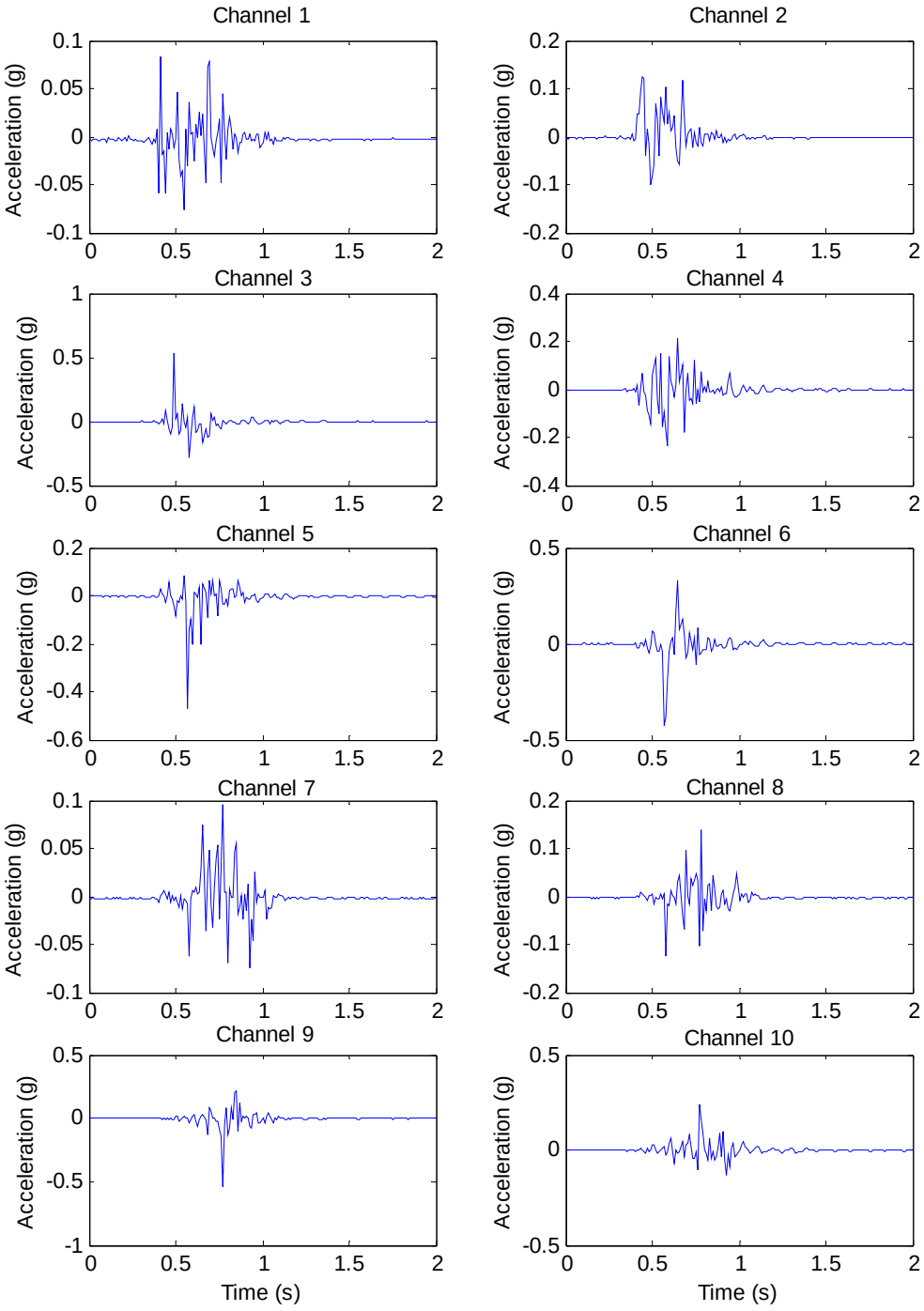

Figure 6-33 Typical Vertical Acceleration Time History Due to Vehicular Traffic

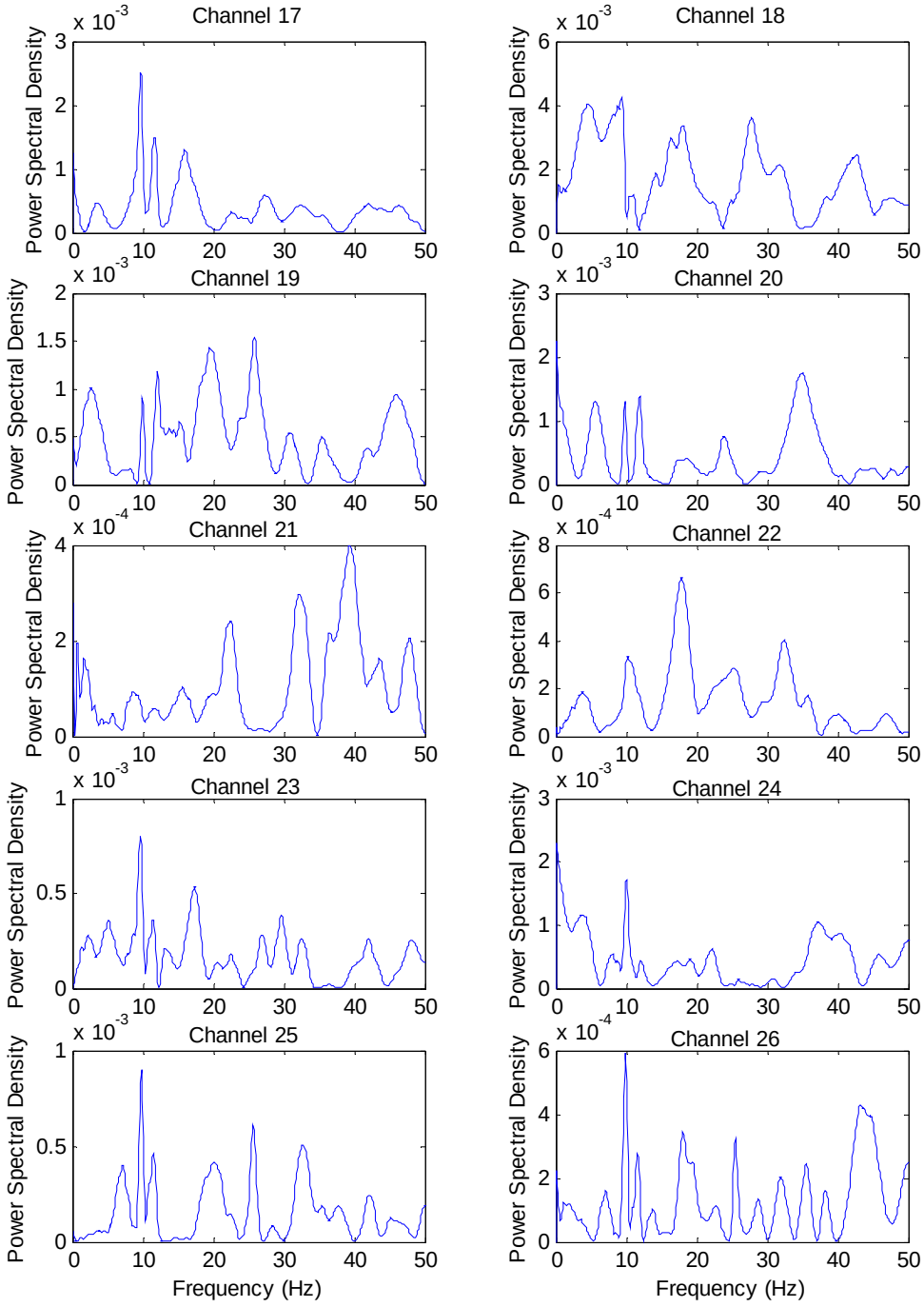

Figure 6-34 Typical Power Spectral Density of Vertical Acceleration Due to Vehicular Traffic

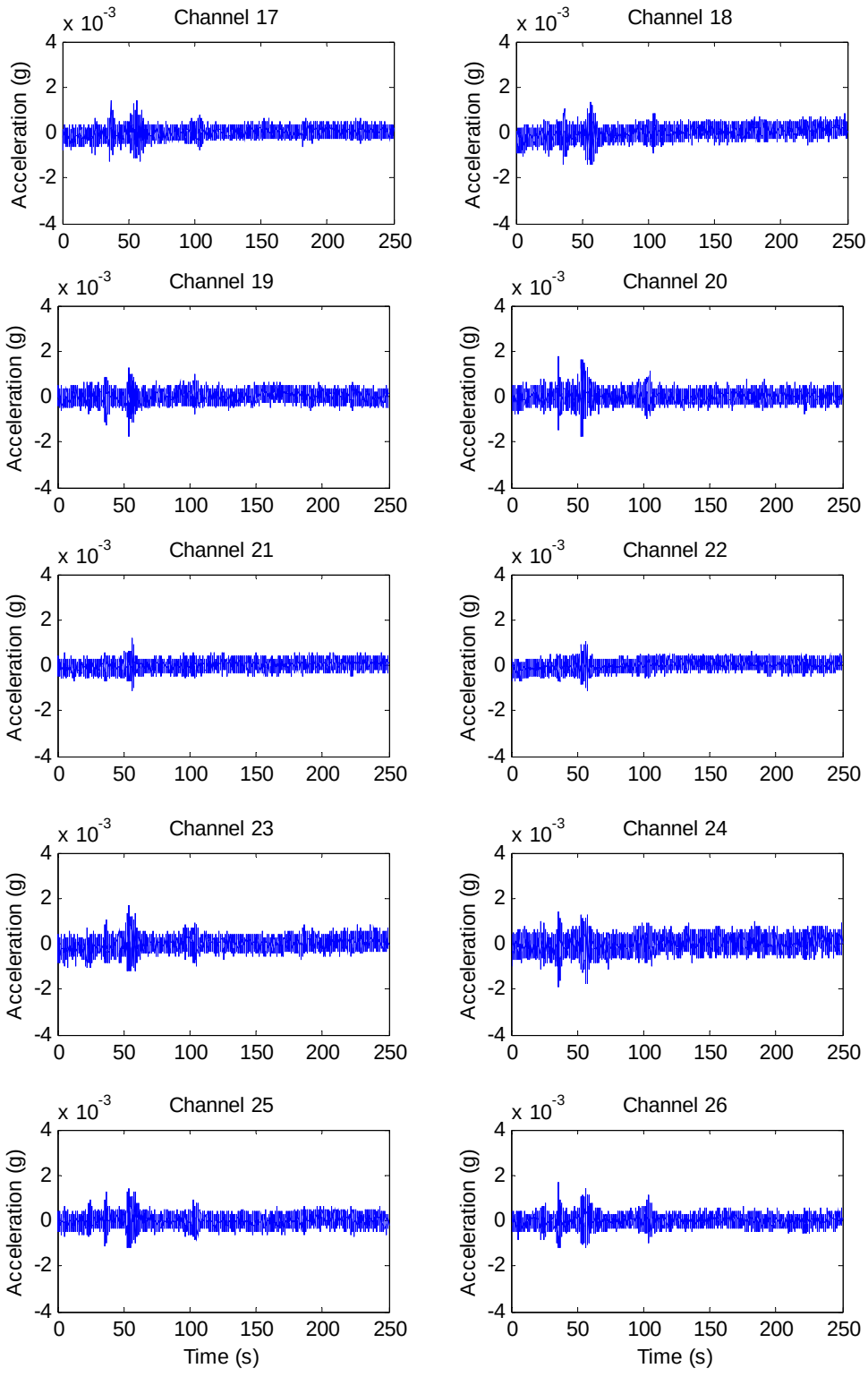

Figure 6-35 Typical Vertical Acceleration Time History Due to Other Ambient Sources

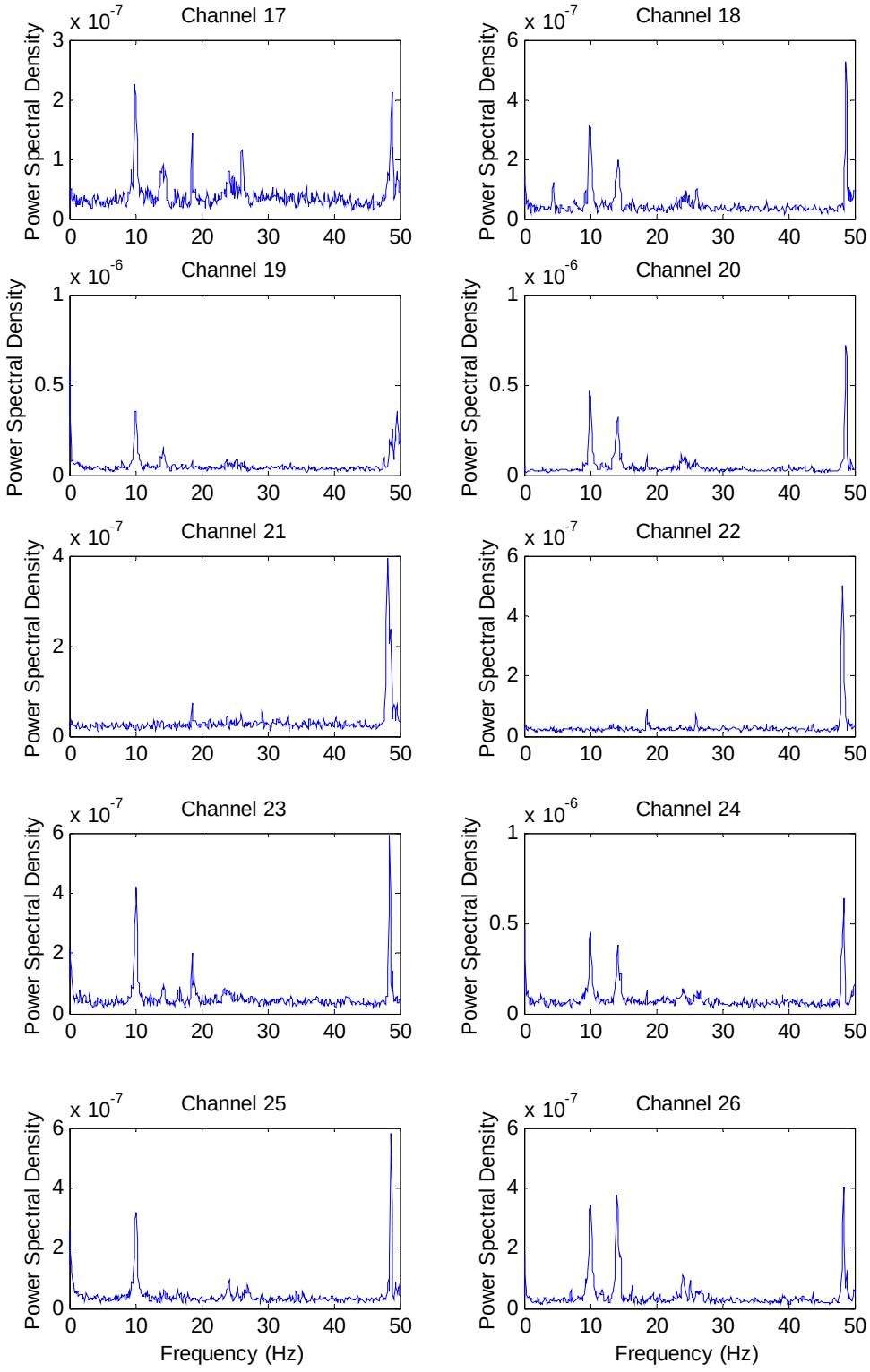

Figure 6-36 Typical Power Spectral Density of Vertical Acceleration Due to Other Ambient Sources

6.6.2 Natural Frequency Variations

Data sets collected at different times were analyzed and the resulting natural frequencies were compared. The frequencies identified in the May 2001 forced vibration modal test was considered as the "baseline" set as it represents the pristine condition of the bridge. All other data sets are recorded by the health monitoring system during the normal operation of the bridge. Both the TDD method and FNExT method described in Chapter 3 are used to analyze the operational data sets. Results from the two methods generally show very good agreement. In cases where there are discrepancies between the results from different methods, an averaged value is used for further study.

It should be noted that the bridge is located in an area where daily temperature varies greatly. So in order to minimize the effect of daily temperature change on the results, all data sets analyzed were collected during the period between 2:00 AM and 3:00 AM. Only the natural frequencies of the first two fundamental modes of the structure are consistently identified through all operational data sets. Thus the discussion that follows is limited to the first two modes only. It is observed that the first and second natural frequency experienced a significant drop between the time of May 2001 and April 2002. The first natural frequency dropped almost 1 Hz from 11.03 Hz to 10.06 Hz (Table 6-5). The second natural frequency also showed a drop of approximately 0.6 Hz. This drop is believed to be caused by the settlement of the abutments and piers, which can considerably change the structural boundary conditions. Year-to-year frequency variation showed no clear trend after April 2002. But the first natural frequencies measured in the month of April showed distinct differences from

those measured in the month of July, with the average of the April frequencies approximately 0.31 Hz higher than the average of July frequencies. The natural frequencies of the second mode showed greater dispersion compared with those of first mode. The frequencies in July in 2002 and 2003 are lower than in April of the corresponding year. But in 2004 and 2005, the trend is reversed. Considering the fact that the average daily temperature at the bridge site in the month of July (approximately 38 °C, see (NOAA 2001)) is much higher than that of the month of April (approximately 30 °C), it can be concluded from these observations that the seasonal variation of temperature can have a significant impact on natural frequencies. At the same time, the effect of damage, if any, on the natural frequencies seems to be small and may not be observable given the greater effect of varying environmental conditions.

Table 6-5 Variation of Natural Frequencies at Different Months of the Year

Date		Natural Frequencies (Hz)	
		1st Mode	2nd Mode
May, 2001 (Baseline)		11.03	13.11
April	2002	10.06	12.50
	2003	10.16	12.10
	2004	10.06	12.01
	2005	9.77	11.71
July	2002	9.76	12.20
	2003	9.77	11.91
	2004	9.76	12.30
	2005	9.57	11.91

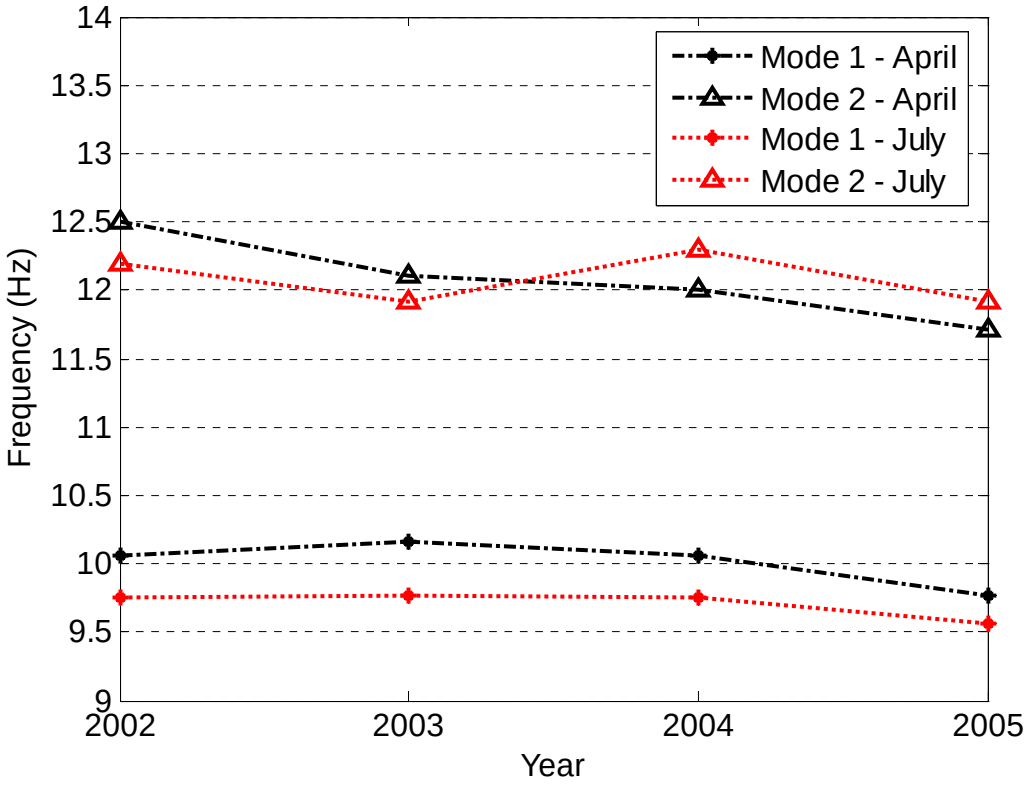

Figure 6-37 Variation of Natural Frequencies at Different Months of the Year

6.6.3 Mode Shape Variations

The baseline mode shapes of the first two fundamental modes are plotted in Figure 6-38. The baseline mode shapes are obtained from the forced vibration modal testing described in Section 6.3. Five sets of mode shapes identified from operational vibration data of the bridge are plotted in Figure 6-39 to Figure 6-43 as examples. For comparison purposes, all modes shapes except the first one are identified from operational data recorded during the month of April of each year.

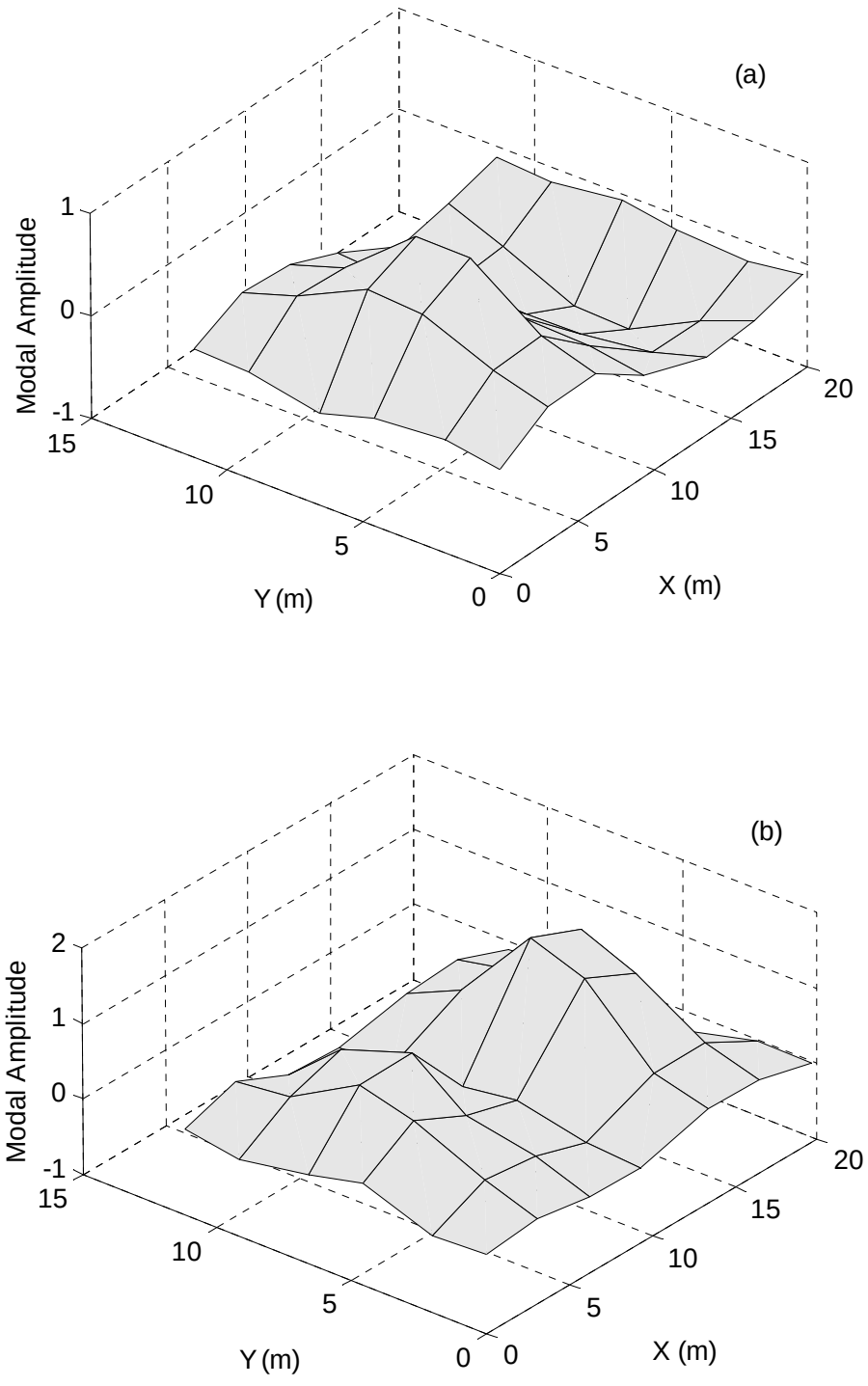

Figure 6-38 Baseline Mode Shapes: (a) 1st Mode (b) 2nd Mode

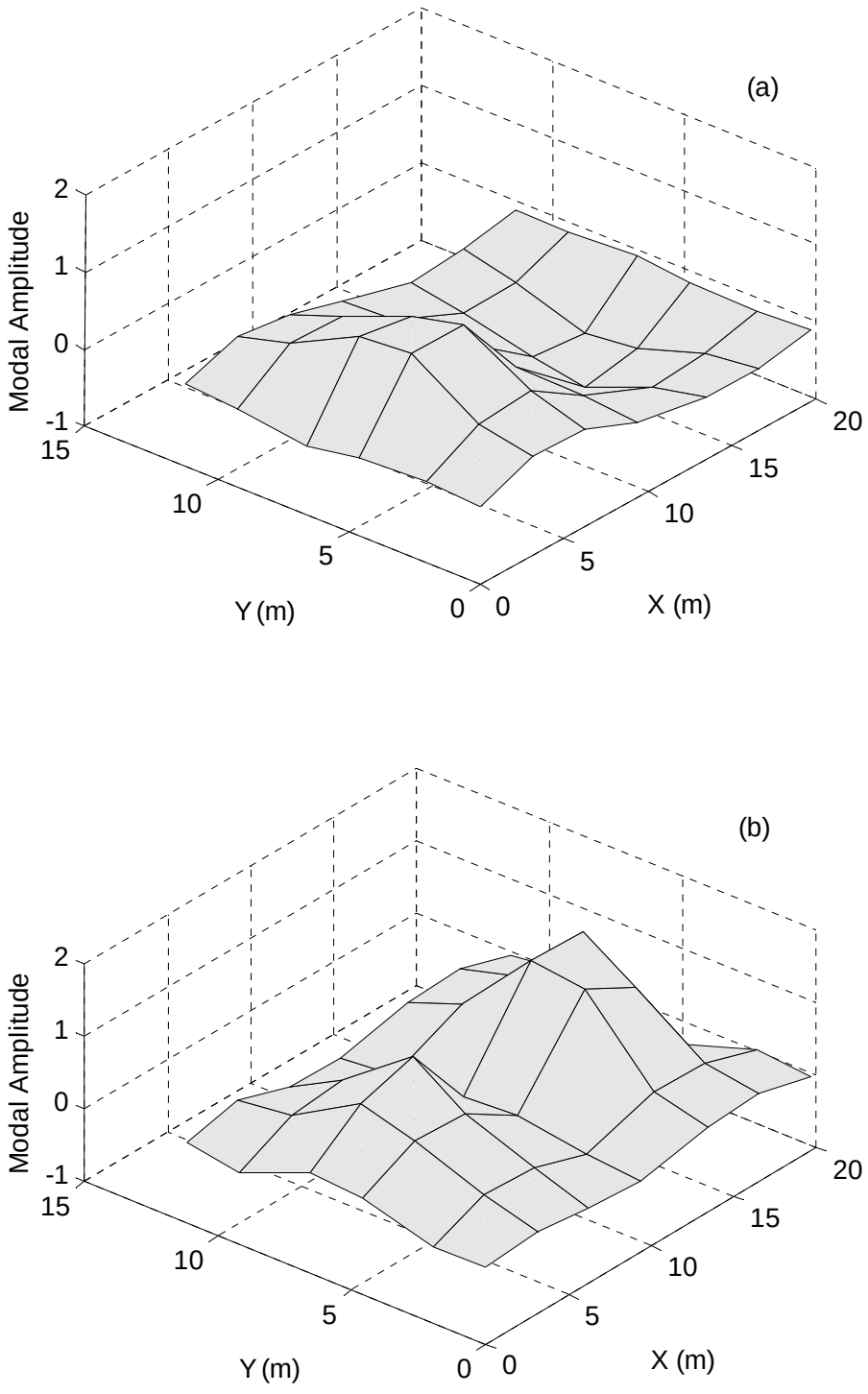

Figure 6-39 Mode Shapes of the Bridge As of October 01, 2001: (a) 1st Mode (b) 2nd Mode

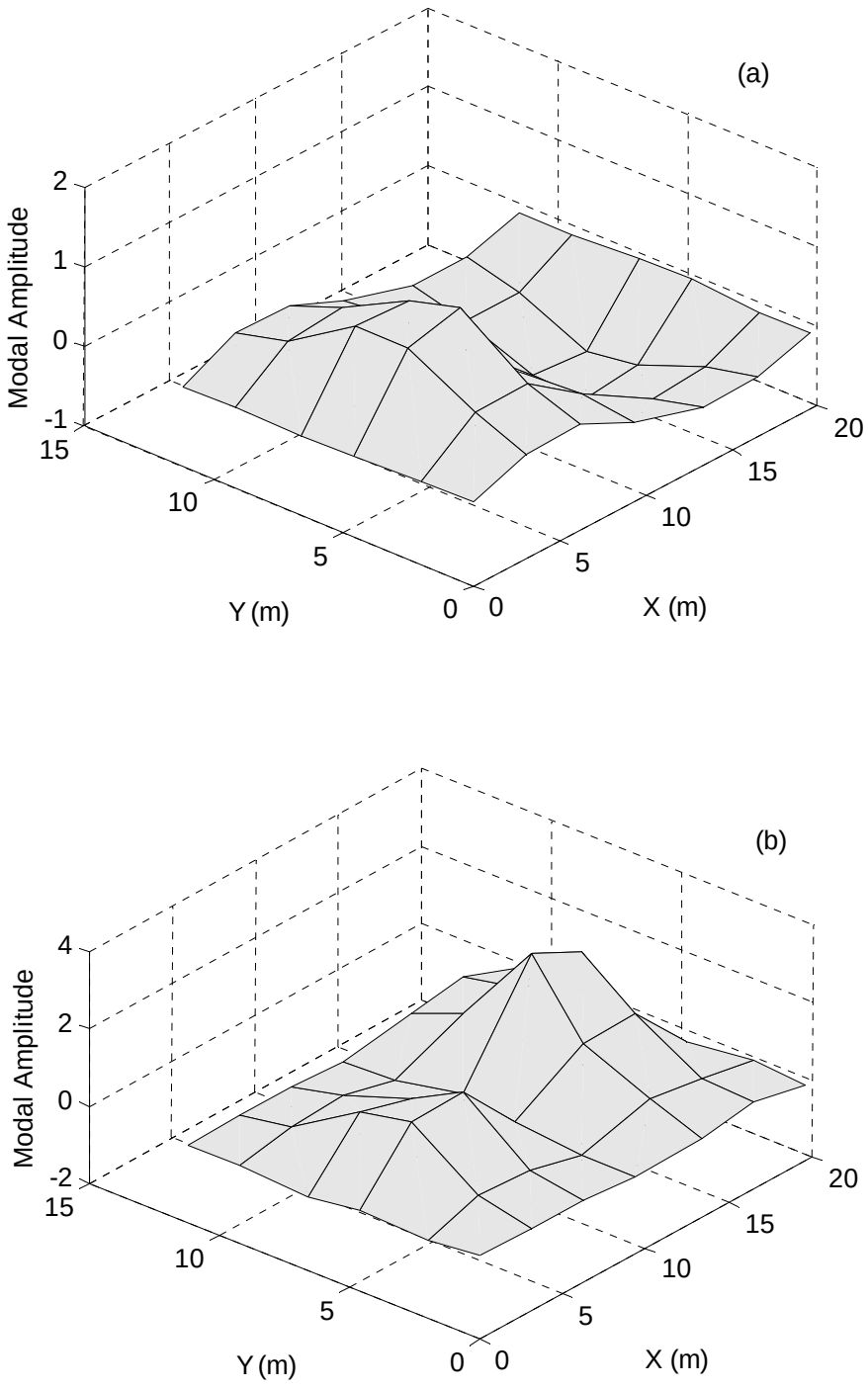

Figure 6-40 Mode Shapes of the Bridge As of April 30, 2002: (a) 1st Mode (b) 2nd Mode

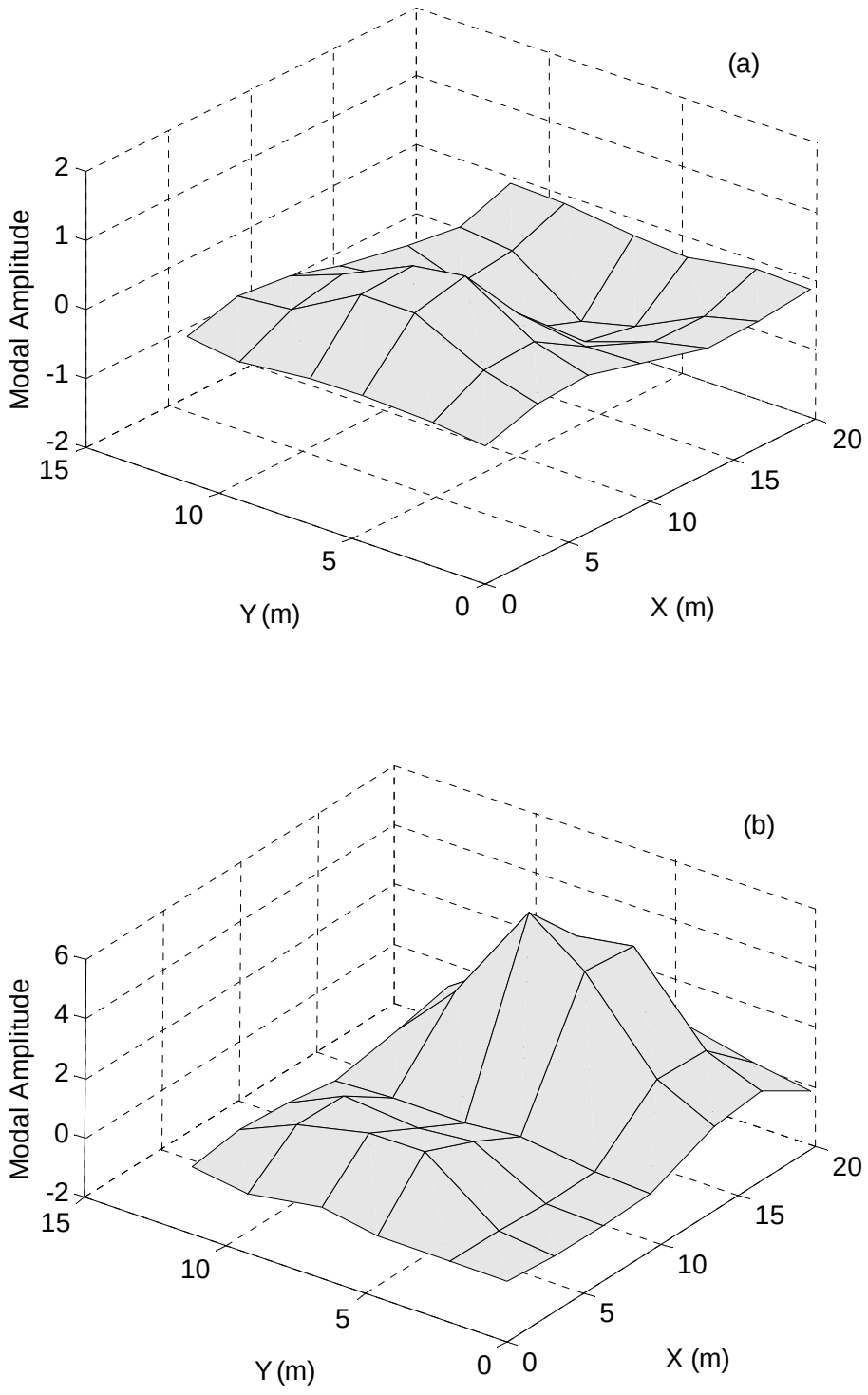

Figure 6-41 Mode Shapes of the Bridge As of April 10, 2003: (a) 1st Mode (b) 2nd Mode

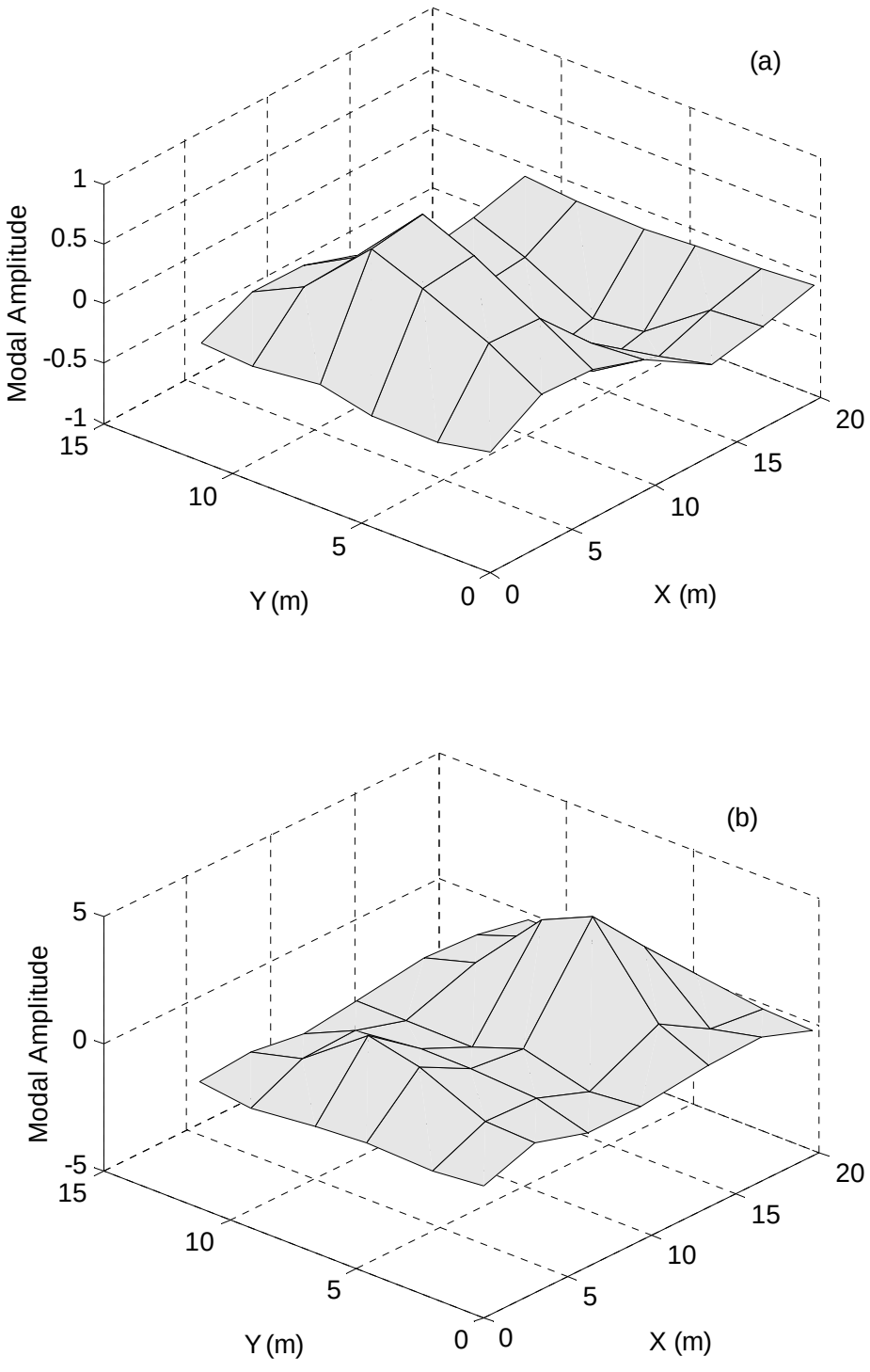

Figure 6-42 Mode Shapes of the Bridge As of April 04, 2004: (a) 1st Mode (b) 2nd Mode

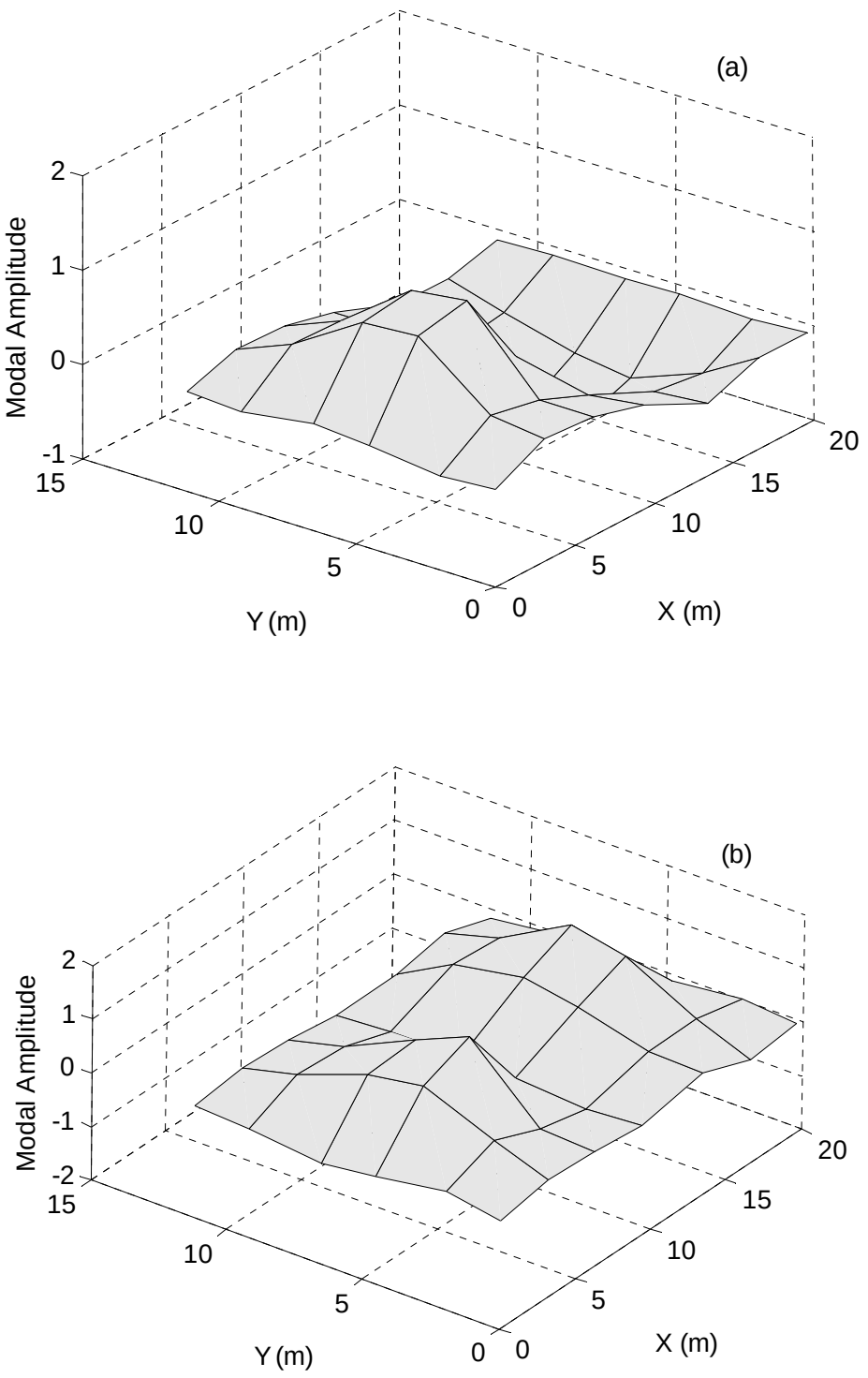

Figure 6-43 Mode Shapes of the Bridge As of April 24, 2005: (a) 1st Mode (b) 2nd Mode

The variations of mode shapes can be quantified using the Modal Assurance Criterion (West 1984). The MAC values between each operational mode shape and the baseline mode shape are listed in Table 6-6 and plotted in Figure 6-44.

Table 6-6 MAC Values between Operational Mode Shapes and the Baseline

Date	MAC Values	
	1st Mode	2nd Mode
May 03, 2001	1.0000	1.0000
October 01, 2001	0.9603	0.9752
April 30, 2002	0.9692	0.8521
April 10, 2003	0.9574	0.8585
April 04, 2004	0.9435	0.8495
April 24, 2005	0.9214	0.8113

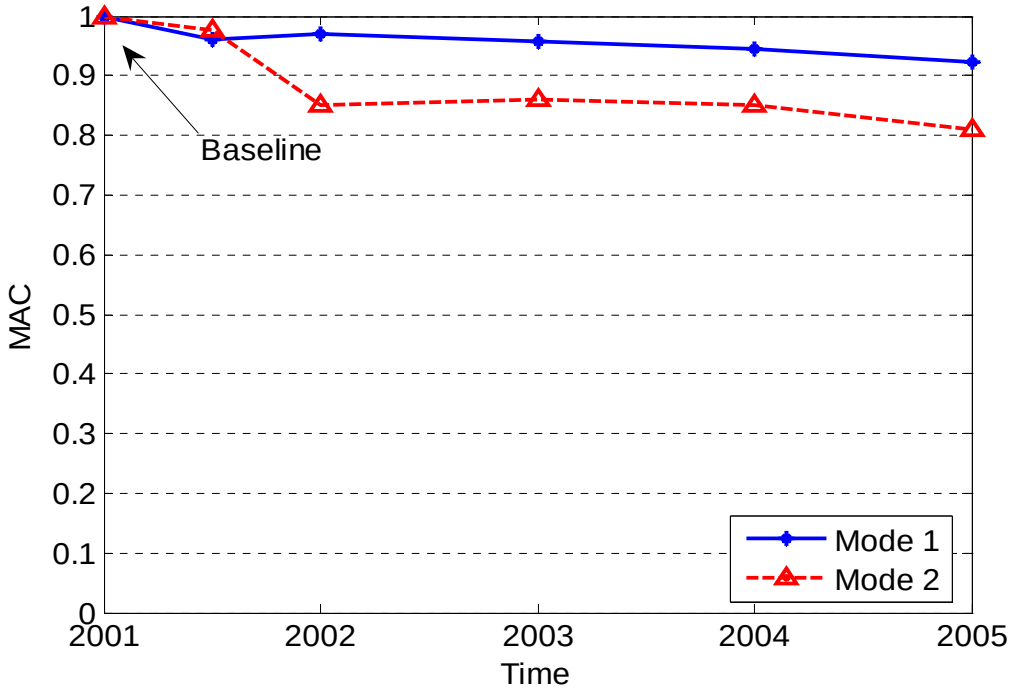

Figure 6-44 Variation of MAC Values with Time

The MAC values of the 1st mode drops from unity to approximately 0.9692 on April 2002, a year from when the baseline test was conducted. The MAC values further drops to 0.9574 and 0.9435 on April of 2003 and April of 2004, respectively. On April of 2005, the MAC value of the 1st mode stands at 0.9214. For the 2nd mode, the MAC values drops to about 0.8521 after a year and stayed at around 0.85 for the two subsequent years. It drops to 0.8113 on April of 2005. While the general trend of MAC values indicates that the fundamental mode shapes of the structure experienced significant change between year 2001 and 2005, it is unclear which region sees the most change and to what extent.

6.6.4 Damage Localization

Once the mode shape is identified from operational data, the EMSDI method described in Chapter 4 is applied to detect damage in the structure. The 2D version of the algorithm (Section 4.4) is used for this case due to the plate-like nature of the bridge.

The bridge structure is divided into 6 segments in the bridge longitudinal direction (X direction) and 5 segments in the bridge transverse direction (Y direction), shown in Figure 6-45. The separation line between two segments coincides with the line formed by connecting adjacent accelerometers. Each region at the intersection of two segments in perpendicular directions forms the smallest element for EMSDI calculation. The total number of elements equals to 30. Element Modal Strain Damage Index is calculated for each element using Eq. (4.32).

The EMSDI difference between the baseline and the data sets at October 2001, April 2002, April 2003, April 2004 and April 2005 are plotted in Figure 6-46 to Figure

6-50. The magnitude of the EMSDI difference is represented by the height of the 3D bar at each element location. A sudden change of EMSDI difference magnitude indicates potential damage areas. It is noted that most of the higher EMSDI difference values are concentrated in the North span towards the centerline of the bridge.

The vibration measurements used to calculate the EMSDI are inevitably contaminated with noise from various sources. It is expected that the resulting EMSDI will show some scatter due to measurement noise, e.g., An EMSDI value greater than zero does not necessarily mean an element is damaged. In order to better distinguish the potential damaged regions, the mean and standard deviation of the EMSDI difference can be calculated using the following fomula:

$$\overline{\Delta}_{EMSDI} = \frac{\sum_{i=1}^{n} \Delta_{EMSDI}^{i}}{n} \tag{6.1}$$

$$\sigma_{\Delta}^{2} = \frac{\sum_{i=1}^{n} \left(\Delta_{EMSDI}^{i} - \overline{\Delta}_{EMSDI} \right)^{2}}{n-1} \tag{6.2}$$

where Δ_{EMSDI}^{i} stands for the EMSDI difference of the i^{th} element, n stands for the number of elements and $\overline{\Delta}_{EMSDI}$ stands for the mean value of EMSDI difference. σ_{Δ} is the standard deviation of EMSDI difference. The normalized EMSDI difference is then defined as:

$$\tilde{\Delta}_{EMSDI}^{i} = \frac{\left| \Delta_{EMSDI}^{i} \right|}{\sigma_{\Delta}} \tag{6.3}$$

in which, $\tilde{\Delta}^{i}_{EMSDI}$ is the normalized value for the i^{th} element. A threshold can be set based on the normalized EMSDI difference to separate potential damaged regions with those that are probably not damaged. For the current case, regions with $\tilde{\Delta}^{i}_{EMSDI} > 1$, i.e., normalized EMSDI difference larger than one standard deviation, and regions with $\tilde{\Delta}^{i}_{EMSDI} > 2$, i.e., normalized EMSDI difference larger than two standard deviations, are plotted in Figure 6-51 to Figure 6-55 and Figure 6-56 to Figure 6-60, respectively. The first threshold corresponds to a confidence level of 68.26% assuming the EMSDI difference is normally distributed. The second threshold corresponds to a confidence level of 95.46%. The results are summarized as follows:

For the case of 68% confidence level threshold, for October 1st, 2001 data set, probable damage regions are indicated at elements (2, 1), (2, 2), (3, 1), and (3, 2) , where the first coordinate inside the bracket is the row number of the element and the second coordinate stands for the column number. For April 30th, 2002 data set, damage is indicated at elements (2, 2), (2, 3), (3, 1) and (3, 2). For April 10th, 2003 data set, damage is indicated at elements (3, 2), (3, 3), (4, 3) and (5, 2). For April 4th, 2004 data set, damage is indicated at elements (3, 1), (4, 1) and (4, 2). For April 24th, 2005 data set, the probable damage region is indicated at elements (1, 2), (2, 2), (2, 3) and (3, 4).

For the case of 95% confidence level threshold, for October 1st, 2001 data set, probable damage regions are indicated at the element (2, 2) and element (3, 1). For April 30th, 2002 data set, damage is indicated at element (2, 2) and element (3, 2). For April 10th, 2003 data set, damage is indicated at elements (3, 2) and (3, 3). For April 4th,

2004 data set, probable damage region is indicated at element (4, 2). Finally for April 24th, 2005 data set, damage is indicated at element (2, 2).

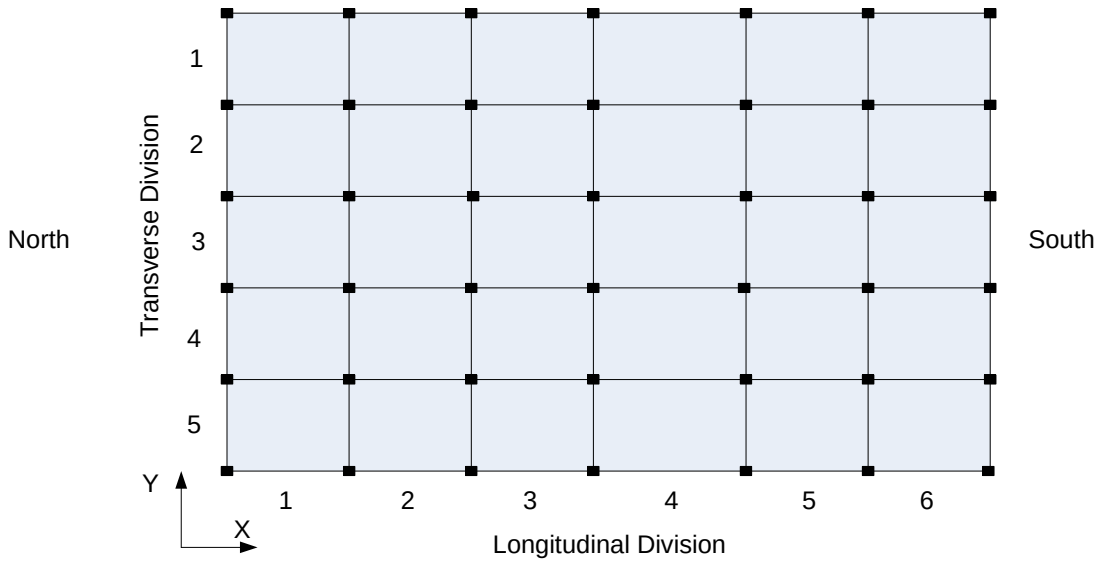

Figure 6-45 Division of the Bridge Structure into Segments (Black Squares Represent Accelerometer Locations)

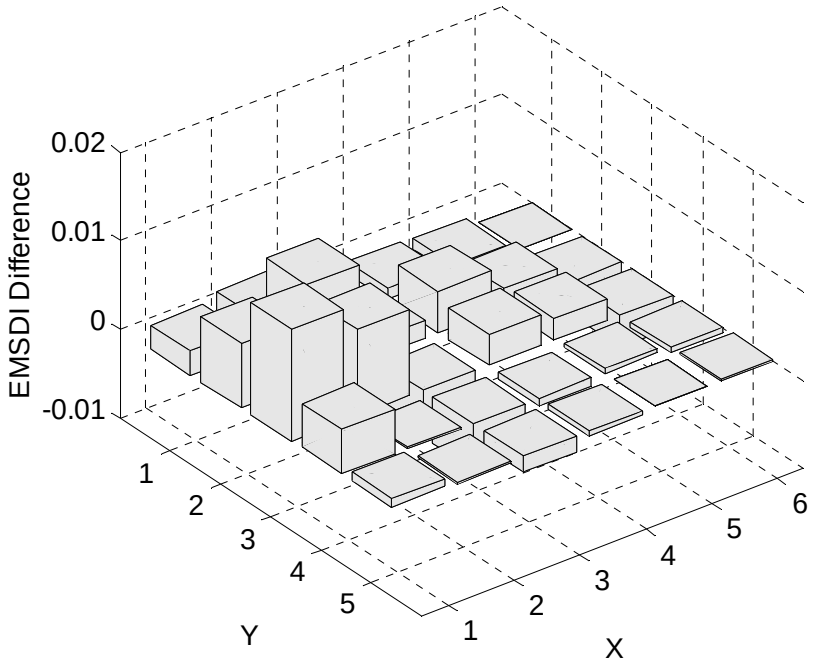

Figure 6-46 EMSDI Difference Between October 01, 2001 and the Baseline

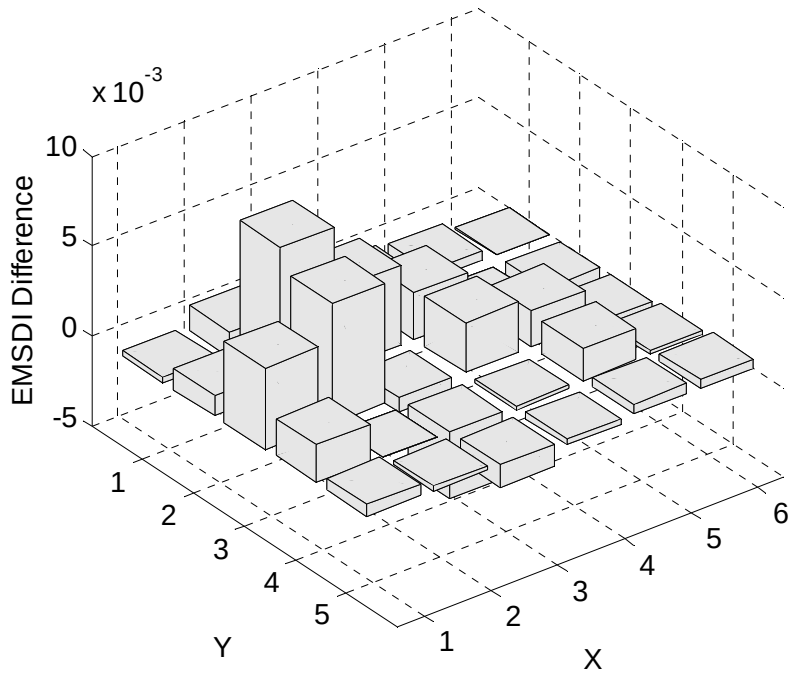

Figure 6-47 EMSDI Difference Between April 30, 2001 and the Baseline

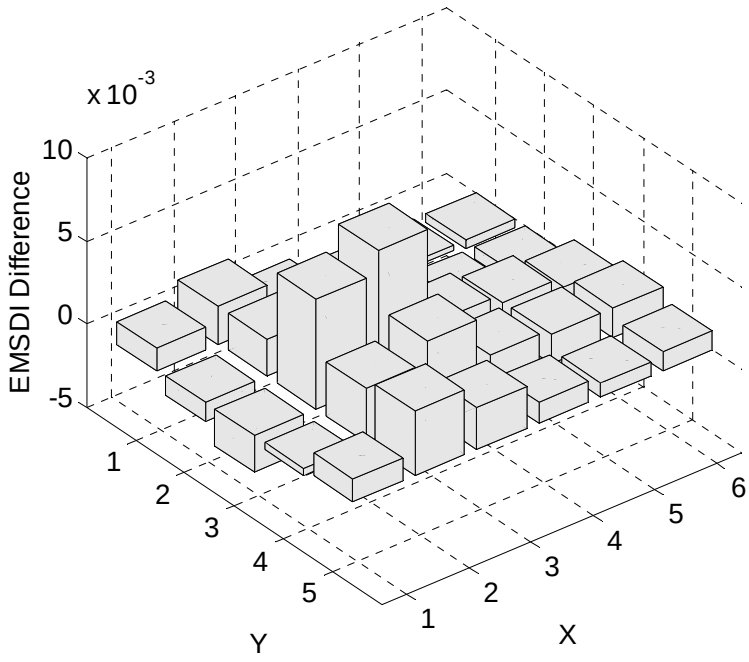

Figure 6-48 EMSDI Difference Between April 10, 2003 and the Baseline

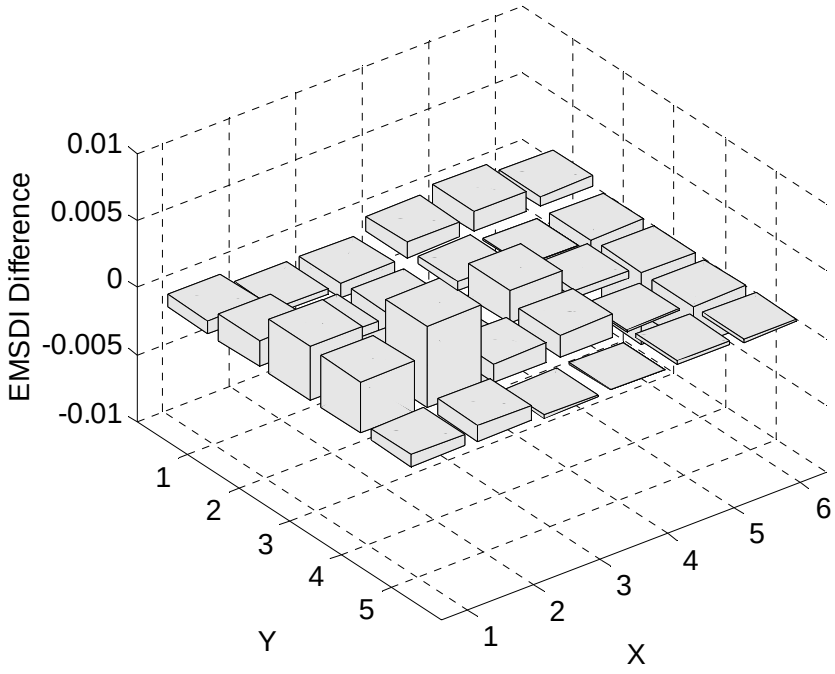

Figure 6-49 EMSDI Difference Between April 04, 2004 and the Baseline

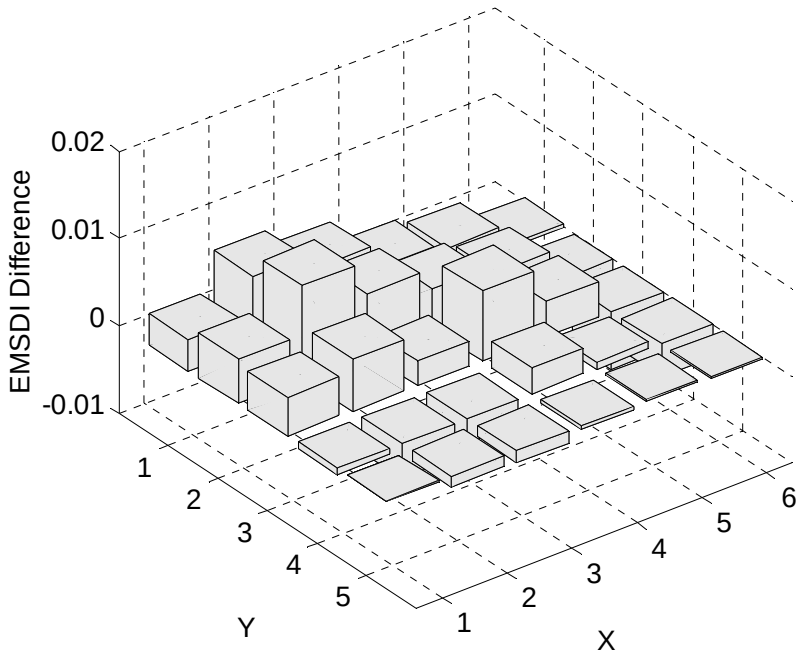

Figure 6-50 EMSDI Difference Between April 24, 2005 and the Baseline

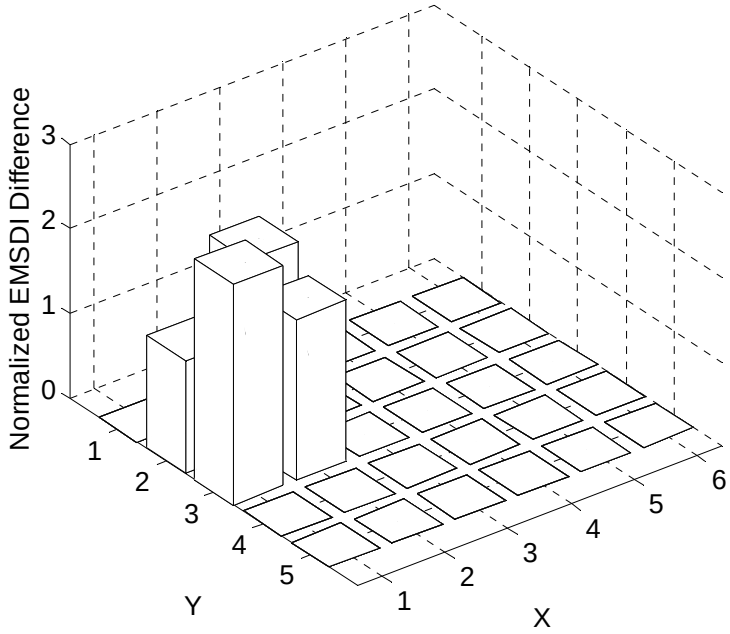

Figure 6-51 Probable Damage Regions (68% Confidence Level) – October 01, 2001

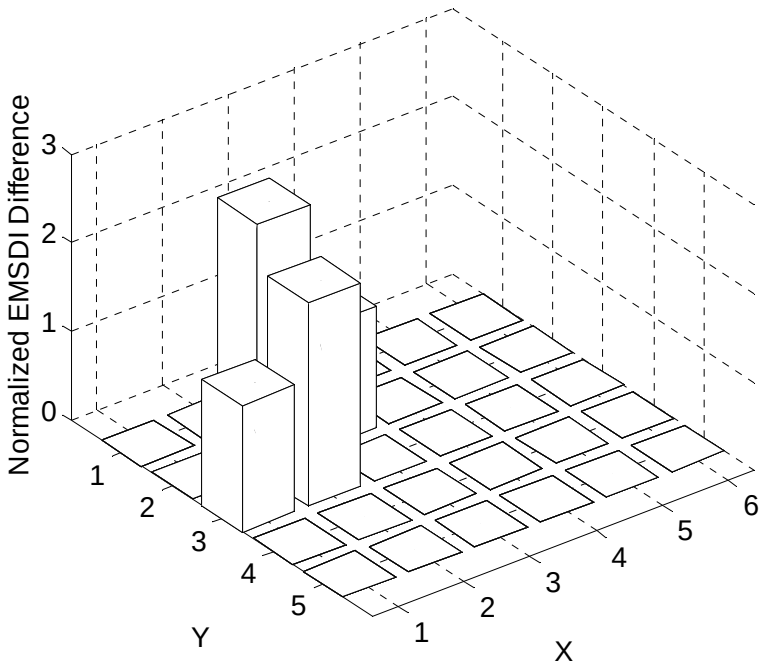

Figure 6-52 Probable Damage Regions (68% Confidence Level) – April 30, 2002

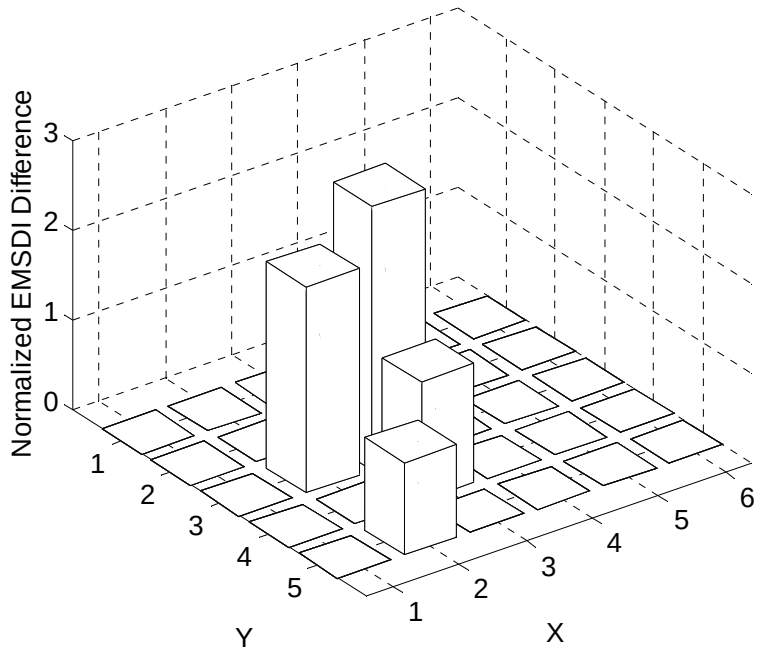

Figure 6-53 Probable Damage Regions (68% Confidence Level) – April 10, 2003

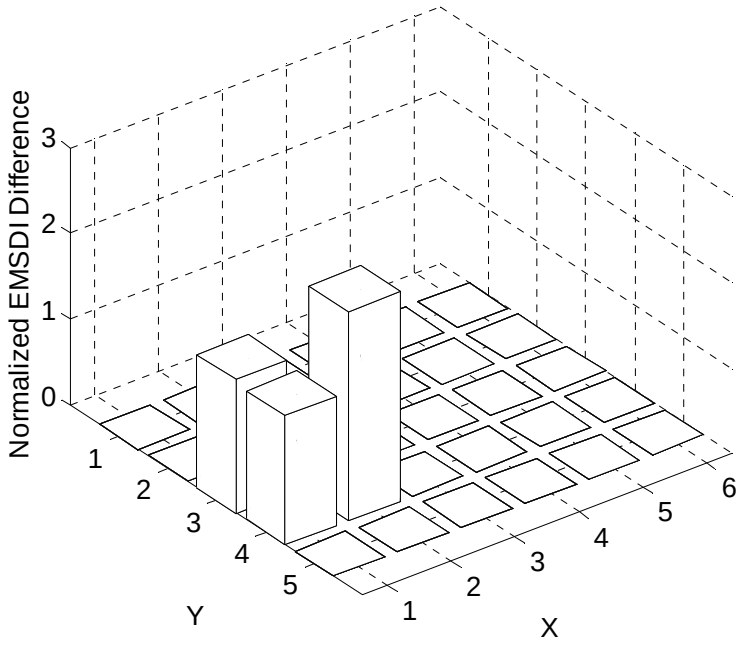

Figure 6-54 Probable Damage Regions (68% Confidence Level) – April 04, 2004

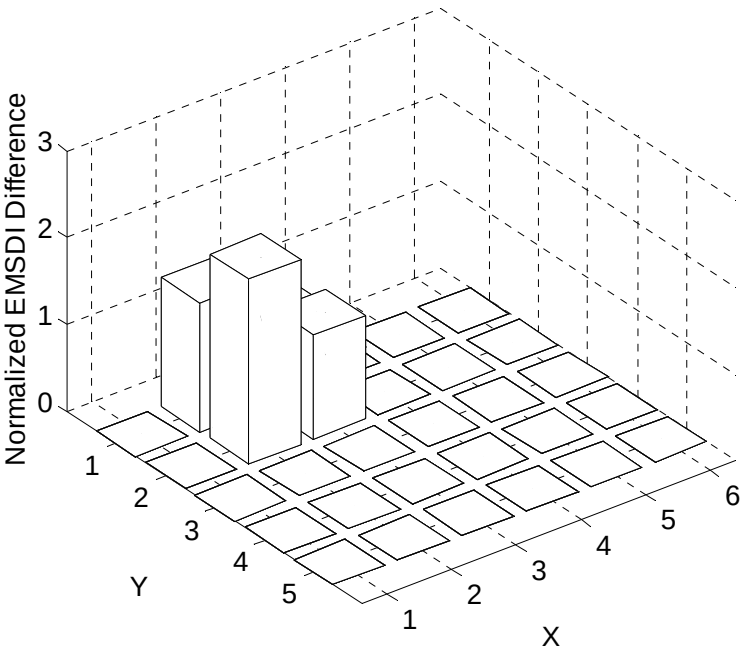

Figure 6-55 Probable Damage Regions (68% Confidence Level) – April 24, 2005

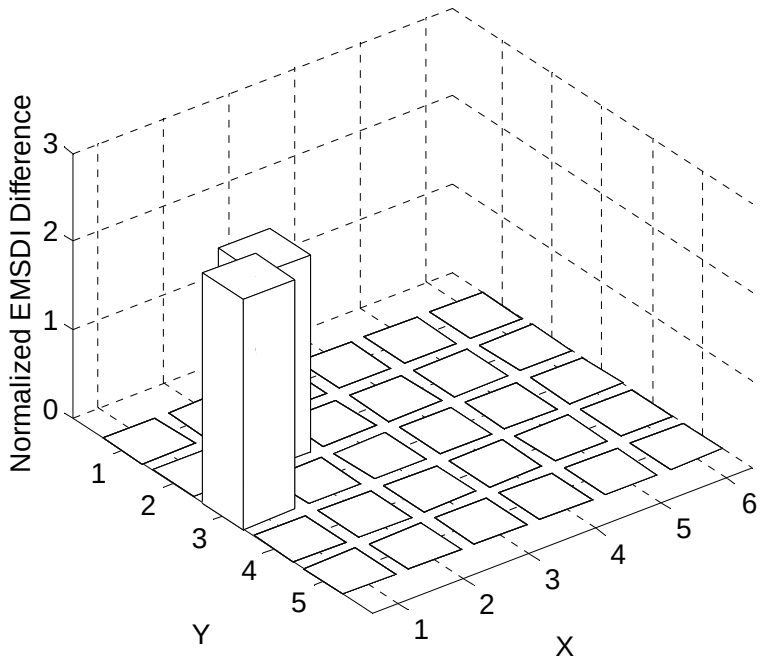

Figure 6-56 Probable Damage Regions (95% Confidence Level) – October 01, 2001

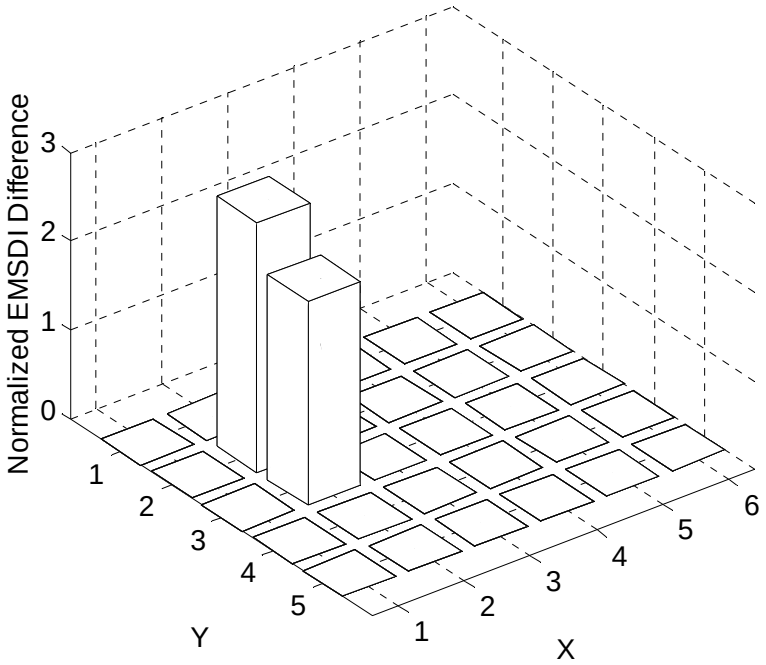

Figure 6-57 Probable Damage Regions (95% Confidence Level) – April 30, 2002

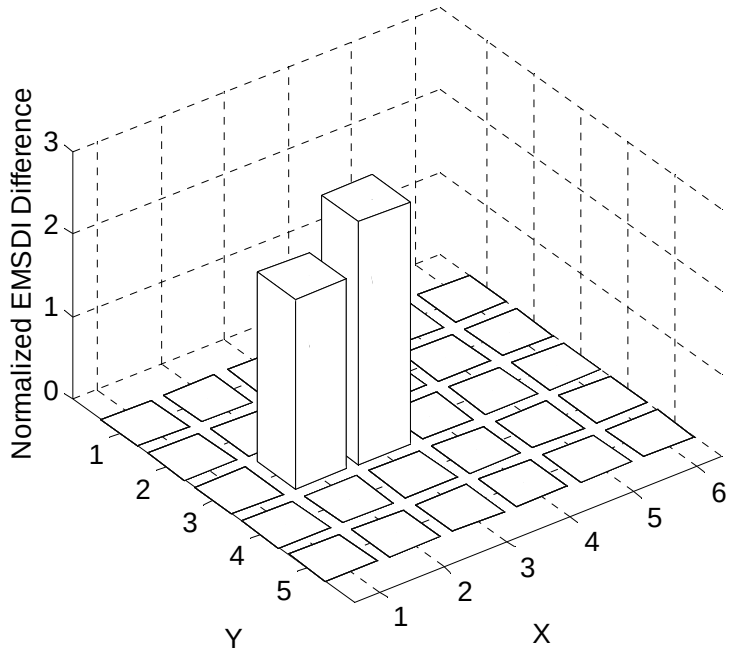

Figure 6-58 Probable Damage Regions (95% Confidence Level) – April 10, 2003

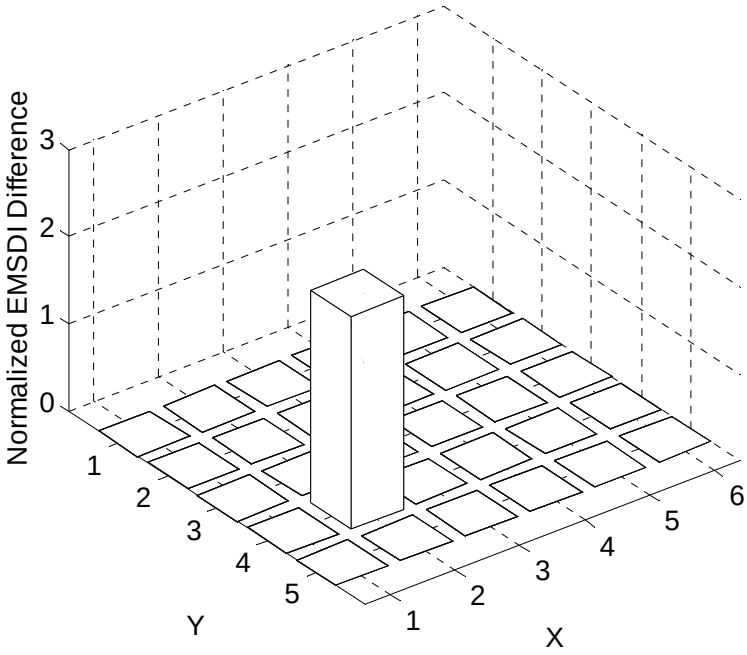

Figure 6-59 Probable Damage Regions (95% Confidence Level) – April 04, 2004

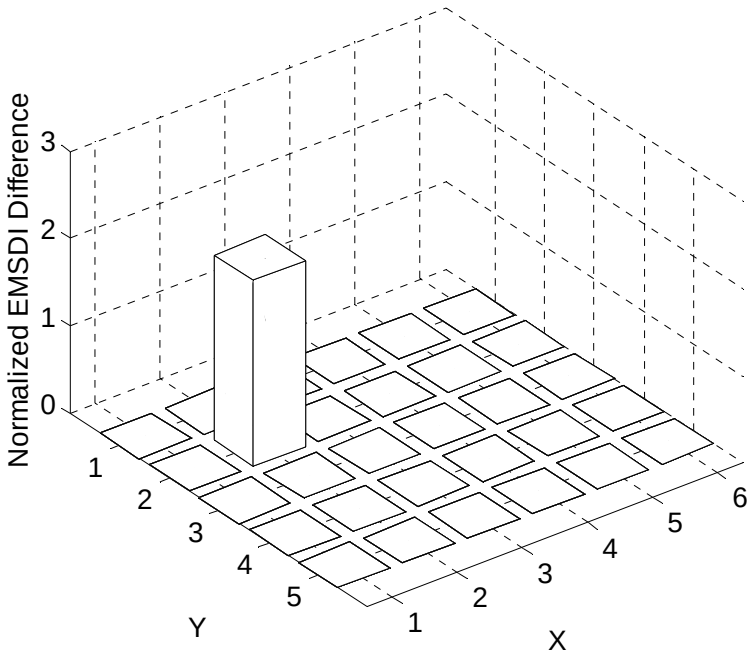

Figure 6-60 Probable Damage Regions (95% Confidence Level) – April 24, 2005

6.7 Finite Element Model Updating

The bridge is modeled with 4 node elastic shell elements using finite element package ANSYS (ANSYS 2004). The superstructure of the bridge behaves in a manner similar to a 2D plate, with the main girders and the deck panels forming an integral plate-like structure. The substructure of the bridge, including abutments and center columns, is not the main interest in this study and is modeled with soil springs. The results of the initial modal test described in Section 6.3 show that the dominant modes of the superstructure are indeed similar to those of a plate, thus supporting this simplification. Geometric and material properties of the structure are obtained from design and construction documents (Burgueño et al. 1999; Seible et al. 1998a; Seible et al. 1998b). Results from investigations of the properties of various structural components are also utilized as a reference (Burgueño 1999; Davol 1998; Zhao 1999).

The elastic shell element (SHELL63) used to model the superstructure has two orthotropic material properties, E_x and $E_{y,}$ with E_x in the bridge longitudinal direction and E_y in the bridge transverse direction. In the bridge longitudinal direction, the superstructure can be divided into sections with different longitudinal stiffness, as shown in Figure 6-61. These sections include 2 edge girder sections, 4 middle girder sections, 5 deck sections and 2 barrier sections. The edge girder section consists of the composite subdivision of the edge girder and a sector of the deck panel immediately above it. Full composite action is assumed between the girder and the deck panel. Similarly, the middle girder section consists of one middle girder and the tributary deck panel above it. In between girder sections, the deck sections are composed of the FRP

composite deck alone. The barrier section is composed of the concrete road barrier and a sector of deck panel beneath it. For each section, equivalent material properties are calculated from design and construction documents. The initial values of material properties for each section are listed in Table 6-7.

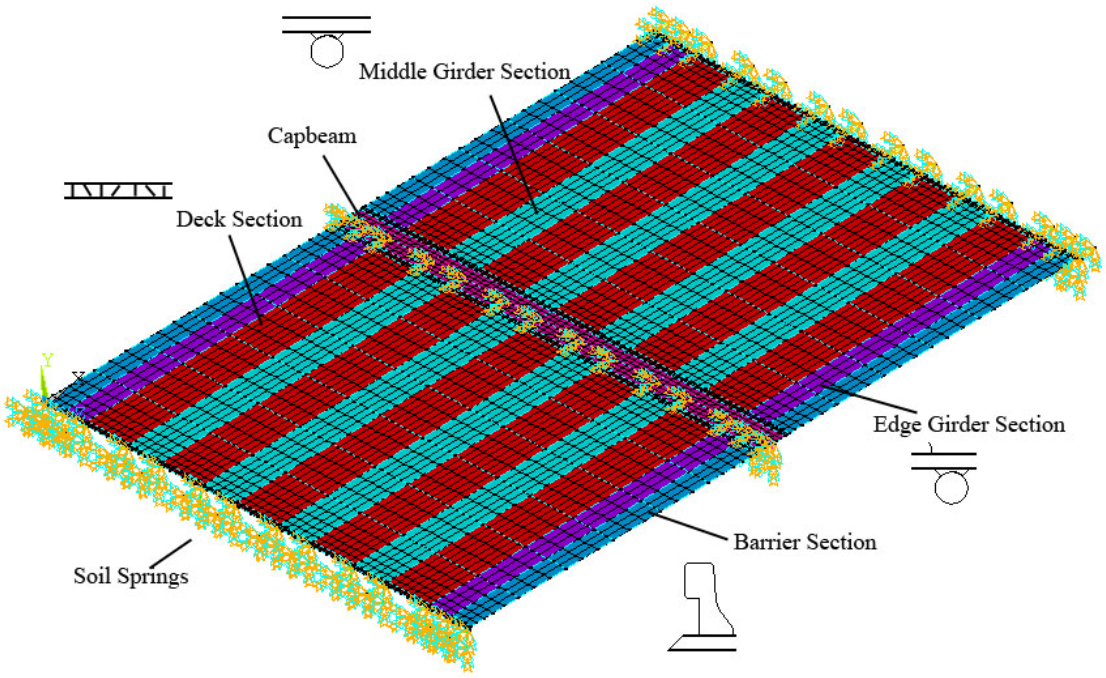

Figure 6-61 Finite Element Model of the Kings Stormwater Channel Bridge

In the bridge transverse direction, the stiffness is assumed to be uniform across the bridge span. The initial value of the transverse stiffness is estimated from the manufacturing documents of the PMC deck panel (Seible et al. 1998b) and is also listed in Table 6-7.

The capbeam is considered to be composed of homogeneous material and is also modeled with shell elements. The initial material property values for the capbeam are E_x

= E_y = 29.6 GPa for the Young's modulus and ρ = 2410 kg/m^3 for the mass density, based on design and construction documents.

The boundary conditions of the superstructure at the abutments and the pier top are modeled with three translational springs in mutually perpendicular directions and one rotational spring in the Z direction (COMBIN14 element in ANSYS). The springs simulate the restraining effect that the abutments and the piers exert on the superstructure. The initial values of the spring stiffness are estimated from design documents and are listed in Table 6-8.

Table 6-7 Initial Values of Equivalent Material Properties

	Young's Modulus (GPa)		Mass Density (kg/m^3)
	E_x	E_y	ρ
Middle Girder Section	45.0	11.7	1600
Edge Girder Section	60.0	11.7	2077
Deck Section	4.88	11.7	690
Barrier Section	1110	11.7	5467
Capbeam	29.6	29.6	2410

The completed finite element model consists of 4332 elements and 13212 degrees-of-freedom.

Table 6-8 Initial Values of Spring Stiffness

Spring Location / Direction	Translational Spring Stiffness	Rotational Spring Stiffness
	K_t (N/m)	K_r (N·m/rad)
Abutment Longitudinal	8.8E9	-
Abutment Vertical	7.2E9	-
Abutment Transverse	1.3E11	-
Abutment Rotational (North)	-	1.0E8
Abutment Rotational (South)	-	1.0E8
Capbeam Longitudinal	8.8E9	-
Capbeam Vertical	7.2E9	-
Capbeam Transverse	2.2E9	-
Capbeam Rotational	-	1.0E8

6.7.1 Updating of the Baseline Model

Modal analysis of the FE model is performed with initial values of material properties and spring constants. The natural frequencies and mode shapes of the first 20 modes are extracted. Table 6-9 compares the natural frequencies of the initial FE model with those measured experimentally from the pristine structure shortly after it was constructed (Bolton and Stubbs 2001). Nine modes are measured experimentally but only the first 7 modes are used for comparison because the last two experimental modes show higher uncertainty. The fourth column in Table 6-9 lists the relative difference between the experimental and FE model frequencies. The relative difference is defined as the absolute difference between the experimental value and the FE value divided by the experimental value. As expected, the experimental and the FE values show some

discrepancies. The magnitudes of the relative differences vary between 7.58% and 22.0%. The largest relative difference between experimental and FE values is for the 6th mode at 22%. It is evident that updating of the finite element model is needed to calibrate the initial FE model so that it can better represent the baseline structure.

Table 6-9 Comparison of Experimental Natural Frequencies and Initial FE Model Frequencies

Mode	Natural Frequencies (Hz)		Difference (%)
	FE Model	Experiment	
1	9.522	11.033	13.7
2	10.302	13.11	21.4
3	12.788	15.36	16.7
4	13.797	16.921	18.5
5	16.472	19.005	13.3
6	19.945	25.585	22.0
7	24.758	26.79	7.58

6.7.1.1 Selection of Uncertain Structural Parameters

The uncertain structural parameters that lead to this discrepancy are considered to be the equivalent Young's moduli of middle girder, edge girder, deck and barrier sections in the bridge longitudinal direction, equivalent Young modulus of each section in the bridge transverse direction, and the spring stiffness constants. The Young's modulus of the capbeam listed in Table 6-7 is considered to be estimated relatively accurately and hence should not be regarded as an uncertain parameter. Mass densities of each equivalent section are also considered to be accurately estimated and hence should not be treated as uncertain parameters. Out of the nine spring constants, the two transverse spring constants have no impact on the vertical modes of the structure and are thus also excluded.

The remaining 10 structural parameters – middle girder longitudinal stiffness E_x, edge girder E_x, deck E_x, barrier E_x, deck transverse stiffness E_y, abutment and capbeam vertical and longitudinal spring stiffness, rotational spring stiffness at two abutments and the capbeam – are checked for their impact on the dynamic response of the bridge. A numerical perturbation method is used to find out the sensitivity of natural frequencies to each of the parameters. The results are plotted in Figure 6-62. From Figure 6-62 it is clear that the natural frequencies are most sensitive to variations of deck transverse stiffness, center girder longitudinal stiffness and barrier longitudinal stiffness. At the same time, natural frequencies are not sensitive to the stiffness of vertical soils springs, the stiffness of longitudinal springs, and the stiffness of rotational springs at the abutments.

Based on the sensitivity analysis, 6 unknown structural parameters are selected for updating: middle girder longitudinal stiffness, edge girder longitudinal stiffness, deck longitudinal stiffness, barrier longitudinal stiffness, deck transverse stiffness and rotational spring stiffness at the capbeam.

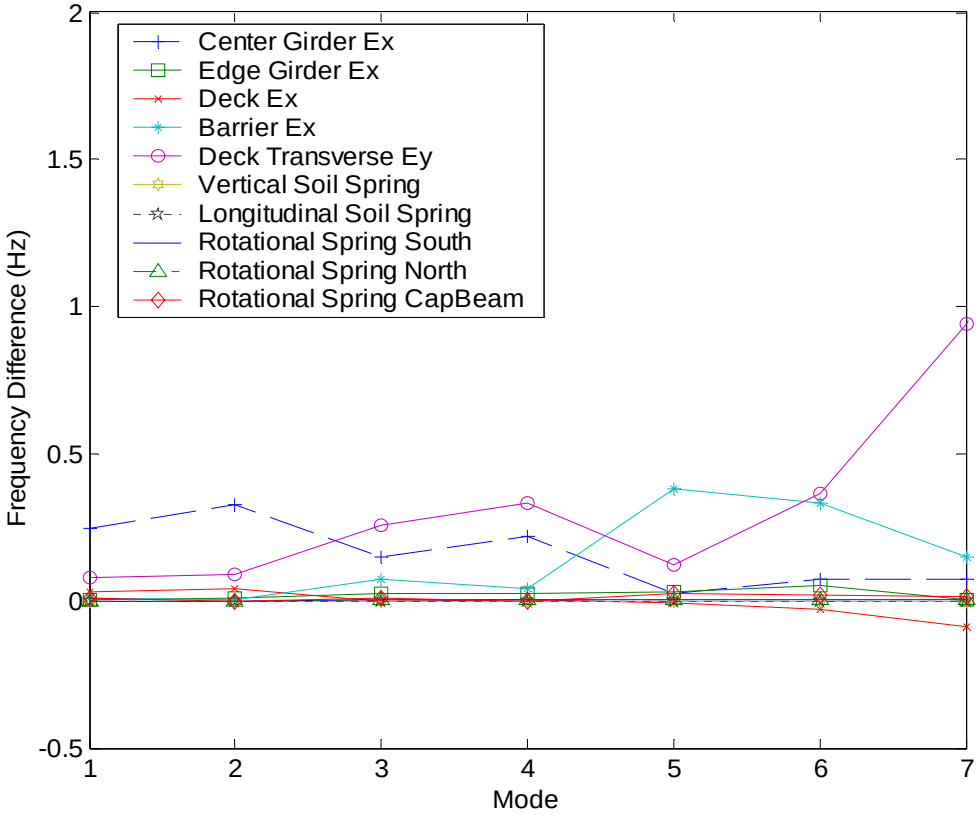

Figure 6-62 Sensitivity of Structural Parameters

6.7.1.2 Model Updating Process and Results

Natural frequencies residues are chosen to form the residue vector. All modes are weighted equally and no additional weighting is applied. MAC values are used to pair FE modes with experimental modes although modal amplitudes are not explicitly included in the residue vector.

The model updating problem is solved using the procedure outlined in Section 5.2. A constrained minimization algorithm described in Section 5.2.3.3 is used as the solution procedure. The initial and updated natural frequencies are listed in Table 6-10.

The relative frequency differences of both cases with respect to the experimental values are plotted in Figure 6-63. A significant reduction in frequency residues can be observed. Only the 6th and 7th mode have a relative difference larger than 5%.

Table 6-10 Initial and Updated FE Frequencies

Mode	Natural Frequencies (Hz)			Difference (%)	
	Experiment	Initial FE Model	Updated FE Model	Initial	Updated
1	11.033	9.522	11.138	13.7	0.95
2	13.11	10.302	13.311	21.4	1.53
3	15.36	12.788	14.725	16.7	4.13
4	16.921	13.797	16.800	18.5	0.72
5	19.005	16.472	19.080	13.3	0.39
6	25.585	19.945	23.848	22.0	6.79
7	26.79	24.758	28.309	7.58	5.67

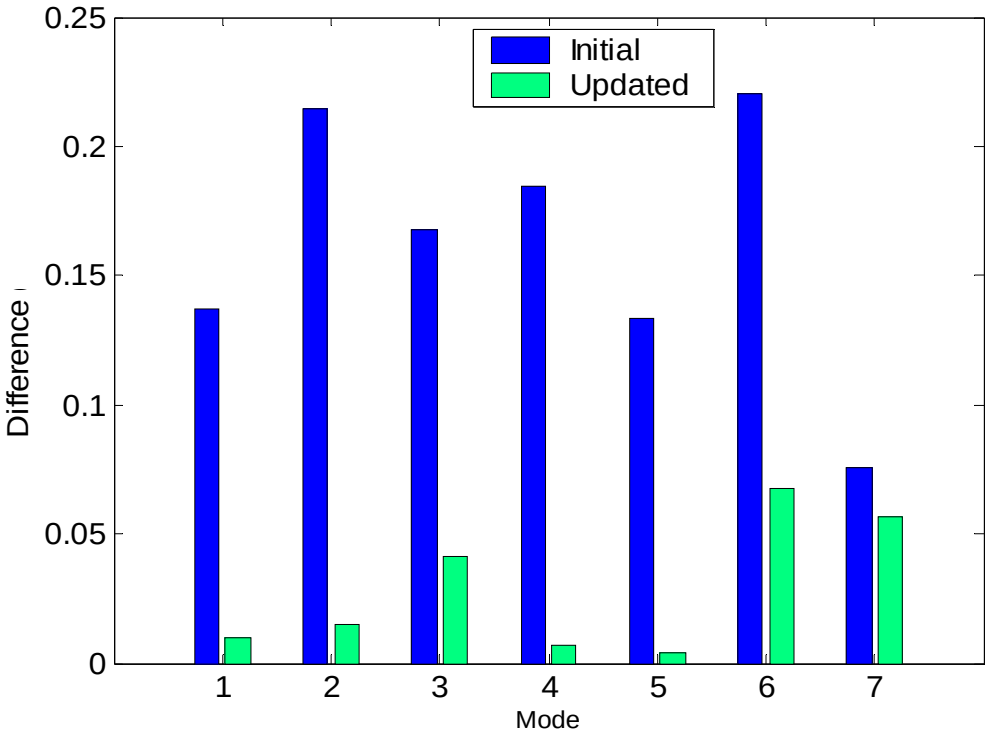

Figure 6-63 Relative Frequency Differences of Initial and Updated Model Compared with Experimental Data

The variation of correction factors α_k (as defined in Eq. (5.13)) during updating iterations is plotted in Figure 6-64. The identified structural parameters are listed in Table 6-11. It can be seen that the model updating yields a significant correction for the longitudinal stiffness of the middle and edge girder sections as well as the barrier section. The longitudinal and transverse stiffness of the deck also experienced minor correction. The only parameter for which the identified value is smaller than the initial value is the rotational spring stiffness at the capbeam.

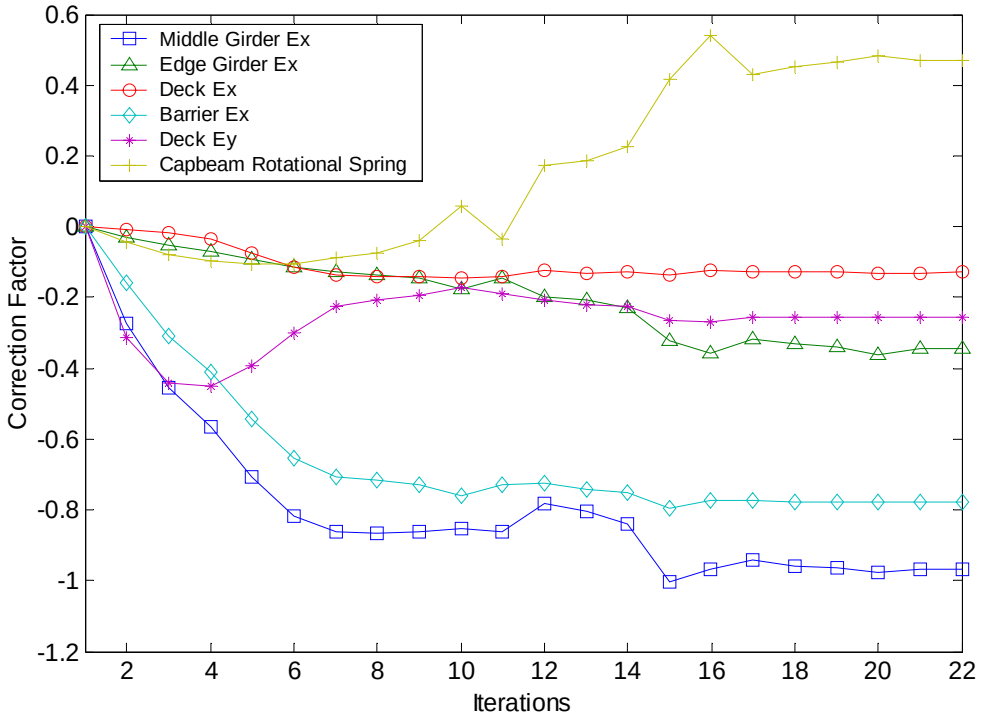

Figure 6-64 Variation of Correction Factors

Table 6-11 Identified Structural Parameters

Parameter	Initial Value	Updated Value
Middle Girder E_x	45.0 GPa	88.3 GPa
Edge Girder E_x	60.0 GPa	80.9 GPa
Deck E_x	4.88 GPa	5.51 GPa
Barrier E_x	1110 GPa	1972 GPa
Deck E_y	11.72 GPa	14.7 GPa
Capbeam Rotational Spring	1.0×10^8 N·m/rad	5.339×10^7 N·m/rad

Finally, the mode shapes of the calibrated baseline FE model are plotted side-by-side with their experimental counterparts in Figure 6-65 and Figure 6-66. It can be seen that although the modal amplitudes are not included in the residue vector for model updating, good mode shape correspondence is still obtained. This indicates that the FE model used is able to accurately simulate the dynamic response of the structure and the identified structural parameters are good estimates of their true values.

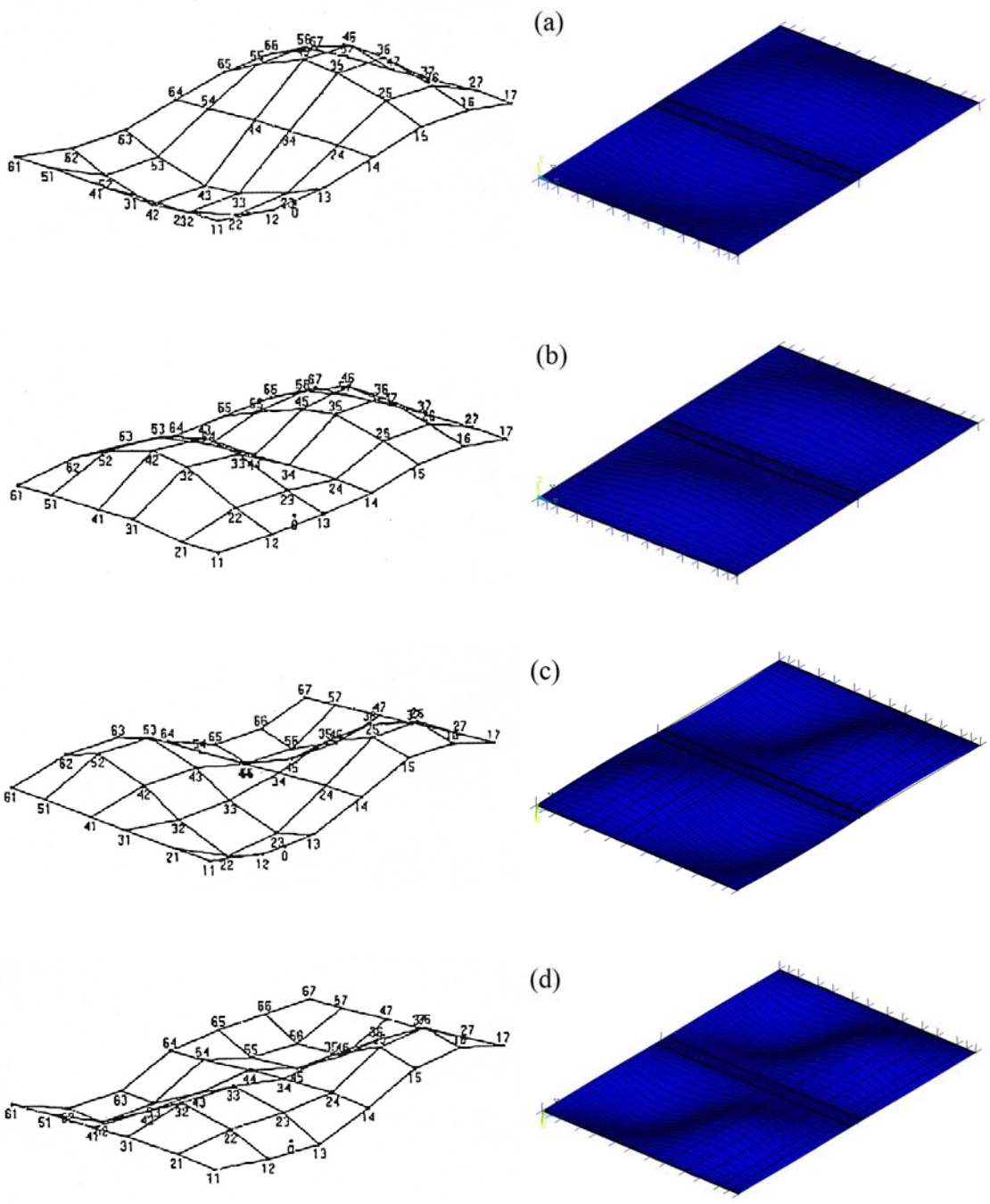

Figure 6-65 Updated Baseline FE Model Mode Shapes: (a) 1st Mode (b) 2nd Mode (c) 3rd Mode (d) 4th Mode

Experimental Mode Shapes **Finite Element Mode Shapes**

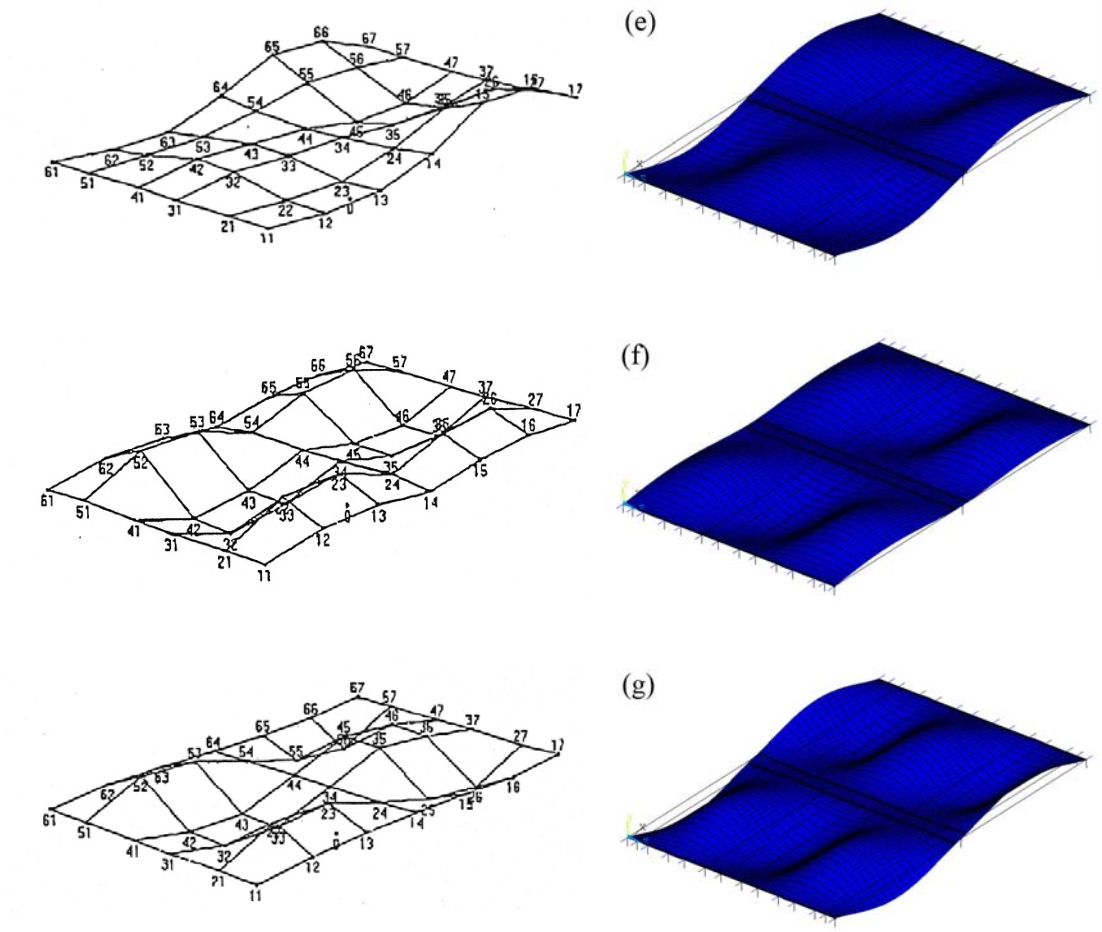

Figure 6-66 Updated Baseline FE Model Mode Shapes: (e) 5th Mode (f) 6th Mode (g) 7th Mode

6.7.2 Finite Element Model Updating with Health Monitoring Data

Once a calibrated baseline FE model is obtained, modal parameters of the structure identified through the continuous monitoring process described in Section 6.6 can be used to update the model to reflect the condition of structure at any given time.

6.7.2.1 Selection of Updating Parameters

In order to locate and quantify the potential damage areas in the bridge, the superstructure of the bridge is divided into 208 divisions, as shown in Figure 6-67. In the bridge longitudinal direction, the division follows the sections described in Section 6.7, i.e., 2 edge girder sections, 4 middle girder sections, 5 deck sections and 2 barrier sections. In the bridge transverse direction, the bridge superstructure is divided into 8 subsections per span. The longitudinal and transverse stiffness of each division, E_x and E_y, are potential updating parameters. All parameters are assumed to vary independently. The capbeam rotational spring stiffness provides another additional parameter, thus bringing the total number of independent parameters to 417.

The identified modal parameters are limited in both spatial domain (only 42 vertical DOFs are measured) and frequency domain (only the first two modes are identified). The high number of independent unknown parameters will obviously cause the ill-conditioning of the FEMU problem. To avoid this problem, the damage localization results are used to reduce the number of unknown parameters to be updated. The superstructure of the bridge is divided into 30 regions for purpose of damage localization (Figure 6-45). If one of the regions is considered as potential damage area, then only the divisions covered by and immediately adjacent to that region are assumed

to contribute to the list of unknown structural parameters. In this way, the number of unknown structural parameters is effectively kept at minimum and ill-conditioning of the FEMU problem can be avoided.

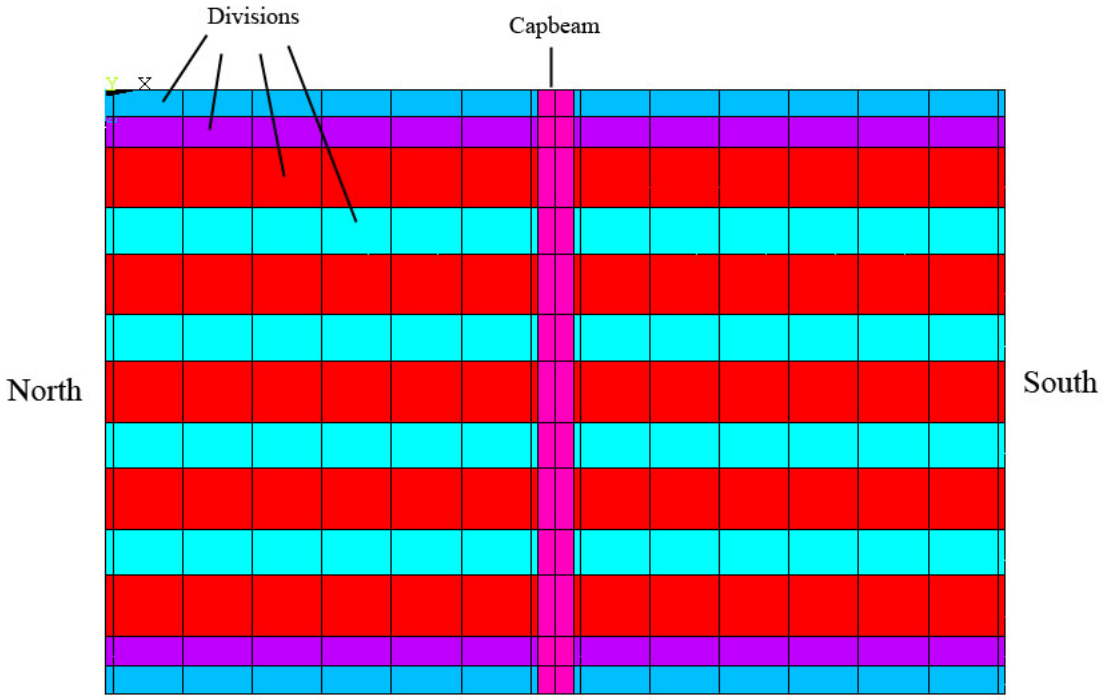

Figure 6-67 Superstructure Divisions for Model Updating

For illustration purpose, the potential damage area and divisions selected for model updating for the data set of April 24, 2005 are plotted in Figure 6-68. The small rectangle represents the potential damage region indicated by the damage localization algorithm. The large rectangle represents the divisions selected for updating. The total number of unknown parameters is 72 for this case.

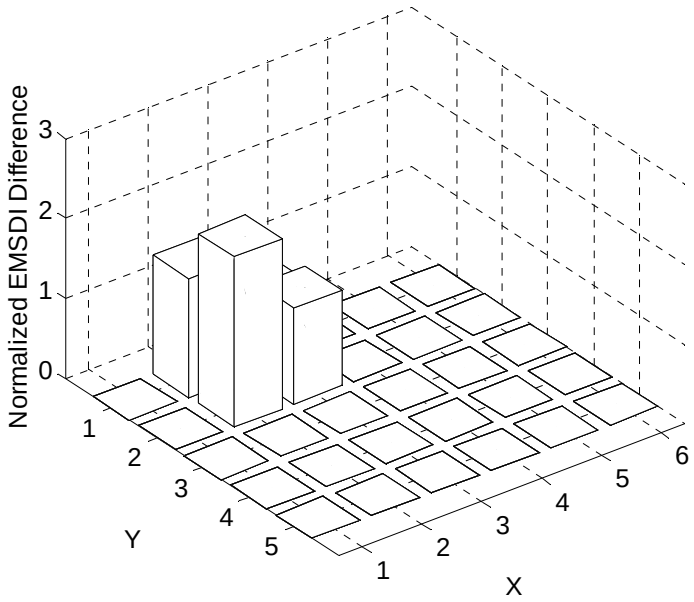

(a) EMSDI Difference

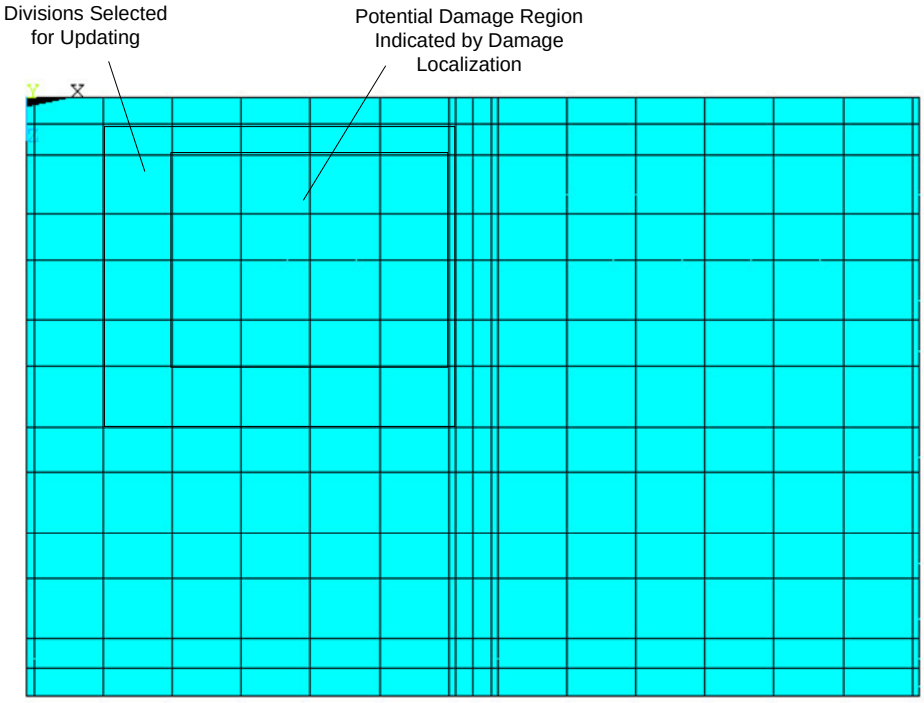

(b) Divisions Selected for Updating

Figure 6-68 Potential Damage Region and Divisions Selected for Updating (April 2005 Data Set)

6.7.2.2 Residues and Objective Functions

The residues utilized in this case are the mode shape and frequency differences between FE and experimental data of the first two modes. Since measurement noise is expected in the experimentally measured mode shape data, a smoothing function similar to that utilized in the EMSDI technique described in Section 4.2 is applied to the mode shape difference:

$$\min f(x) = p\sum_{i=1}^{N+1}\left(\frac{\phi(x_i)-\phi_i^m}{\sigma_\phi}\right)^2 + (1-p)\int_{x_1}^{x_{N+1}}\left(\phi''(x)\right)^2 dx \qquad (6.4)$$

The total number of residues is 84.

The objective function is formed by applying different weighting to residues. Frequency residues are given a higher weighting of 10 while mode shape residues are given a weighting of 1.

6.7.2.3 Model Updating Results

The mode shape residues before and after updating are plotted in Figure 6-69 through Figure 6-72. The X and Y axis in the figures are along the longitudinal and transverse direction of the bridge, respectively. The X axis starts from the northern abutment of the bridge. The locations of the bars correspond to the sensor locations. It should also be noted that the magnitudes of the scale of the Z axis in the four figures are different. It can be seen that the overall magnitude of the mode shape residues are significantly reduced by the updating, indicating better correlation between the FE model and experimental data is achieved.

The identified correction factors for the longitudinal stiffness of each division are plotted in Figure 6-73. Again, the X and Y axis are along the longitudinal and transverse direction of the bridge, respectively. The labels along each axis represent the coordinates of each division. The X axis starts at the northern abutment and stops at the capbeam. For clarity, only the correction factors of the northern span are plotted. Since no unknown parameter from the southern span is included in the updating process, the correction factors at the southern span are all zero.

The highest values of the correction factor can be seen at divisions (8, 2) and (8, 3), adjacent to the capbeam. The values of the correction factors at those two locations as seen in Figure 6-73 equal to 0.56 and 0.62, respectively. These values represent a 56% and 62% reduction in longitudinal stiffness at respective divisions.

The identified correction factors for the transverse stiffness of each division are plotted in Figure 6-74. The maximum magnitude of correction factors in the transverse direction is in the order of 0.06 ~0.07 and appears to be evenly distributed across the region selected for updating.

6.7.2.4 Validation of FEMU Results

Through an onsite visual inspection, it was found that several of the expansion joints between the deck panels and the abutments as well as the capbeam had deteriorated significantly due to heavy use and improper construction, as shown in Figure 6-75. Water from occasional heavy rainfall penetrated the affected joint and accelerated deterioration. The relative location of the weakend expansion joint and the areas showing largest reduction in longitudinal stiffness is shown in Figure 6-76. The

identified heavily damaged region through FEMU appears to correlate well with the observation that expansion joints between the deck and the capbeam had deteriorated.

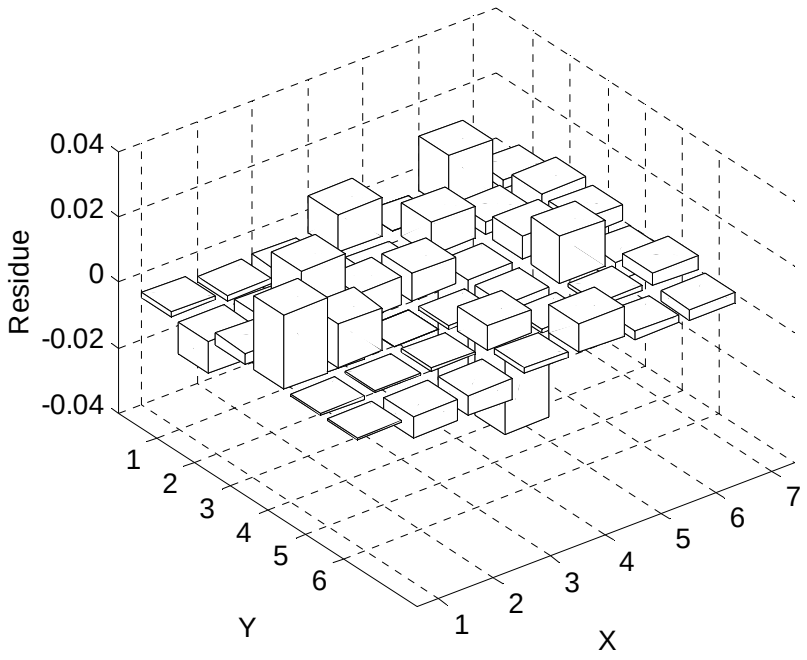

Figure 6-69 Mode Shape Residues of the 1st Mode Before Updating

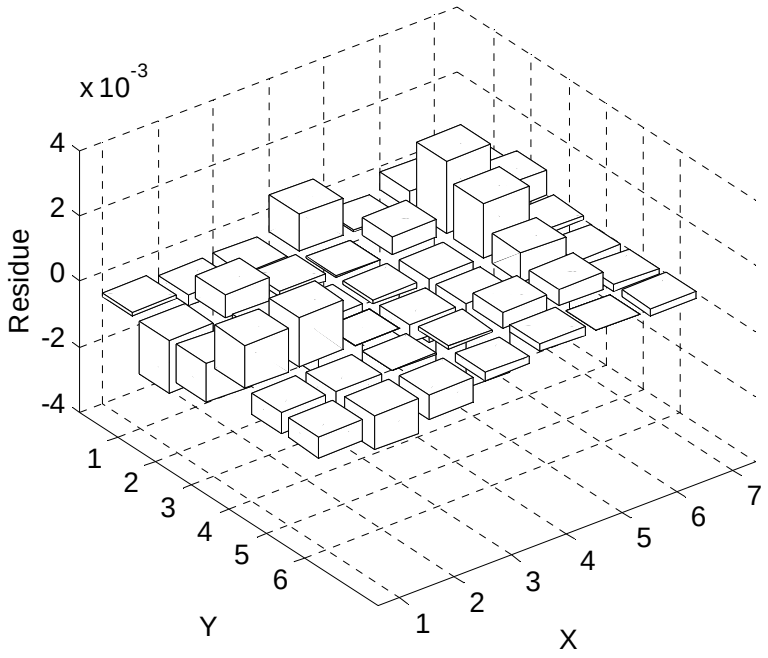

Figure 6-70 Mode Shape Residues of the 1st Mode After Updating

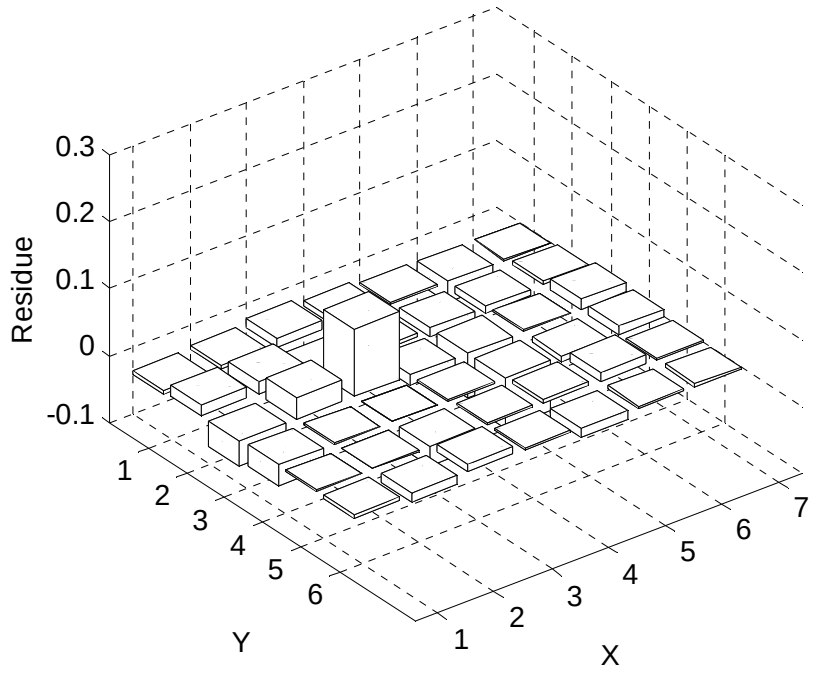

Figure 6-71 Mode Shape Residues of the 2nd Mode Before Updating

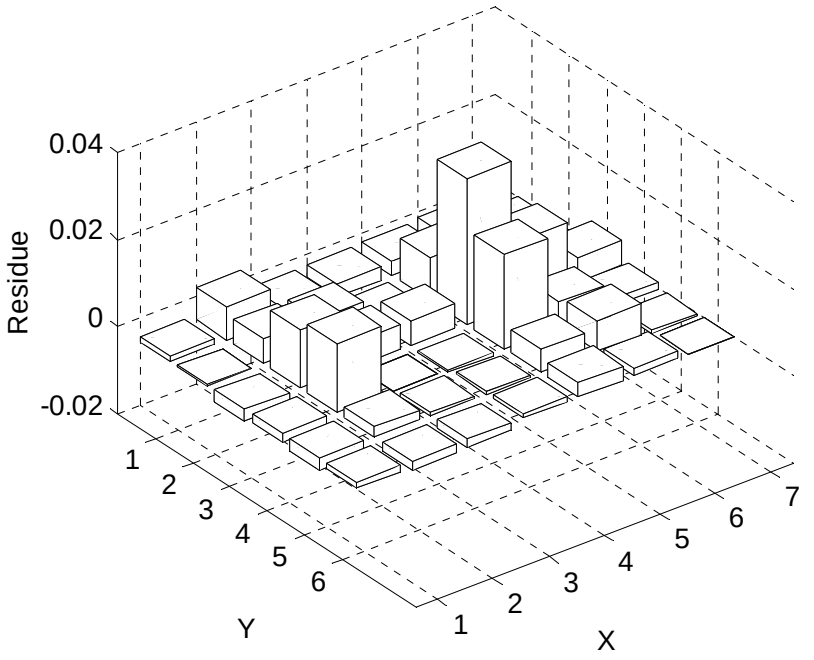

Figure 6-72 Mode Shape Residues of the 2nd Mode After Updating

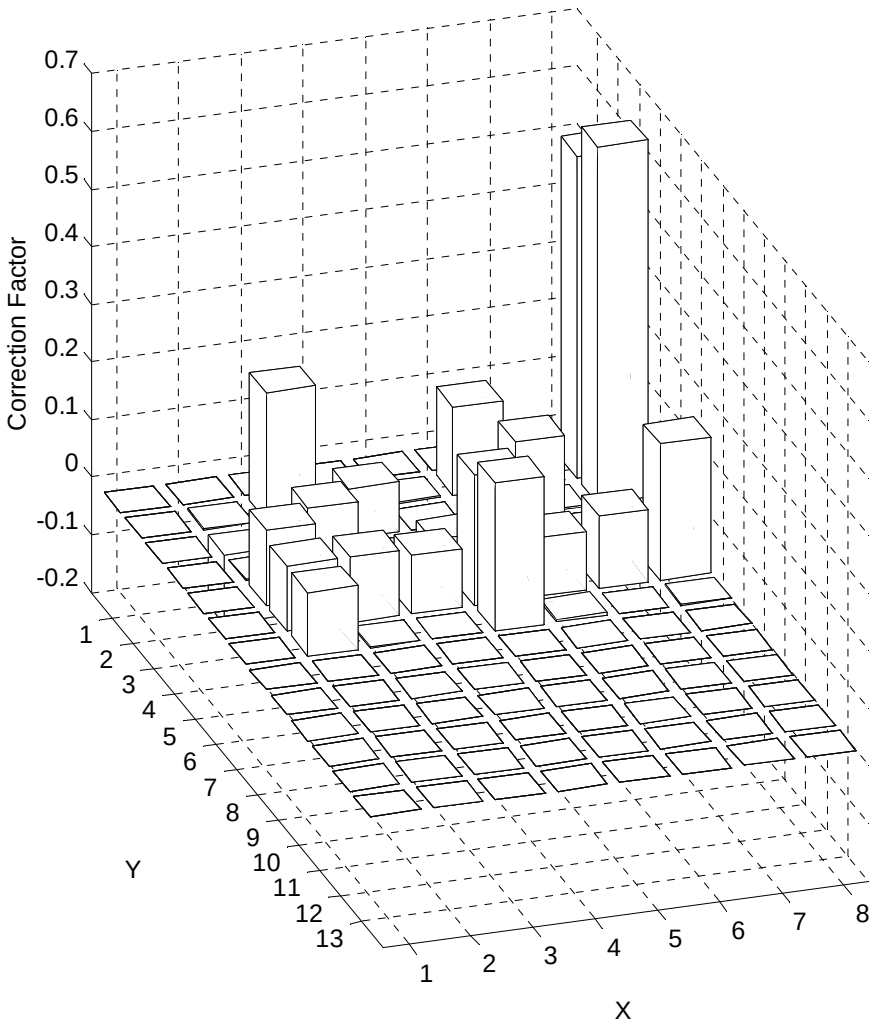

Figure 6-73 Identified Correction Factors in the Longitudinal Direction

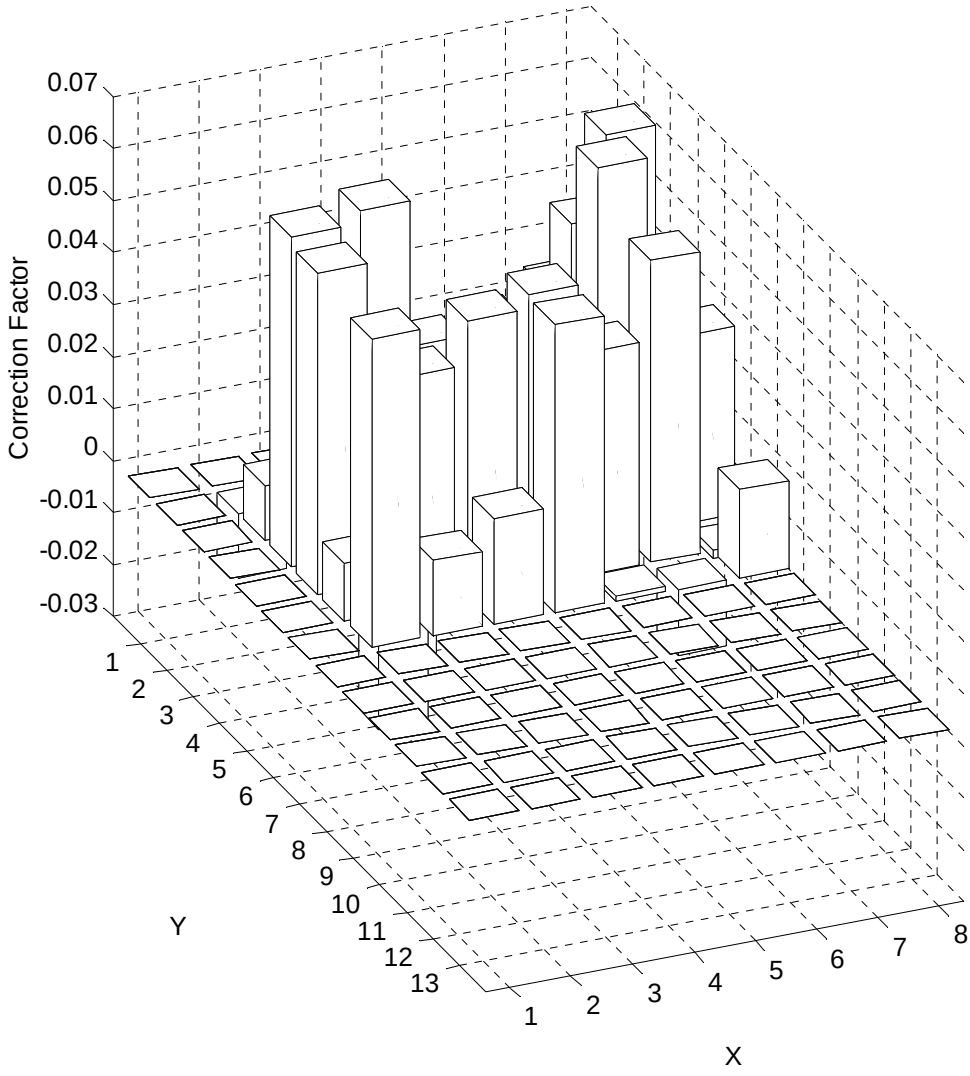

Figure 6-74 Identified Correction Factors in the Transverse Direction

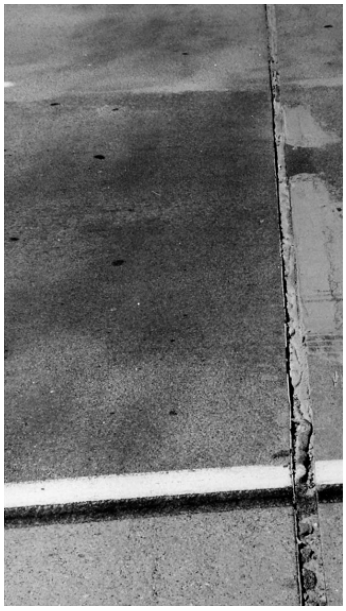

Figure 6-75 Weakened Expansion Joints

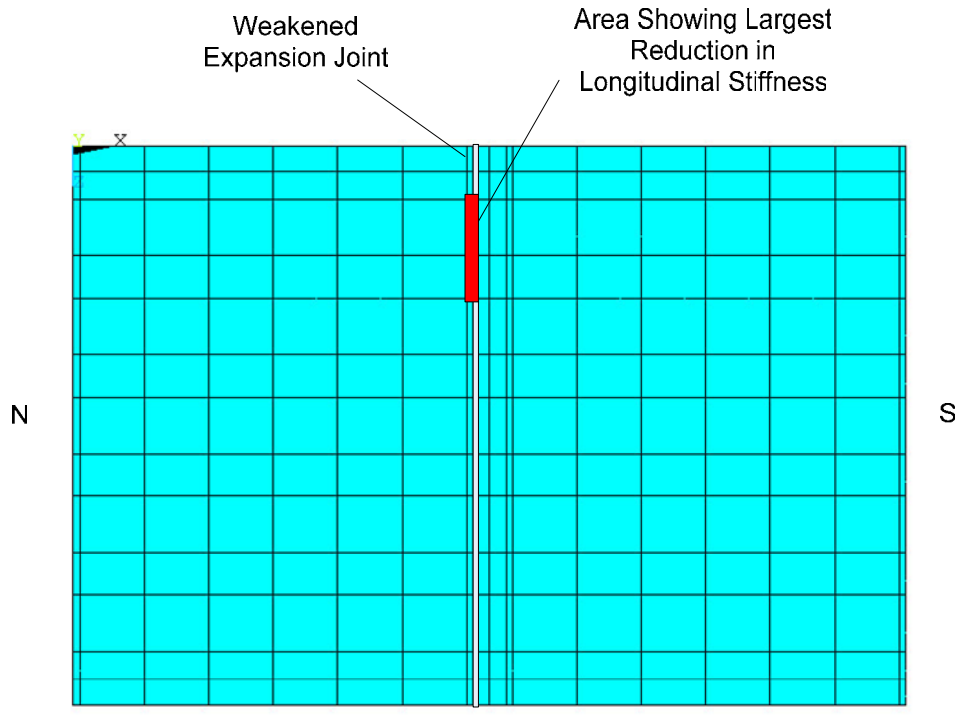

Figure 6-76 Relative Location of the Weakened Expansion Joint and the Area Showing Largest Reduction in Longitudinal Stiffness

6.8 Conclusions

This chapter discusses the implementation of a Structural Health Monitoring system on a highway bridge based on the Vibration-Based Structural Health Monitoring Paradigm laid out in the previous chapters.

The basic characteristics of the bridge structure are first introduced. The initial static and dynamic characterization is then described. The initial characterization provides information regarding the initial state of the bridge when it was constructed. In service static characterization was performed a year after the completion of the bridge in order to track the change in static performance.

The instrumentation of continuous monitoring system is then presented. Both the hardware components, including the data sensing, acquisition, transmission and archiving systems, and the software components of the system are described.

Operational modal analysis is used to extract modal parameters from the collected ambient vibration responses of the structure. The identified modal parameters are used as input for damage localization algorithm. The possible damage regions obtained through damage localization helps to narrow down the number of unknown parameters used in the finite element model updating process.

A baseline finite element model well-correlated with experimental modal data is obtained through FEMU. The results of the subsequent updating provide detailed information regarding the location and severity of the damage. The results appear to agree with the visual inspection results.

Chapter 7 Conclusions

In this dissertation, a new Vibration-based Structural Health Monitoring methodology for highway bridges is proposed. The methodology is composed of the following steps: First, the initial structural behavior is determined and calibration of the initial structural model is performed. Second, through continuous monitoring of the dynamic response, vibrational features of the structure are identified in terms of modal parameters. Next, damage localization is performed based on the comparison of identified modal parameters with the initial values determined for the structure in its pristine condition. Finite Element Model Updating is then performed to update the structural model to reflect the change in structural dynamic response over time. This provides the basis for the future use of the updated model to predict the capacity and remaining life of the structure.

This research is motivated by the need to improve the efficiency and accuracy of the current highway bridge inspection and maintenance practice. In order to meet the challenges posed by the trend of deteriorating infrastructure in the United States, there exists a need to migrate from current 'time-based' maintenance scheme to a 'condition-based' maintenance scheme due to both operational and socio-economic reasons. To this end, structural health monitoring provides a new and unique approach. Structural health monitoring is defined as the use of in-situ, nondestructive sensing and analysis of structural characteristics for the purpose of estimating the severity of damage and

evaluating the consequences of damage on the structure. The application of SHM on bridge structures will enable the condition of the bridge to be constantly monitored using an appropriate non-destructive evaluation (NDE) technique. Timely, quantitative condition assessment can be provided. On the other hand, structural health monitoring systems can also contribute to rapid post-extreme-event condition screening. With automated monitoring systems in place on critical life-line structures, the condition of these structures can be evaluated shortly after an extreme event has occurred and potentially give the cognizant authority faster access to the affected areas thus improving public safety.

After a careful review of current existing structural health monitoring applications on highway bridges, it is concluded that work to date on structural health monitoring systems for civil structures has been useful, but resembles existing bridge management systems and can not meet the requirements outlined above. A new Vibration-Based Structural Health Monitoring paradigm is thus proposed. The three key components within this paradigm are Operational Modal Analysis, Vibration-Based Damage Detection and Finite Element Model Updating.

An extensive literature review of Level III and Level IV Vibration-Based Damaged Detection techniques is first provided. By comparing the relative merits and shortcomings of the various methods proposed to date, promising techniques and areas that need further research are identified.

The problem of identifying modal parameters from the measured ambient vibration of the structure is then addressed. A new method to perform the identification

in the frequency domain is proposed. Compared with traditional methods, the proposed method is demonstrated to improve the efficiency of identification without loss of accuracy.

The new Vibration-Based Damage Detection algorithm based on energy criterion is proposed in Chapter 4. The method addresses two major disadvantages of traditional techniques based on modal curvature, i.e., noise propagation and sparse measurement. The proposed method is shown to perform superiorly under adverse conditions typically seen in real world applications.

The use of Finite Element Modal Updating technique to obtain calibrated model of the structure for health monitoring purposes is discussed in Chapter 5. Special attention is paid to the ill-conditioning of the identification problem. New ways of reducing the number of unknown parameters by making use of the information obtained during the damage detection process is proposed.

In Chapter 6, the implementation of a long-term structural health monitoring system on a highway bridge is discussed and some of the monitoring results evaluated. Operational Modal Analysis algorithms are successfully implemented to extract modal parameters from ambient vibrations. The use of an energy based damage identification technique is shown to be able to successfully detect localized damage in the structure. Finite element model updating is carried out to quantify the extent of damage and its impact on structural behavior.

7.1 Design and Implementation of Vibration-Based Health Monitoring System for Highway Bridges

Based on the experience gained during the research performed for this dissertation, the following steps are suggested for the design and implementation of future vibration-based health monitoring systems for highway bridges:

1. The target structure should be surveyed and studied carefully in order to establish its baseline structural and response characteristics. Dynamic responses should be measured at appropriate locations on the structure during its typical operational conditions during the initial survey. Mobile instrumentation should be used in order to investigate as many locations as possible. These locations will form the basis of potential sensor locations for a long term health monitoring system. Currently, acceleration is usually the preferred type of measurement in terms of dynamic response. The magnitude and frequency content of the acceleration collected during typical operation conditions of the structure will dictate the type and parameters of the sensors to be used in the health monitoring system. For example, the maximum amplitude range of the sensor at specific locations should be able to accommodate the largest acceleration the structure is expected to experience at that particular location. Also, the accelerometers selected should be able to accurately measure the frequency range over which the structural modes of interest are located. Or more generally, the accelerometer should be able to accurately measure the frequency range where most of the signal power of the response is located. For many large

civil engineering structures, the dominant structural modes as well as the majority of the signal power in the response due to ambient excitation exists in the lower end of frequency spectrum – less than 1 Hz in many cases. Traditional piezoelectric accelerometers have limited accuracy operating in such low frequency ranges. Capacitive or resistive accelerometers are thus more suitable for such types of applications. In cases where the health monitoring system is also expected to collect data during extreme events such as earthquakes or hurricanes, actual structural response induced by extreme events might not be available during the design and implementation stage of the health monitoring system. Predicted response based on finite element models of the structure and past knowledge of the excitation due to extreme events can be used in place of this data.

2. Modal analysis should be performed to identify the initial modal parameters. Operational modal analysis can be used for identification when responses caused by ambient excitation are used. The excitation and response level used for identification should correspond to those typical of normal operation of the structure in order to minimize the effect of nonlinearity. Alternatively, forced excitation sources such as an impact hammer or an electromagnetic shaker can also be utilized. In the case where forced excitation source is utilized, attention must be paid to make sure that the amplitude and frequency characteristics of the forced excitation is similar to that of the ambient excitation the structure is likely to be subjected to during its daily operations. The characteristics of the identified dominant modes should be studied carefully in order to determine the

number and location of the sensors needed to effectively characterize these modes. The minimum number of sensors needed to successfully identify a mode can be determined by Shannon's sampling theorem (Stubbs 1996). The density of the sensor network will also be determined by the intended spatial resolution of the damage localization. In order to successfully identify localized damage, the number of sensors needed is usually much larger than that dictated by Shannon's sampling theorem.

3. Once the type, number and location of the sensors in the sensing system are determined, the data acquisition, transmission and archiving system can be designed accordingly in the third step. Apart from the necessary requirements imposed by the need to interface with the sensing system, another important characteristic of the data acquisition system is the sampling rate. The sampling rate should be determined by the frequency range of interest identified in the second step. Generally speaking, the Nyquist frequency, or half of the sampling frequency, should be larger than the highest frequency of interest. But due to some practical considerations such as avoiding aliasing effects, the Nyquist frequency is usually selected to be at least two times the highest frequency of interest. The amount of data collected is directly proportional to the sample rate and the number of sensors or channels simultaneously measured. For large civil engineering structures, tens of thousands of samples may be recorded every second and the data acquisition, transmission and archiving system must be designed to accommodate that.

4. A baseline finite element model, initially built based on design documents, should then be updated using the identified modal parameters by means of the finite element model updating method described in Chapter 5 of this dissertation. Uncertain structural parameters should be identified using sensitivity analysis. The finite element model updated with identified values of structural parameters is a better presentation of the baseline structure. Depending on the modal parameter used in the model updating process, the 'baseline' model can represent the pristine state of the structure or its state at a selected point in time. The latter case usually happens when an existing structure needs to be monitored and modal parameters from its pristine state are not available. The model updating process can also be augmented by the static response measured during load tests.

5. Once the hardware of the monitoring system is in place, continuous monitoring of the structure should be performed. Operational modal analysis can be used to extract modal parameters from the measured structural response using algorithms presented in Chapter3.

6. Damage localization should then be performed utilizing the identified modal parameters and techniques as described in Chapter 4. The baseline finite element model is constantly updated, again using the methods discussed in Chapter 5. The change between each updated model can be considered as a record of the changes that the actual structure has been experiencing.

7. Estimation of present structural capacity and remaining life can be performed at each stage. The detailed method to evaluated remaining capacity and life of the structure is not covered in this dissertation, but can be found in Lee (2005).

7.2 Suggestions for Future Research

Operational modal analysis is becoming a relatively mature technology with a broad array of standard techniques. However, some of the inherent assumptions that underlie all techniques, such as the white noise excitation assumption, remain to be verified. Moreover, there exists no uniform framework to evaluate the statistical properties of the modal parameters identified through various methods. Further, the performance of different methods cannot be easily compared. The study of environmental effects has gradually drawn more attention but much work still remains to be done.

Damage identification is one of the key components in a structural health monitoring system. Currently, there is a significant lack of research in terms of evaluating the statistical characteristics of the various damage detection algorithms proposed to date, including the one proposed in this dissertation. In contrast to the already well-accepted probability-based design philosophies, most damage identification methods are still based on a deterministic framework. Future research should lead to the integration of a statistical framework into the damage identification process. Operational variability must be quantified and confidence bounds given.

Extreme value statistics and Bayesian statistical models can be utilized to provide valuable insights to the statistical properties of the identification results.

Finite element model updating has shown to be an efficient technique for damage diagnostics. However, it is not always an easy task to guarantee the accuracy and validity of a finite element model. Some of the current challenges involve the non-uniqueness of the solution, ill-conditioning of the identification problem, and numerical convergence problems of the optimization algorithm. Although some of these challenges are inherent to the inverse identification problem to which the FEMU problem belongs, others can be solved or alleviated through the use of appropriate techniques. For example, dense sensor networks could be used to improve the spatial dimension of measured data, thus reducing the ill-conditioning of the problem. Dynamic properties other than mode shapes and frequencies could also be used to provide higher sensitivity to structural changes. Globally robust optimization algorithms can be adopted to alleviate the convergence problem.

Lastly, on a broader scale, the current approach to the structural health monitoring problem can be divided into two distinct areas: 1) Using structure dynamic properties to detect structural changes at global level, and 2) Using local NDE methods to locate and quantify damages in local components. Both approaches have their own advantages and limitations. Neither alone can satisfy all the stringent requirements from the end users. A new multi-level structural health monitoring system integrating global- and local-level diagnostics needs to be developed. Global-level techniques can be used to provide rapid condition screening, locate the proximities of the anomalies and

evaluate their influence on global structural behavior, while local NDE techniques can be applied to the identified damage region in order to better define the location and severity of the damage and its effect on local components. Mission-tailored new sensor technologies such as piezoelectric and fiber-optic sensors with wireless communication capabilities will be essential to reduce the system cost and improve efficiency.

References

AASHTO. (1998). *AASHTO LRFD Bridge Design Specifications*.

Abdel Wahab, M. M., and De Roeck, G. (1999). "Damage detection in bridges using modal curvatures: Application to a real damage scenario." *Journal of Sound and Vibration*, 226(2), 217.

Abdel Wahab, M. M., De Roeck, G., and Peeters, B. (1999). "Parameterization of damage in reinforced concrete structures using model updating." *Journal of Sound and Vibration*, 228(4), 717.

Abdo, M. A. B., and Hori, M. (2002). "A numerical study of structural damage detection using changes in the rotation of mode shapes." *Journal Of Sound And Vibration*, 251(2), 227-239.

Abe, M., and Siringoringo, D. M. (2003). "Structural health monitoring of long span bridges." Structural Health Monitoring and Intelligent Infrastructure, Z. S. Wu and M. Abe, eds., 171-179.

Adams, R. D., Cawley, P., Pye, C. J., and Stone, B. J. (1978). "A vibration technique for non-destructively assessing the integrity of structures." *Journal of Mechanical Engineering Science*, 20(2), 93-100.

Allemang, R. J. (1999). "Vibrations: Experimental Modal Analysis (Class Notes)." University of Cincinnati, Cincinnati, Ohio.

Anderson, P. (1997). "Identification of civil engineering structures using vector ARMA model," Aalborg University, Aalborg, Denmark.

ANSYS. (2004). *ANSYS 8.1 Complete User's Manual Set*, ANSYS, Inc., Canonsburg, PA.

Araki, Y., and Miyagi, Y. (2005). "Mixed integer nonlinear least-squares problem for damage detection in truss structures." *Journal of Engineering Mechanics*, 131(7), 659.

Arun, K. S. (1989). "Principal components algorithms for ARMA spectrum estimation." *IEEE Transactions on Acoustics, Speech, and Signal Processing*, 566.

Asmussen, J. C., Brincker, R., and Ibrahim, S. R. (1999). "STATISTICAL THEORY OF THE VECTOR RANDOM DECREMENT TECHNIQUE." *Journal of Sound and Vibration*, 226(2), 344.

Asmussen, J. C., Ibrahim, S. R., and Brincker, R. "Random decrement: Identification of structures subjected to ambient excitation." Santa Barbara, CA, USA, 914.

Au, F. T. K., Cheng, Y. S., Tham, L. G., and Bai, Z. Z. (2003). "Structural damage detection based on a micro-genetic algorithm using incomplete and noisy modal test data." *Journal of Sound and Vibration*, 259(5), 1081.

Baruch, M. (1997). "Modal data are insufficient for identification of both mass and stiffness matrices." *Aiaa Journal*, 35(11), 1797-1798.

Bathe, K.-J., and Bathe, K.-J. (1996). *Finite element procedures*, Prentice Hall, Englewood Cliffs, N.J.

Bendat, J. S., and Piersol, A. G. (1996). *Random Data: Analysis and Measurement Procedures*, John Wiley & Sons, New York, U.S.A.

Berman, A. (2000). "Inherently incomplete finite element model and its effects on model updating." *Aiaa Journal*, 38(11), 2142-2146.

Berman, A., and Nagy, E. J. (1983). "IMPROVEMENT OF A LARGE ANALYTICAL MODEL USING TEST DATA." *AIAA Journal*, 21(8), 1168.

Biggs, M. C. (1975). "Constrained Minimization Using Recursive Quadratic Programming." Towards Global Optimization, L. C. W. Dixon and G. P. Szergo, eds., North-Holland, 341-349.

Bolton, R., and Stubbs, N. (2001). "Modal Analysis Results for Kings Storm Composite Structure Based on 3 May 01 Test, Interim Report." Texas Engineering Experiment Station, College Station, Texas.

Brincker, R., Ventura, C. E., and Andersen, P. "Damping estimation by frequency domain decomposition." Kissimmee, FL, 698.

Brincker, R., Zhang, L., and Anderson, P. "Output-Only Modal Analysis by Frequency Domain Decomposition." *International Seminar on Modal Analysis (ISMA 25)*, Katholieke Universiteit Leuven, Belgium.

Burgueño, R. (1999). "System characterization and design of modular fiber reinforced polymer (FRP) short- and medium-span bridges," Ph.D. Dissertation, University of California, San Diego.

Burgueño, R., Karbhari, V. M., Seible, F., and Kolozs, R. T. (2001). "Experimental dynamic characterization of an FRP composite bridge superstructure assembly." *Composite Structures*, 54, 427-444.

Burgueño, R., Seible, F., Karbhari, V. M., Davol, A., and Zhao, L. (1999). "Manufacturing and Construction Support Document for the Kings Stormwater Channel Bridge." Division of Structural Engineering, University of California, San Diego.

Chakraverty, S. (2005). "Identification of structural parameters of multistorey shear buildings from modal data." *Earthquake Engineering and Structural Dynamics*, 34(6), 543.

Chapra, S. C., and Canale, R. P. (2001). *Numerical methods for engineers: with software and programming applications*, McGraw-Hill, Boston.

Chase, S. B., and Laman, J. A. (2000). "Dynamics and Field Testing of Bridges." Transportation in The New Millennium: State of the Art and Future Directions, Perspectives from the Transportation Research Board Standing Committees.

Chiang, D.-Y., and Cheng, M.-S. (1999). "Modal Parameter Identification from Ambient Response." *AIAA Journal*, 37(4), 513-519.

Cole, H. A., Jr. (1973). "ON-LINE FAILURE DETECTION AND DAMPING MEASUREMENT OF AEROSPACE STRUCTURES BY RANDOM DECREMENT SIGNATURES." *NASA Contractor Reports*, 77.

Cornwell, P., Doebling, S. W., and Farrar, C. R. (1999). "Application of the strain energy damage detection method to plate-like structures." *Journal of Sound and Vibration*, 224(2), 359.

Davol, A. (1998). "Structural characterization of concrete filled fiber reinforced shells," Ph.D. Dissertation, University of California, San Diego.

De Boor, C. (2001). *A practical guide to splines*, Springer, New York.

Doebling, S. W., Farrar, C. R., and Prime, M. B. (1998). "Summary review of vibration-based damage identification methods." *Shock and Vibration Digest*, 30(2), 91.

Doebling, S. W., Farrar, C. R., Prime, M. B., and Shevitz, D. W. (1996). "Damage Identification and Health Monitoring of Structural and Mechanical Systems from Changes in Their Vibration Characteristics: A Literature Review." *LA-13070-MS*, Los Alamos National Laboratory Report LA-13070-MS, Los Alamos, New Mexico.

Ewins, D. J. (2000). *Modal testing: theory, practice, and application*, Research Studies Press, Baldock, Hertfordshire, England; Philadelphia, PA.

Farrar, C. R. (2005). *Principles of Structural Health Monitoring, Class Notes*.

FHWA. (2001). "Reliability of Visual Inspection for Highway Bridges, Volumn I: Final Report." U.S. Department of Transportation, Federal Highway Administration.

Formenti, D., and Richardson, M. H. "Parameter Estimation from Frequency Response Measurements Using Rational Fraction Polynomials." *Proceedings of the 1st International Modal Analysis Conference*.

Friswell, M. I., and Mottershead, J. E. (1995). *Finite element model updating in structural dynamics*, Kluwer Academic Publishers, Dordrecht; Boston.

Gola, M. M., Soma, A., and Botto, D. (2001). "On theoretical limits of dynamic model updating using a sensitivity-based approach." *Journal of Sound and Vibration*, 244(4), 583.

Golub, G. H., and Van Loan, C. F. (1996). *Matrix computations*, Johns Hopkins University Press, Baltimore.

Green, P. J., and Silverman, B. W. (1994). *Nonparametric Regressionand Generalized Linear Models*, Chapman and Hall, London.

Guan, H., Batti, J., Sikorsky, C. S., and Karbhari, V. M. (2002). "Kings Stromwater Channel Bridge Load Test." *TR-2002/09*, Department of Structural Engineering, University of California, San Diego.

Guan, H., Karbhari, V. M., and Sikorsky, C. S. (2006). "Web-Based Structural Health Monitoring of a FRP Composite Bridge." *Computer-Aided Civil and Infrastructure Engineering*, 21, 39-56.

Guillaume, P., Hermans, L., and Van der Auweraer, H. "Maximum likelihood identification of modal parameters from operational data." Kissimmee, FL, USA, 1887.

Hemez, F. M. (1993). "Theoretical and Experimental Correlation Between Finite Element Models and Modal Tests in the Context of Large Flexible Space Structures," University of Colorado, Boulder, Colorado.

Hjelmstad, K. D., and Shin, S. (1996). "Crack identification in a cantilever beam from modal response." *Journal of Sound and Vibration*, 198(5), 527.

Housner, G. W., Bergman, L. A., Caughey, T. K., Chassiakos, A. G., Claus, R. O., Masri, S. F., Skelton, R. E., Soong, T. T., Spencer, B. F., and Yao, J. T. P. (1997). "Structural control: Past, present, and future." *Journal Of Engineering Mechanics-Asce*, 123(9), 897-971.

HPWREN. (2003). "High Performance Wireless Research and Education Network." San Diego.

Ibrahim, S. R., and Mikulcik, E. C. (1977). "METHOD FOR THE DIRECT IDENTIFICATION OF VIBRATION PARAMETERS FROM THE FREE RESPONSE." *Shock and Vibration Bulletin*(47), 197.

James III, G. H., Carne, T. G., and Lauffer, J. P. (1993). "The Natural Excitation Technique (NExT) for Modal Parameter Extraction From Operating Wind Turbines." Sandia National Laboratories, Albuquerque, New Mexico, U.S.A.

Janzra, M., and Nielsen, J. (2006). "A simulated annealing-based method for learning Bayesian networks from statistical data." *International Journal of Intelligent Systems*, 21(3), 335.

Juang, J.-N., and Pappa, R. S. (1985). "EIGENSYSTEM REALIZATION ALGORITHM FOR MODAL PARAMETER IDENTIFICATION AND MODEL REDUCTION." *Journal of Guidance, Control, and Dynamics*, 8(5), 620.

Kaouk, M., and Zimmerman, D. C. (1994). "Structural damage assessment using a generalized minimum rank perturbation theory." *AIAA Journal*, 32(4), 836.

Karbhari, V. M., Seible, F., Burgueño, R., Davol, A., Wernlli, M., and Zhao, L. (2000). "Structural Characterization of Fiber-Reinforced Composite Short- and Medium-Span Bridge Systems." *Applied Compoiste Materials*, 7, 151-182.

Khan, A. Z., Stanbridge, A. B., and Ewins, D. J. (1999). "Detecting damage in vibrating structures with a scanning LDV." *Optics and Lasers in Engineering*, 32(6), 583.

Kim, B.-H., Stubbs, N., and Sikorsky, C. "Local Damage Detection Using Incomplete Modal Data." *20th IMAC*, 435-441.

Kim, B. H., Stubbs, N., and Park, T. (2005). "Flexural damage index equations of a plate." *Journal of Sound and Vibration*, 283, 341-368.

Kim, J.-T., Ryu, Y.-S., Cho, H.-M., and Stubbs, N. (2003). "Damage identification in beam-type structures: frequency-based method vs mode-shape-based method." *Engineering Structures*, 25, 57-67.

Kim, J. T., and Stubbs, N. (2003). "Crack detection in beam-type structures using frequency data." *Journal of Sound and Vibration*, 259(1), 145.

Lange, K. (2004). *Optimization*, Springer, New York.

Lay, D. C. (2003). *Linear algebra and its applications*, Addison Wesley, Boston.

Lee, H. S., Park, C. J., and Park, H. W. (2000). "Identification of geometric shapes and material properties of inclusions in two-dimensional finite bodies by boundary parameterization." *Computer Methods in Applied Mechanics and Engineering*, 181(1-3), 1.

Lee, L. S.-w. (2005). "Monitoring and Service Life Estimation of Reinforced Concrete Bridge Decks Rehabilitated with Externally Bonded Carbon Fiber Reinforced Polymer (CFRP) Composites," Unviersity of California, San Diego, La Jolla, CA.

Li, S., and Brown, D. L. (1995). "Application of a unified matrix polynomial approach (UMPA) to perturbed boundary condition (PBC) testing." *Mechanical Systems & Signal Processing*, 9(1), 77.

Lifshitz, J. M., and Rotem, A. (1969). "Determination of Reinforced Unbonding of Composites by a Vibration Technique." *Journal of Composite Materials*, 3, 412-423.

Ljung, L. (1999). *System Identification theory for the user*, Prentice Hall PTR.

Lus, H., Betti, R., and Longman, R. W. (1999). "Identification of linear structural systems using earthquake-induced vibration data." *Earthquake Engineering and Structural Dynamics*, 28, 1449-1467.

Mackerle, J. (1999). "Finite-element modelling of non-destructive material evaluation: A bibliography (1976-1997)." *Modelling and Simulation in Materials Science and Engineering*, 7(1), 107.

Maeck, J., and De Roeck, G. (1999). "Dynamic Bending and Torsion Stiffness Derivation from Modal Curvatures and Torsion Rates." *Journal of Sound and Vibration*, 225(1), 153-170.

Maeck, J., Wahab, M. A., Peeters, B., De Roeck, G., De Visscher, J., De Wilde, W. P., Ndambi, J. M., and Vantomme, J. (2000). "Damage identification in reinforced concrete structures by dynamic stiffness determination." *Engineering Structures*, 22(10), 1339.

Maia, N. M. M., and Montalväao e Silva, J. M. (1997). *Theoretical and experimental modal analysis*, Research Studies Press; Wiley, Hertfordshire, England / New York.

MATLAB. (2004). *MATLAB User Guides*, The MathWorks, Inc.

Moore, M., Rolander, D., Graybeal, B., Phares, B., and Washer, G. (2001). "Highway Bridge Inspection: State-of-the-Practice Study." *FHWA-RD-01-033*, Federal Highway Administration.

National Instruments, I. (1999). "Building an Interactive Web Page with DataSocket." National Instruments.

NBIS. (1998). "National Bridge Inspection Standards." Code of Federal Regulations, U.S. Government Printing Office via GPO Access. revised April 1,1998.

Ni, Y. Q., Fan, K. Q., Zheng, G., Chan, T. H. T., and Ko, J. M. "Automatic modal identification of cable-supported bridges instrumented with a long-term monitoring system." San Diego, CA, United States, 329.

Niazy, A. M. (1991). "Seismic performance evaluation of suspesnsion bridges," Ph.D. Dissertation, University of Southern California.

NOAA. (2001). "Climatological Data, Vol 105." NOAA.

Pai, P. F., Kim, B.-S., and Chung, J. H. (2004). "Dynamics-based damage inspection of an aircraft wing panel." *Journal of Intelligent Material Systems and Structures*, 15(11), 803.

Pandey, A. K., Biswas, M., and Samman, M. (1991). "Damage Detection from Changes in Curvature Mode Shapes." *Journal of Sound and Vibration*, 145(2), 321-332.

Peeters, B., and De Roeck, G. "One year monitoring of the Z24-bridge: Environmental influences versus damage events." San Antonio, TX, USA, 1570.

Reinsch, C. H. (1967). "Smoothing by spline functions." *Numerical Mathematics*, 10, 177-183.

Ren, W.-X., and De Roeck, G. (2002a). "Structural damage identification using modal data. I: Simulation verification." *Journal of Structural Engineering*, 128(1), 87.

Ren, W.-X., and De Roeck, G. (2002b). "Structural damage identification using modal data. II: Test verification." *Journal of Structural Engineering*, 128(1), 96.

Richardson, M. H., and Formenti, D. L. "PARAMETER ESTIMATION FROM FREQUENCY RESPONSE MEASUREMENTS USING RATIONAL FRACTION POLYNOMIALS." Orlando, FL, USA, 167.

Roberts, M. J. (2004). *Signals and Systems - Analysis Using Tranform Methods and MATLAB*, McGraw Hill.

Rytter, A. (1993). "Vibration Based Inspection of Civil Engineering Structures," Ph.D. Thesis, University of Aalborg, Denmark.

Salawu, O. S. (1997). "Detection of structural damage through changes in frequency: a review." *Engineering Structures*, 19(9), 718.

SAP2000. (2004). *SAP2000 Version 9 Manuals*.

Sazonov, E., and Klinkhachorn, P. (2005). "Optimal spatial sampling interval for damage detection by curvature or strain energy mode shapes." *Journal of Sound and Vibration*, 285(4-5), 783.

Schnur, D. S., and Zabaras, N. (1990). "Finite element solution of two-dimensional inverse elastic problems using spatial smoothing." *International Journal for Numerical Methods in Engineering*, 30(1), 57.

Seible, F., Karbhari, V. M., Hegemier, G. A., Burgueño, R., Davol, A., and Zhao, L. (1998a). "Carbon/Epoxy Shell Fabrication Specification for the Kings Stormwater Channel Bridge." *TR-98/10*, Division of Structural Engineering, University of California, San Diego.

Seible, F., Karbhari, V. M., Hegemier, G. A., and Zhao, L. (1998b). "PMC Deck System Fabrication Specification for the Kings Stormwater Channel Bridge." *TR-98/09*, Division of Structural Engineering, University of California, San Diego.

Shi, Z. Y., Law, S. S., and Zhang, L. M. (1998). "Structural damage localization from modal strain energy change." *Journal of Sound and Vibration*, 218(5), 825.

Shi, Z. Y., Law, S. S., and Zhang, L. M. (2000). "Structural damage detection from modal strain energy change." *Journal of Engineering Mechanics*, 126(12), 1216.

Sikorsky, C., Stubbs, N., Park, S., Choi, S., and Bolton, R. "Measuring Bridge Performance using Modal Parameter Based Non-Destructive Damage Detection." *the 17th International Modal Analysis Conference*, 1223-1229.

Sohn, H., Farrar, C. R., Hemez, F. H., Shunk, D. D., Stinemates, D. W., and Nadler, B. R. (2003). "A Review of Structural Health Monitoring Literature: 1996-2001." *LA-13976-MS*, Los Alamos National Laboratory Report LA-13976-MS, Los Alamos.

Stubbs, N. (1990). "Global Non-Destructive Damage Evaluation in Solids." *The International Journal of Analytical and Experimental Modal Analysis*, 5(2), 67-79.

Stubbs, N., and Kim, J. T. (1996). "Damage localization in structures without baseline modal parameters." *AIAA Journal*, 34(8), 1644-1649.

Stubbs, N., and Park, S. (1996). “Optimal Sensor Placement for Mode Shapes Via Shannon’s Sampling Theorem.” *Microcomputers in Civil Engineering*, 11, 411-419.

Teughels, A. (2003). "Inverse Modelling of Civil Engineering Structures Based on Operational Modal Data," Catholic University of Leuven, Leuven, Belgium.

Teughels, A., De Roeck, G., and Suykens, J. A. K. (2003). "Global optimization by coupled local minimizers and its application to FE model updating." *Computers and Structures*, 81(24-25), 2337.

Teughels, A., Maeck, J., and De Roeck, G. (2002). "Damage assessment by FE model updating using damage functions." *Computers and Structures*, 80(25), 1869.

Udwadia, F. E. (2005). "Structural identification and damage detection from noisy modal data." *Journal of Aerospace Engineering*, 18(3), 179.

Van Overschee, P., and De Moor, B. (1993). "Subspace algorithms for the stochastic identification problem." *Automatica*, 29(3), 649.

Vandiver, J. K. (1977). "DETECTION OF STRUCTURAL FAILURE ON FIXED PLATFORMS BY MEASUREMENT OF DYNAMIC RESPONSE." *JPT, Journal of Petroleum Technology*, 29, 305.

Vernon, F. L. "Wireless networks and sensor connectivity: HPWREN." *2001 SINE conference*.

Vold, H., Kundrat, J., Rocklin, G. T., and Russell, R. "MULTI-INPUT MODAL ESTIMATION ALGORITHM FOR MINI-COMPUTERS." Detroit, MI, Engl, 820194.

Welch, P. D. (1967). "Use of fast fourier transform for estimation of power spectra -- Method based on time averaging over short, modified periodograms." *IEEE Transactions on Audio and Electroacoustics*, AU-15(2), 70.

West, W. M. "Illustration of the use of modal assurance criterion to detect structrual changes in an orbiter test specimen." *Air Force Conference on Aircraft Structural Integrity*, 1-6.

Yam, L. H., Li, Y. Y., and Wong, W. O. (2002). "Sensitivity studies of parameters for damage detection of plate-like structures using static and dynamic approaches." *Engineering Structures*, 24(11), 1465.

Yeo, I., Shin, S., Lee, H. S., and Chang, S.-P. (2000). "Statistical damage assessment of framed structures from static responses." *Journal of Engineering Mechanics*, 126(4), 414.

Yoshimoto, R., Mita, A., and Okada, K. (2005). "Damage detection of base-isolated buildings using multi-input multi-output subspace identification." *Earthquake Engineering and Structural Dynamics*, 34(3), 307.

Yuan, P., Wu, Z., and Ma, X. (1998). "Estimated mass and stiffness matrices of shear building from modal test data." *Earthquake Engineering & Structural Dynamics*, 27(5), 415.

Yuen, M. M. F. (1985). "NUMERICAL STUDY OF THE EIGENPARAMETERS OF A DAMAGED CANTILEVER." *Journal of Sound and Vibration*, 103(3), 301.

Zang, C., Chen, G., Ewins, D. J. "Finite Element Model Updating with Modal Data." *The International Modal Analysis Conference*, St. Louis.

Zhang, Q. W., Chang, C. C., and Chang, T. Y. P. (2000). "Finite element model updating for structures with parametric constraints." *Earthquake Engineering and Structural Dynamics*, 29(7), 927.

Zhao, L. (1999). "Characterization of deck-to-girder connections in FRP composite superstructures."

Zhao, L., Karbhari, V. M., and Seible, F. (2001a). "Results of test of the Kings Stormwater Channel Bridge Under Paver Loads." *TR 2001/05*, Department of Structural Engineering, University of California, San Diego.

Zhao, L., Sikorsky, C., Seible, F., and Karbhari, V. M. "Field Monitoring of the Kings Stormwater Channel Advanced Composite Bridge." *6th Caltrans Seismic Research Workshop*, Sacramento.